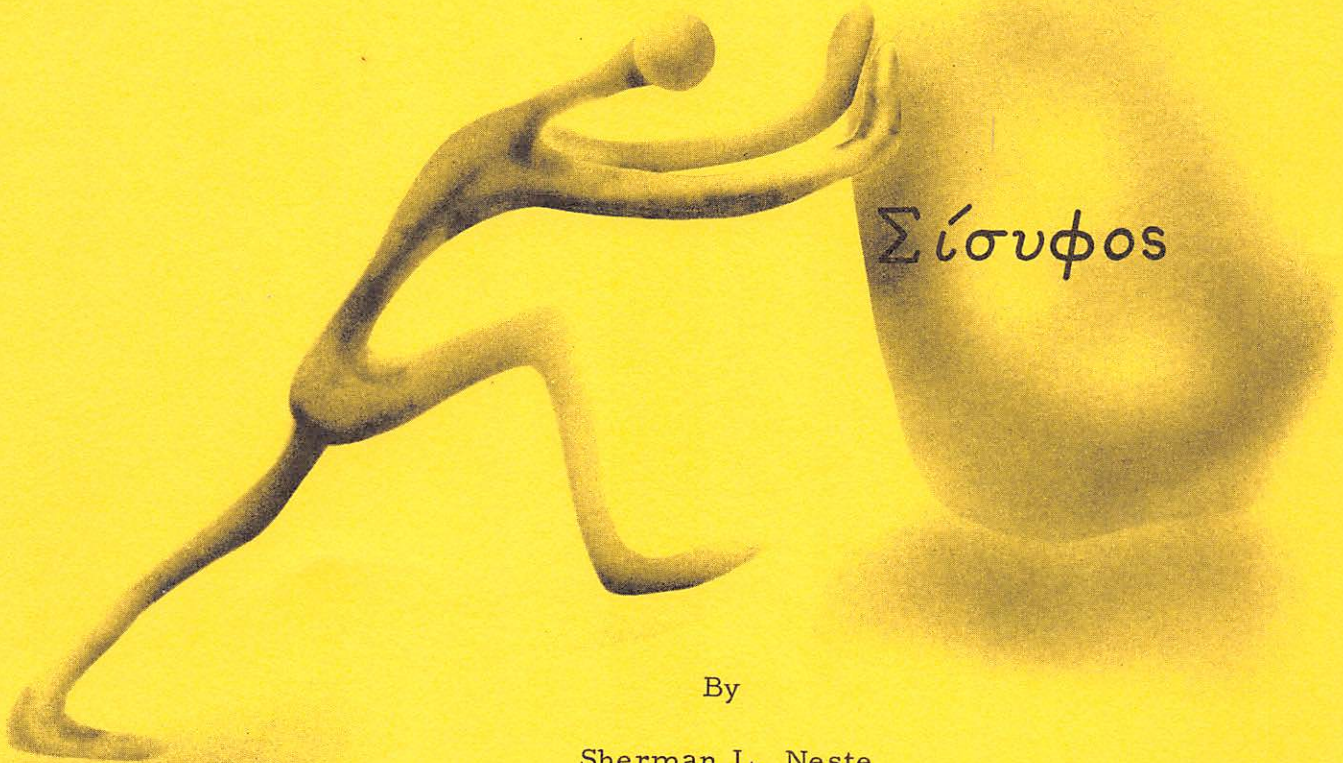


FINAL REPORT

PIONEER F/G (10/11) DATA ANALYSIS OF THE
ASTEROID/METEOROID ASTRONOMY EXPERIMENT

JUNE 1976



By

Sherman L. Neste
Robert K. Soberman
Kurt Lichtenfeld

PREPARED UNDER CONTRACT NAS 2-6559

NATIONAL AERONAUTICS AND SPACE ADMINISTRATION

SPACE SCIENCES LABORATORY



**GENERAL
ELECTRIC**
SPACE DIVISION

JUNE 1976

PIONEER F/G (10/11) DATA ANALYSIS OF THE
ASTEROID/METEOROID ASTRONOMY EXPERIMENT

By

Sherman L. Neste
Robert K. Soberman
Kurt Lichtenfeld

Prepared under Contract NAS 2-6559
GENERAL ELECTRIC COMPANY
Space Sciences Laboratory
Philadelphia, Pennsylvania

For

NATIONAL AERONAUTICS AND SPACE ADMINISTRATION

TABLE OF CONTENTS

SECTION		PAGE
	SUMMARY	vii
I.	INTRODUCTION	1
II.	BACKGROUND	2
	A. Near-Earth Meteoroid Astronomy	2
	B. Asteroid Astronomy	17
	C. Asteroid Belt Models	23
III.	THE ASTEROID/METEOROID DETECTOR ON PIONEERS 10 AND 11	30
	A. Pioneer Spacecraft and Mission Profile	30
	B. Concept of the Asteroid/Meteoroid Detector	33
	C. System Design Considerations	40
	D. Optical Subsystem	41
	E. Electronics Subsystem	53
IV.	OBSERVATIONAL RESULTS OF THE ASTEROID/METEOROID DETECTOR	58
	A. Description of Data Obtained	58
	B. Data Reduction Procedure	61
V.	ANALYSIS OF DATA AND PRESENTATION OF RESULTS	70
	A. Analysis Procedure	70
	B. Size and Spatial Distribution Obtained From Measure- ments on Pioneer 10	77
	C. Gegenschein Brightness Obtained From Measurements on Pioneer 10	82
	D. Size Distribution Obtained From Measurements on Pioneer 11	86

TABLE OF CONTENTS (Continued)

SECTION	PAGE
VI. CONCLUSIONS	90
REFERENCES	92
APPENDIX A: LIGHT REFLECTION FROM PARTICLES	
APPENDIX B: AMD CALIBRATION AND SENSITIVITY MEASUREMENTS	
APPENDIX C: DATA MEASURED BY THE AMD	
APPENDIX D: DERIVATION OF EQUATIONS RELATING PARTICLE RANGE, SIZE AND TRANSIT TIME	
APPENDIX E: TABULATION OF PARTICLE CONCENTRATION	
APPENDIX F: COMPUTER SIMULATION OF ANALYSIS PROCEDURE	
APPENDIX G: DERIVATION OF GEGENSCHNEIDEN BRIGHTNESS EQUATION	
APPENDIX H: CALCULATION AND TABULATION OF GEGENSCHNEIDEN BRIGHTNESS	
APPENDIX I: LIST OF SYMBOLS	
APPENDIX J: PUBLICATIONS OF AMD RESULTS	

LIST OF TABLES

Table		PAGE
1.	Received Data from a Typical AMD Event	60
Appendix Tables		
C1.	Entry and Exit Times for Events Measured by the AMD on Pioneer 10	
C2.	Backgrounds and Peak Signals for Events Measured by the AMD on Pioneer 10	
C3.	Entry and Exit Times for Events Measured by the AMD on Pioneer 11	
C4.	Backgrounds and Peak Signals for Events Measured by the AMD on Pioneer 11	
E1.	Particle Concentration from 1-2 AU Determined from Pioneer 10	
E2.	Particle Concentration from 2-3.5 AU Determined from Pioneer 10	
E3.	Particle Concentration from 1-3.5 AU Determined from Pioneer 11	
H1.	Gegenschein Brightness as a Function of Heliocentric Distance	

LIST OF ILLUSTRATIONS

Figure	Page
1. Cross Sections of the Capacitor and Pressurized-Cell Types of Meteoroid Detector	11
2. Cross Section of a Combined Thin-Film Ionization and Acoustic Impact Detector that can Measure the Particles Time of Flight	12
3. Illustration of the Disparity Between Early Meteoroid Flux Measurements	14
4. Current Best Estimate of the Cumulative Terrestrial Influx as a Function of Particle Mass and Diameter	15
5. Frequency Curve of Eccentricities from the Palomar-Leiden Survey	19
6. Frequency Curve of Inclinations, not Corrected for Completeness from the Palomar-Leiden Survey	19
7. Cumulative Number of Asteroids Defined by the Revised MDS and PLS Data	21
8. Various Asteroidal Mass Distributions Models at 2.5 AU	26
9. Asteroid Radial Distribution	27
10. Asymmetry of the Asteroid Belt with Heliocentric Longitude, λ	28
11. Pioneer Mission Profile	31
12. Pioneer Spacecraft	32
13. Two-Dimensional Model of the AMD Concept	35
14. Model of the AMD System	37
15. Geometry of the AMD System Illustrating the Unknown Variables	37
16. Variation of Event Rate with Field-of-View and Aperture	42
17. Variation of Image Shape Across the Field-of-View	44

	Page
18. Mirror, Optical System	45
19. Telescope Cross Section	46
20. Sensor Assembly	48
21. AMD Sensor, Front View	49
22. AMD Sensor, Rear View	50
23. Preamplifier Schematic	51
24. AMD Electronics	56
25. AMD Block Diagram	57
26. Background Scan From Pioneer 10 (Channels A and B)	63
27. Background Scan From Pioneer 10 (Channels C and D)	64
28a. Events Detected by AMD on Pioneer 10 as a Function of Heliocentric Distance	68
28b. Events Detected by AMD on Pioneer 11 as a Function of Heliocentric Distance	69
29. Examples of Three-Fold Coincidence	72
30. Sample of the Sensitive Volume Variation During One Day of Pioneer 10 Mission	74
31. Variation in Sensitive Volume During Transit to 3.5 AU on Pioneer 10	76
32. Particle Size Distribution for Five Segments of Preasteroid Belt Region From Pioneer 10	78
33. Particle Size Distribution for Three Regions of the Asteroid Belt From Pioneer 10	79
34. Combined Particle Size Distributions From Pioneer 10 (1.0-3.5 AU)	81
35. Mass Concentration Due to All Particles and the Smallest Particles From Pioneer 10	83
36. Variation of Gegenschein Brightness with Heliocentric Distance From Pioneer 10	85
37. Particle Size Distribution From Pioneer 11 (1.0-3.5 AU)	88
38. Particle Size Distributions From Pioneers 10 and 11	89

Appendix Figures	Page
B1. Absolute Response of the Pioneer 10 Asteroid/ Meteoroid Detector	113
B2. Relative Response of the Pioneer 10 Asteroid/ Meteoroid Detector	114
B3. Minimum Detectable Signal	120
B4. Equipment Used for Simulating and Detecting Particles in the Laboratory	121
F1. Results of Computer Simulation of Data Analysis Techniques	143
G1. Spatial Density for Gegenschein Brightness Calculation	145
G2. Volume Element for Gegenschein Brightness Calculation	146

SUMMARY

The techniques and instrumentation employed to investigate the interplanetary particulate environment are summarized. The models which resulted from these investigations are presented to provide a basis for discussing the results of measurements made from the Pioneer 10 and 11 spacecraft by the Asteroid/Meteoroid Detector (AMD).

The spatial concentration and size distribution for particulates measured in situ by the AMD between 1.0 and 3.5 AU are presented. The size distribution includes particle radii from about 35 μm to 10 cm. Extrapolations from the smallest particle sizes measured show good agreement with the results of the particle penetration detector carried on the same spacecraft.

Pioneer 10 results indicate that a single size distribution seems appropriate for all but the smallest sizes measured. The exponent of the radius dependency in the region of the asteroid belt varies from approximately -1.7 for the smallest to approximately -3.2 for the largest sizes measured. In the region from 1 to 2 AU the exponent approaches -0.75 for the smallest sizes. The data also show evidence for the existence of a planetary sweeping effect in the vicinity of Mars orbit and in the near earth vicinity.

The zodiacal light brightness as measured from Pioneer 10 is found to vary approximately as the inverse square of solar distance out to about 2.25 AU and then decreases more rapidly. This is the type of variation measured by photometers on the same spacecraft. The absolute value of the zodiacal light brightness is found to be too high by a factor of ten. A possible explanation for this discrepancy is offered.

Results from the AMD on Pioneer 11 show good agreement with the concentrations derived from the Pioneer 10 data to within about a factor of two. However, the number of events measured by the AMD on Pioneer 11 was considerably less than the number measured from Pioneer 10. Thus, it was not considered statistically valid to divide the Pioneer 11 data into regimes of heliocentric distance to obtain the zodiacal light brightness variation.

I. INTRODUCTION

The objective of the Asteroid/Meteoroid experiment was to determine the meteoroid and asteroid environment encountered in the region of the solar system beyond the earth's orbit. This report presents the results of the data obtained by the Asteroid Meteoroid Detector (AMD) on Pioneers 10 and 11. In order to place the AMD experiment in proper perspective, a brief summary of the techniques and instrumentation previously employed to investigate the interplanetary particulate environment is given in Section II. The environmental models which resulted from these investigations are presented to provide a basis for discussing the results of measurements made by the AMD from the Pioneer 10 and 11 spacecraft.

Section III develops the characteristics of the present approach by relating the electrical, optical and mechanical aspects of the AMD instrument to the basic concept by which the instrument functions. Section IV describes the observational results of this experiment together with the data reduction procedure. Section V details the analysis procedure and states the conclusions regarding the interplanetary particulate population which are a logical consequence of the analysis. The conclusions of the present investigation are summarized in Section VI.

II. BACKGROUND

II. A. Near-Earth Meteoroid Astronomy

Meteoroids, the small particles which inhabit the solar system, were undoubtedly first observed as "shooting stars" when their trajectories intersected with the position of the earth and they burned up in the earth's atmosphere. The term meteor, which is of Greek origin meaning "phenomenon in the sky", was used to describe this observable result of meteoroid interaction with the atmosphere. Occasionally, if the meteoroid were initially large enough, some portion of it would survive the transit through the earth's atmosphere and be discovered as a meteorite, usually by accident. However, it was not until the years following the great Leonid shower of 1883 that an extraterrestrial origin was ascribed to the bodies producing the meteor phenomena. Since that time, the investigations designed to determine the nature and origin of these extraterrestrial bodies have developed into a complex and extensive program of meteoroid astronomy. The initial scientific motives for conducting the investigations have, more recently, been joined by the need to obtain engineering data on the particulate environment for spacecraft hazard evaluation.

The techniques used to obtain data on the meteor phenomena were, of course, limited by the state of the current technology. As a result, there was a logical progression in the complexity of the concepts and instrumentation used in the investigations. The earliest astronomical tool, the telescope, was of relatively little use due to its narrow field of view. Thus, the first observations were best made with the naked eye.

A rather extensive catalog of hourly meteor rates (C. P. Olivier, 1960; 1965) has been compiled from data collected by the American Meteor Society from the period 1901 to 1963. The data was obtained by observers, mostly Japanese and American, who recorded the number of meteor trails observed during a given period of time. However, observations of this type are subject to several inherent sources of error which can only be minimized by a large data sample. For example, two observers viewing the same area of sky from the same location would probably report different rates due to differences in eye sensitivity. Also, the rates show a decrease during the last hour of observation for a given night due either to the approach of morning twilight or the probable eye fatigue of the observer.

In addition to determining the meteor influx, the observers in many cases also plotted or described the observation. During the time required for plotting, any meteors appearing would be missed so it was necessary to apply a correction to the number of reported meteors. Another type of correction was needed to account for the visibility conditions during the observation period. Of course, even after applying these corrections, some uncertainty must be ascribed to the results.

If the same meteor is seen by two observers a few miles apart it is possible to determine the actual height and location of the meteor by triangulation. However, the most important parameter for determining the origin of meteors, the velocity, could rarely be determined to an accuracy greater than 50 per cent by visual observations. Considering the fact that an error of 41 per cent in the heliocentric velocity spells the difference between a circular and parabolic orbit, it was obvious that a more accurate method of measuring the velocity was needed.

It was not until 1936, however, that a systematic program for photographing meteors from two stations was begun by the Harvard photographic meteor project. The cameras were equipped with rotating shutters to periodically interrupt the meteor trail to introduce a time scale in the measurements so that velocity information could be obtained. The first results were published in 1938 (Whipple) for six meteors photographed from the two stations. Five of the meteors were shown to be elliptic (the other was uncertain) which was the first experimental indication that meteors were probably members of the solar system. Due to their high precision, the results obtained from twin station photography completely superseded previous results obtained from visual observations. The Harvard group continued their work until 1958 and their results probably comprise the most extensive source of photographic meteor data.

Another program for meteor observation was begun in 1963 with the Prairie Meteorite Network (McCrosky and Boeschenstein, 1965). It consists of a system of 16 camera stations located in the midwestern United States designed to obtain data on very bright meteors. The stations were designed for automatic operation and required attention only when the film supply was exhausted, i. e., every few weeks. An observation was considered successful if the same meteor trail was recorded by at least two stations. The trails recorded by the two cameras could be converted from the film coordinate system by utilizing the known coordinates of the stars recorded on the films. Thus, a plane determined by the trail and the observing station could be defined. The intersection of the planes determined from two stations served to define the meteor trajectory. The goals of the Prairie Network were to obtain the trajectory of the body, to extrapolate it backward to an orbit, and to extrapolate it forward to an impact point, and if

possible, recover the resulting meteorite. In order to obtain this latter objective, the greatest possible precision was required in determining the spatial coordinates near the end of the visible trajectory of the body. This, of course, is also the region of the trajectory which is most subject to the distorting effects of gravity and atmospheric refraction, which make the measurement more difficult.

Another technique for detecting meteors involves active radar systems. A meteoroid entering the earth's atmosphere will collide with air molecules in its path, ionize some of them, and thus create an ionized trail. If this ionized trail is sufficiently dense and persists long enough, it can be detected by radio equipment; hence, the name radio meteor. However, because of selection effects only meteors of intermediate velocity can be detected by this method. The fastest meteors produce ionized trails at high altitudes which diffuse into the background before being detected. The slowest meteors, on the other hand, do not produce a sufficiently intense electron trail to be detected.

An extensive program for observing meteors by this method was begun in 1962 with the Radio Meteor Project located at Havana, Illinois. The project was initiated at Harvard College Observatory under the direction of Dr. Whipple and transferred to the Smithsonian Astrophysical Observatory in 1966. The detection system consisted of eight stations designed to obtain multiple observations of ionization trails resulting from meteoroids entering the earth's atmosphere. The system was essentially an enlargement of one constructed at Jodrell Bank, England several years earlier, but was capable of detecting much fainter meteors. As a result of the increased sensitivity, the Havana network could observe much slower meteors than was previously possible and, therefore, less bias (elimination of slow meteors) was introduced in the measurements.

The results of the Radio Meteor Project comprise the largest and most accurate collection of radio meteor distributions available at the present time (Cook, et al., 1972; Southworth and Sekanina, 1973).

The detection methods discussed to this point have been indirect in that it was the interaction of the body with the atmosphere which was observed. There are, however, a large number of measurement techniques, most of which have been more recently developed, in which there is a direct interaction between the body of interest and the measuring instrument. The development of rocket and satellite technology was, of course, essential to the implementation of these methods. These direct measurements are basically of two types: particle collection experiments and impact sensitive experiments.

The early collection measurements consisted of exposing specially prepared surfaces to the space environment during a rocket or balloon flight and then returning them to the laboratory where they were analyzed using optical or electron microscopes. A major problem, however, was to prevent the test surfaces from being contaminated during the exposure as well as during laboratory preparation and examination. The data obtained from these experiments has been severely attacked on the grounds that most particles studied were not of extraterrestrial origin but were contaminants picked up in the laboratory (Farlow, 1968).

Attempts were made to relate the results of the particle collections made within the earth's atmosphere to an extraterrestrial particle flux. However, due to the uncertainty of the effects of vertical winds which can greatly affect the number and size distribution of particles in the atmosphere (Soberman, 1967) such correlations are no longer deemed valid. It was agreed by the Cosmic Dust Panel of the International Committee on Space

Research (COSPAR) that particle collections within the atmosphere should be reported as concentrations per unit volume rather than relating them to the extraterrestrial flux.

Difficulties similar to those mentioned above also exist for particle collections made from earth orbiting satellites. Specifically, the criticism stems from the fact that contaminants are known to exist in the vicinity of the spacecraft, especially manned spacecraft. Thus, all collection results are given minimum weight in determining the extraterrestrial particle flux.

Experiments requiring that the object forcefully interact with the measuring apparatus range from simple cratering experiments to complex impact ionization experiments. Usually, the extent of the information obtained regarding the characteristics of the impacting particle is related to the complexity of the experiment.

The first type of impact experiment consisted of attaching an acoustic detector (piezoelectric or capacitive-type microphone) to a metal plate. The detectors were originally mounted on the skin of the rocket or satellite and any impact on the vehicle could be detected. However, it was soon noticed that mechanical and thermal stresses in the vehicle were also picked up. As a result, future detectors were mounted on a calibrated plate acoustically isolated from the vehicle.

A more serious problem associated with the results of acoustic detectors involves their sensitivities. Early results of U. S. scientists indicated that the detector was momentum sensitive (McCracken, et al., 1961). However, Soviet scientists reported that the detector was energy sensitive (Nazarova, 1960). The discrepancy was somewhat resolved by further measurements which indicated that at low velocities (less than 4 km/sec) the detector was momentum sensitive while at higher velocities

(greater than 10 km/sec) the signal appeared more closely related to energy.

However, there still exists controversy over the validity of the acoustic detector results. Some investigators (Nillson, 1966; Konstantinov, et al., 1967) felt that the acoustic sensors were measuring "creaking" due to thermal gradients. On the other hand, thermal stability tests have shown (Bohn, et al., 1968) that thermal noise could not account for a significant number of the events recorded. More recently, studies have shown that the piezoelectric acoustic detectors are sensitive to high-energy cosmic rays (Sitte, 1971; Berg and Gerloff, 1971). Thus, in view of the difficulties and uncertainties associated with this type of sensor the data obtained by them is only used to set an upper limit to the meteoroid flux.

A relatively simple method of obtaining information on the meteoroid population is to examine a surface which has been exposed to the space environment for a known length of time. Meteoroids impacting the surface will produce craters which can be analyzed as to number, diameter and depth. Dividing the number of craters by the product of the area and exposure time will yield the flux per unit area. Relationships between the crater dimensions and the velocity and density of the impacting object have been experimentally determined in the laboratory (Fish, 1965). Thus, it is possible to estimate the flux of meteoroids as a function of meteoroid mass by analyzing the crater characteristics.

Results utilizing the crater technique were first obtained from Project Gemini (Hemenway and Hallgren, 1968). Specially prepared stainless steel surfaces were left on the Agena target vehicle of the Gemini 8 mission and subsequently recovered four months later by an astronaut during extravehicular activity on

the Gemini 10 mission. Three craters were identified as being of meteoric origin. Cratering results were also obtained from analysis of fourteen windows of the Gemini spacecraft (Zook, et al., 1970). Although several microscopic pits were discovered on each window, only one was deemed of meteoric origin. However, problems in interpreting the data were encountered on these experiments due to contaminants on the surfaces.

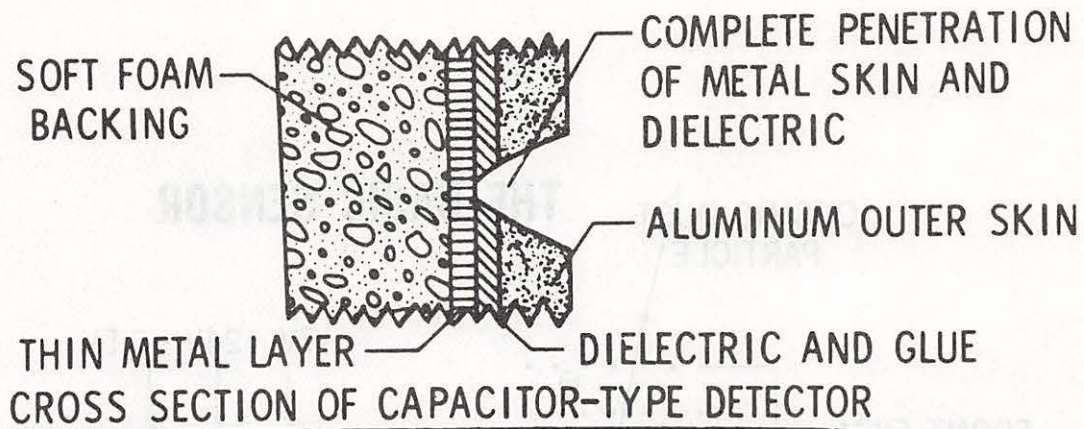
The most extensive experiment designed to determine the meteoroid flux in the near earth region was probably the penetration type detector of Project Pegasus. The program consisted of a series of three satellites, each instrumented with a total detecting area of 194.5 m^2 . The sensors consisted of capacitor detectors, which were momentarily discharged by the ionization produced when a micrometeoroid penetrated the sensor. The capacitors consisted of aluminum sheets ($0.5 \text{ m} \times 1 \text{ m}$) with thicknesses of $40, 200$ and 400μ bonded to a 12μ layer of mylar dielectric with a 0.67μ copper layer on the opposite surface to form the other condenser plate. The varying thickness of the aluminum sheets permitted the flux to be determined as a function of particle mass. A major problem was again that of calibrating the sensor, i. e., determining the minimum projectile mass required to penetrate each thickness of aluminum (Naumann, et al., 1969). The penetration results of the Pegasus project were used in setting the design criteria for the Apollo missions.

The pressure cell type of penetration detector was used on Explorers XVI and XXIII, the Lunar Orbiter satellites, and is currently in use on Pioneers 10 and 11 (Kinard and O'Neal, 1971). These detectors consist of arrays of pressure cells which require that the impacting particle cause sufficient damage to the cell to produce a gas leak. The pressure cell detector is thus somewhat more sensitive than a capacitor type detector of the

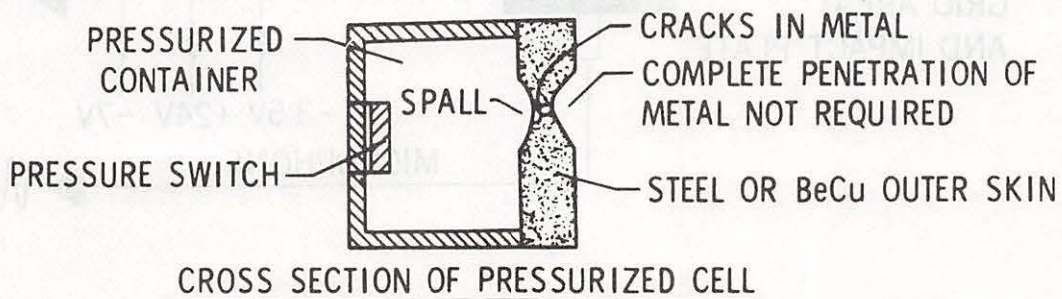
same skin composition and thickness since a complete penetration is not required for a detection (see Figure 1).

In order to reduce the uncertainties which are inherent in any single type of detector, experiments utilizing multiple techniques have been flown. The most sophisticated experiment of this type was flown on Pioneers 8 and 9 (Berg and Gerloff, 1971). The sensor combines a thin film ionization detector and an acoustic impact detector as shown in Figure 2. A meteoroid penetrates the thin front film and then proceeds to the impact plate. The plasma generated by the impact or penetration is detected on the wire grids as shown. In addition, the time of flight between the front and rear films is measured to give an indication of the particle velocity. The films are also segmented, like chess boards, so that some directional information can be obtained. The directional and time of flight information has been used to approximate orbits of some particles (Berg and Gerloff, 1971). However, as mentioned earlier, the piezoelectric acoustic detectors of the type used in this experiment have been shown to be sensitive to noise associated with high energy cosmic rays.

As is apparent from the foregoing discussion, most in situ detection techniques consist of exposing a specially prepared surface to the space environment and recording the number of particle "interactions" with that surface during a given period of time. The surface is usually sensitive to particles of a minimum mass and larger, so that it is logical to express the flux in cumulative terms, i. e., number of particles/unit area/unit time of mass m and larger. Theoretically, if instruments of varying sensitivity are used to measure the meteoroid flux, it should be possible to determine a flux as a function of mass. However, if the results of the many measuring techniques (not all of which were discussed above) are integrated into a single flux-mass diagram the disper-



Capacitor Type



Pressure Cell Type

Figure 1. Cross Sections of the Capacitor and Pressurized - Cell Types of Meteoroid Detector

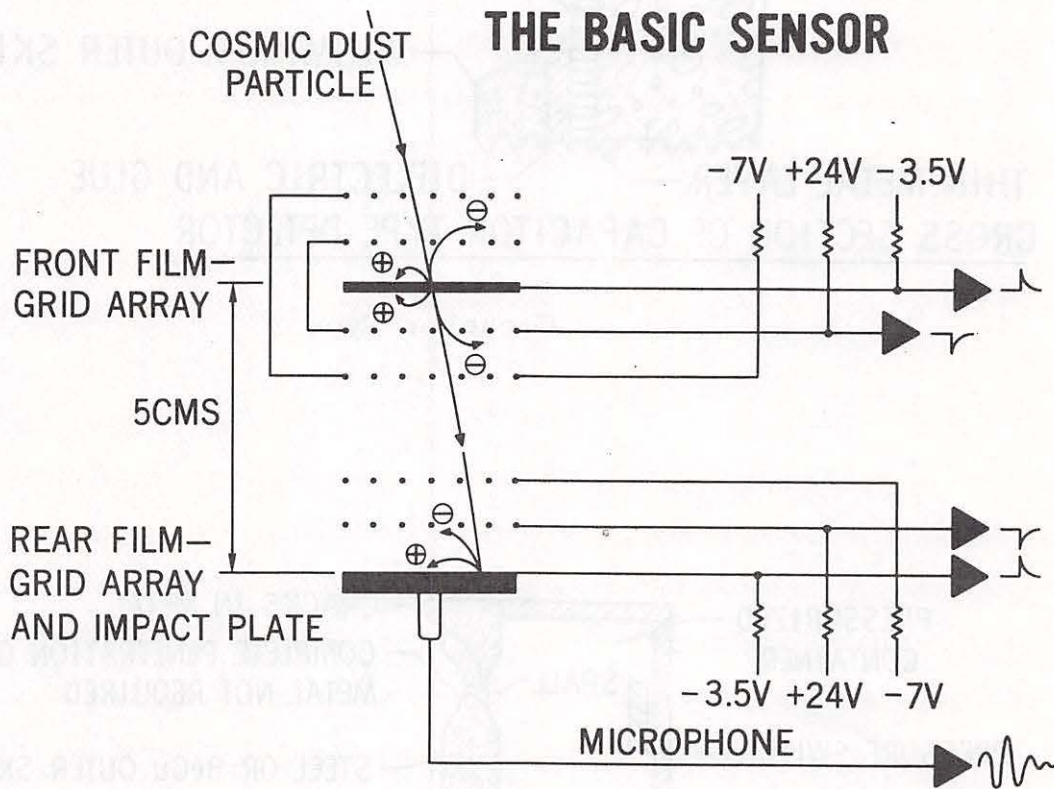


Figure 2. Cross Section of a Combined Thin-Film Ionization and Acoustic Impact Detector that can Measure the Particles Time of Flight. (After Berg and Gerloff [1971].)

sion in the results is several orders of magnitude (see Figure 3).

Obviously, it was necessary to derive a better estimate of the near-earth meteoroid flux which could be used as a design criterion for space vehicles. By considering all the available data and weighting the measurements according to reliability, such an estimate for masses between 1 and 10^{-12} gram was derived (Cour-Palais, 1969). The resulting curve is shown in Figure 4 along with specific data points for some experiments. The uncertainty limits placed on the curve and the extension to smaller masses were estimated by Soberman (1971). The curve can be expressed mathematically as (Cour-Palais, 1969):

$$\log_{10} \Phi = -14.37 - 1.21 \log_{10} m, \quad 10^{-6} \leq m \leq 10^0 \quad (1)$$

$$\log_{10} \Phi = -14.34 - 1.58 \log_{10} m - 0.063 (\log_{10} m)^2, \quad 10^{-12} \leq m \leq 10^{-6}$$

At the time of the initiation of the Pioneer missions to Jupiter the curve of Figure 4 represented the best preflight estimate of the environment to be encountered in the near-earth region. Preflight models predicted that the variation of the interplanetary particulate concentration could be described by a simple power law of the form S^{-k} where S is heliocentric distance. The value assigned to k depended on the source mechanism for the particles. Most of the models were derived from earth-based meteor measurements which gave values of k ranging from 1 to 2 (e.g., Southworth, 1967). As a modification to such a power law spatial distribution, Öpik (1951) predicted that there would be a decrease in the small particle concentration in the vicinity of a planet's orbit due to collisions of the particles with the planet as they slowly spiral into the sun under the Poynting-Robertson effect (Robertson, 1937). Another major question con-

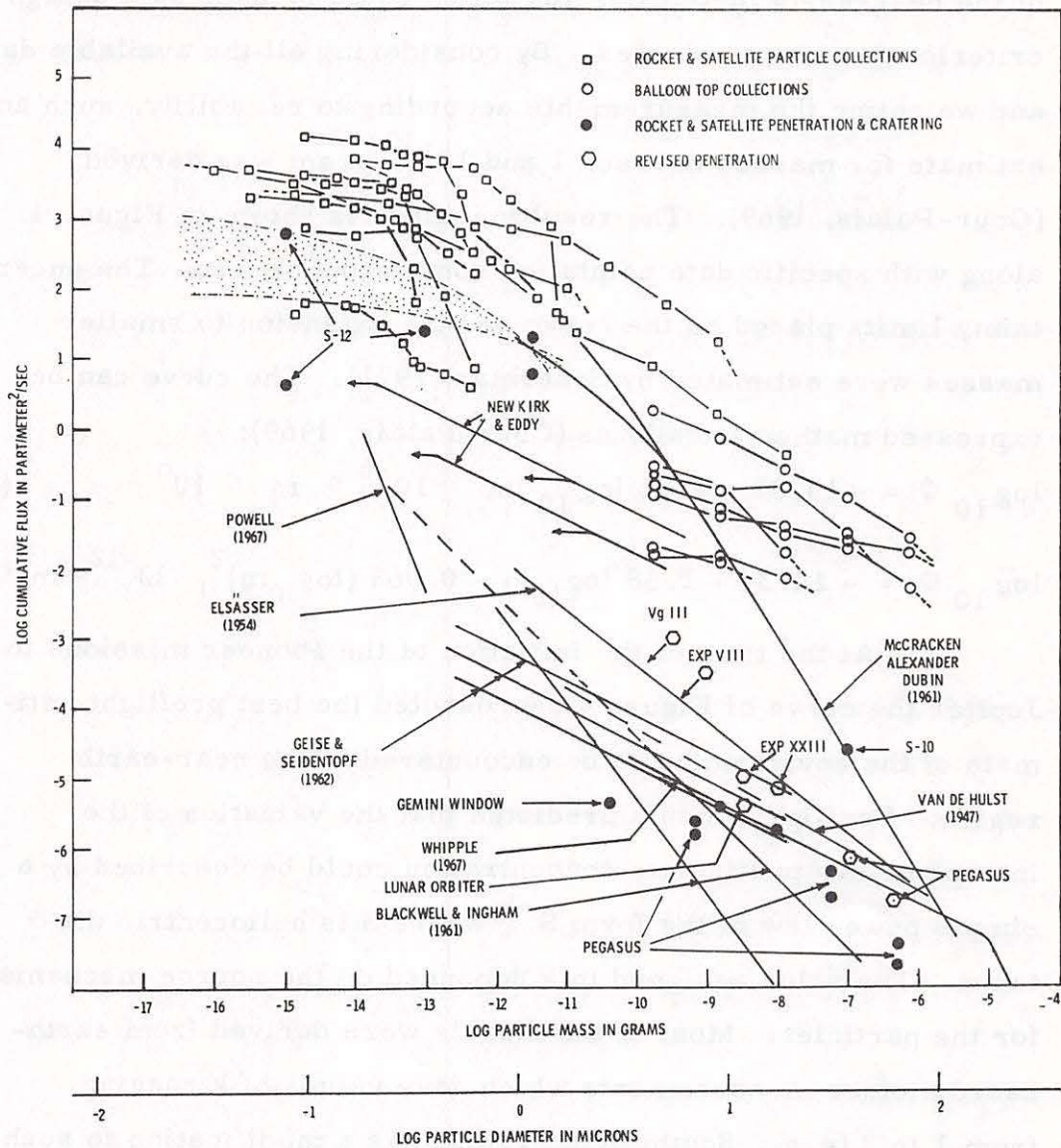


Figure 3. Illustration of the Disparity Between Early Meteoroid Flux Measurements (Density = 3 gm/cm^3)

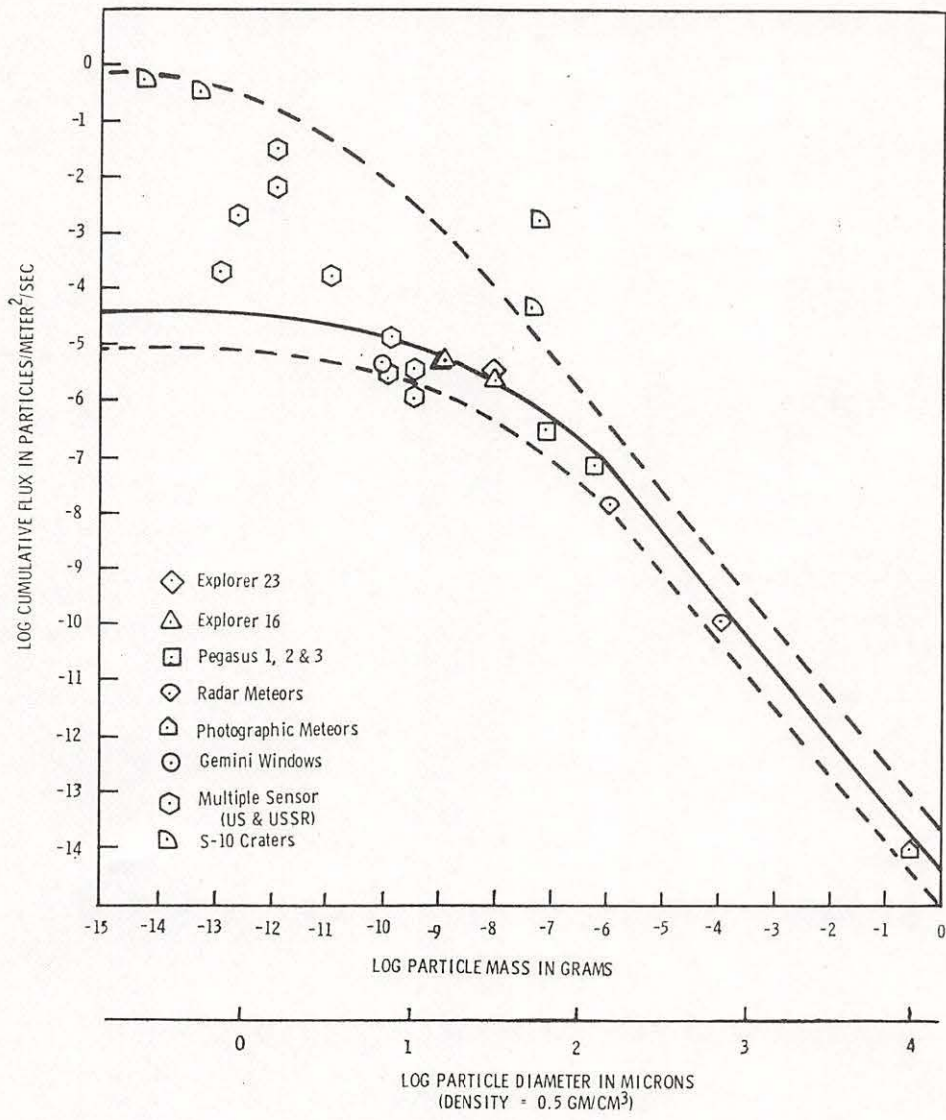


Figure 4. Current Best Estimate of the Cumulative Terrestrial Influx as a Function of Particle Mass and Diameter. For mass > 10⁻¹² gram, the curve is after the NASA Meteoroid Environment Model, 1969.

II. B. Asteroid Astronomy

The term asteroid, meaning "starlike", is generally applied to the group of bodies found moving about the sun between the orbits of Mars and Jupiter. The history of the study of asteroids actually began with the search for a "missing planet" which was predicted to exist at 2.8 AU by the Titus-Bode relation for planetary distances from the sun. The expression related the heliocentric distances of the planets to that of the earth by the equation:

$$S = 0.4 + 0.3 \times 2^n \quad (2)$$

where $n = -\infty$ for Mercury, 0 for Venus, 1 for Earth, 2 for Mars, etc. The missing planet would have $n = 3$ ($S = 2.8$ AU).

At a congress in 1796 a group of astronomers decided to begin a systematic search for the predicted planet. However, the first discovery of an asteroid was not achieved by members of that group, but by Piazzi at Palermo in 1801 who was making observations for compiling a new star catalog. On successive nights of observation he noticed that one of the "stars" had moved relative to the others, and thus accidentally discovered the first, and largest, asteroid which he named Ceres. By 1807, three more bright asteroids, Pallas, Juno and Vesta had been discovered. It was not until 1845 that another asteroid was discovered, but since that time the number of known asteroids has increased at an average rate of several per year. At the present time, orbital elements have been calculated for approximately 1,700 asteroids, while over 2,000 additional asteroids have been observed.

Photographic techniques have accounted for a majority of observational data on asteroids. Long time-exposures using telescope-camera combinations which are synchronized with the motion of the stars relative to the earth reveal the asteroid as a trailed image on the photographic plate. The process can essentially be reversed by guiding the telescope to follow the asteroid

and produce trailed images for the stars.

Prior to the flights of the Pioneer spacecraft, all information regarding the characteristics of the asteroid population had been obtained using earth-based telescopic and photographic techniques. Extensive studies, in particular, the McDonald Asteroid Survey (Kuiper, et al., 1958) and the Palomar-Leiden Survey (Van Houten, et al., 1970), have been conducted to obtain information to characterize the faintest asteroids (mean opposition magnitude 20.6). Plots of the number of asteroids versus their eccentricities and inclinations are given in Figures 5 and 6, respectively. The distribution of eccentricities peaks at about 0.17 which is consistent with a value obtained for the brighter asteroids (Watson, 1956). The distribution of inclinations was a maximum near 3° which is considerably less than that found for the brighter asteroids (Watson, 1956). This difference is not surprising, however, since the Palomar-Leiden Survey was confined to a region near the ecliptic and thus the survey is incomplete regarding objects of large inclination.

Another characteristic of the asteroid population is the existence of gaps in the distribution of the orbital periods. These gaps correspond to periods in resonance with Jupiter. Further evidence for Jupiter's influence on asteroid orbits is demonstrated by the tendency of their perihelia to become aligned with that of Jupiter (Kresak, 1967).

The essential characteristic of the asteroid belt required for spacecraft hazard evaluation is, of course, the concentration of particles as a function of mass. To obtain this parameter, the apparent magnitudes (m_{app}) of the observed asteroids were converted to absolute magnitudes (g) defined by:

$$g = m_{app} - 5 \log Sr_e - f(\gamma) \quad (3)$$

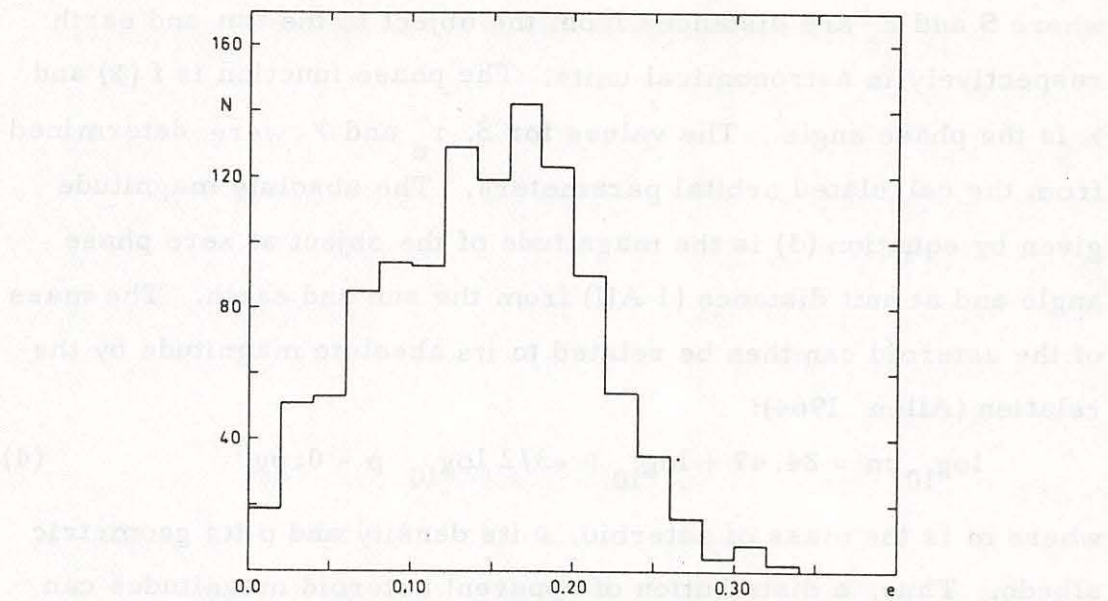


Figure 5. Frequency Curve of Eccentricities from the Palomar-Leiden Survey

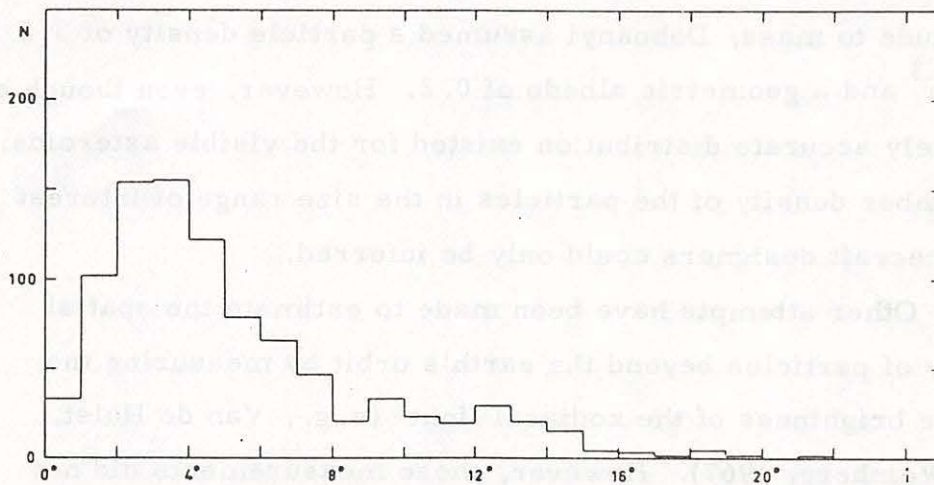


Figure 6. Frequency Curve of Inclinations, not Corrected for Completeness, from the Palomar-Leiden Survey

where S and r_e are distances from the object to the sun and earth respectively in astronomical units. The phase function is $f(\gamma)$ and γ is the phase angle. The values for S , r_e and γ were determined from the calculated orbital parameters. The absolute magnitude given by equation (3) is the magnitude of the object at zero phase angle and at unit distance (1 AU) from the sun and earth. The mass of the asteroid can then be related to its absolute magnitude by the relation (Allen, 1964):

$$\log_{10} m = 24.47 + \log_{10} \rho - 3/2 \log_{10} p - 0.6g \quad (4)$$

where m is the mass of asteroid, ρ its density and p its geometric albedo. Thus, a distribution of apparent asteroid magnitudes can be converted to the desired mass distribution.

On the basis of the above relations, and the results of the McDonald Survey (MDS) and Palomar-Leiden Survey (PLS), Dohnanyi (1972) obtained a distribution for the cumulative number of asteroids as a function of absolute magnitude and mass. The results are plotted in Figure 7. In the conversion from absolute magnitude to mass, Dohnanyi assumed a particle density of 3.5 gm/cm^3 and a geometric albedo of 0.2. However, even though a relatively accurate distribution existed for the visible asteroids, the number density of the particles in the size range of interest to spacecraft designers could only be inferred.

Other attempts have been made to estimate the spatial density of particles beyond the earth's orbit by measuring the surface brightness of the zodiacal light* (e. g., Van de Hulst, 1947; Weinberg, 1967). However, these measurements did not provide sufficient data to determine a unique size distribution or

*Sunlight scattered by widely dispersed particles in interplanetary space near the ecliptic plane.

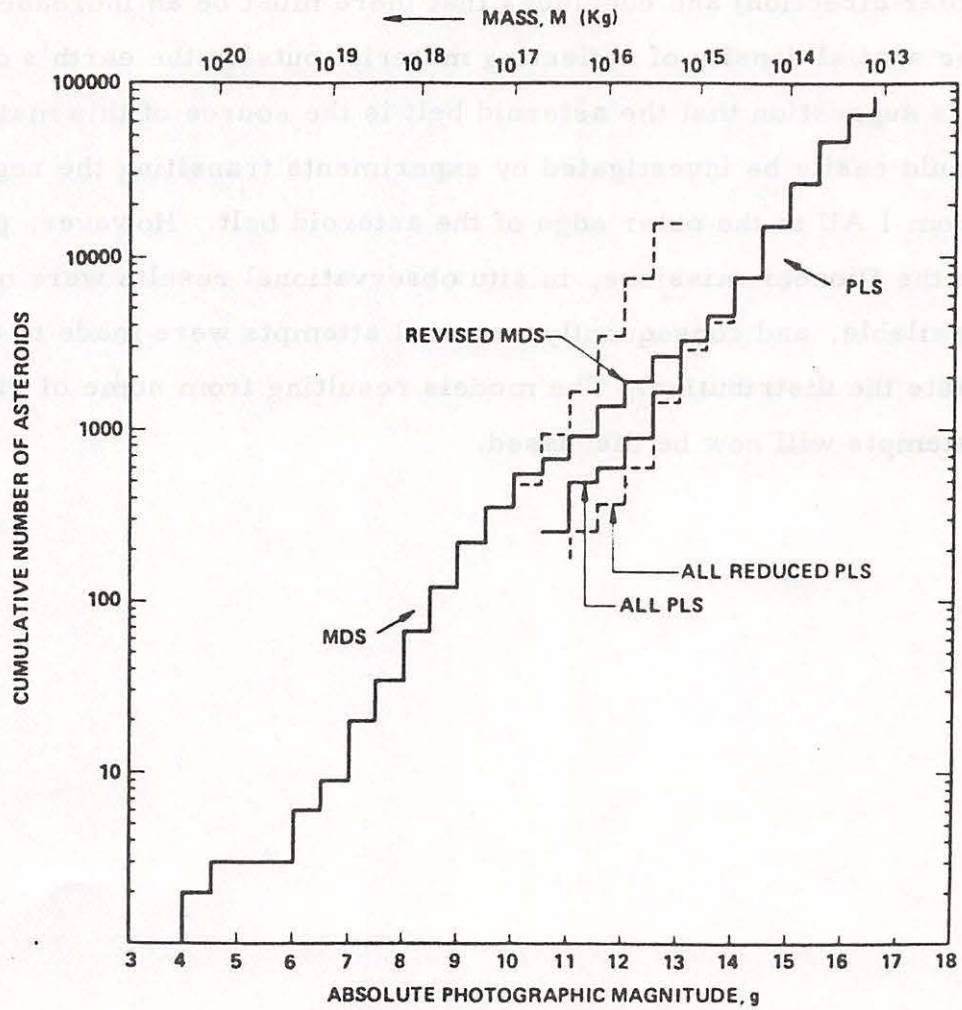


Figure 7. Cumulative Number of Asteroids Defined by the Revised MDS and PLS Data (after Dohnanyi, 1972).

the variation of particle concentration with heliocentric distance. More recently, Roosen (1970) has made measurements on the gegenschein (observed brightening of the zodiacal cloud in the anti-solar direction) and concludes that there must be an increase in the spatial density of reflecting material outside the earth's orbit. His suggestion that the asteroid belt is the source of this material could easily be investigated by experiments transiting the region from 1 AU to the outer edge of the asteroid belt. However, prior to the Pioneer missions, in situ observational results were not available, and consequently, several attempts were made to estimate the distribution. The models resulting from some of these attempts will now be discussed.

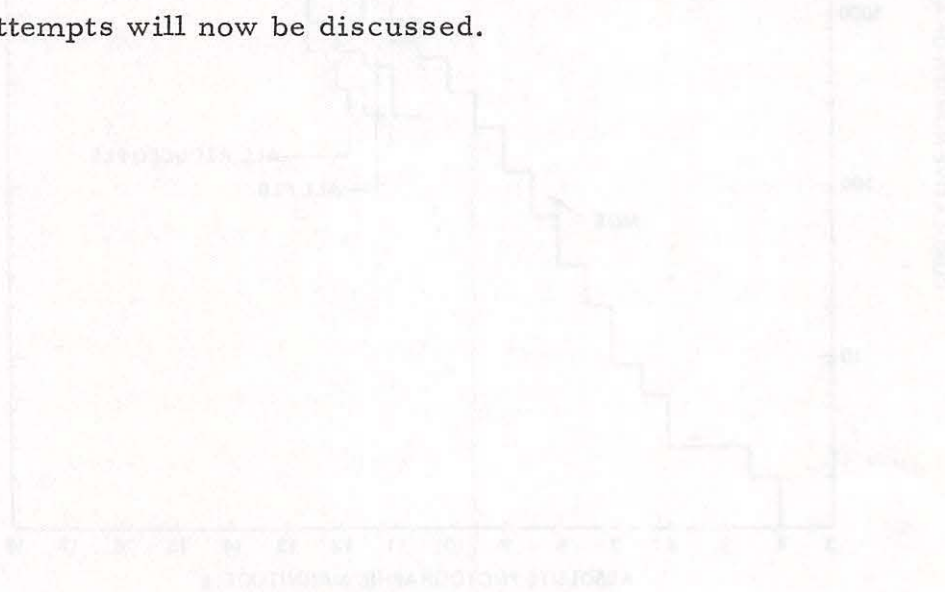


Figure 1. Comparison of the number of particles per unit volume of the zodiacal cloud as a function of heliocentric distance. The solid line is the model of Roosen (1970) and the dashed line is the model of Donnay (1975).

II. C. Asteroid Belt Models

Current models of the small particle number density within the asteroid belt are usually expressed by a relationship of the form:

$$N(m) = C m^{-\beta} \quad (5)$$

where $N(m)$ is the number of asteroids of mass m and larger and C and β are constants. The major uncertainty, and point of controversy, between the various models lies in determining the value of β , since C is assumed fixed by the visible asteroids. Several theoretical and experimental studies have been developed to determine the value of β and thus predict the spatial density of the smaller asteroids.

Attempts have been made to estimate the number of smaller bodies in the asteroid belt by analyzing the lunar and Martian crater distributions. However, several sources of uncertainty are inherent in this approach: (1) it is not known if the craters are of asteroidal origin or were caused by comet nuclei, secondary ejecta, or volcanism; (2) the craters become eroded by smaller meteoroids on the moon and by wind on the Martian surface causing the smaller craters to disappear more rapidly than the larger ones; (3) the age of the impacted surface is not known; (4) it is possible that the surface is saturated and the large craters obliterate many of the smaller particles making it impossible to determine the number of impacting particles and consequently the original distribution. The analyses of Marcus (1966, 1968) indicate that saturation has taken place on the lunar continents and the Martian surface. Thus, accurate estimates of the asteroidal influx cannot be determined by this method.

Several attempts have been made to determine the value of β in equation (5) by theoretical and experimental studies regarding the collision and subsequent fragmentation of rocks.

Piotrowski (1953) uses such a "grinding mechanism" to argue that the particle concentrations near the size of 10 millimeters should follow a $\beta = 1$ law. However, Anders (1965) does not believe that the fragmentation history of the asteroids has progressed as far as does Piotrowski and favors a value of β more nearly equal to 0.67. More recently, Hellyer (1970) also finds a value of $\beta = 0.67$ appropriate for the most massive asteroids while a distribution with $\beta = 0.8$ is indicated for the smaller bodies.

Dohnanyi (1969) considers the problem in much detail by using experimental results of hypervelocity impacts to determine a rock crushing law. He also derives a "fragmentation equation" to describe the change in the mass distribution of a population of particles undergoing mutual collision and fragmentation. His studies predict a stable cumulative mass distribution of the form:

$$N(m) = C m^{-.84} \quad (6)$$

which is in good agreement with the results of the MDS survey.

Recovered meteorites, which are believed to be of asteroidal origin, have been used by Hawkins (1964) to estimate the cumulative mass distribution in space. He predicted that the stony and iron meteorites would follow distributions of m^{-1} and $m^{-.77}$, respectively. Hawkins (1960) earlier pointed out that the distribution of terrestrial rocks approaches m^{-1} as they are crushed.

The gegenschein measurements (Weinberg, 1964) were used by Kessler (1968) to put an upper limit on the asteroidal spatial density. By assuming that the gegenschein was due entirely to backscattering of sunlight from asteroidal particles of a given size an upper limit could be determined for particles of that size.

In order to illustrate the uncertainty in the mass distribution of asteroidal meteoroids, the various theoretical models

which have been discussed are shown in Figure 8. The upper limit proposed by Kessler and the spatial density of the observed asteroids are also shown for comparison.

Other aspects of the asteroidal population which have received considerable attention are the radial and longitudinal distributions, i. e., the variation in spatial density with heliocentric distance and longitude. Kessler (1969), using a computer, calculated the fraction of time that a given catalogued asteroid spends at a given heliocentric distance S and longitude λ . The result can be expressed as (Kessler, 1970)

$$\log_{10} N = 0.84 \log m - 15.79 + f_S(S) + g(S) \cos \lambda \quad (7)$$

where N is the cumulative number of asteroids per cubic meter of mass m and larger. The radial distribution is given by $f_S(S)$ and is shown graphically in Figure 9. The assymetry of the belt is given by $g(S) \cos \lambda$ and is illustrated in Figure 10.

It can be seen from Figure 9 that the radial distribution peaks near 2.5 A.U. The structure which occurs near 1.5 AU indicates that there may be some gravitational interaction between Mars and the asteroids which approach its orbit. It should be noted here that Öpik (1951) predicted decreases in the particle spatial concentration near planetary orbits due to a planetary sweeping effect.

It is apparent from the foregoing discussion that the information obtained from earth-based measurements of the asteroidal population cannot be used to obtain accurate estimates of the small particle distribution. The state of knowledge regarding the small particle population of the asteroid belt was similar to knowledge of the near-earth meteoroid environment before the use of spacecraft made in situ observations possible.

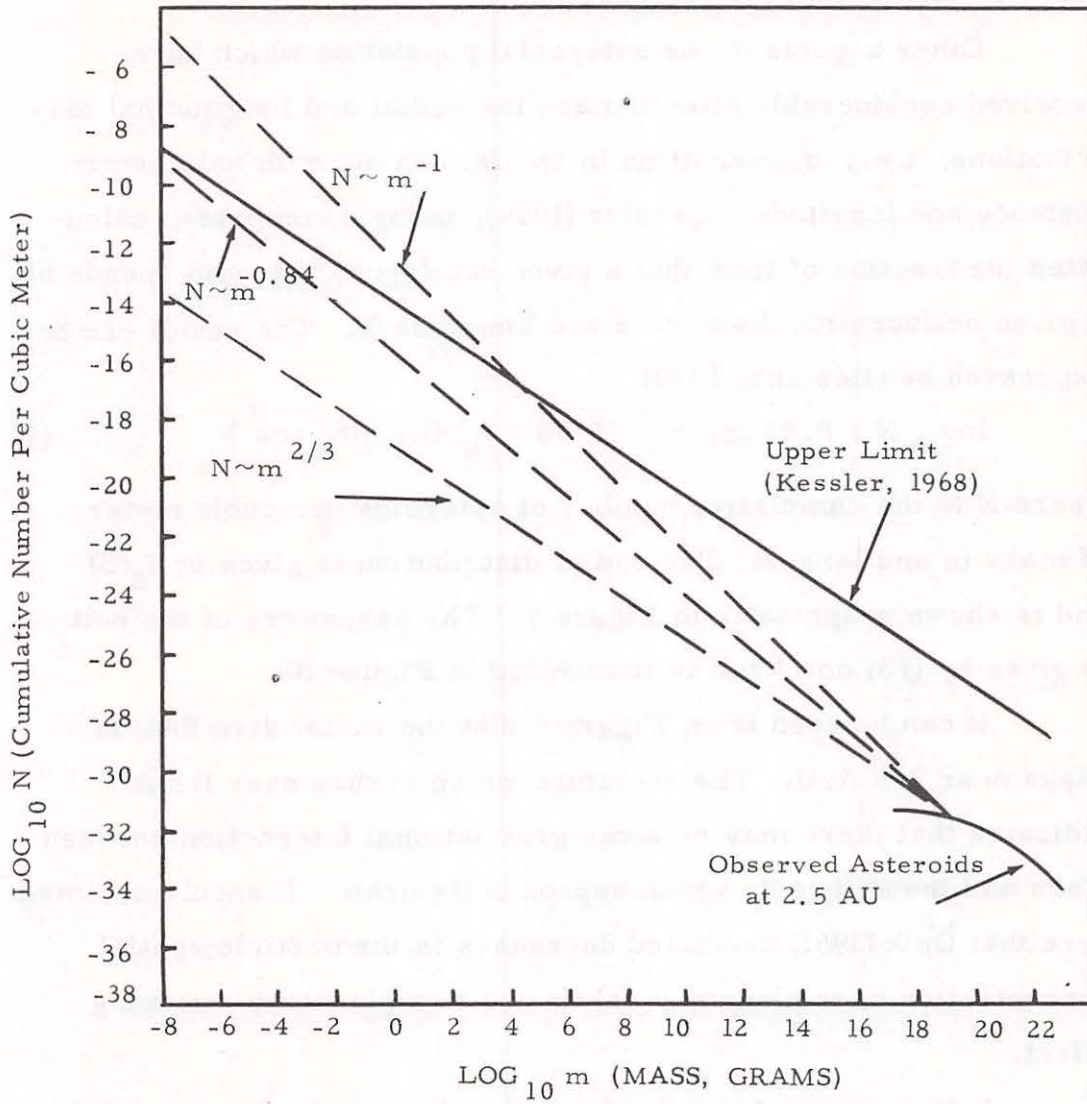


Figure 8. Various Asteroidal Mass Distributions Models at 2.5 A.U. (after Kessler, 1970).

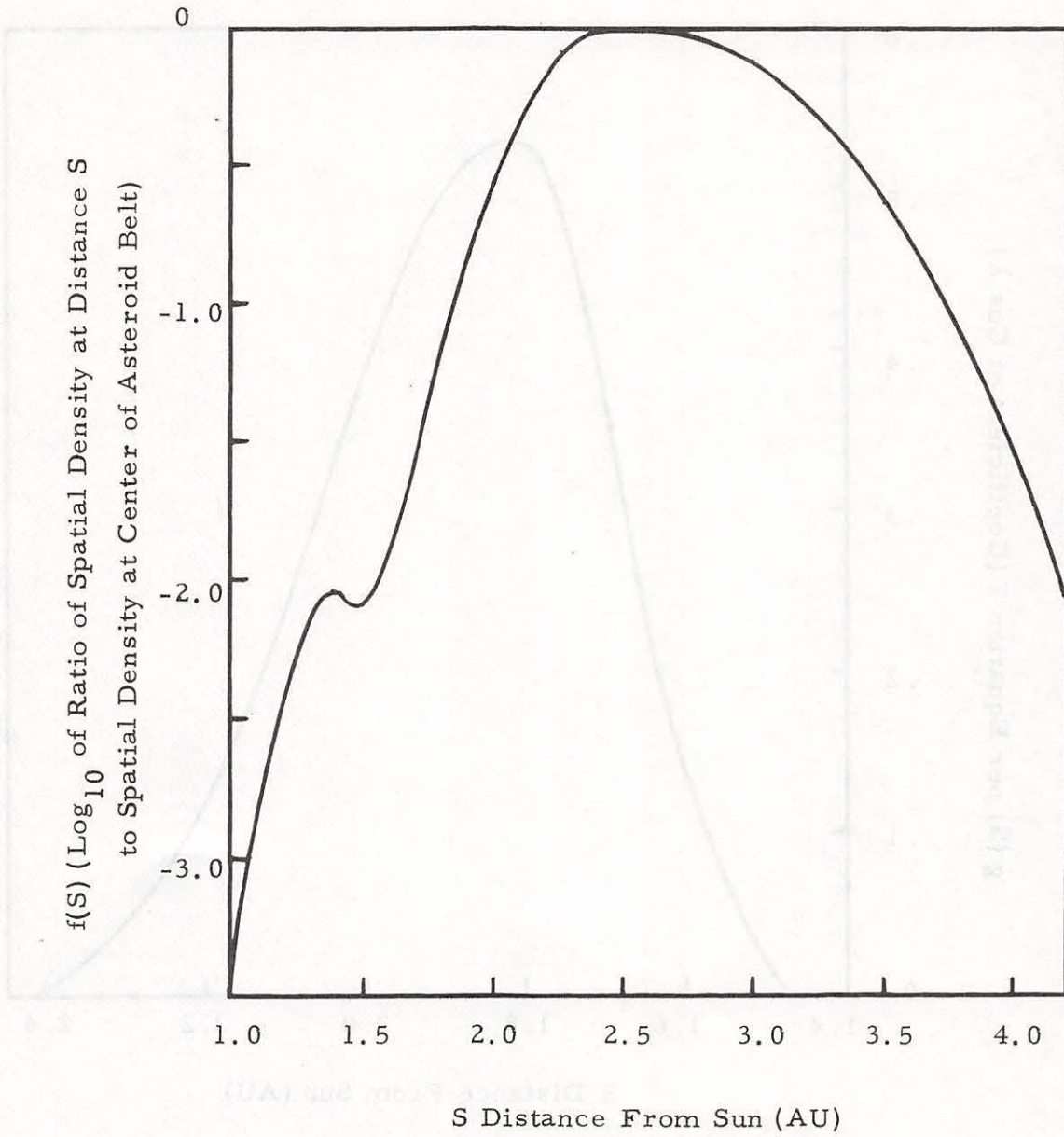


Figure 9. Asteroid Radial Distribution (after Kessler, 1970)

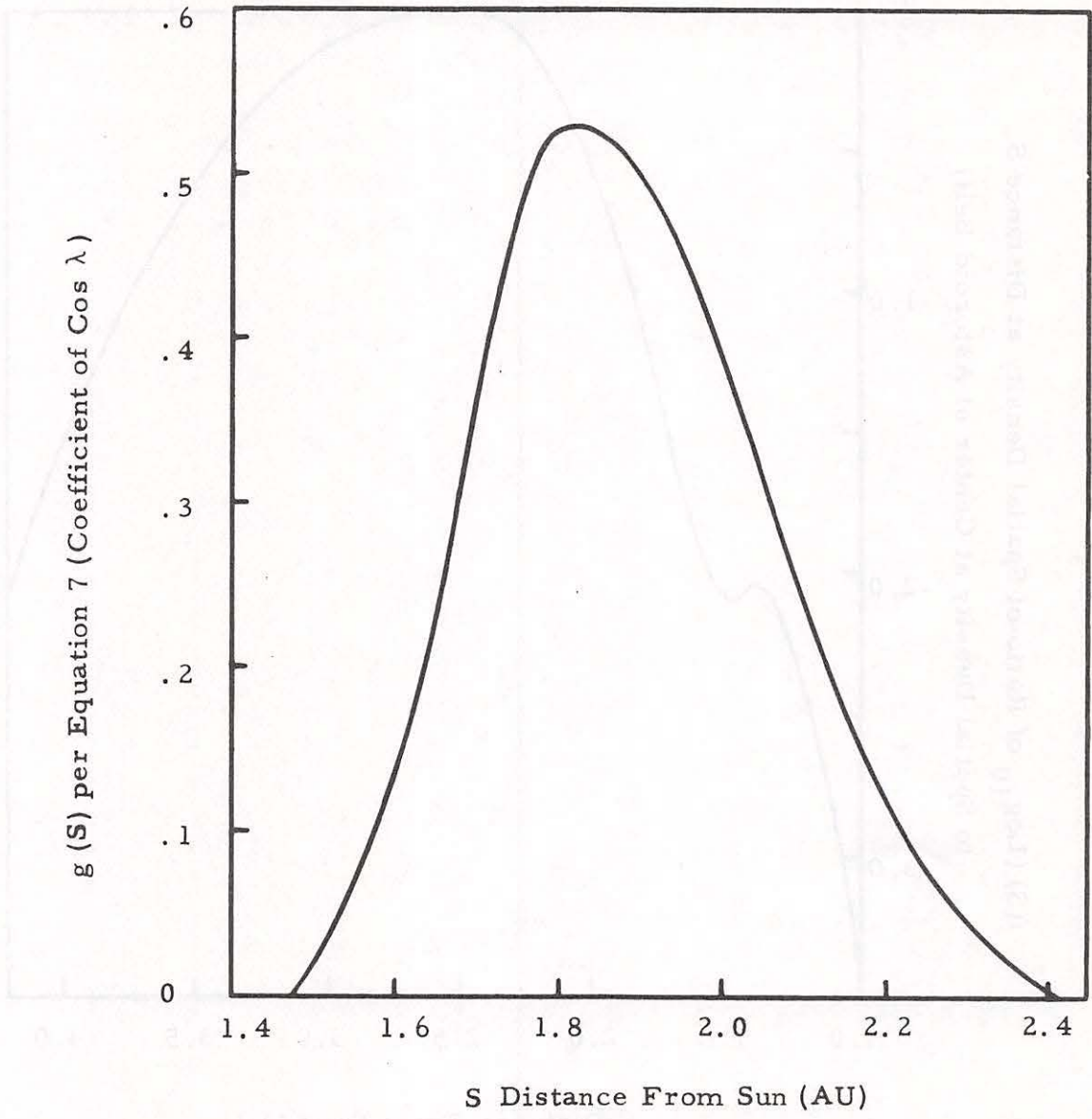


Figure 10. Asymmetry of the Asteroid Belt with Heliocentric Longitude, λ (after Kessler, 1970)

In order to reduce these uncertainties, three experiments designed to measure the small particle environment were flown on the Pioneer 10 and 11 spacecraft. The first of these experiments is the Sky Mapping Mode of the Imaging Photopolarimeter, conducted by investigators from the State University of New York at Albany. The maps obtained are measurements of the diffuse sky glow which consists of zodiacal light as well as integrated starlight and diffuse galactic light. After subtracting out the starlight most of the remainder is the zodiacal light (sunlight scattered from small particles). This experiment thus obtained the zodiacal light brightness as well as its variation with heliocentric distance.

The second small particle experiment, conducted by investigators from the NASA Langley Research Center, was the Meteoroid Detector which detected particles as they penetrated pressurized cells mounted in arrays on the spacecraft. This experiment was sensitive to particles of about 10^{-9} grams (about 10 microns) and consequently it determined the cumulative concentration for particles of that size and larger.

The third experiment was the Asteroid/Meteoroid Detector (AMD) which observed sunlight reflected from particles passing through its fields of view. The concept and functional characteristics of the AMD are presented in the following section. The observational data from the AMD, its analysis and interpretation are then presented in the concluding sections.

III. THE ASTEROID/METEOROID DETECTOR ON PIONEERS 10 AND 11

III. A. Pioneer Spacecraft and Mission Profile

As a prelude to discussing the specifics of the Asteroid/Meteoroid Detector on Pioneer 10, a few comments regarding the general nature of the spacecraft and its mission profile are in order.

The Pioneer 10 spacecraft was launched from Cape Kennedy on 2 March 1972 on a trajectory passing through the asteroid belt toward a Jupiter flyby on 4 December 1973. Approximately one year later, on 5 April 1973, its twin Pioneer 11 was launched on a similar trajectory and encountered Jupiter on 2 December 1974. The trajectory profile together with significant mission events is shown in Figure 11.

The spacecraft (see Figure 12) were spin stabilized at a rate of approximately 5 revolutions per minute with their high gain antennas pointing toward the earth throughout the mission. The total weight of the spacecraft was approximately 560 pounds, of which approximately 60 pounds were allotted to the eleven scientific experiments. Average power requirements of approximately 35 watts were supplied to the spacecraft telemetry and scientific experiments via four Radioisotope Thermoelectric Generators (RTG's) mounted on booms extending outward from the spin axis. The spacecraft attitude was controlled by thrusters located near the outer edges of the high gain antenna. Figure 12 shows the placement of the essential components required for telemetry and attitude control. In the lower portion of this figure, the Meteoroid Detectors and the Asteroid/Meteoroid Detector are shown in their locations behind the high gain antenna.

It was in light of these basic characteristics of the Pioneer spacecraft and the mission profiles that the concept of the Asteroid/Meteoroid Detector (AMD) was developed to measure the particulate environment between the orbits of Earth and Jupiter.

PIONEER/JUPITER MISSION EVENTS

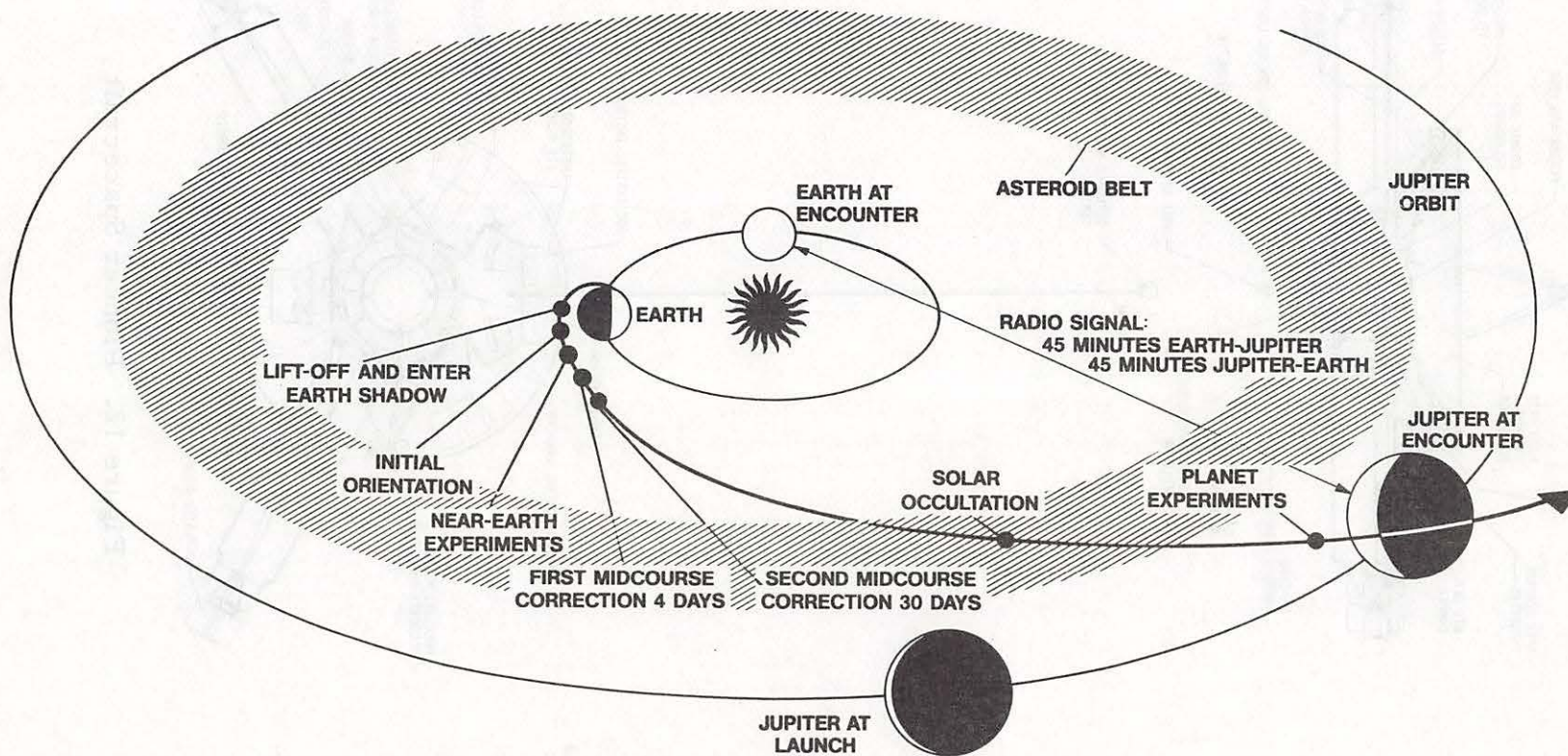


Figure 11. Pioneer Mission Profile

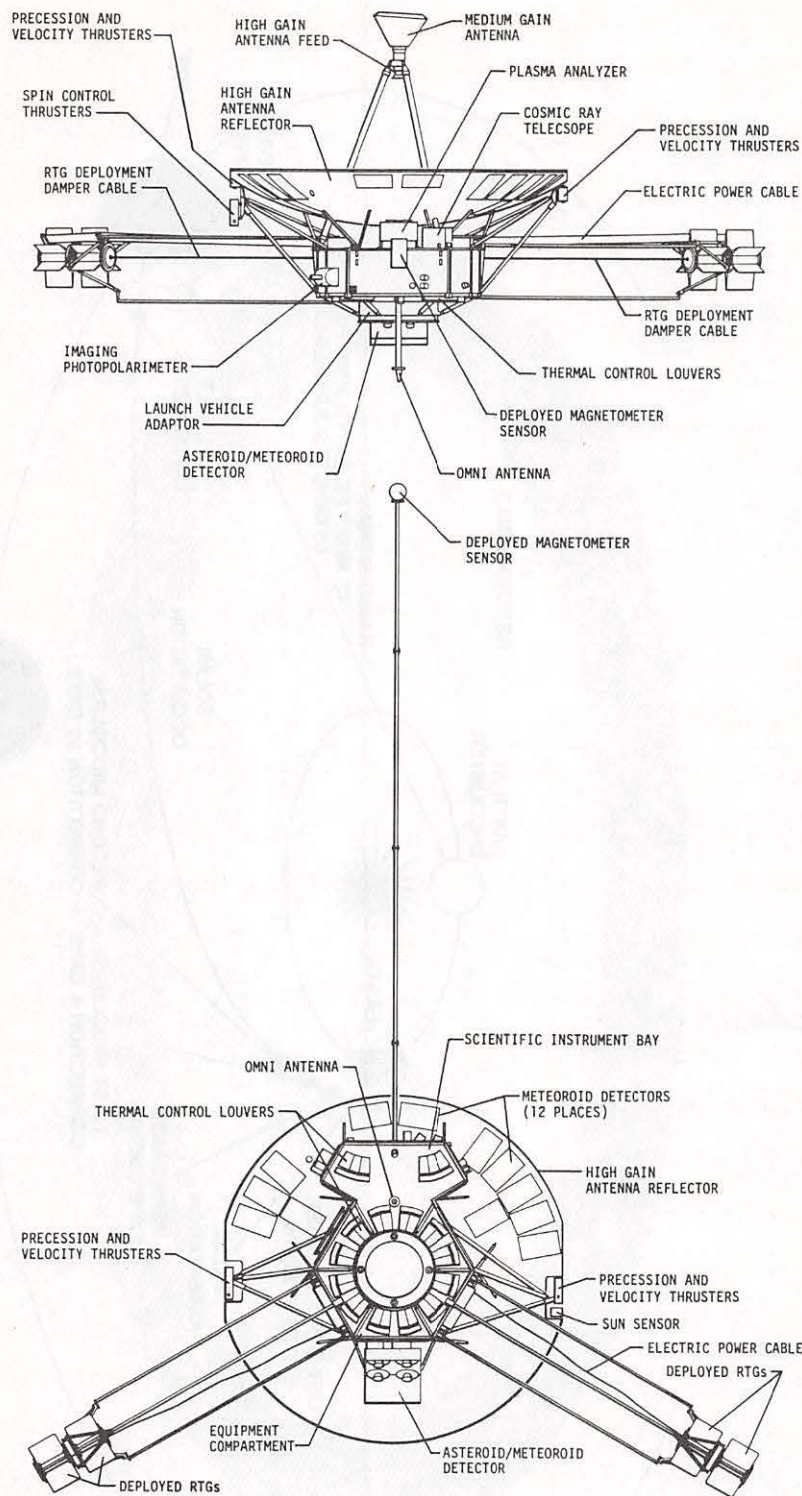


Figure 12. Pioneer Spacecraft

III. B. Concept of the Asteroid/Meteoroid Detector

It is well known that a body in space will reflect sunlight by which it can be seen or detected. If an optical detector is oriented in space such that it looks away from the sun, we can approximate the amount of light incident on the aperture which results from the sunlight reflected by an assumed spherical object appreciably larger than the wavelengths of the incident light.

Thus,

$$I = \frac{I_0 r \pi a^2 f(\gamma)}{4 \pi R^2 S^2} = \frac{I_0 r}{4 S^2} \left(\frac{a}{R}\right)^2 f(\gamma) \quad (8)$$

where I is the intensity of the reflected sunlight incident on the optics; I_0 is the solar illumination at the object at 1 AU from the sun; r is the bond albedo of the object; a is the radius of the object; R is the distance from the object to the detector; S is the distance from the sun in astronomical units; and $f(\gamma)$ is the phase law for light scattering from a sphere. We have assumed in this equation that the object is diffusely reflecting the sunlight uniformly in all directions. A more detailed discussion of this approximation formula and its applicability is given in Appendix A.

Using equation (8), one can calculate the size of an object that can be seen against a dark background. However, it is clear from the equation that a single detector would have no way of distinguishing different objects which had the same a/R ratio (i. e., a small object at close range from a large object far away). Two optical systems which have a base line separation could, however, establish the range distance R if they both saw the object. The problem, however, (well known in earth based meteor astronomy) is to get both optical systems to see the object simultaneously and then be able to reduce the data appropriately. The Asteroid/Meteoroid Detector will yield data similar to the photographic data, but (like radio meteor astronomy) in a form which can be rapidly tele-

metered and reduced by a computer.

To explain the AMD concept, we will start with a highly simplified two dimensional model. Consider two optical systems (A and B) with well defined fields of view (angular acceptance angle 2α) looking out in the x-y plane. If the optic axes are parallel and they are separated by a distance d , we will have a situation like that shown in Figure 13. Any luminous object which crosses through the intersecting fields of view (such as the line labelled mm in Figure 13) would be detected by each of the optical systems. We would then have pulses coming out of the optical system detectors of the type shown in the lower portion of Figure 13. For our meteoroid case in space, we can safely say that the linear velocity of the illuminated object will not change during its transit. Then, from Figure 13, we can see that the velocity component in the x direction can be written as:

$$v_x = \frac{d}{t_1} \quad (9)$$

At the same time, the mean angular velocities can be written as:

$$\bar{\omega}_A = \frac{2\alpha}{t_2} \quad (10)$$

and

$$\bar{\omega}_B = \frac{2\alpha}{t_3} \quad (11)$$

We can, therefore, write:

$$R_A = \frac{v_x}{\bar{\omega}_A} = \frac{d t_2}{2\alpha t_1} \quad (12)$$

and

$$R_B = \frac{v_x}{\bar{\omega}_B} = \frac{d t_3}{2\alpha t_1} \quad (13)$$

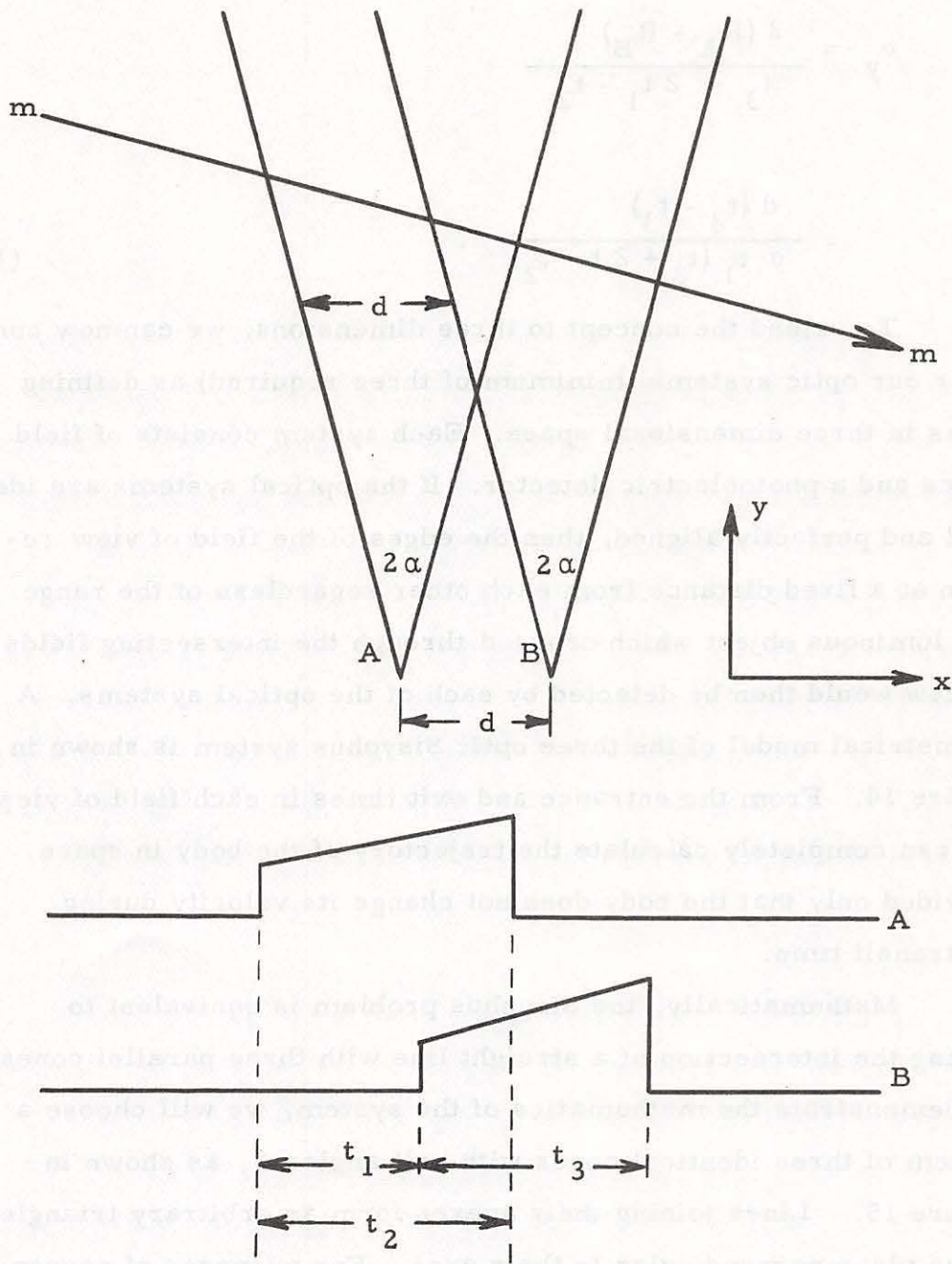


Figure 13. Two-Dimensional Model of the AMD Concept

We can, thus, write:

$$\begin{aligned}
 v_y &= \frac{2(R_A - R_B)}{t_3 + 2t_1 - t_2} \\
 &= \frac{d(t_2 - t_3)}{\alpha t_1 (t_3 + 2t_1 - t_2)} \quad (14)
 \end{aligned}$$

To extend the concept to three dimensions, we can now consider our optic systems (minimum of three required) as defining cones in three dimensional space. Each system consists of field optics and a photoelectric detector. If the optical systems are identical and perfectly aligned, then the edges of the field of view remain at a fixed distance from each other regardless of the range. Any luminous object which crossed through the intersecting fields of view would then be detected by each of the optical systems. A geometrical model of the three optic Sisyphus system is shown in Figure 14. From the entrance and exit times in each field of view, one can completely calculate the trajectory of the body in space provided only that the body does not change its velocity during the transit time.

Mathematically, the Sisyphus problem is equivalent to finding the intersection of a straight line with three parallel cones. To demonstrate the mathematics of the system, we will choose a system of three identical cones with half angles α , as shown in Figure 15. Lines joining their apexes form an arbitrary triangle in the plane perpendicular to their axes. For purposes of convention, the vector from the base of the i^{th} cone to the particle's entrance into that cone is designated \vec{p}_i and the vector to the particle's exit is $\vec{\sigma}_i$. The corresponding angles of entrance and exit in the plane of the apexes are θ_i and ψ_i . Times of entrance and exit at the i^{th} cone are designated τ_{ij} , where j is 1 for an entrance point or 2

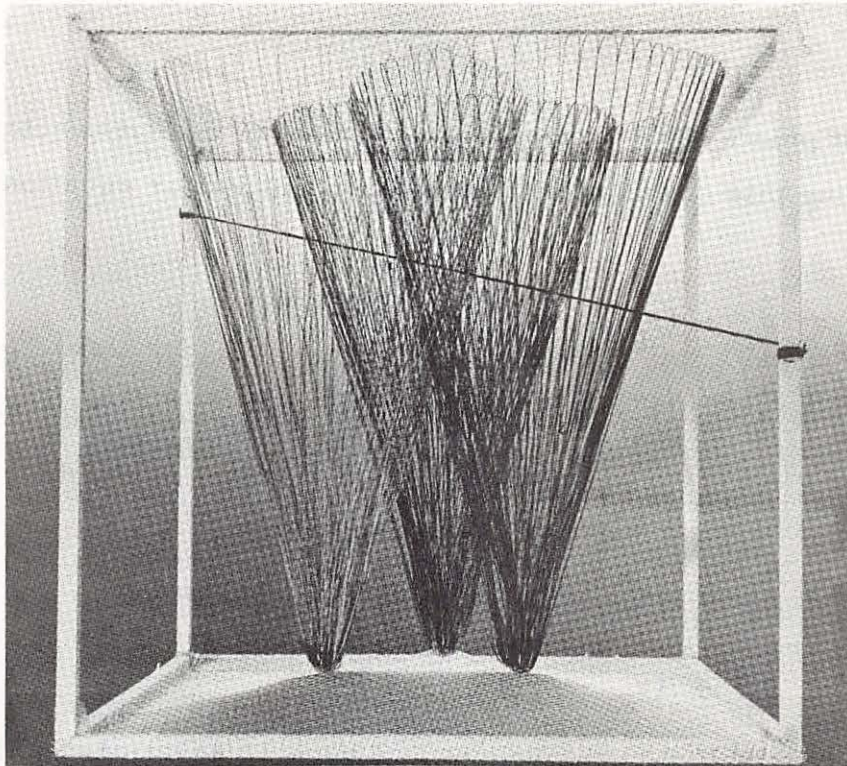


Figure 14. Model of the AMD System

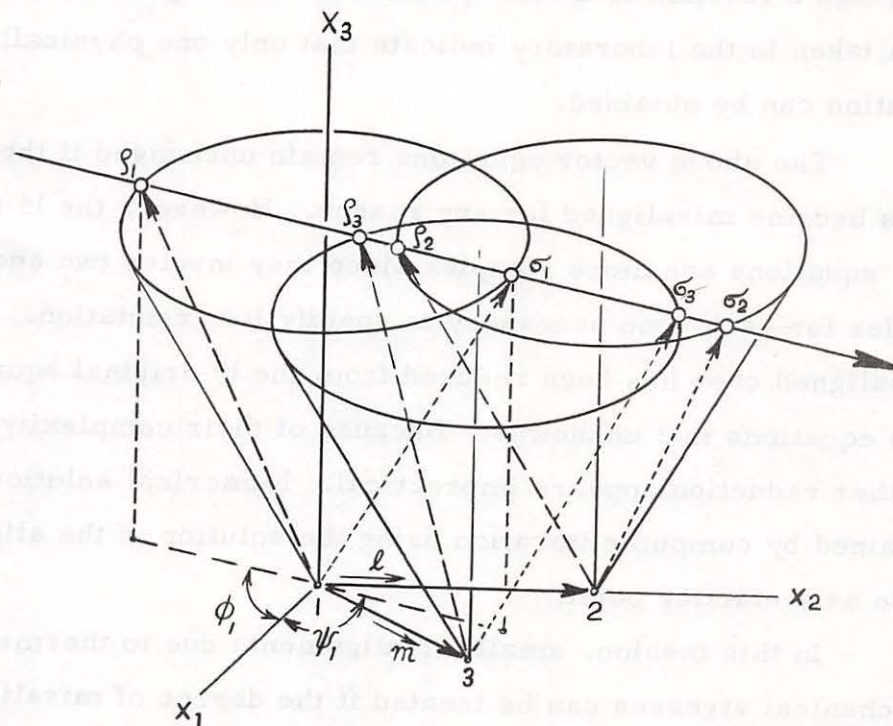


Figure 15. Geometry of the AMD System Illustrating the Unknown Variables (Φ and Ψ are shown only for cone 1).

for an exit point. The vector \vec{v} is an arbitrary velocity vector.

Using this convention, five independent vector equations result:

$$\begin{aligned}
 \vec{\sigma}_1 &= \vec{\rho}_1 + (\tau_{12} - \tau_{11}) \vec{v} \\
 \vec{\rho}_2 &= \vec{\rho}_1 + (\tau_{21} - \tau_{11}) \vec{v} - \vec{\ell} \\
 \vec{\sigma}_2 &= \vec{\rho}_1 + (\tau_{22} - \tau_{11}) \vec{v} - \vec{\ell} \\
 \vec{\rho}_3 &= \vec{\rho}_1 + (\tau_{31} - \tau_{11}) \vec{v} - \vec{m} \\
 \vec{\sigma}_3 &= \vec{\rho}_1 + (\tau_{32} - \tau_{11}) \vec{v} - \vec{m}
 \end{aligned} \tag{15}$$

By breaking these into components, we have 15 equations in 15 unknowns ρ_i , σ_i , θ_i , ψ_i , and three components of \vec{v} - so a solution exists. Although a solution to these equations is not unique, analyses of all data taken in the laboratory indicate that only one physically meaningful solution can be obtained.

The above vector equations remain unchanged if the cone axes become misaligned for any reason. However, the 15 component equations are more complex since they involve two additional angles for each cone necessary to specify its orientation. This misaligned case has been reduced from the 15 original equations to 3 equations in 3 unknowns. Because of their complexity, further reduction appears impractical. Numerical solutions are obtained by computer iteration using the solution of the aligned case as a starting point.

In this fashion, small misalignments due to thermal and mechanical stresses can be treated if the degree of misalignment is known. This misalignment is determined by using the planet Jupiter as a calibration source.

From the foregoing it follows that independent of the amplitude of the signals detected by the individual optical systems, one can mathematically establish the three velocity components and the range of the luminous body. Using this calculated range, one can solve equation (8) for the product of the reflectivity and the cross-sectional area, and thus determine the mean radius of the body to an uncertainty of the square root of the reflectivity.

From the real time at which the event took place, the known position and orientation in space of the vehicle from which the measurement was made and the three velocity components of the body, the complete orbit of the body in the solar system can be determined. Since the basic measurement includes the total background radiation, one also obtains the intensity of light due to the aggregate of zodiacal and asteroidal particles in the field of view. Since an absolute calibration standard is available in the form of incremental differences in starlight (when a bright star or planet transits the field of view), one thus obtains, as an additional measurement, variations in the zodiacal or asteroidal light.

III. C. System Design Considerations

The spacecraft limitations on weight and power together with its mode of stabilization greatly reduced the extent to which the AMD could be optimized. Ideally, a system of this type would maximize the telescope aperture to obtain high signal to noise ratios and maximize the separation distance between telescopes to fully utilize the parallax aspect of the system. However, such an optimized system would have quickly exceeded the allotted weight budget. In addition, spin stabilization of the spacecraft not only prevented minimizing the background by looking at a "dark" region of the sky, but required that the instrument be capable of processing large and rapid changes in the sky background. It was, therefore, necessary to design a system which, although capable of performing the desired measurements, could not fully develop the potential of the concept.

The parameters entering into the instrument design are essentially of two types: optical and electronic. The detailed optical design consists mainly of determining the physical parameters of the telescopes such as aperture diameter, field of view, focal length and surface contour of the telescope mirrors. The telescopes' separation and their orientation relative to the spacecraft are indirectly determined by the spacecraft configuration and mission profile. Photo-multiplier tubes convert the optical output of the telescopes into electrical inputs to the electronics. The electronics includes the necessary threshold and logic circuitry, clocks and counters, analog to digital converters, and storage registers.

III. D. Optical Subsystem

Instrument sensitivity and event rate calculations performed in the early development phase of the program were used to establish the telescope aperture diameter and field of view. As shown in Figure 16 the anticipated event rate based on the near earth meteoroid environment model (Cour-Palais, 1969) was relatively independent of the field of view while it was almost directly proportional to the aperture diameter. However, the maximum diameter compatible with the available weight was 20 cm and as a result this was the value used. From optical design considerations, the smallest possible field of view was desired to minimize the aberrations. However, too small a field of view would reduce the probability of detecting individual stars or planets for use in instrument alignment and sensitivity calibrations. A value of 7.5° for the full angular field of view was chosen as an acceptable compromise for the Pioneer 10 mission.

Normally, the requirements of a large aperture and short focal length optics to yield very sharp images over as large a field as 7.5° could be achieved only with multi-element highly corrected systems such as camera lenses. For eight-inch aperture optics, an aerial camera type lens would have been prohibitively heavy for this interplanetary experiment. However, the problem became soluble by using specialized optics which were designed to optimize the peculiar requirements of the Sisyphus system.

- a) The images needed to be sharp only at the edge of the field stop where the images enter and exit the field of view. Over the inner zones of the field stop plane, this requirement was not necessary because there the optical system acts merely as a light bucket.

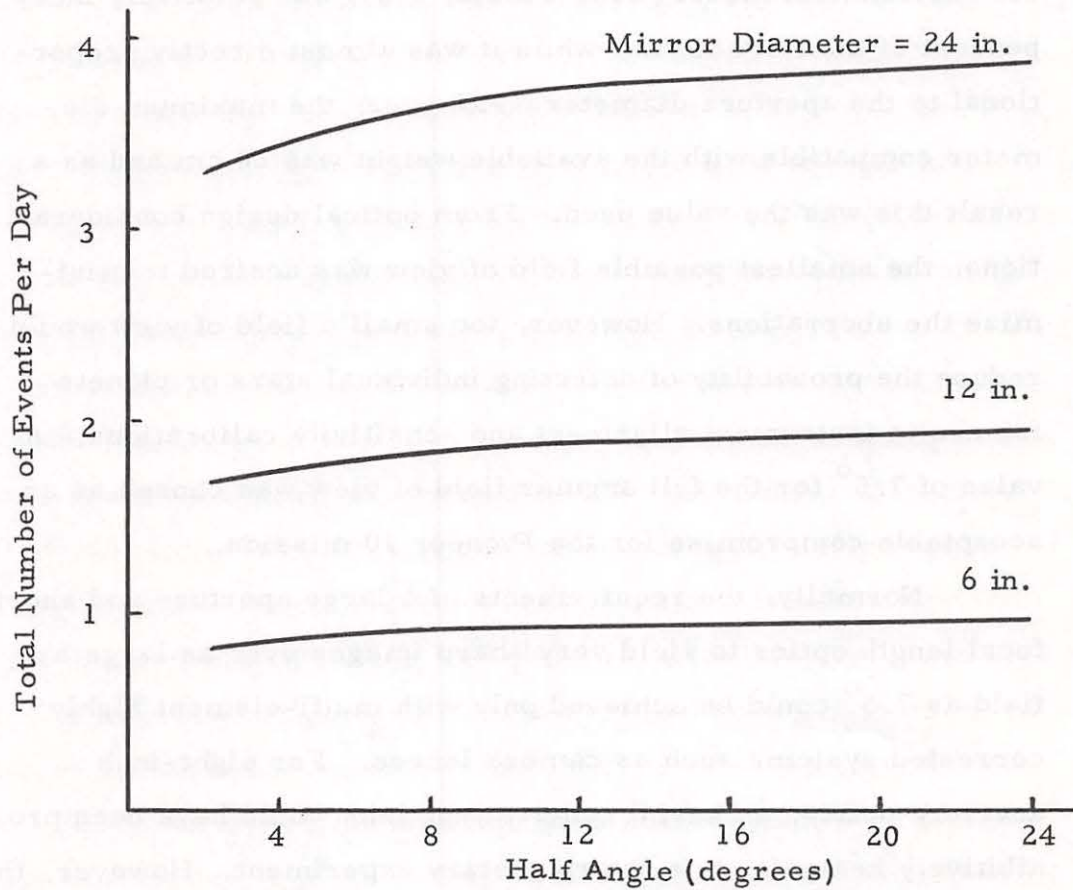


Figure 16. Variation of Event Rate with Field-of-View and Aperture (based on NASA Near Earth Meteoroid Environment).

- b) At the edges of the field of view, the images needed only be sharp in the radial direction so that the images enter and exit the field of view rapidly. A small elongation of the image in the tangential direction would not do any harm. This concept is illustrated in Figure 17 where the short lines indicate the shape of the image at various times as the particle moves across the field of view.

Various wide angle systems, such as those due to Schmidt, Maksutov and Baker-Schmidt, were considered. The Schmidt and Baker-Schmidt system required rather long tube lengths which was undesirable for space flight due to structural considerations. The Maksutov system had the disadvantage that it required a rather thick and heavy refractive corrector element in front which was unrealistic for space flight. The Ritchey-Chrétien system, in which both the primary and secondary mirrors are conics (often hyperboloids), turned out to be best suited for the Sisyphus optics. This system is aplanatic (free of coma and spherical aberrations) for an arbitrarily wide field of view. Therefore, of the various optical systems currently known, the Ritchey-Chrétien appeared to meet the requirements best. The optics chosen for the Pioneer mission are shown in Figure 18. The layout of a single unit is shown in Figure 19.

The sensor subsystem included four reflecting telescopes of Ritchey-Chrétien design, with 20 cm apertures and 20 cm effective focal length. Each telescope was supported on a central tubular housing which contained a photomultiplier tube, dynode resistor assembly, and preamplifier. The photomultiplier tubes were RCA C7151 Q, modified to include an S-20 photocathode. A "light tube" was placed between the field stop (at the conical for-

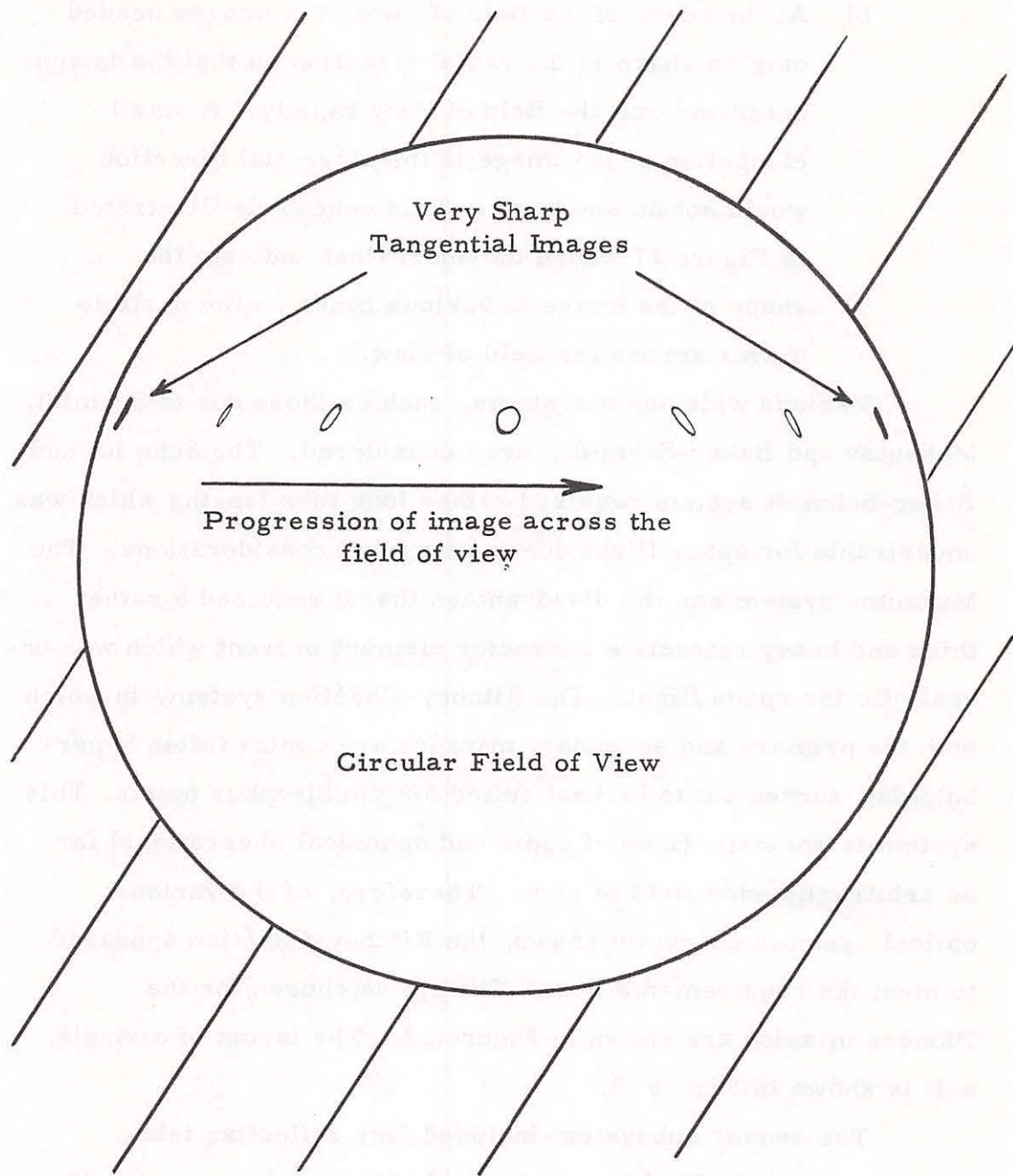


Figure 17. Variation of Image Shape Across the Field-of-View

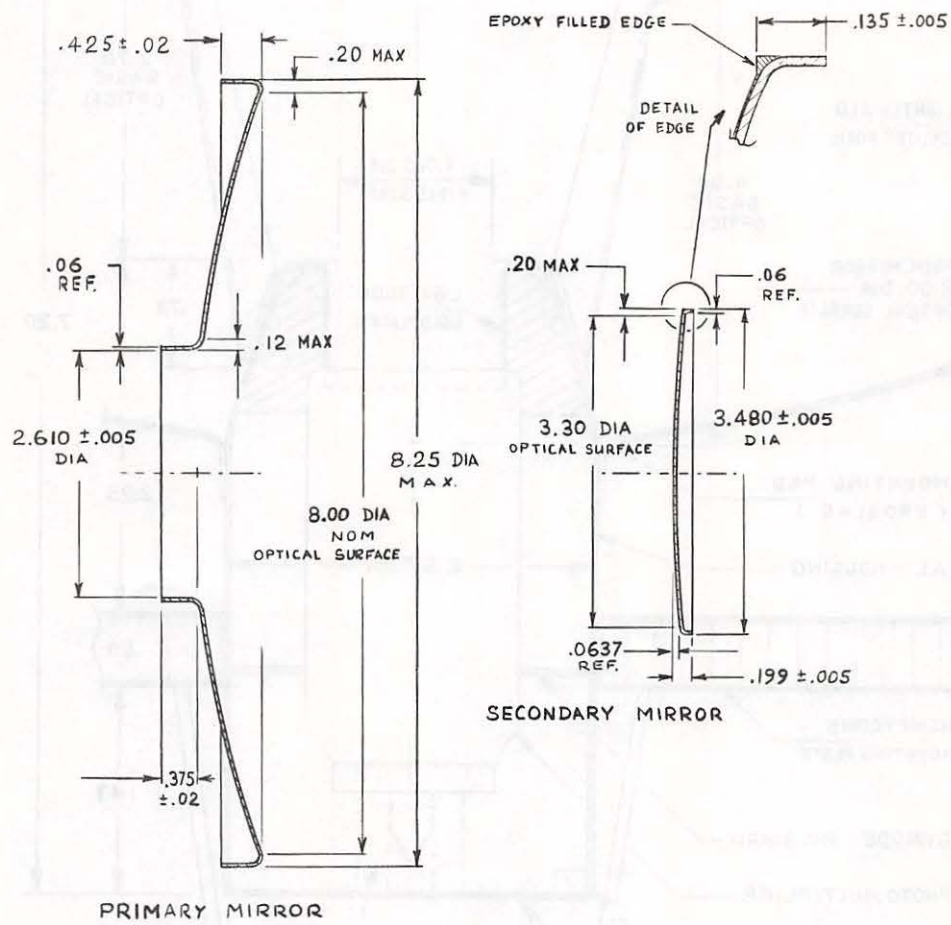


Figure 18. Mirror, Optical System

NOTE:
DIMENSIONS
ARE IN INCHES

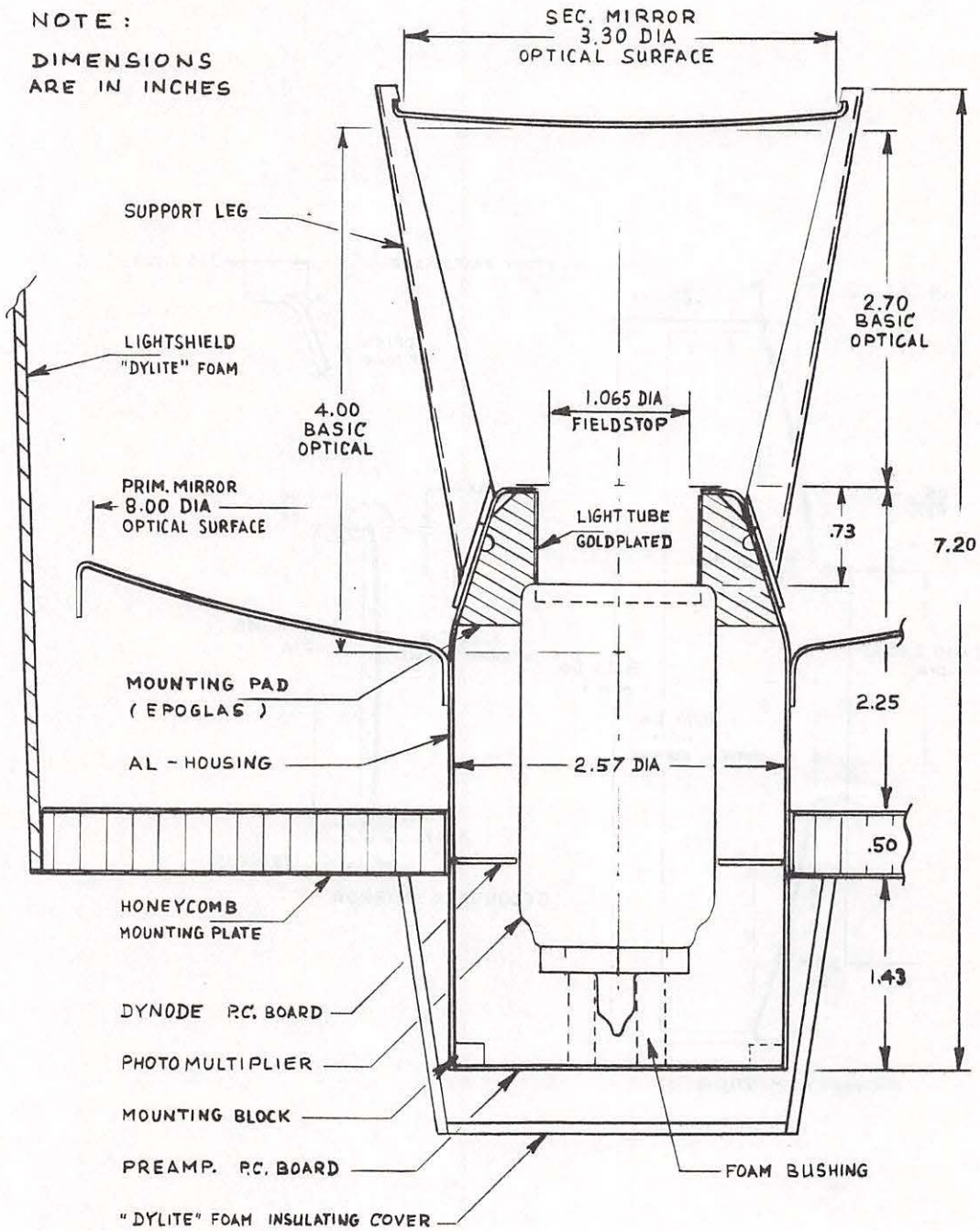


Figure 19. Telescope Cross Section

ward end of the housing) and the photomultiplier tube face. This light tube was a very thin, 1.9 cm long, 3.0 cm diameter, stainless steel cylinder whose inside surface was gold-coated to provide a reflectivity of 0.7 or better. By placing the photo-cathode away from the focal plane, the spot size is blurred to reduce the effect of local variations in photocathode sensitivity; the light tube reflects energy which would otherwise not reach the limited area of the photocathode.

Four telescope assemblies, a high voltage power supply, and a cable harness are mounted on a 44.5 cm square honeycomb panel. All assemblies, except the high-voltage power supply, are bonded to the panel. To provide shielding against stray sunlight reflections from other vehicle equipment, a lightshield of .05 cm thick polystyrene foam is bonded to the honeycomb panel. Coatings of aluminized mylar protect the polystyrene against solar radiation during part of the spacecraft trajectory. Total weight of the Optical Sensor Subsystem (Figures 20, 21, and 22) is about 2.1 Kg (including panel).

Photomultiplier tube power is supplied to each dynode chain from a central 1700-volt supply, consisting of a transformer/voltage multiplier; this high voltage power supply receives its square wave drive from the main dc-to-dc converter of the electronics power supply. The gains of the photomultiplier tubes are equalized by adjustment of high voltage series dropping resistors.

Each preamplifier (Fig. 23) is comprised of an NH-0003 operational amplifier preceded by a 2N3954 dual field effect transistor, with another dual FET switching bandwidth to "wide" ($\tau_r = 0.7 \mu s$), "medium" ($\tau_r = 2 \mu s$), or "narrow" ($\tau_r = 25 \mu s$) upon receipt of the appropriate commands. The preamplifiers have a quasi-logarithmic gain curve with two break-points to extend the dynamic range. The diodes which provide this non-linear function

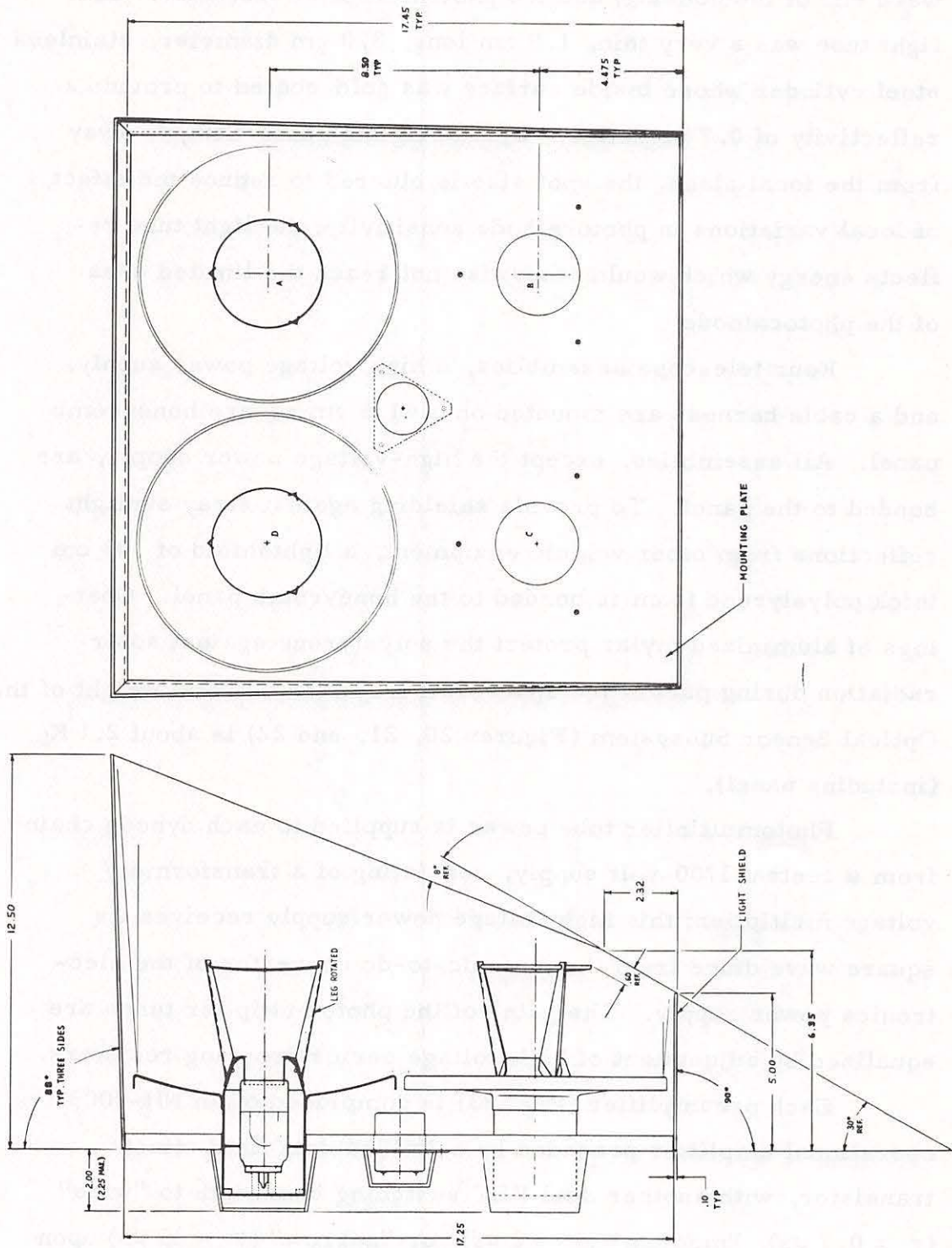


Figure 20. Sensor Assembly

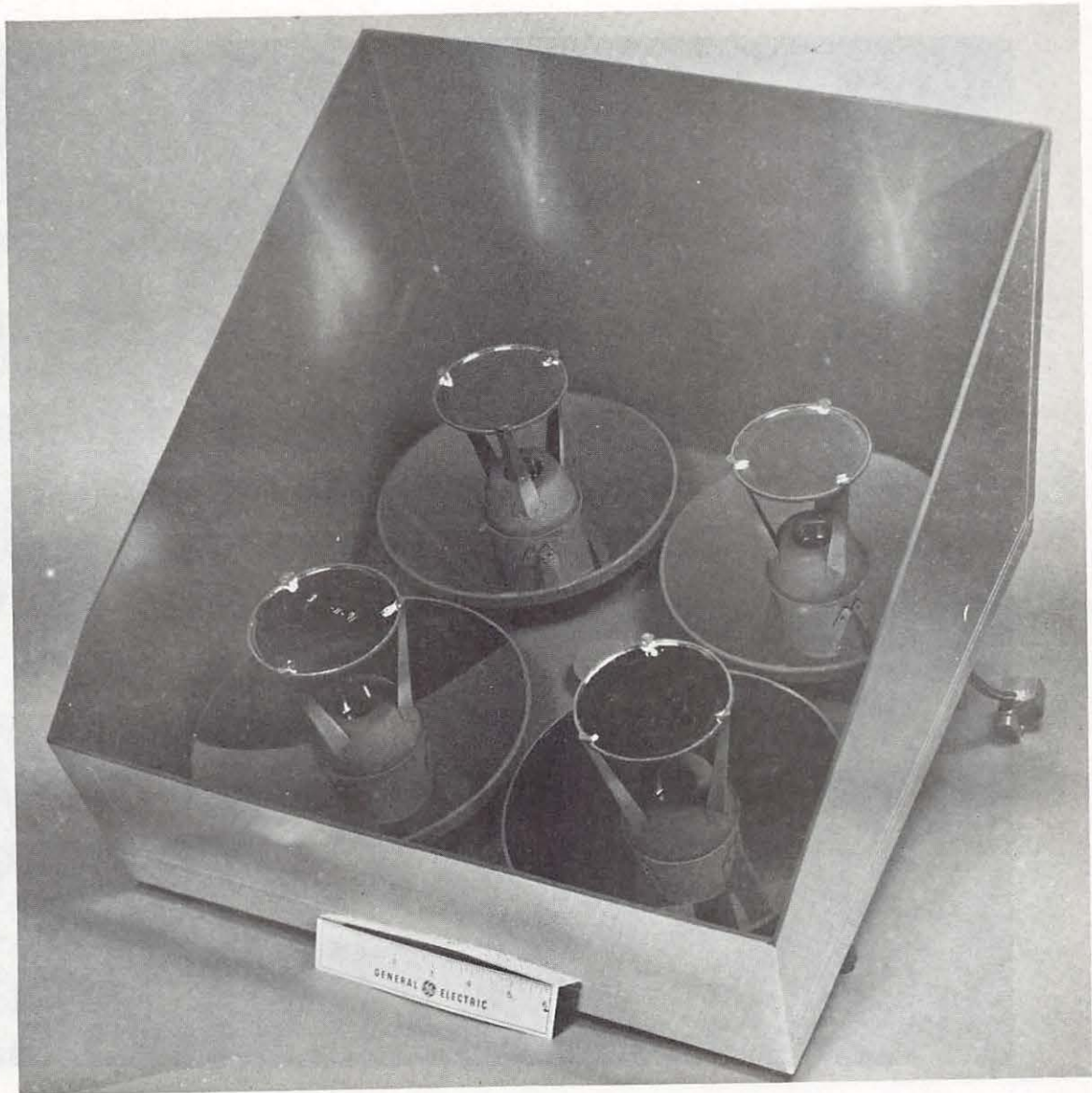


Figure 21. AMD Sensor, Front View

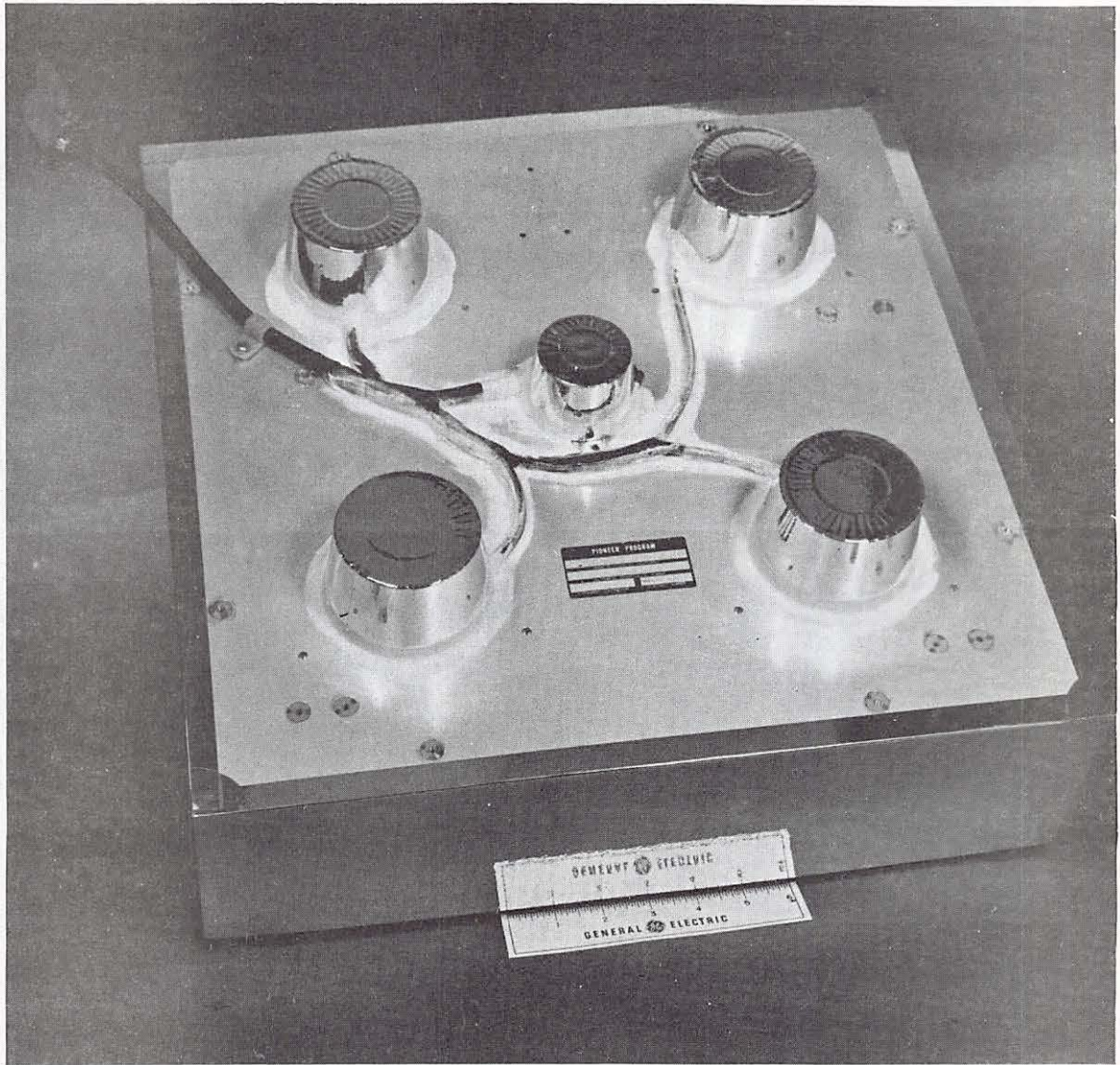


Figure 22. AMD Sensor, Rear View

are matched over a wide range of temperatures (-57°C to $+66^{\circ}\text{C}$). In telescope "A", a forward-biased germanium diode (1N695) has been added, to serve as temperature monitor; the voltage drop across the junction is a practically ($\pm 2\%$) linear function of temperature over the operating range of 40°C to -196°C , with a slope of 0.6 mV/deg. at 10^5 A through the diode.

Figure 12 shows the location of the AMD optical sensor behind the high gain antenna dish on the Pioneer 10 vehicle. The optical axes of the telescopes are oriented at an angle of 45° relative to the spacecraft spin axis. Since the high gain antenna is nominally directed toward the earth, this location enables the sensor to look in the approximate anti-solar direction as required. The angle of 45° was chosen to maximize the probability of scanning across bright calibration stars during the mission. Although this orientation resulted in large background variation as the spacecraft rotated, it was felt to be the optimum configuration consistent with the Pioneer 10 configuration and the mission profile.

III. E. Electronics Subsystem

As a sunlit particle traverses the fields of view of the optical sensors, its entrance times (into each of the sensor fields) and exit times (from these fields) are measured by counting clock pulses, and the results are stored for read-out. Particle brightness (in each field of view) is measured in a peak detector, converted to digital form, and stored for read-out.

The average dc background levels (each channel separately) are detected using a 47 millisecond time-constant to provide the "Background" signal outputs. Four short-time-constant peak detectors provide the "Peak" signal outputs.

Since the input signals are very close to the noise levels, floating self-adaptive thresholding circuits (one per channel) are used. Threshold level is at $1.1 \times$ dc background, plus $1.5 \times$ noise peak, for "normal" setting and $1.2 \times$ dc background plus $1.5 \times$ noise peak for "high". As soon as the threshold is exceeded, the level is dropped to $1.1 \times$ (or $1.2 \times$) dc background, only, by switching out the noise peak contribution.

When the signal in any channel exceeds the threshold, all entrance and exit counters are started. As the sunlit particle enters into (or exits from) a field of view, the corresponding entrance (or exit) counter is stopped. Note that the entrance counter of the channel which first saw the particle (and started all the counters) will be stopped immediately after starting. Thus, a typical event will find one entrance counter near zero, and the other entrance counters and the exit counters stopped at varying counts, depending on particle range, velocity and trajectory.

The digital data (position, entrance count, exit count), as well as the A-to-D converted background and peak signals, are stored in parallel-in/serial-out registers in 264 bits which are read out sequentially. In order to meet the extreme constraints on power and weight, full use is made of complementary symmetry

MOS integrated circuitry (COSMOS). The counters/registers are COSMOS hybrids.

As stated earlier, the system operates at a very low signal-to-noise ratio; this results in a large number of "false alarms" in each channel, due to the noise contribution of the background. In order to make sure that only "legitimate events" are registered in the counters, there is a three-out-of-four coincidence circuit which further requires coincidence to be at least 3.2 microsecond duration.

A second logic circuit rejects signals which recur at the spacecraft spin rate. Such signals are attributed to stars, and to limit the amount of data telemetered, are recorded only once. Nevertheless, since a set of selected stars are used for calibration purposes, this star exclusion circuit can be disabled on command to permit repeated observation of a given star. Such observations are necessary to determine post-launch alignment of telescopes and the response of the sensor system to sources of known brightness and spectral characteristics, the type of information important for the interpretation of zodiacal light measurements and the solution of system equations.

During the time when no "events" are registered, the system reads the background only. In order to provide a trajectory reference for "events", and to permit "mapping" of the background, the Pioneer vehicle generates a spoked wheel of 512 bits per revolution, referred to an index pulse. The AMD electronics divides the 512 bits by 4, and takes a sample of this number at the time the data are taken; thus, a position is recorded to an accuracy of $360^{\circ}/128$, i. e., about 2.8° . In the normal "star exclusion enabled" mode, any event recurring at the vehicle spin rate, i. e., reappearing in the same 2.8° (or adjacent)

position sector in succession, is identified as a "Star" and excluded from read-out after the first time it is encountered.

Finally, in addition to the two basic thresholds which are available on ground command, three preamplifier bandwidth settings can be commanded to improve signal-to-noise ratio under conditions of high ambient noise, for slower particles, and during star calibration.

The electronics subsystem is housed in a black-anodized aluminum box. Four multilayer boards are supported from a central "mother" -board which is squeezed between the two halves of the aluminum housing for rigidity. Two centrally located boxes provide additional support. Polyurethane foam is sandwiched between the boards for damping. Two connectors interface with the spacecraft and the optics, respectively. The total weight of the electronics box as shown in Figure 24 is 0.83 Kg. A block diagram of the electronics subsystem illustrating its interface with the previously discussed optical subsystem is shown in Figure 25.

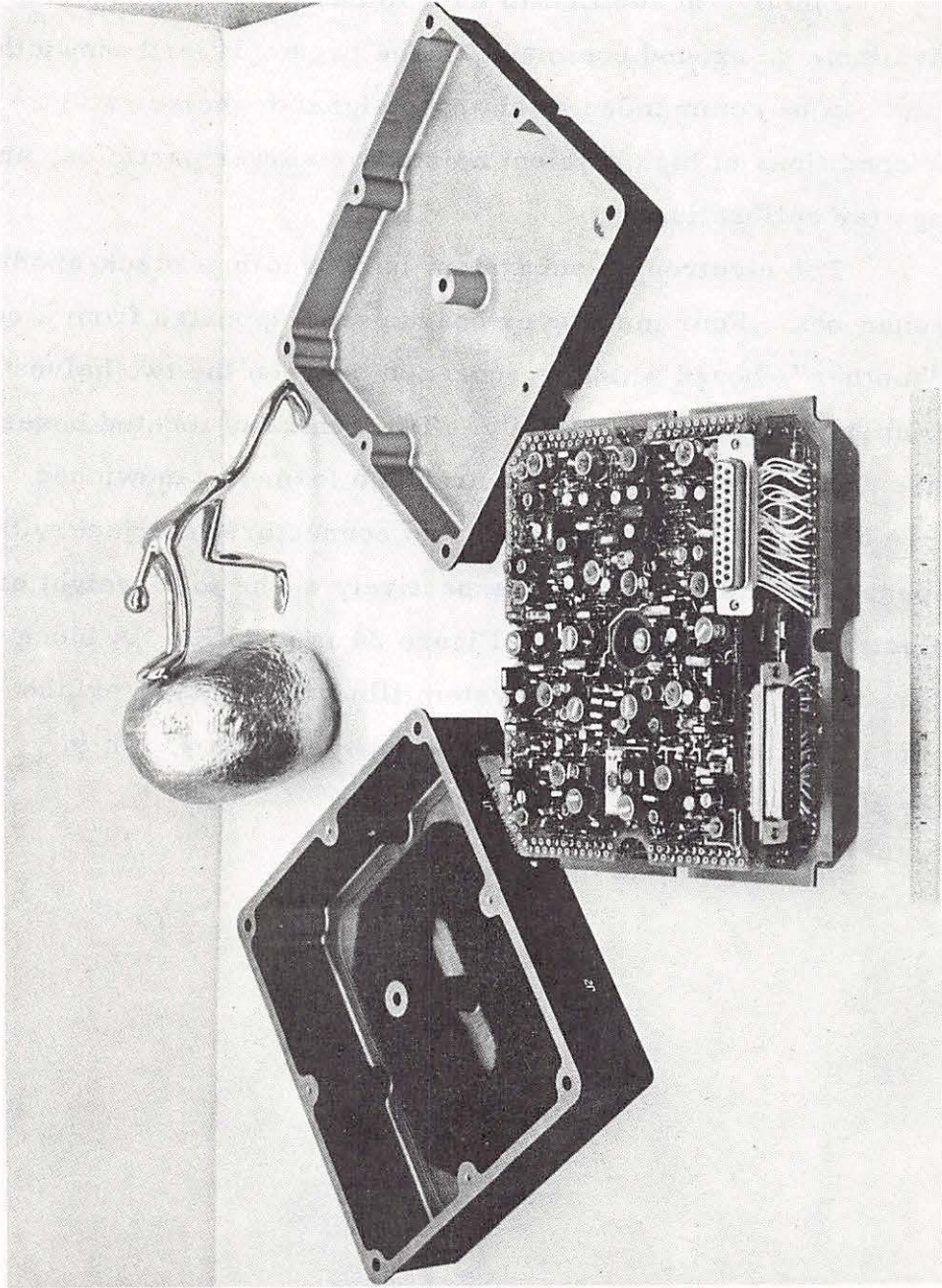


Figure 24. AMD Electronics

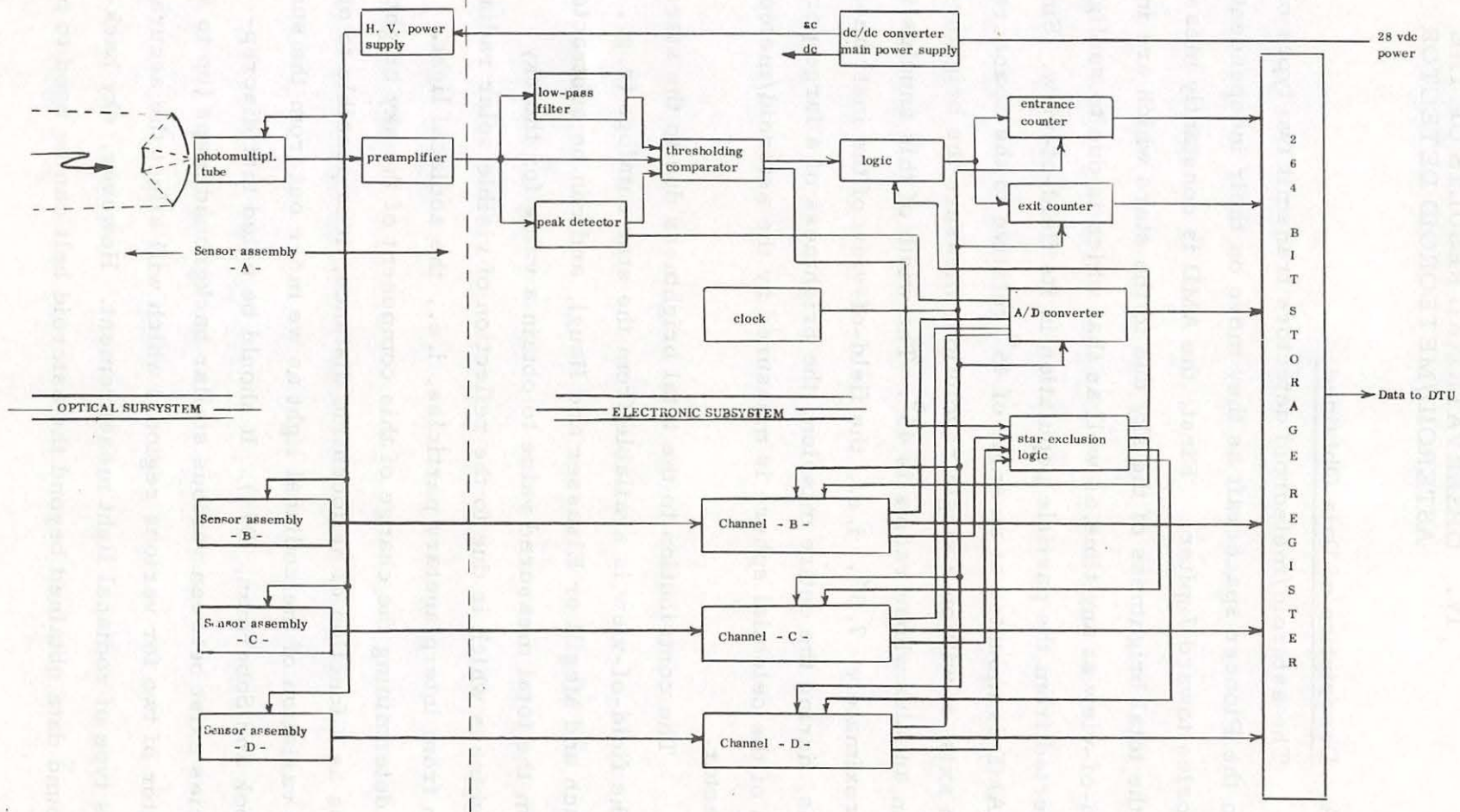


Figure 25. AMD Block Diagram

IV. OBSERVATIONAL RESULTS OF THE ASTEROID/METEOROID DETECTOR

IV.A. Description of Data Obtained

The asteroid/meteoroid detectors transmit two types of data from the Pioneer spacecraft as they move on their independent trajectories toward Jupiter. First, the AMD is constantly measuring the total brightness of the sky due to the stars which are in its field-of-view at any time, as well as that which is due to sunlight reflected from the particle population in its field-of-view. Since the AMD is mounted at an angle of 45° relative to the spacecraft spin axis, it will, on a single revolution, measure the brightness of an annulus whose radius is 45° . The width of this annulus is approximately 7.5° , i. e., the field-of-view of the instrument. Thus, during the entire mission, the brightness of a large portion of the celestial sphere is measured by the asteroid/meteoroid detector.

The contribution to the total brightness due to the stars in the field-of-view is available from the star catalogs (e. g., Roach and Megill or Elsasser and Haug), and can be subtracted from the total measured value to obtain a value for the sky brightness which is due to the reflection of visible solar radiation from interplanetary particles, i. e., the zodiacal light. By determining the change of this component of the sky brightness as a function of heliocentric distance, it is possible to obtain the variation of the zodiacal light as we move out from the sun (Zook and Soberman, 1974). It should be noted that discrepancies exist between various stellar background maps (up to a factor of two for various regions) which will affect the accuracy of this type of zodiacal light measurement. However, sky background data obtained beyond the asteroid belt can be used to provide

the proper conditions.

The second type of data obtained by the AMD consists of individual particle detections as a bright particle transits the fields-of-view of the four telescopes. As the particle moves through the fields-of-view, the times of entry and exit for each field-of-view are recorded and transmitted as event data. In addition, the sky background at the time of the event, and the signal level due to the reflected sunlight from the particle, are transmitted to complete the individual event data. The received (measured) data for a typical event are shown in Table 1. From the individual event data, it is first possible to obtain a spatial distribution of particles as a function of size and heliocentric distance. Secondly, it is possible to obtain a value for the gegenschein, i. e., the brightness of the zodiacal light in the anti-solar direction. And finally, it was expected that the heliocentric orbit of particles which demonstrated high signal to noise ratios would be obtained. However, the reduction of the data which is required before the analysis to obtain this information can begin merits considerable discussion.

TABLE 1 RECEIVED DATA FROM A TYPICAL AMD EVENT

DATE: 10-15-72

TIME; 9:15:20

CHANNEL	BACKGROUND (BITS)	PEAK (BITS)	ENTRANCE TIME (BITS)	EXIT TIME (BITS)
A	26	37	47	331
B	16	24	0	413
C	40	69	67	490
D	36	53	32	520

THRESHOLD: Normal

BANDWIDTH: Narrow

STAR EXCLUSION: Enable

For background and peak one bit equals .00975 volts. For entrance and exit times one bit equals 1.6 μ sec in narrow bandwidth.

TABLE 1. RECEIVED DATA FROM A TYPICAL AMD EVENT

IV. B. Data Reduction Procedure

Since the asteroid/meteoroid detector is an electro-optical instrument, we must consider the possibility that events which are detected may, in fact, be caused by sources other than meteoric particles passing through its field-of-view. Therefore, each event which is recorded by the AMD must be screened to determine if it is indeed a valid event.

False events may be due to any of the following sources: 1) stars, 2) planets, 3) spacecraft generated particles, 4) solar protons, 5) sudden increases in the background, or 6) electronic or optical noise. If a given event could not be attributed to any of these sources, it was considered to be a true particle detection.

Events which were due to stars or planets being observed as the instrument scanned across the object can be quite easily sorted out of the event data. A given star or planet will obviously occur in the same sector of the spacecraft rotation and therefore, this repetitive occurrence allows them to be easily discarded. In fact, the passage of a star or planet through the field-of-view of the instrument is the means whereby the instrument sensitivity is compared to the preflight laboratory calibration measurements (Appendix B). Since the sensitivity of the instrument was such that a very bright star was required to exceed the threshold, i. e., approximately a zero magnitude star was required even in the darkest portion of the sky, it was not a difficult task to identify any event which may have been due to a star since the number of stars of this magnitude is not large. During the transit of the Pioneer vehicles from 1 to 3.5 astronomical units, only two stars were observed to have been recorded, namely; Arcturus and Rigil Kentaurus (α Centauri). The planet Jupiter was observed by the instrument for two periods of a few weeks during the spacecraft's transit to 3.5 AU and was used to determine the alignment

of the four telescopes at those times. Figures 26 and 27 show typical background scans with Arcturus and Jupiter in the fields-of-view. Also shown in these figures is the increased background in several sectors due to direct solar illumination of the light shield.

The third possible source of false events, spacecraft particles, are more difficult to discriminate against since they may occur randomly and probably would not be repetitive in the same sector of revolution. It seems likely that the greatest occurrence of this type of event would be during or shortly after a spacecraft thruster firing. However, events were observed only for spacecraft precession maneuvers and these events occurred in the same sector immediately after the thruster firing and could be easily discarded. It is unlikely that particles which merely become dislodged from the spacecraft would move into the AMD fields-of-view since the AMD location on the spacecraft (see Figure 12) would require a force to accelerate them parallel to the spacecraft's spin axis. However, in the absence of such a force, the only direction possible for a particle leaving the spacecraft would be perpendicular to the spacecraft spin axis due to the spacecraft's rotation. Furthermore, any particle originating from the spacecraft would be moving at a relatively slow velocity and therefore if it were detected by the AMD, it would have a very long time duration in the fields-of-view and could be eliminated by this consideration.

It is possible that a real interplanetary particle impacting the spacecraft would cause ejecta to be emitted at a high velocity, but, it is unlikely that a significant number of events detected by the AMD can be due to this phenomenon. Hypervelocity impact studies (Gault, et al., 1963) indicate that ejecta which have velocities comparable to the projectile velocity have low ejection

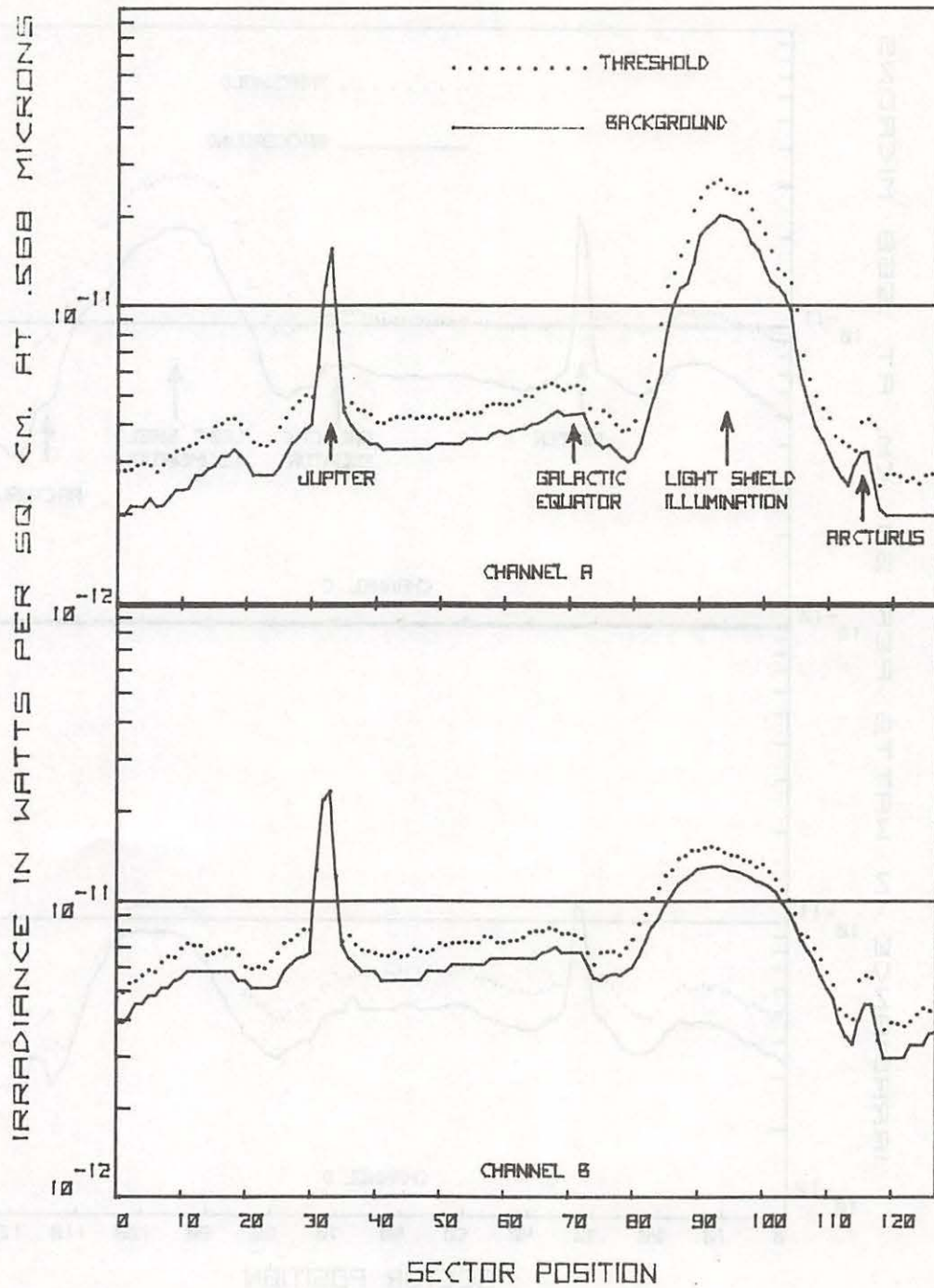


Figure 26. Background Scan From Pioneer 10
 (Channels A and B)

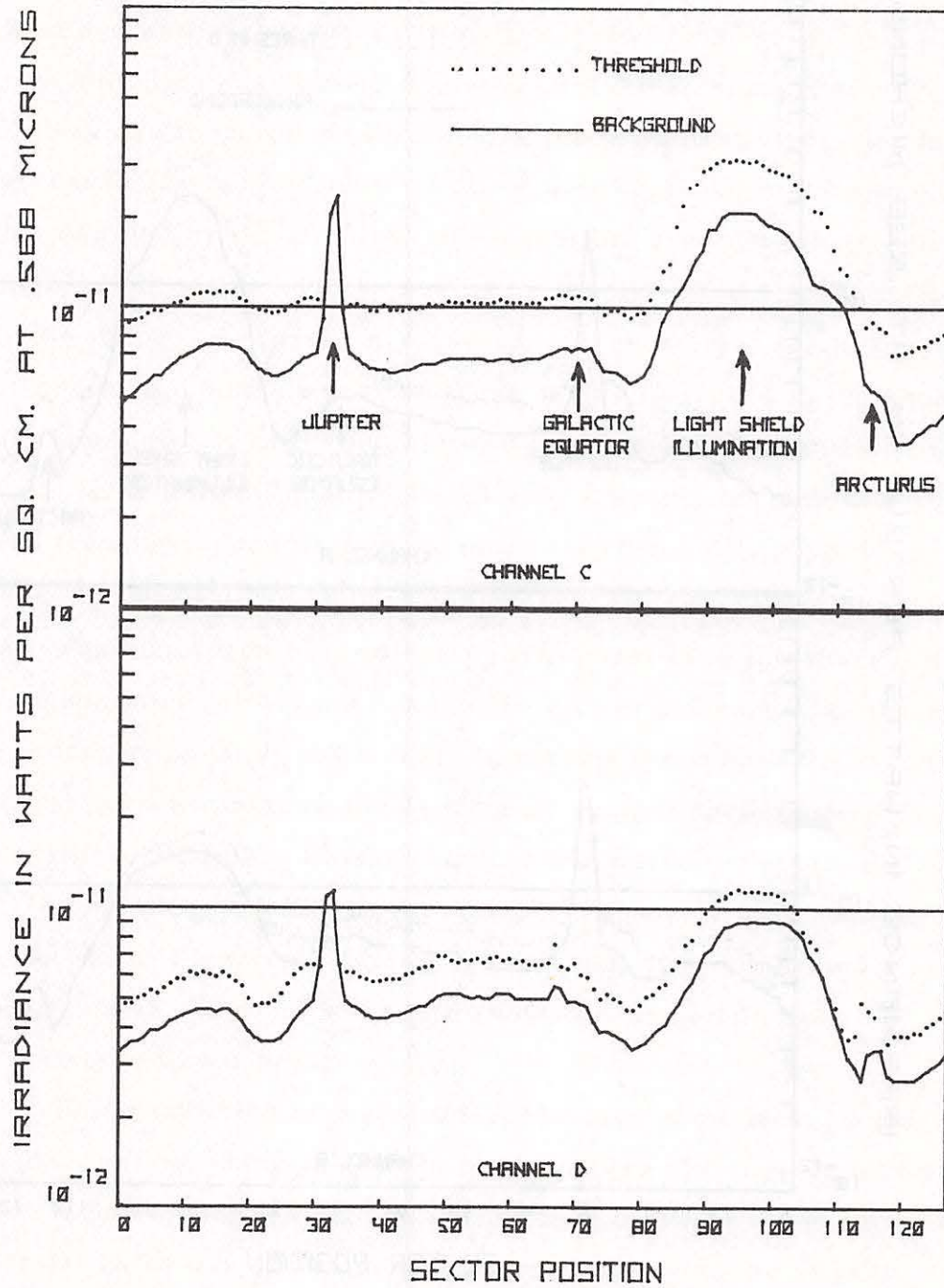


Figure 27. Background Scan From Pioneer 10
 (Channels C and D)

angles measured with respect to the local horizontal. If ejecta of this type pass through the AMD field-of-view they will be in the spacecraft shadow and not be detected. Most ejecta, however, have velocities an order of magnitude or more less than that of the projectile and have large ejection angles ($\gtrsim 45^\circ$). The probability of these ejecta passing through the fields-of-view is low due to their high ejection angles. Moreover, if they were detected they would have unusually long transit times and would be eliminated on that basis. Therefore, it is felt that particles originating from the spacecraft cannot contribute to a significant fraction of the events detected by the AMD.

During August of 1972, the Pioneer 10 spacecraft was subjected to an intense solar bombardment due to a very high level of solar activity. During this period of time, hundreds of events were detected by the AMD due to the interaction of the solar protons with the photomultiplier tubes used in the optical subsystem of the AMD. However, most of these events had very low signal levels and very short transit times. The data obtained during this period of time provided a good base for discriminating against this type of possible false event. All events which were detected during these periods of increased solar activity were eliminated unless their signal levels and times were markedly different from those characteristic of the solar proton type events.

Sudden increases in the background were observed only during those periods when the light shield surrounding the four telescopes was directly illuminated by the sun. Since this phenomenon occurred only during a specific period in the rotation cycle and was easily observed (Figures 26 and 27), events resulting from it were easily discarded by referring to the background scans.

Finally, it is conceivable that random noise due to the star field background may cause a false event. However, the three-fold coincidence requirement which is incorporated into the electronics design makes the probability of this occurrence very low and it is therefore unlikely that a significant number of the events are due to this source. In addition, this possibility was tested in the laboratory by allowing the instrument to observe a simulated star background which varied in a sinusoidal manner to determine if, in fact, the instrument was susceptible to this type of false event. This test was conducted for approximately one week during which no events were recorded.

The preceding steps were applied to each event to establish whether or not it should be regarded as a true particle detection. After applying this screening process to all events detected between 1 and 3.5 AU by the AMD on Pioneer 10, it was determined that 232 real events had been detected during this portion of the mission. Figure 28a shows the number of events detected during each day of the Pioneer 10 spacecraft's journey to 3.5 AU as a function of heliocentric distance. It should be noted that this figure has not been adjusted to reflect the change in instrument sensitivity as the spacecraft moved away from the sun.

The analysis of the Pioneer 11 AMD data was made more difficult than was the case with Pioneer 10 because one of the channels malfunctioned early in the mission (at 1.1 AU from the sun), resulting in its triggering on noise continually. Thus, only two of the channels had to trigger for an event to be recorded. The malfunction is attributed to a thermally induced crack in the envelope of the photomultiplier resulting in degradation of the photocathode. Therefore, in addition to the previously discussed screening procedure, the following criteria were used in screening the Pioneer 11 data:

1. The transit time in two or more channels had to be at least 75 μ sec. This criterion eliminated most of the noise-generated events (almost all of which were of short duration) and took account of the poor reliability of particle detection closer than 10 m to the detectors.

2. Either four-fold coincidence was required, or the peak intensity in the malfunctioning channel had to exceed a pre-determined value (7 data bits). Although the sensitivity of that channel degraded considerably, it did not go to zero (as evidenced by its response to Jupiter, which was 8 data bits) and could still be used as a gross indicator of real particles.

The above selection process yielded a total of 51 events between 1.0 and 3.5 AU. This number was considerably less than that used to derive the Pioneer 10 results, primarily because of the elimination of close-range events, which had been included in the Pioneer 10 analysis.

The final step in preparing the event data for subsequent analysis was to store the measured values of the time, background and signal level for each event in a computer data bank in order to facilitate future calculation and manipulation of the basic data. A computer listing of this data appears in Appendix C.

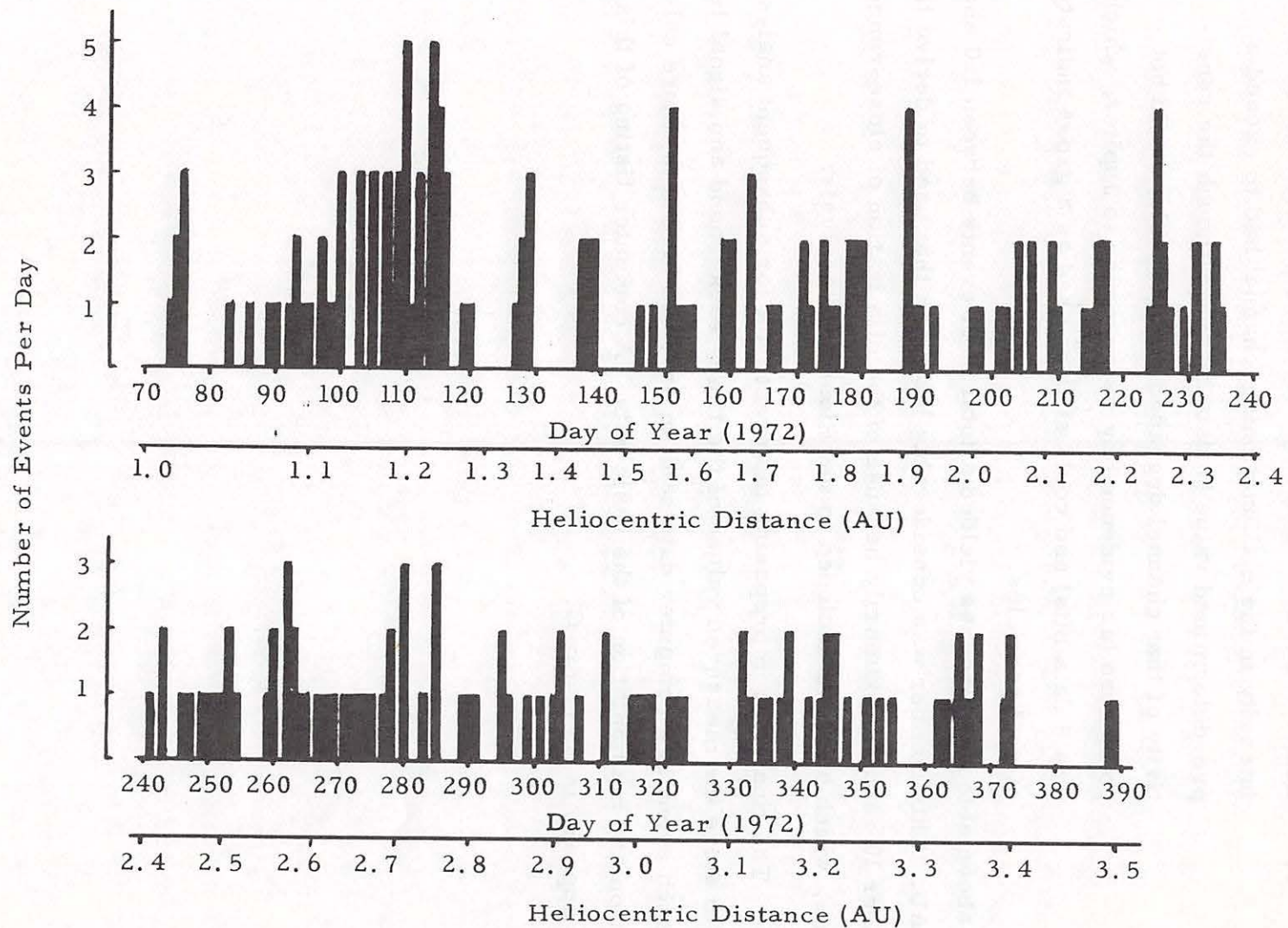


Figure 28a. Events Detected by AMD on Pioneer 10 as a Function of Heliocentric Distance

Number of Events Per Day

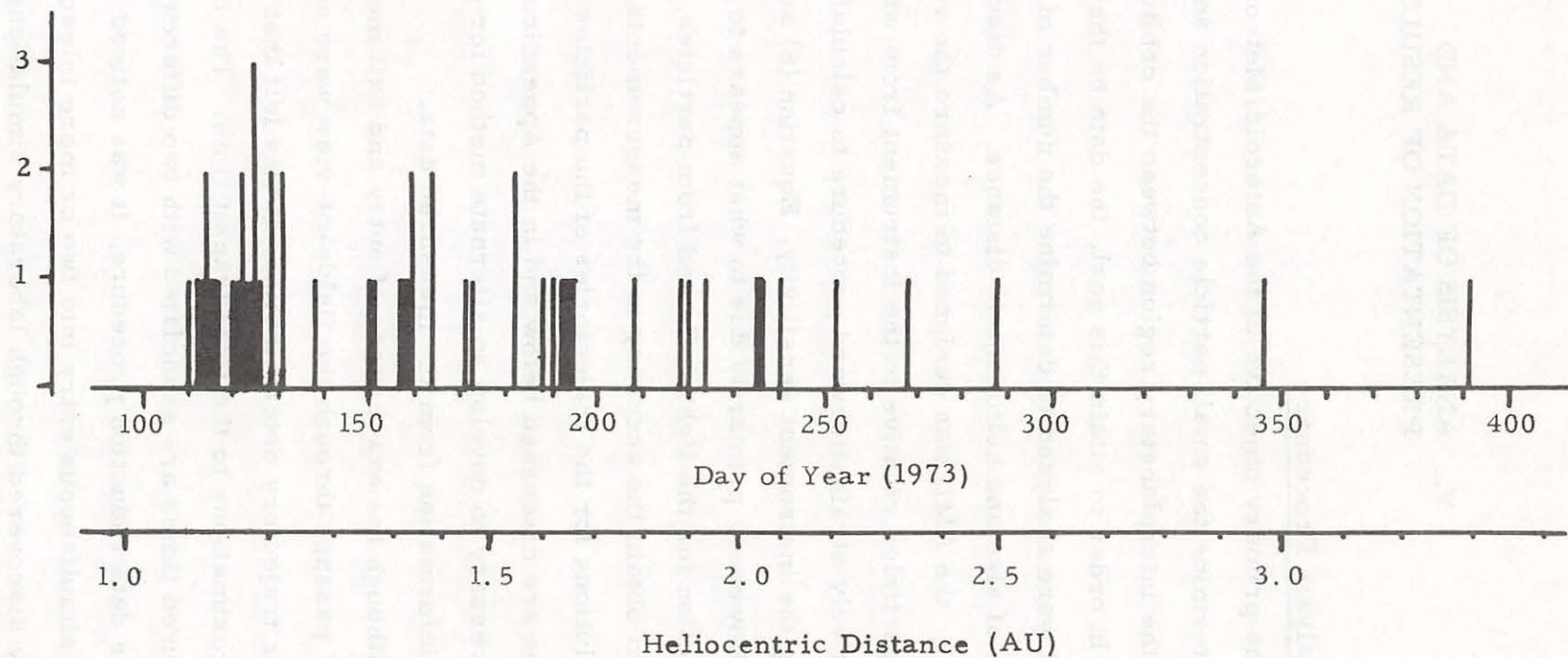


Figure 28b. Events Detected by AMD on Pioneer 11 as a Function of Heliocentric Distance.

V. ANALYSIS OF DATA AND PRESENTATION OF RESULTS

V.A. Analysis Procedure

The primary objective of the Asteroid/Meteoroid Detector was to determine the small particle concentration and size distribution in the interplanetary region between the orbits of Earth and Jupiter. In order to attain this goal, the data on the particles measured were analyzed to determine the number of particles as a function of size and heliocentric distance. As discussed in Section III, the AMD was designed to measure the velocity and range of particles relative to the instrument from which it would be a relatively straightforward procedure to calculate the particle size using the instrument sensitivity, Equation (8) and an assumed albedo. However, primarily due to what appears to be a peculiar phase function for the light reflected from particles, it was not possible to obtain the accuracy in the measurements required to derive solutions for the trajectories of the particles. These difficulties are discussed below and in the Appendices. Therefore, it was necessary to develop an alternate method for extracting the required information from the measured data.

Although the exact times of entry and exit measured for the particles' passage through the fields-of-view were not accurate enough for trajectory determination, it was felt that they were good approximations to the total transit time. The inaccuracies in the measured times are associated with two different phenomena. During the data reduction procedure, it was noticed that many events indicated simultaneous entry into two or more telescopes. It was eventually discovered through laboratory simulations that this behavior was due to cross talk between channels in the electronics. Further testing indicated that this problem was associated only with

the entrance counters and that the exit times were not affected by this anomaly. Laboratory testing also indicated that the cross talk occurred only when a telescope was triggered by a light pulse (i. e., a particle entering the field-of-view).

Another apparent anomaly was indicated by the fact that some of the events measured did not display the required coincidence between three fields-of-view. This behavior was ascribed to the fact that if the signal plus the associated noise dropped below threshold, the exit clock for that channel would not be restarted when the signal again came above threshold. This situation is illustrated in Figure 29. The result of this behavior is that the exit times measured may in some cases be too small and the resulting transit time too short. It is conceivable that positive noise spikes could also cause the exit counters to continue running after the particle had exited from the field-of-view. This, however, is unlikely since it would require a succession of several positive noise spikes. On the basis of the foregoing, it was concluded that the most accurate estimate of the transit time for a given event would be the longest transit time recorded by one of the four telescopes. Thus, in the following discussions the term transit time will refer to the longest transit time.

Since the velocities of the particles detected could not be obtained from the measured data, it was necessary to use approximate values based on the assumption that most of the particles detected were of asteroidal origin, moving in nearly circular orbits. For each particle detected, its circular orbital velocity was calculated corresponding to the position of the spacecraft (i. e., its radial distance from the sun) from Equation (16).

$$v \text{ (particle)} \simeq 29.8 \sqrt{\frac{S_0}{S}} \text{ km/sec} \quad (16)$$

where S_0 and S are the heliocentric distances of the earth and the

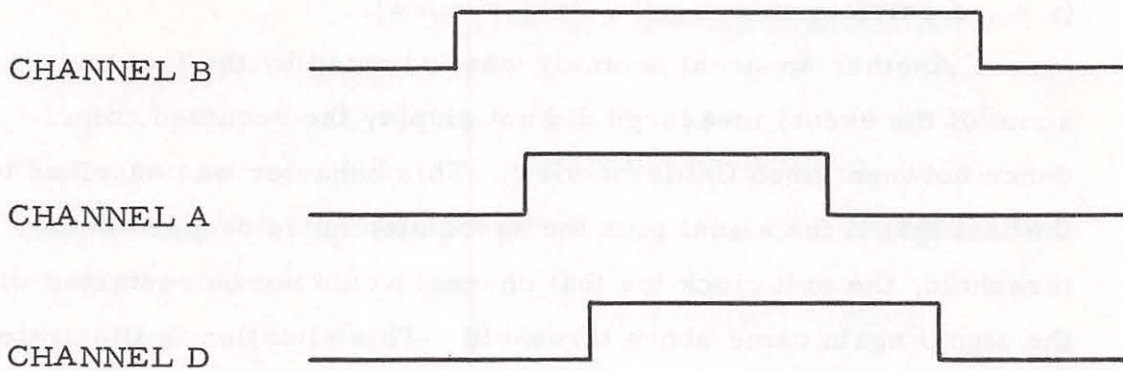


Figure 29. (a)

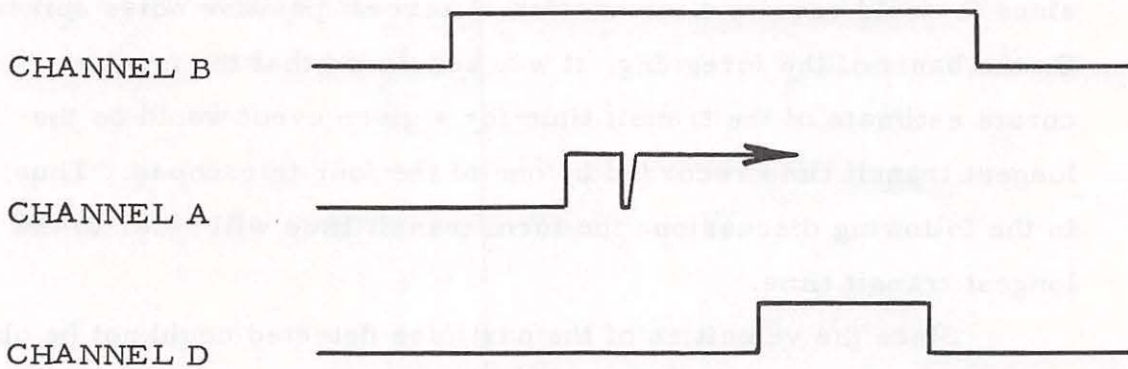


Figure 29. (b)

Figure 29. Examples of Three-Fold Coincidence. (a) Signal Above Threshold in all Three Channels Simultaneously. (b) Signal Drops Below Threshold in Channel A and Then Exceeds Threshold Again.

spacecraft respectively. Using the assumed circular orbit velocity and the known spacecraft velocity, the relative encounter velocity with the spacecraft was calculated for each event.

It should be pointed out here that the ability of the AMD to detect particles is a function of the size of the particles. This sensitivity can be defined in terms of a range to radius ratio. For example, a ratio of 10^5 would imply that a particle of radius 1 centimeter would be detectable out to a range of 1 kilometer. The value of this ratio is, of course, dependent upon the background signal due to stars in the field-of-view as was discussed in Section III. As the background and peak (due to noise in the background) increase, the minimum signal required to exceed threshold also increases, resulting in a corresponding decrease in the range to radius sensitivity ratio. Typical examples of the varying background and threshold levels were shown in Figures 26 and 27. The heliocentric distance of the particles also affects the sensitivity of the instrument since the solar radiation available for reflection from the particles decreases as the square of the heliocentric distance.

These sensitivity variations are manifested in what will be referred to as the sensitive volume of the instrument. If we consider each telescope field-of-view to define a conical volume in space within which particles can be seen, it is possible to calculate the size of this volume for various particle sizes. The size of this volume varies during the spacecraft rotation due to the changing background (Figures 26 and 27) and decreases throughout the mission due to the decreasing solar radiation. A typical variation in the sensitive volume (for particles of radius 0.5 mm) during one spacecraft rotation cycle is shown in Figure 30. The variations in sensitive volume are correlated with the background changes illustrated in Figures 26 and 27, as expected. In

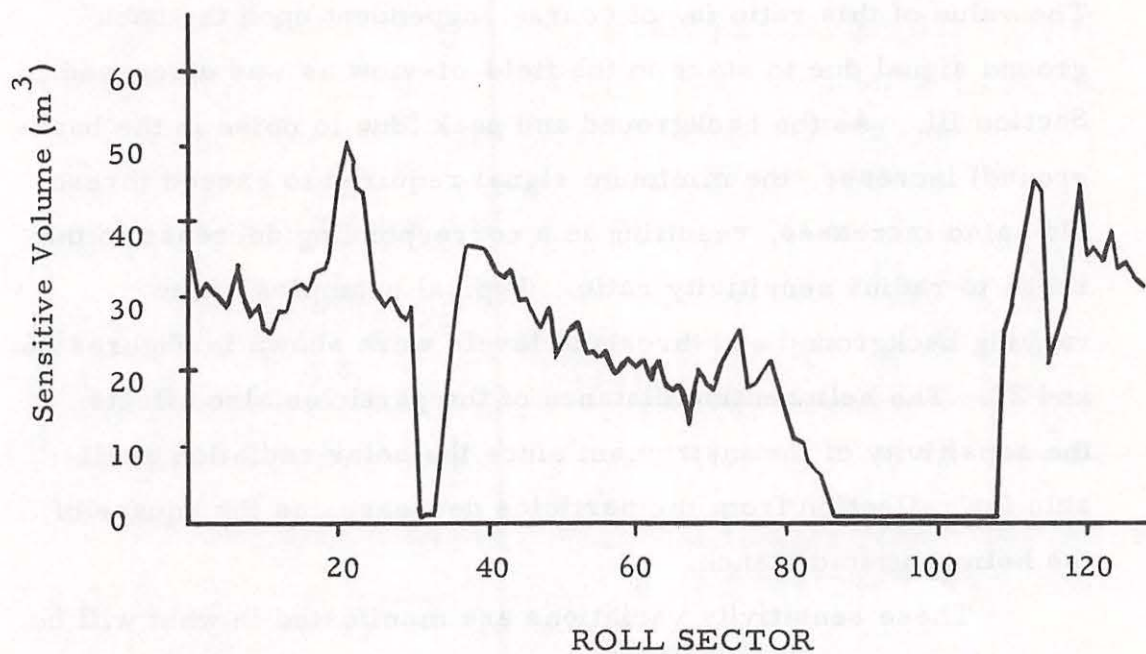


Figure 30. Sample of the Sensitive Volume Variation During One Day of Pioneer 10 Mission

Figure 31 the variation in average sensitive volume is shown for Pioneer 10 as a function of heliocentric distance for the two bandwidth modes in which the AMD was operated. The solid line in this figure shows the mean value as bandwidth modes were switched during the mission. The dashed lines deviate from the expected inverse cube variation due to changes in the spacecraft attitude which affected the average particle scattering angle.

As shown in Appendix D, the average particle transit time, $\bar{\tau}$, can be expressed as:

$$\bar{\tau} = \frac{\pi \alpha R}{2 v} \quad (17)$$

where R is the range to the detector, α is the field-of-view half angle and v is the particle encounter velocity relative to the instrument assuming a circular orbit for the particle. Rewriting Equation (8) yields the following expression for the particle range to the detector

$$R = \left(\frac{I_o r f(\gamma)}{I_{\min}} \right)^{1/2} \frac{S_o}{S} a \quad (18)$$

where I_o is the solar irradiance at 1 AU, I_{\min} is the minimum irradiance that can be detected (Appendix B), r is the bond albedo, $f(\gamma)$ is the scattering phase function, S_o and S are the heliocentric distances of the earth and the particle respectively and a is the particle radius. Thus, from Equations (17) and (18), the particle range, size and sensitive volume within which it could be seen can be calculated.

The cumulative spatial concentration of the particles can then be calculated from the expression:

$$N = \frac{\Delta \tau}{T \Delta V} \quad (19)$$

where T is the effective observation time and $\Delta \tau$ is the total dwell time (transit time) of particles in the volume element ΔV . N is the

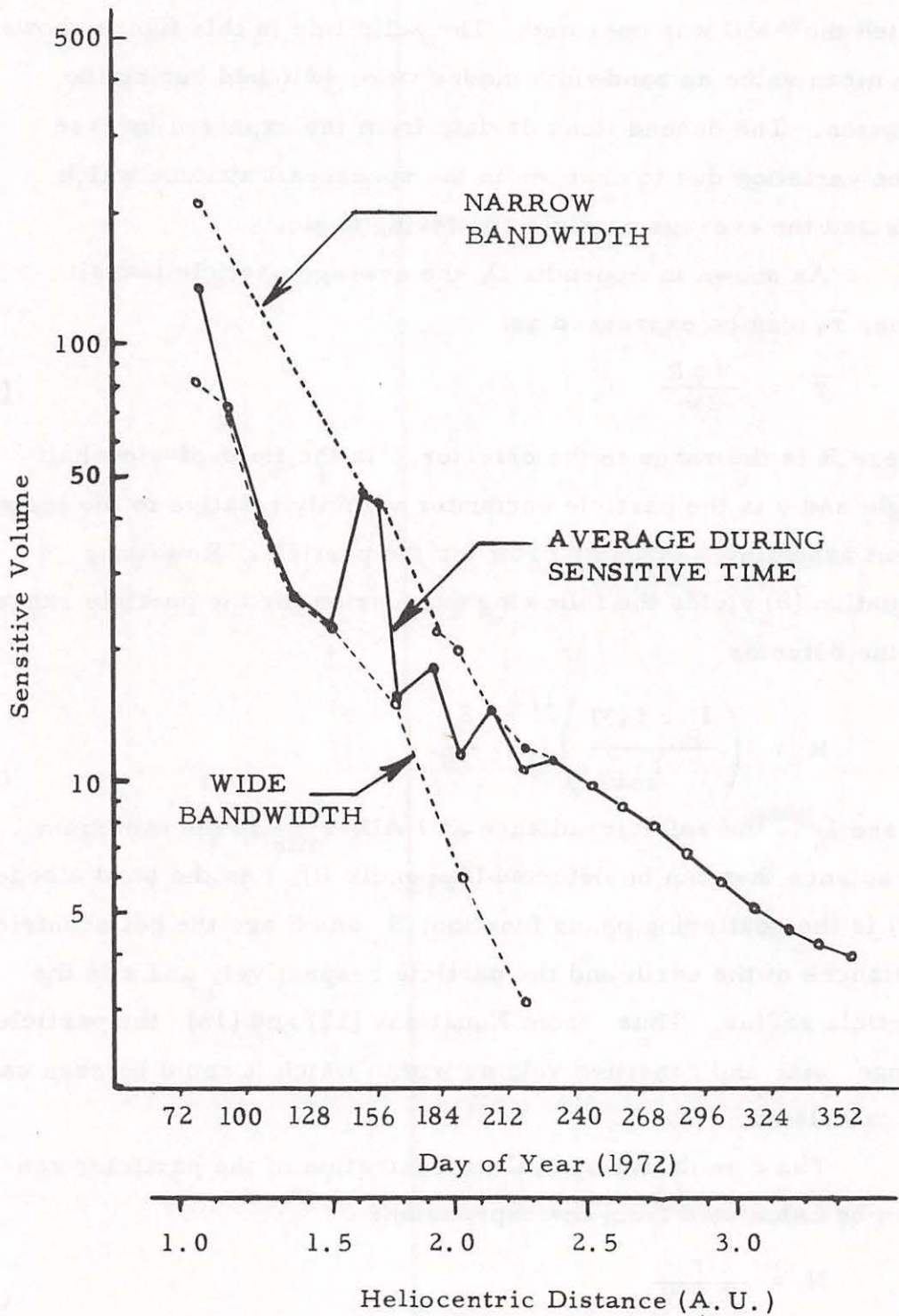


Figure 31. Variation in Sensitive Volume During Transit to 3.5 AU. on Pioneer 10

number per unit volume of all particles which can be detected in the volume element.

In deriving the spatial concentrations and size distributions, the measured transit time of each particle and the calculated encounter velocity were used to determine its range from the instrument via Equation (17). The AMD sensitivity at the time of the particle detection then determined the particle size. An observation time was then defined (e. g., time corresponding to a change in spacecraft heliocentric distance of 0.2 AU) and an average sensitive volume computed for each particle size range during the observation time. The cumulative spatial concentration was then calculated for each size grouping using Equation (19). The tabulated results are given in Appendix E.

In order to validate this analysis procedure and prove that it was not introducing a bias into the results, the method was tested using a computer simulation of the problem (see Appendix F). This simulation also provided a means of estimating the uncertainties associated with the results due to the various assumptions.

V. B. Size and Spatial Distribution Obtained From Measurements on Pioneer 10

The data obtained during the flight of the Pioneer 10 spacecraft were separated into two heliocentric regions for analysis. The data obtained prior to entering the asteroid belt (1.0 - 2.0 AU) comprise one set while the data obtained during the transit of the asteroid belt were placed in the second group.

In analyzing the data apparent variations in the size distribution with heliocentric distance were noticed. To investigate this, the preasteroid belt data were separated into five equal heliocentric segments while the data obtained in the asteroid belt were treated in three such segments. The results are shown in Figures 32 and 33 respectively.

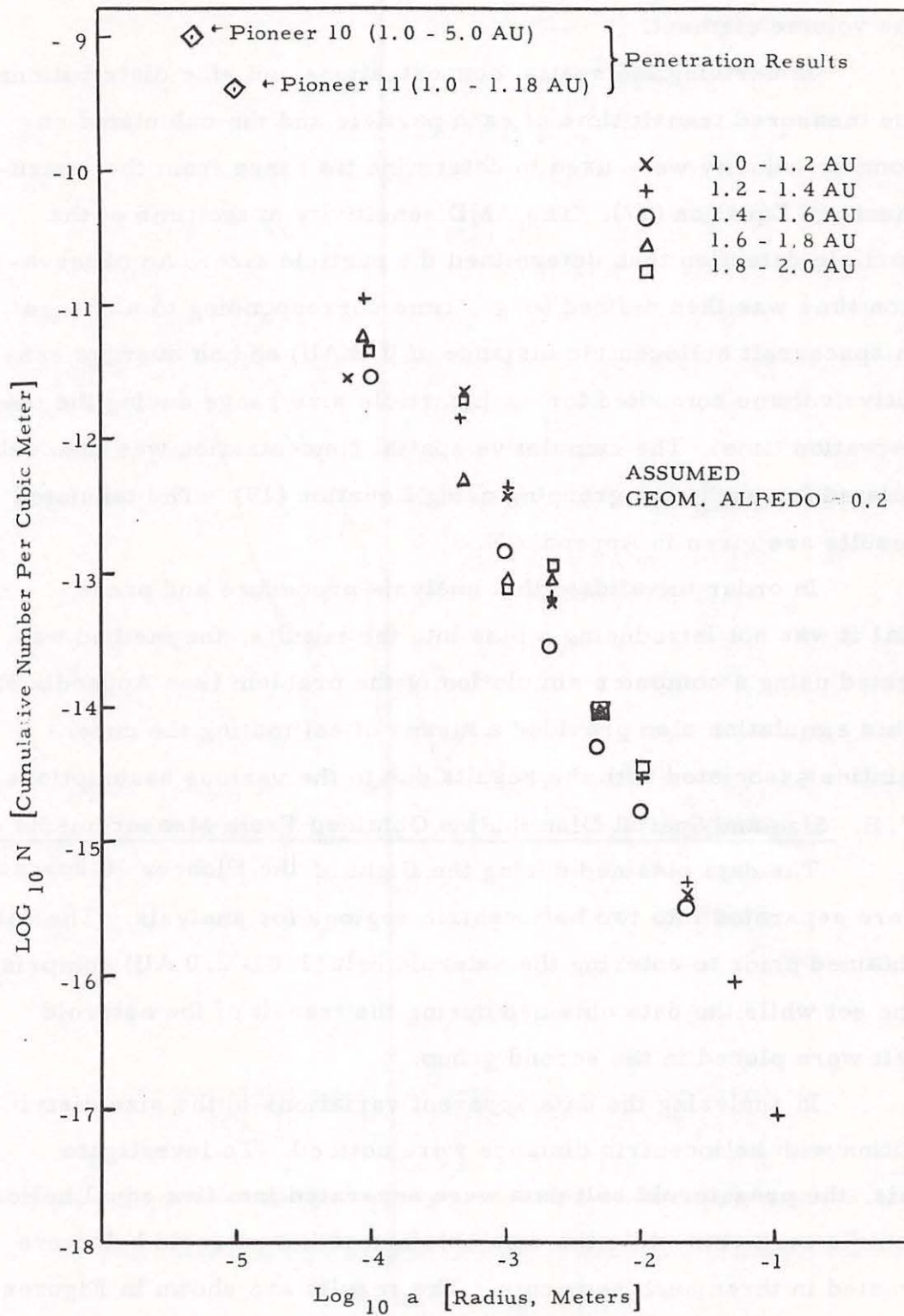


Figure 32. Particle Size Distribution for Five Segments of Pre-asteroid Belt Region From Pioneer 10

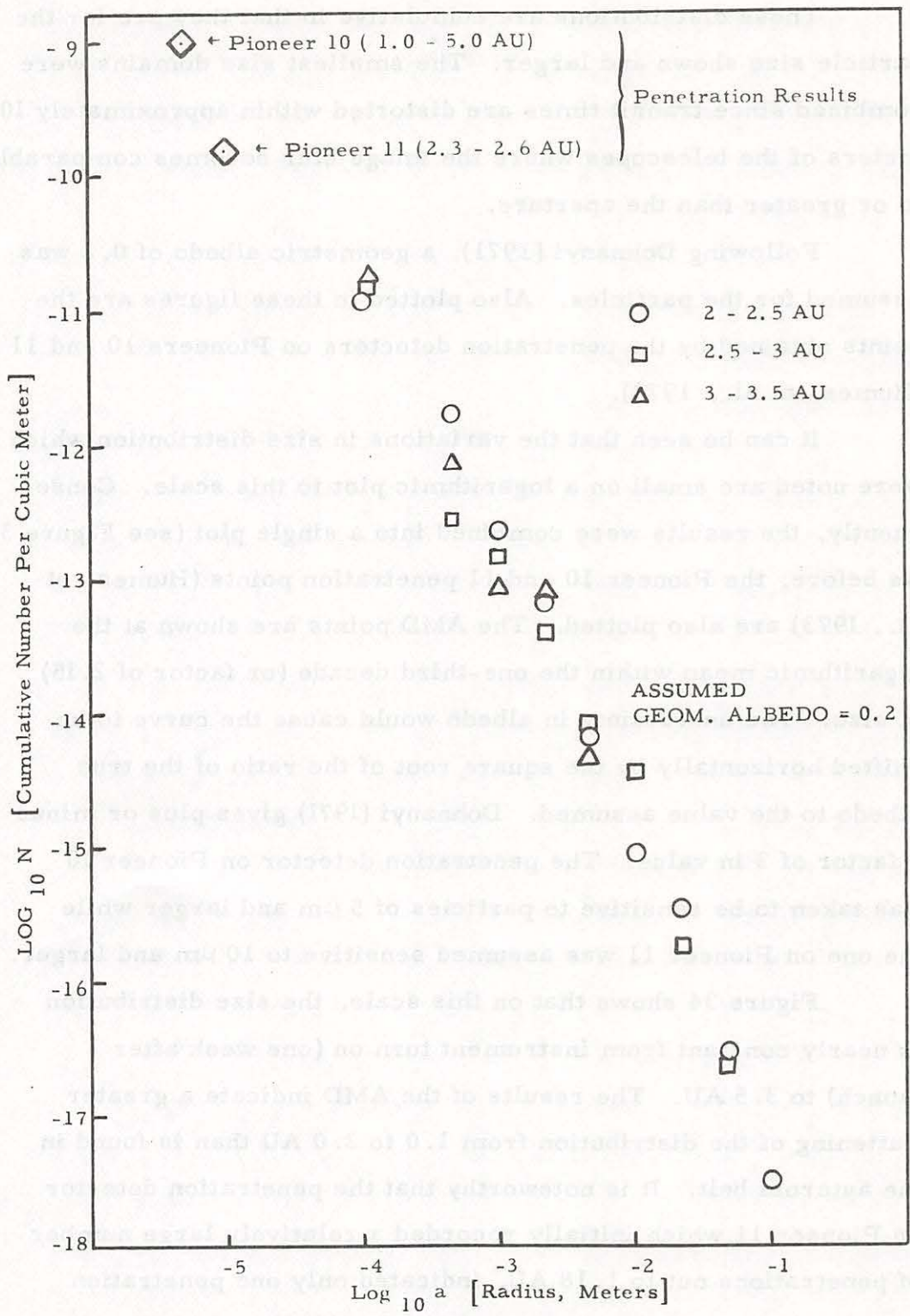


Figure 33. Particle Size Distribution for Three Regions of the Asteroid Belt From Pioneer 10

These distributions are cumulative in that they are for the particle size shown and larger. The smallest size domains were combined since transit times are distorted within approximately 10 meters of the telescopes where the image blur becomes comparable to or greater than the aperture.

Following Dohnanyi (1971), a geometric albedo of 0.2 was assumed for the particles. Also plotted in these figures are the points obtained by the penetration detectors on Pioneers 10 and 11 (Humes, et al., 1973).

It can be seen that the variations in size distribution which were noted are small on a logarithmic plot to this scale. Consequently, the results were combined into a single plot (see Figure 34). As before, the Pioneer 10 and 11 penetration points (Humes, et al., 1973) are also plotted. The AMD points are shown at the logarithmic mean within the one-third decade (or factor of 2.15) of size. The uncertainty in albedo would cause the curve to be shifted horizontally by the square root of the ratio of the true albedo to the value assumed. Dohnanyi (1971) gives plus or minus a factor of 3 in value. The penetration detector on Pioneer 10 was taken to be sensitive to particles of 5 μm and larger while the one on Pioneer 11 was assumed sensitive to 10 μm and larger.

Figure 34 shows that on this scale, the size distribution is nearly constant from instrument turn on (one week after launch) to 3.5 AU. The results of the AMD indicate a greater flattening of the distribution from 1.0 to 2.0 AU than is found in the asteroid belt. It is noteworthy that the penetration detector on Pioneer 11 which initially recorded a relatively large number of penetrations out to 1.18 AU, indicated only one penetration between 1.18 and 2.3 AU (Humes, et al., 1973). No data point for this region was assigned by the investigators but it should be in keeping with the trend of the present results between 1.0

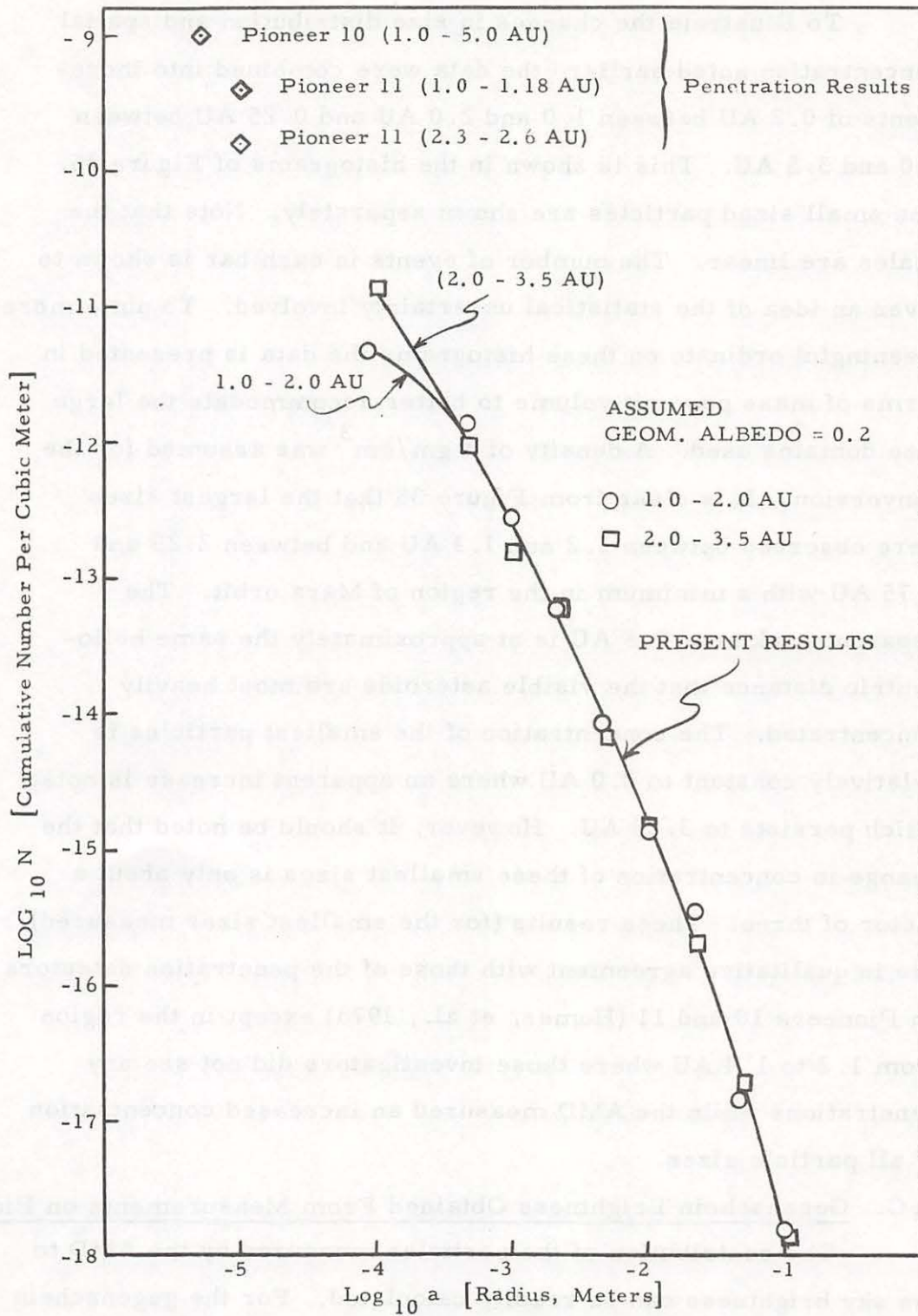


Figure 34. Combined Particle Size Distributions From Pioneer 10 (1.0 - 3.5 AU)

and 2.0 AU.

To illustrate the changes in size distribution and spatial concentration noted earlier, the data were combined into increments of 0.2 AU between 1.0 and 2.0 AU and 0.25 AU between 2.0 and 3.5 AU. This is shown in the histograms of Figure 35. The small sized particles are shown separately. Note that the scales are linear. The number of events in each bar is shown to give an idea of the statistical uncertainty involved. To put a more meaningful ordinate on these histograms the data is presented in terms of mass per unit volume to better accommodate the large size domains used. A density of 3 gm/cm^3 was assumed for the conversion. It is clear from Figure 35 that the largest sizes were observed between 1.2 and 1.3 AU and between 2.25 and 2.75 AU with a minimum in the region of Mars orbit. The apparent peak near 2.5 AU is at approximately the same heliocentric distance that the visible asteroids are most heavily concentrated. The concentration of the smallest particles is relatively constant to 2.0 AU where an apparent increase is noted which persists to 3.25 AU. However, it should be noted that the change in concentration of these smallest sizes is only about a factor of three. These results (for the smallest sizes measured) are in qualitative agreement with those of the penetration detectors on Pioneers 10 and 11 (Humes, et al., 1973) except in the region from 1.2 to 1.4 AU where those investigators did not see any penetrations while the AMD measured an increased concentration of all particle sizes.

V.C. Gegenschein Brightness Obtained From Measurements on Pioneer 10

The contribution of the particles measured by the AMD to the sky brightness can be readily calculated. For the gegenschein this can be done from the relationship (van de Hulst, 1947):

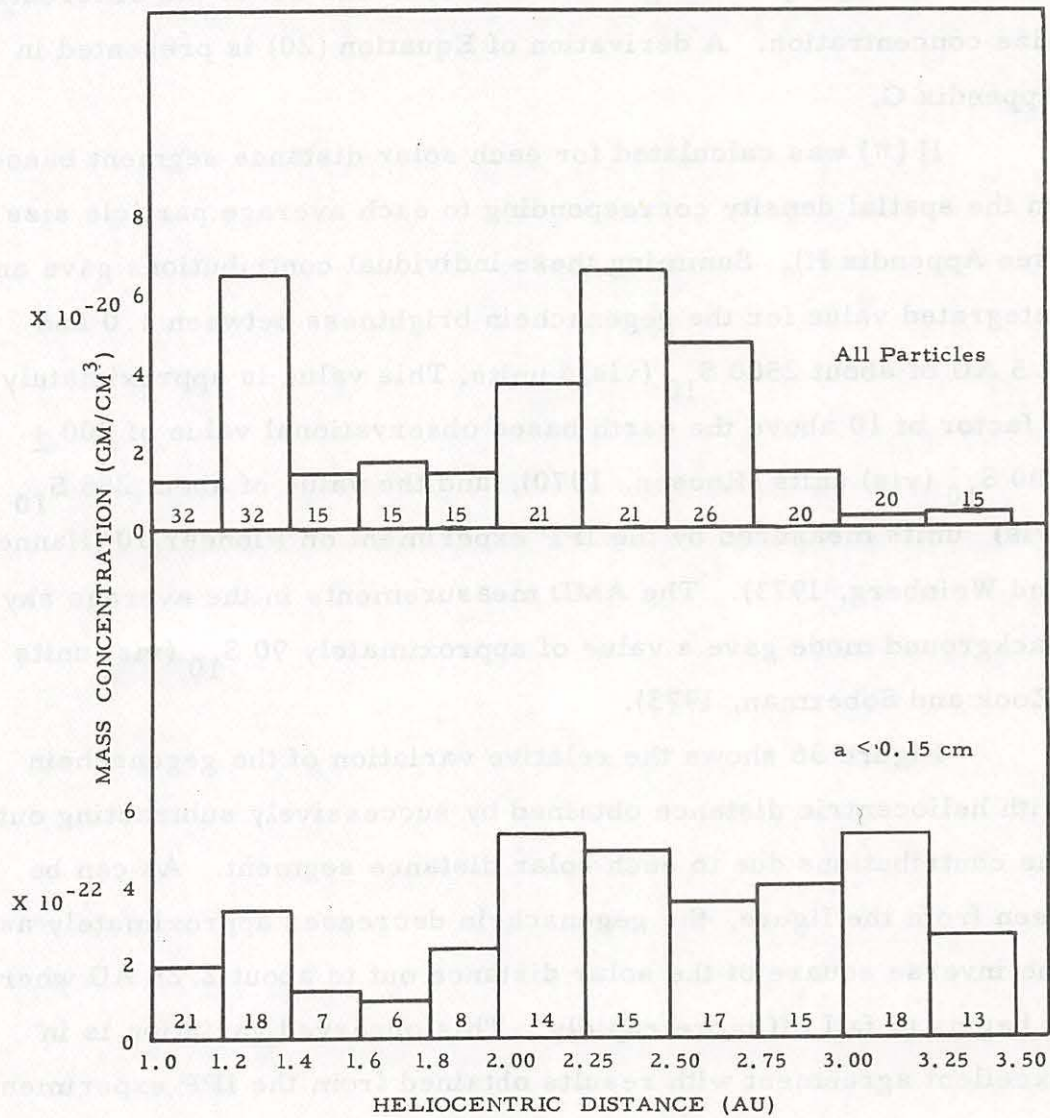


Figure 35. Mass Concentration due to all Particles and the Smallest Particles From Pioneer 10. (The Number of Particles is Shown in Each Bar).

$$H(\pi) = I_0 S_0^2 \int_{S_1}^{S_2} \int_{a_{\min}}^{\infty} \frac{p a^2}{S^2} dN(a, S) dS \quad (20)$$

where $H(\pi)$ is the backscatter brightness per unit solid angle, and, as before, I_0 is the solar irradiance at 1 AU, S_0 and S are the heliocentric distances to the earth and particles respectively, a is the particle radius, p is the geometric albedo and dN is the differential size concentration. A derivation of Equation (20) is presented in Appendix G.

$H(\pi)$ was calculated for each solar distance segment based on the spatial density corresponding to each average particle size (see Appendix H). Summing these individual contributions gave an integrated value for the gegenschein brightness between 1.0 and 3.5 AU of about $2500 S_{10}(\text{vis})^*$ units. This value is approximately a factor of 10 above the earth based observational value of $200 \pm 100 S_{10}(\text{vis})$ units (Roosen, 1970), and the value of about $255 S_{10}(\text{vis})$ units measured by the IPP experiment on Pioneer 10 (Hanner and Weinberg, 1973). The AMD measurements in the average sky background mode gave a value of approximately $90 S_{10}(\text{vis})$ units (Zook and Soberman, 1973).

Figure 36 shows the relative variation of the gegenschein with heliocentric distance obtained by successively subtracting out the contributions due to each solar distance segment. As can be seen from the figure, the gegenschein decreases approximately as the inverse square of the solar distance out to about 2.25 AU where it begins to fall off more rapidly. This observed variation is in excellent agreement with results obtained from the IPP experiment

*One $S_{10}(\text{vis})$ unit is defined as a brightness equal to that of a stellar distribution of one tenth magnitude (visible) star per square degree.

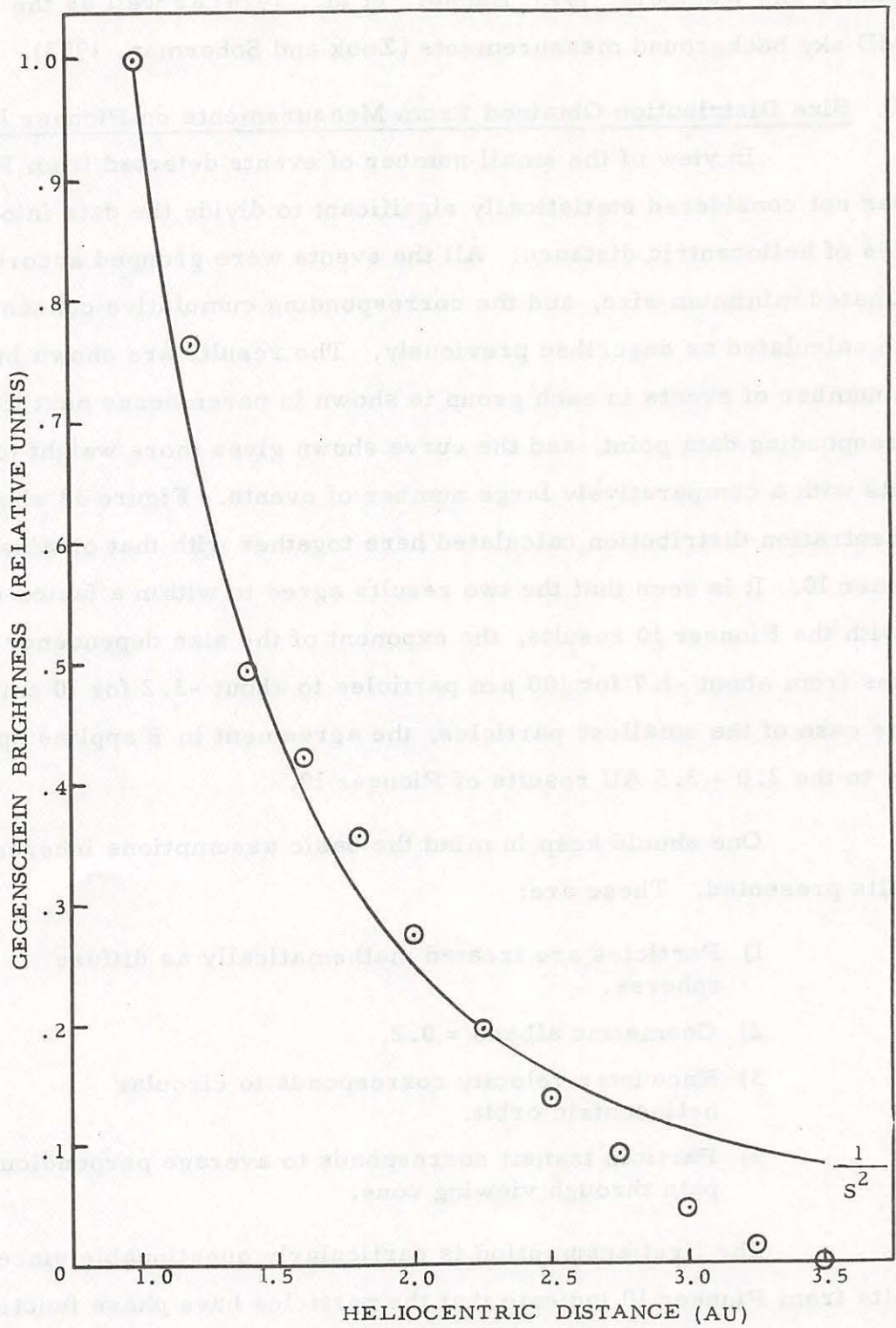


Figure 36. Variation of GEGENSCHHEIN BRIGHTNESS with HELIOCENTRIC DISTANCE From Pioneer 10.

(Hanner and Weinberg, 1973; Hanner, et al., 1974) as well as the AMD sky background measurements (Zook and Soberman, 1973).

V.D. Size Distribution Obtained From Measurements on Pioneer 11

In view of the small number of events detected from Pioneer 11, it was not considered statistically significant to divide the data into regimes of heliocentric distance. All the events were grouped according to estimated minimum size, and the corresponding cumulative concentrations were calculated as described previously. The results are shown in Figure 37. The number of events in each group is shown in parentheses next to the corresponding data point, and the curve shown gives more weight to the points with a comparatively large number of events. Figure 38 shows the concentration distribution calculated here together with that obtained from Pioneer 10. It is seen that the two results agree to within a factor of two. As with the Pioneer 10 results, the exponent of the size dependency ($N \sim a^{-\beta}$) varies from about -1.7 for 100 μm particles to about -3.2 for 10 cm bodies. In the case of the smallest particles, the agreement in β applies specifically to the 2.0 - 3.5 AU results of Pioneer 10.

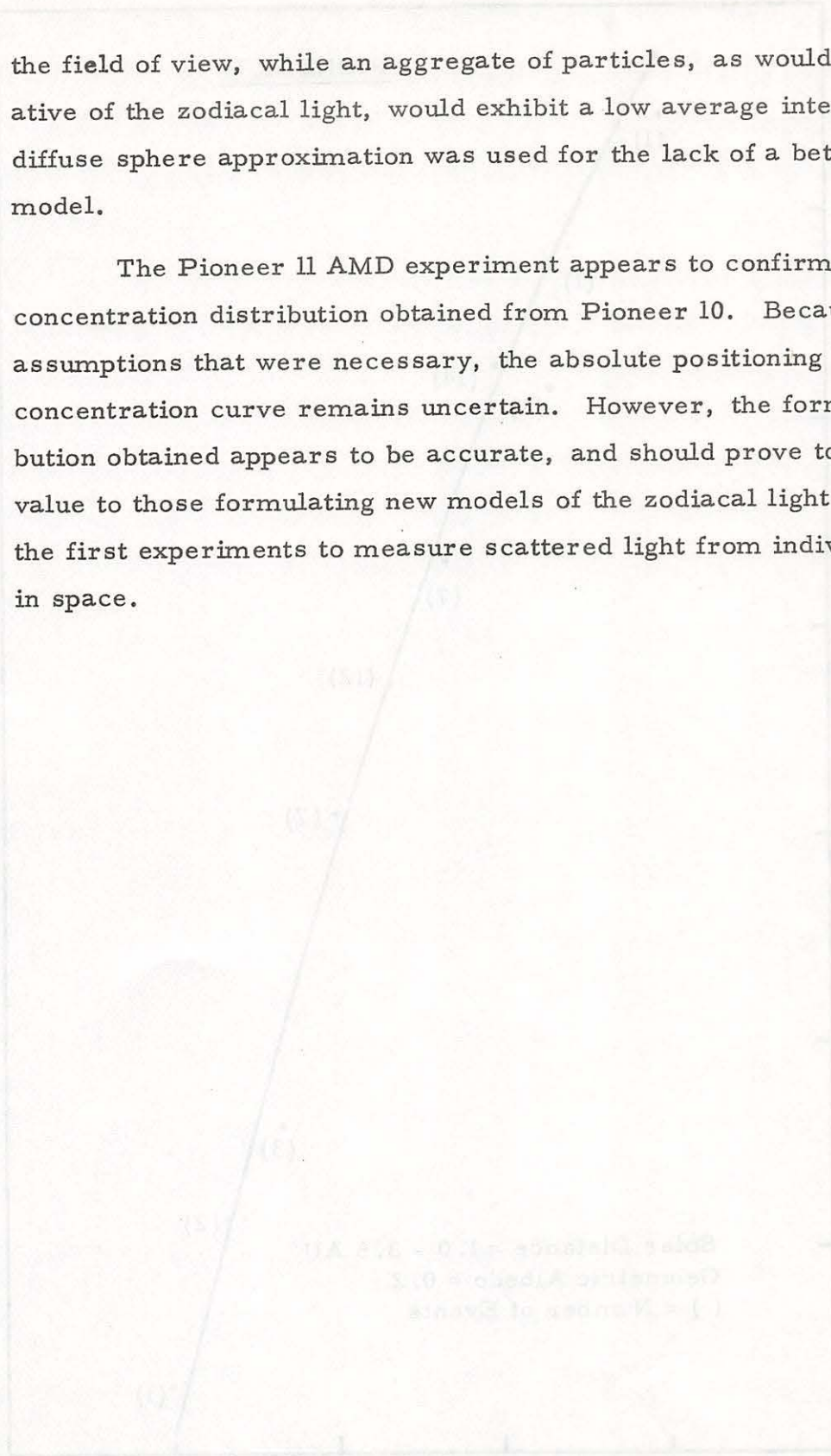
One should keep in mind the basic assumptions inherent in the results presented. These are:

- 1) Particles are treated mathematically as diffuse spheres.
- 2) Geometric albedo = 0.2.
- 3) Encounter velocity corresponds to circular heliocentric orbit.
- 4) Particle transit corresponds to average perpendicular path through viewing cone.

The first assumption is particularly questionable since the results from Pioneer 10 indicate that the particles have phase functions with many high (specular) peaks. Individual rotating particles with such phase functions would be characterized by high peak intensities as they transit

the field of view, while an aggregate of particles, as would be representative of the zodiacal light, would exhibit a low average intensity. The diffuse sphere approximation was used for the lack of a better mathematical model.

The Pioneer 11 AMD experiment appears to confirm the particle concentration distribution obtained from Pioneer 10. Because of the assumptions that were necessary, the absolute positioning of the derived concentration curve remains uncertain. However, the form of the distribution obtained appears to be accurate, and should prove to be of particular value to those formulating new models of the zodiacal light since these were the first experiments to measure scattered light from individual particles in space.



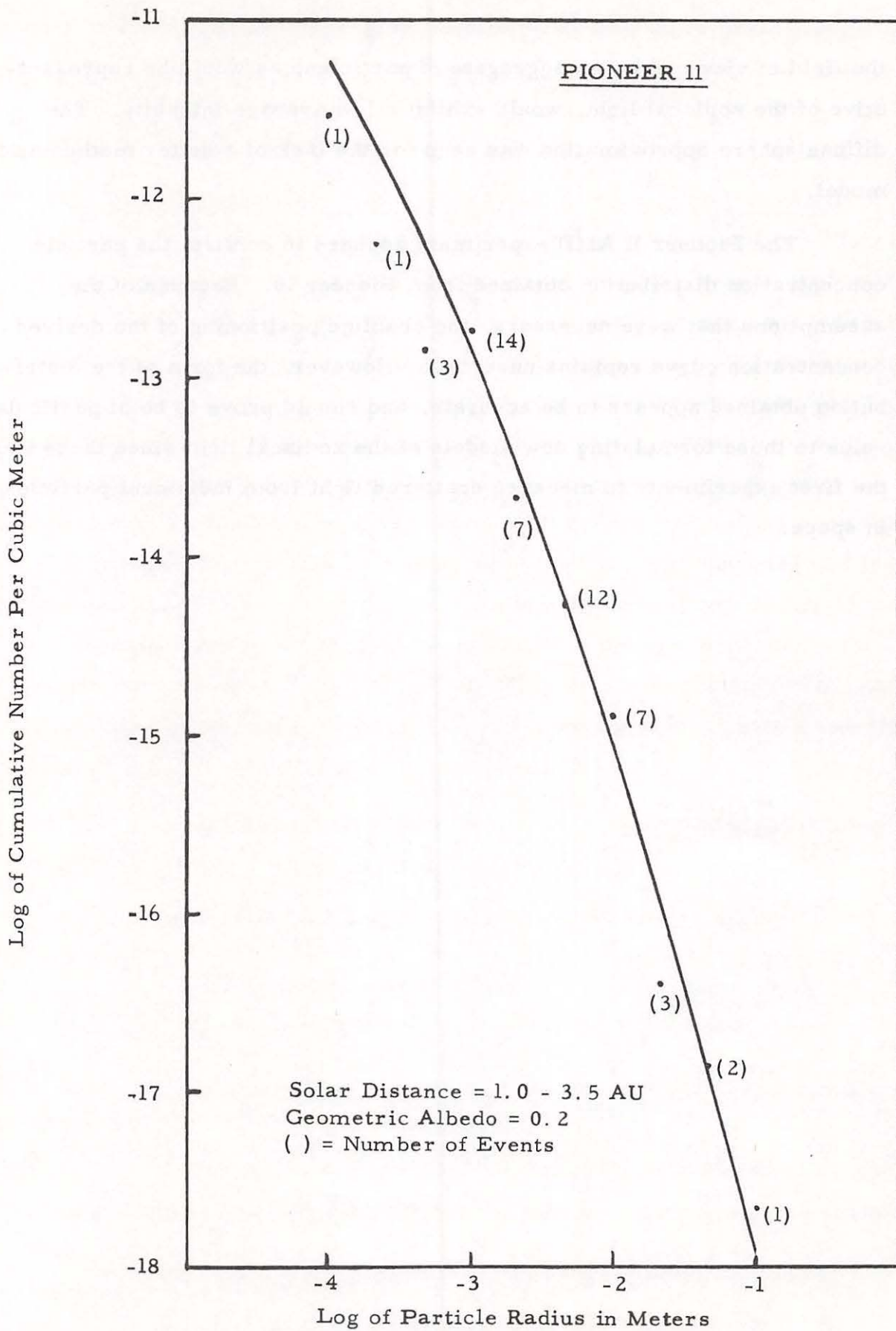


Figure 37. Particle Size Distribution From Pioneer 11
(1.0 - 3.5 AU)

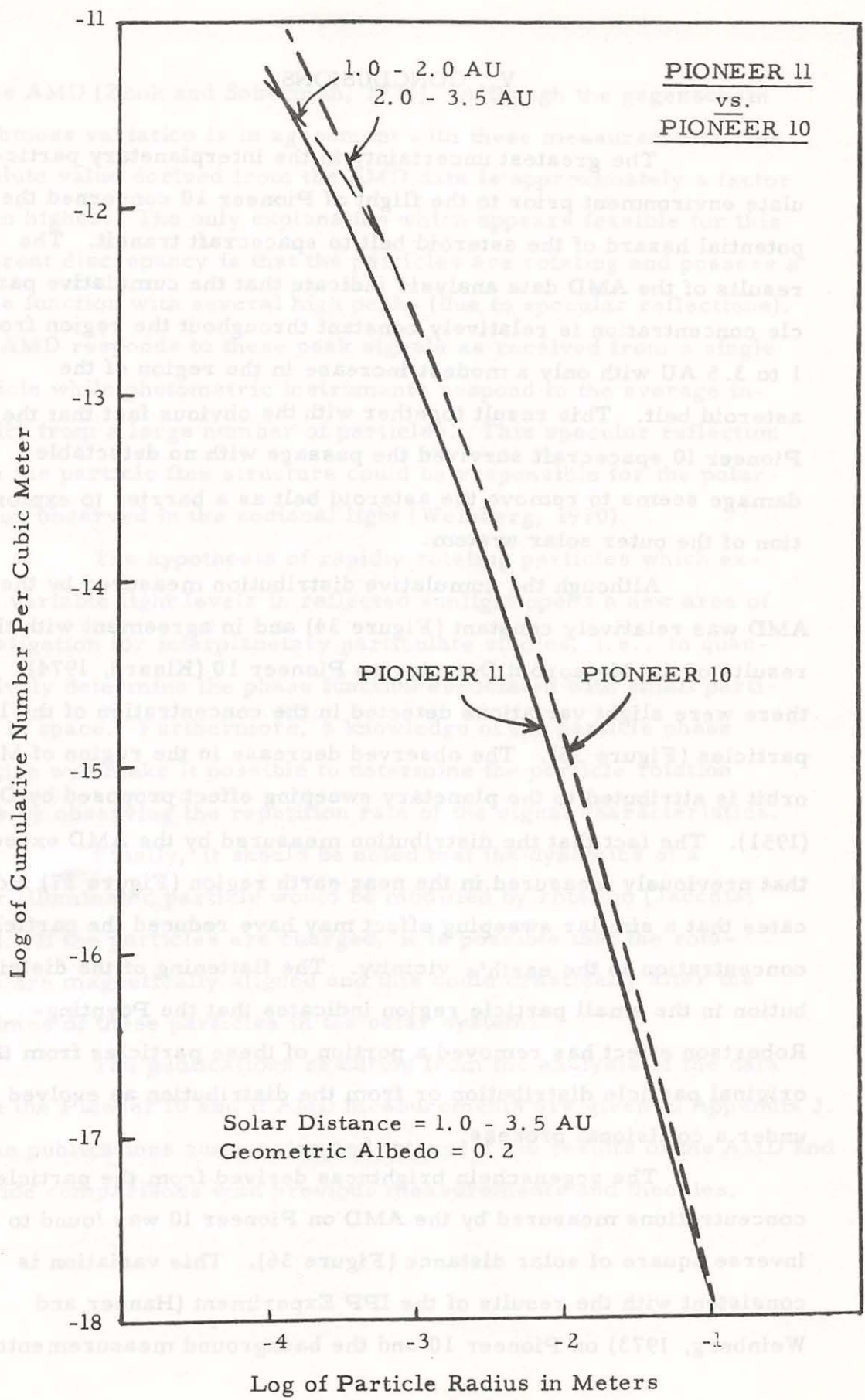


Figure 38. Particle Size Distributions From Pioneer 10 and 11

V. CONCLUSIONS

The greatest uncertainty in the interplanetary particulate environment prior to the flight of Pioneer 10 concerned the potential hazard of the asteroid belt to spacecraft transit. The results of the AMD data analysis indicate that the cumulative particle concentration is relatively constant throughout the region from 1 to 3.5 AU with only a modest increase in the region of the asteroid belt. This result together with the obvious fact that the Pioneer 10 spacecraft survived the passage with no detectable damage seems to remove the asteroid belt as a barrier to exploration of the outer solar system.

Although the cumulative distribution measured by the AMD was relatively constant (Figure 34) and in agreement with the results of the Meteoroid Detector on Pioneer 10 (Kinard, 1974), there were slight variations detected in the concentration of the larger particles (Figure 35). The observed decrease in the region of Mars's orbit is attributed to the planetary sweeping effect proposed by Öpik (1951). The fact that the distribution measured by the AMD exceeds that previously measured in the near earth region (Figure 37) indicates that a similar sweeping effect may have reduced the particle concentration in the earth's vicinity. The flattening of the distribution in the small particle region indicates that the Poynting-Robertson effect has removed a portion of these particles from the original particle distribution or from the distribution as evolved under a collisional process.

The gegenschein brightness derived from the particle concentrations measured by the AMD on Pioneer 10 was found to vary as the inverse square of solar distance (Figure 36). This variation is consistent with the results of the IPP Experiment (Hanner and Weinberg, 1973) on Pioneer 10 and the background measurements

of the AMD (Zook and Soberman, 1974). Although the gegenschein brightness variation is in agreement with these measurements, the absolute value derived from the AMD data is approximately a factor of ten higher. The only explanation which appears feasible for this apparent discrepancy is that the particles are rotating and possess a phase function with several high peaks (due to specular reflections). The AMD responds to these peak signals as received from a single particle while photometric instruments respond to the average intensity from a large number of particles. This specular reflection from the particle fine structure could be responsible for the polarization observed in the zodiacal light (Weinberg, 1970).

The hypothesis of rapidly rotating particles which exhibit variable light levels in reflected sunlight opens a new area of investigation for interplanetary particulate studies, i. e., to quantitatively determine the phase function associated with small particles in space. Furthermore, a knowledge of the particle phase function will make it possible to determine the particle rotation rates by observing the repetition rate of the signal characteristics.

Finally, it should be noted that the dynamics of a solar illuminated particle would be modified by rotation (Jacchia, 1963). If the particles are charged, it is possible that the rotations are magnetically aligned and this could drastically alter the lifetimes of these particles in the solar system.

The publications resulting from the analysis of the data from the Pioneer 10 and 11 AMD measurements are given in Appendix J. These publications summarize and interpret the results of the AMD and provide comparisons with previous measurements and theories.

LIST OF REFERENCES

- Allen, C. W., *Astrophysical Quantities*, 2nd ed. U. of London, The Athlone Press, 1963.
- Anders, E., Fragmentation History of Asteroids. *Icarus*, 4, 398-408, 1965.
- Berg, O. E., and U. Gerloff, More than two years of micro-meteoroid data from two Pioneer satellites. *Space Research*, 11, 225-235, 1971.
- Blackwell, D. E. and M. F. Ingham, Observations of the zodiacal light from a very high altitude station. III. The disturbed zodiacal light and corpuscular radiation. *Monthly Notices Roy. Astronom. Soc.* 122, 143-176, 1961.
- Bohn, J. L., W. M. Alexander, and W. F. Simmons, Results of studies of thermal gradient effects on ceramic transducer sensors used in cosmic dust experiments. *Space Research*, 8, 588-595, 1968.
- Cook, A. F., M. R. Flannery, H. Levy II, R. E. McCrosky, Z. Sekanina, C. Y. Shad, R. B. Southworth, and J. T. Williams, Meteor Research Program, NASA Contractor Report No. NASA-CR-2109, 1972.
- Cour-Palais, B. G., Meteoroid Environment Model - 1969 (Near Earth to Lunar Surface), NASA SP-8013, 1969.
- Dohnanyi, J. S., Collisional model of asteroids and their debris. *J. Geophys. Res.*, 74, 2531-2554, 1969.
- Dohnanyi, J. S., Fragmentation and distribution of asteroids. *Physical Studies of Minor Planets*, edited by T. Gehrels, NASA SP-267, 1971.

- Dohnanyi, J. S., Interplanetary objects in review; statistics of their masses and dynamics. Icarus, 17, 1-48, 1972.
- Elsässer, H., The spatial distribution of the material in the zodiacal light (in German). Zeit. f. Astrophys., 33, 274-285, 1954.
- Farlow, N. H., Electron microscope studies of particles on sampling surfaces recovered from space with sounding rockets. J. Geophys. Res., 73, 4363-4371, 1968.
- Fish, R. H., and J. L. Sommer, Effect of material properties on threshold penetration. Seventh Hypervelocity Symposium, 6, 1965.
- Gault, D. E., E. M. Shoemaker, and H. J. Moore, Spray ejected from the lunar surface by meteoroid impact, NASA Technical Note D-1767, April 1963.
- Giese, R. H., and H. Siedentopf, Optical characteristics of models of interplanetary material (in German). Zeit. f. Astrophys., 54, 200-216, 1962.
- Hanner, M. S., and J. L. Weinberg, Gegenschein observations from Pioneer 10. Sky and Telescope, 45, 217-218, 1973.
- Hanner, M. S., J. L. Weinberg, L. M. DeShields II, B. A. Green, and G. N. Toller, Zodiacal light and the asteroid belt: the view from Pioneer 10. J. Geophys. Res., 79, 3671-3675, 1974.
- Hawkins, G. S., Asteroidal fragments. Astronom. J., 65, 318-322, 1960.
- Hawkins, G. S., Interplanetary debris near the earth. Annual Review of Astronomy and Astrophysics, edited by Leo Goldberg, 2, 149-164, 1964.
- Hellyer, B., The fragmentation of the asteroids. Monthly Notices Roy. Astronom. Soc., 74, 2531-2554, 1969.
- Hemenway, C. L., and D. S. Hallgren, Results from the Gemini S-10 and S-12 micrometeorite experiments. Space Research, 8, 521-535, 1968.

- Humes, D. H., J. M. Alvarez, R. L. O'Neal, and W. M. Kinard, "Cosmic dust encountered by Pioneers 10 and 11." Paper presented at the fall annual meeting of the American Geophysical Union, San Francisco, Calif., 1973.
- Jacchia, L. G., Meteors, meteorites, and comets: interrelations, in The Moon, Meteorites, and Comets, edited by B. M. Middlehurst and G. P. Kuiper, 774 - 798, 1963.
- Kessler, D. J., Upper limit on the spatial density of asteroidal debris. AIAA Journal, 6, 2450, 1968.
- Kessler, D. J., Spatial density of the known asteroids in the ecliptic plane. NASA TM X-58026, 1969.
- Kessler, D. J., Meteoroid Environment Model-1970 (Interplanetary and Planetary), NASA SP-8038, 1970.
- Kinard, W. H., and R. L. O'Neal, Description of Pioneer F and G asteroid belt penetration experiment, in Physical Studies of Minor Planets, NASA SP-267, edited by T. Gehrels, 607-615, 1971.
- Kinard, W. H., R. L. O'Neal, J. M. Alvarez, and D. H. Humes, Pioneer 10 meteoroid penetration data. Space Research, 14, in Press, 1974.
- Konstantinov, B. P., M. P. Bredov, and E. P. Mazets, Experimental data against the hypothesis of a dust cloud around the earth (in Russian). Rep. Acad. Sci., USSR, 174 (3), 1967.
- Kresak, L., The asymmetry of the asteroid belt. Bull. Astron. Inst. Czechoslov., 15, 27-36, 1967.
- Kuiper, G. P., Y. Fujita, T. Gehrels, I. Groeneveld, J. Kent, G. van Biesbroeck, and C. J. van Houten, Survey of asteroids. Astrophys. J. Suppl., Ser. 3, 289-428, 1958.
- Marcus, A. H., A stochastic model for the formation and survival of lunar craters. Icarus, 5, 165-200, 1966.

- Marcus, A. H., Number density of martian craters. Acta. Astronomica, 5, 115-138, 1953.
- McCracken, C. W., W. M. Alexander, and M. Dubin, Direct measurement of interplanetary dust particles in the vicinity of earth. Nature, 192, 441-442, 1961.
- McCrosky, R. L., and M. Boeschenstein, Jr., The Prairie Meteorite Network, SAO Special Report No. 173, 1965.
- Naumann, R. J., D. W. Jex, and C. L. Johnson, Calibration of Pegasus and Explorer 23 Detector Panels, NASA TR R-321, 1969.
- Nazarova, T. N., Results of investigation of the meteoric matter by means of instruments installed on cosmic rockets (in Russian). Artificial Earth Satellites, 5, 38-40, 1960.
- Neste, S. L., and R. K. Soberman, Results of the asteroid/meteoroid particle experiment on Pioneer 10 (1.0 - 3.2 AU), Space Research, 14, 755-759, 1974.
- Newkirk, G., and J. A. Eddy, Light scattering by particles in the upper atmosphere, J. Atmos. Sci., 21, 35-60, 1964.
- Nilsson, C. S., Some doubts about the earth's dust cloud. Science, 153, 1241-1246, 1966.
- Olivier, C. P., Catalog of hourly meteor rates, Smithsonian Contr. Astrophysics, 4, 1-14, 1960.
- Olivier, C. P., Second catalog of hourly meteor rates, Smithsonian Contr. Astrophysics, 8, 171-180, 1965.
- Öpik, E. J., Collision probabilities with the planets and the distribution of interplanetary matter. Proc. Roy. Irish Acad., 54, 165-199, 1951.
- Paddack, S. J., Rotational bursting of small celestial bodies: effects of radiation pressure. J. Geophys. Res., 74, 4379-4381, 1969.

- Piotrowski, S., Collisions of asteroids. Acta. Astronomica, 5, 115-138, 1953.
- Powell, R. S., Analysis of all available zodiacal-light observations. in The Zodiacal Light and the Interplanetary Medium. J. L. Weinberg, ed. NASA SP-150, 225-241, 1967.
- Robertson, H. P., Dynamical effects of radiation in the solar system, Monthly Notices Roy. Astronom. Soc., 97, 423-438, 1937.
- Roosen, R. G., The gegenschein and interplanetary dust outside the earth's orbit. Icarus, 13, 184-201, 1970.
- Sitte, J., Cosmic ray effects on cosmic dust and dust particles. Space Res., 11, 237-247, 1971.
- Soberman, R. K., Extraterrestrial dust concentrations in the upper atmosphere. in Meteor Orbits and Dust, edited by G. S. Hawkins, NASA SP-135, 1967.
- Soberman, R. K., The terrestrial influx of small meteoric particles. J. Geophys. Res., 9, 239-258, 1971.
- Soberman, R. K., S. L. Neste and K. Lichtenfeld, Particle concentrations in the asteroid belt from Pioneer 10, Science, 183, 320-321, 1974a.
- Soberman, R. K., S. L. Neste and K. Lichtenfeld, Optical measurement of interplanetary particulates from Pioneer 10, J. Geophys. Res., 79, 3685-3694, 1974b.
- Southworth, R. B., Space density of radio meteors. in Proc. Symp. Zodiacal Light and Interplanetary Medium, edited by J. Weinberg, NASA SP-150, 1967.
- Southworth, R. B., and Z. Sekanina, Physical and Dynamical Studies of Meteors, NASA Contractor Report No. NASA CR-2316, 1973.
- van de Hulst, H. C., Light scattering by small particles, New York: John Wiley and Sons, Inc., 1957.
- van de Hulst, H. C., Zodiacal light in the solar corona. Astrophysical Journal, 105, 471-488, 1947.

- van Houten, C. J., I. van Houten-Groeneveld, P. Herget, and T. Gehrels, The Palomar-Leiden survey of faint minor planets. Astro. Astrophys. Suppl. 2, 339-448, 1970.
- Watson, F. G., *Between the planets*. Harvard Univ. Press, Cambridge, Mass., 1956.
- Weinberg, J. L., The zodiacal light at 5300 A. Annales d'Astrophysique, 27, 718-738, 1964.
- Weinberg, J. L., Zodiacal light as an indication of the nature of the interplanetary matter: past, present and prospective results. in Meteor Orbits and Dust, edited by G. S. Hawkins, NASA SP-135, 1967.
- Weinberg, J. L., Current problems in the zodiacal light, Space Res., 10, 233-243, 1970.
- Whipple, F. L., Photographic meteor studies I, Proc. Amer. Phil. Soc., 79, 499-548, 1938.
- Zook, H. A., R. E. Flaherty, and D. J. Kessler, Meteoroid impacts on Gemini windows. Planet Space Sci., 18, 953-964, 1970.
- Zook, H. A., and R. K. Soberman, The radial dependence of the zodiacal light. Space Res., 14, 763-767, 1974.

APPENDIX A

LIGHT REFLECTION FROM PARTICLES

The amount of incident radiation which is reflected from a particle is dependent on the particle's effective area, the angle between the incident and reflected radiation, γ (for backscatter $\gamma = \pi$), and the reflecting characteristics of the particle, usually expressed in terms of the albedo. Two types of albedo, the bond albedo and the geometric albedo, are commonly used to relate the incident and reflected radiation. These parameters are defined as follows:

$$\text{Bond Albedo} = A = pq$$

$$= \frac{I}{I_0}$$

where I = total light reflected from sphere

and I_0 = total light incident on sphere

$$\text{Geometric Albedo} = p = \frac{I(\pi)}{I_L(\pi)}$$

where $I(\pi)$ = sphere brightness (backscatter)

and $I_L(\pi)$ = perfectly diffusing Lambertian disc
brightness (backscatter)

$$\text{Note that } q = \frac{A}{p}.$$

The AMD was not sensitive to particles less than 50 microns in diameter, and therefore, all particles detected were approximated as "large objects" since their diameter was at least 1 order of magnitude greater than the light wavelengths of interest. Stated in another fashion, the Mie size parameter $\frac{2\pi a}{\lambda}$ was greater than 100 and large body optical theory could be applied.

Although the exact shape of the observed particles is not known and even though it is highly unlikely that they are spherical, the following theorem justifies treating them as spheres:

"the scattering pattern caused by reflection on large convex particles with random orientation is identical with the scattering pattern by reflection on large spheres of the same material and having the same surface condition."

The proof of this theorem depends in part upon another which states:

"the average geometric cross section of a convex particle with random orientation is 1/4 its surface area."

Rigorous proofs for both of the above theorems are contained in van de Hulst (1957).

Thus, the amount of radiation reflected from a sphere in a given direction γ can be expressed as:

$$H \text{ (watts/ster)} = \frac{I_0 \pi a^2 f(\gamma) r}{S^2 F} \quad (\text{A-1})$$

where I_0 is the solar radiation in watts/cm² at 1 AU, πa^2 is the geometric cross section of a sphere, $f(\gamma)$ is the phase law, r is a reflectivity coefficient, S is the particle's distance from the sun and F is a factor to be determined. The phase law for diffuse scattering of light from a sphere, following Lambert's law is given by van de Hulst (1957) as:

$$f(\gamma) = \frac{8}{3\pi} (\sin \gamma - \gamma \cos \gamma). \quad (\text{A-2})$$

The factor F can be evaluated by setting $r = 1$ (i. e., all incident radiation is reflected) and integrating Equation (A-1) over $d\Omega$. Thus, we have:

$$\frac{I_0 \pi a^2}{S^2} = \frac{1}{F} \frac{I_0 \pi a^2}{S^2} \int_{\Omega} f(\gamma) d\Omega \quad (\text{A-3})$$

$$\text{or } F = \int_{\Omega} f(\gamma) d\Omega$$

$$\begin{aligned}
F &= \int_{\phi=0}^{2\pi} \int_{\gamma=0}^{\pi} \frac{8}{3\pi} (\sin \gamma - \gamma \cos \gamma) \sin \gamma \, d\gamma \, d\phi \\
&= 16/3 \int_0^{\pi} (\sin^2 \gamma - \gamma \cos \gamma \sin \gamma) \, d\gamma \quad (\text{A-4}) \\
&= 16/3 (\pi/2 - 1/8 (-2\pi)) \\
&= 4\pi
\end{aligned}$$

Equation (A-1) then becomes:

$$H \text{ (watts/ster)} = \frac{I_0 \pi a^2 f(\gamma) r}{4\pi S^2} \quad (\text{A-5})$$

Therefore, at a distance R from the sphere the result becomes:

$$\frac{H}{R^2} = I = \frac{I_0 r f(\gamma)}{4S^2} \left(\frac{a}{R}\right)^2 \quad (\text{A-6})$$

as given in Chapter III, where I is in watts/cm².

Finally, from the definition of the bond albedo we can write:

$$\begin{aligned}
A &= \frac{S^2 \int_{\Omega} H \, d\Omega}{I_0 \pi a^2} \\
&= \frac{r \int_{\Omega} f(\lambda) \, d\Omega}{4\pi} \\
&= r \quad (\text{A-7})
\end{aligned}$$

Thus, the parameter r in Equation (A-1) is the bond albedo.

The relationship between the bond albedo and the geometric albedo can be easily calculated for Lambertian radiators.

The phase law for a Lambertian disc is expressed as:

$$f_L(\gamma) = -\cos \gamma. \quad (\text{A-8})$$

The equation analogous to (A-1) is therefore:

$$H_L \text{ (watts/ster)} = \frac{I_o \pi a^2 (-\cos \gamma)}{S^2 F_L} \quad (\text{A-9})$$

where r has been set equal to one. Equating the incident and reflected radiation yields:

$$\begin{aligned} \frac{I_o \pi a^2}{S^2} &= \int_{\Omega} H_L d\Omega \\ &= \frac{-I_o \pi a^2}{S^2 F_L} \int_{\phi=0}^{2\pi} \int_{\pi/2}^{\pi} \cos \gamma \sin \gamma d\gamma d\phi. \end{aligned} \quad (\text{A-10})$$

Completing the integration yields:

$$F_L = \pi. \quad (\text{A-11})$$

Thus, the radiation (watts/cm²) received at a distance R from a Lambertian disc is given by:

$$\frac{H_L}{R^2} = I_L = I_o \frac{f_L(\gamma)}{S^2} \left(\frac{a}{R}\right)^2 \quad (\text{A-12})$$

For backscatter I and I_L are related by the definition:

$$\begin{aligned} p &= \frac{I(\pi)}{I_L(\pi)} = \frac{f(\pi) r}{4 f_L(\pi)} \\ &= 2/3 r \\ &= 2/3 A \end{aligned}$$

Thus, the ratio of the bond albedo to the geometric albedo (A/p) is 1.5. The ratio $A/p = q$ is usually referred to as the phase integral.

APPENDIX B

AMD CALIBRATION AND SENSITIVITY MEASUREMENTS

Sensitivity Measurements in the Laboratory

The laboratory calibrations consisted of two parts: (1) measurement of the instrument response to a nearly monochromatic (λ max = 5680 A, 250 A bandpass) light source of known spectral characteristics, and (2) measurement of the instrument response to a light source of known intensity at various wavelengths. The first of these determined the absolute monochromatic sensitivity of the instrument, while the second determined the instrument bandpass.

Measurement of Absolute Response

Since the instrument electronics employ logarithmic amplifiers it was necessary to perform measurements over a wide range of irradiance levels in order to insure that the proper response was obtained and no extrapolation was needed. The physical constraints of the laboratory and the availability of calibrated light sources required that neutral density filters as well as various current inputs to the lamp be used to obtain the proper range of illumination. Specifically, the illumination intensity ranged over three orders of magnitude from a barely detectable signal to values near the instrument saturation level. All readings were obtained using a calibrated digital voltmeter to insure accuracy.

A source-detector distance of 76.8 meters was used for these measurements. The actual calibration measurements were relatively straight-forward. The procedure was to record

the instrument output (in volts) for each of the neutral density filter and lamp current combinations used. At each reading the background illumination was also recorded to insure that only the known illumination from the lamp was used in determining the system response.

In order to correlate these measured instrument outputs with the light input it was necessary to calculate the irradiance at the optics using the known spectral characteristics of the light source, the transmission characteristics of the neutral density filters and the separation distance of the source and detector. The condensed, graphical results are presented in Figure B1 for the Pioneer 10 flight unit. As can be seen from the figure, channels A, B and C were considered to be equally sensitive while channel B was approximately a factor of two less sensitive.

Measurement of Wavelength Response

A similar procedure was used to determine the instrument response as a function of the wavelength of the light source. In addition to the neutral density filters, spectral filters were used to determine instrument sensitivity as a function of wavelength (i. e., the instrument bandpass). As with previous measurements, the irradiance at the optics was calculated for each of the spectral filters. Figure B2 is the resulting relative wavelength response curve, applicable for all four channels. The double-peaked shape results from modification of the basic S-20 photomultiplier response by the spectral reflectance of the gold-surfaced telescope mirrors.

These curves in Figures B1 and B2 constitute the absolute wavelength response of the Pioneer 10 AMD sensors. To use the curves for predicting the response from a given spectrum, the procedure is as follows:

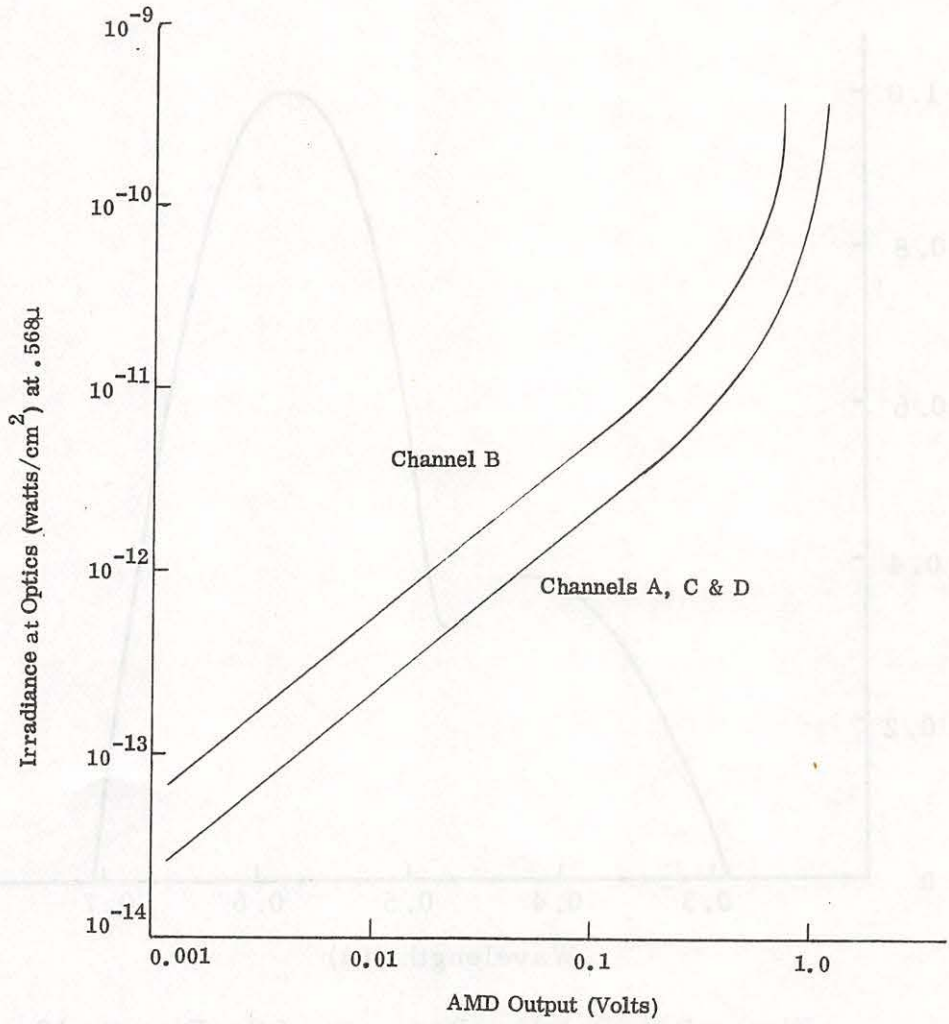


Figure B1. Absolute Response of the Pioneer 10 Asteroid/Meteoroid Detector.

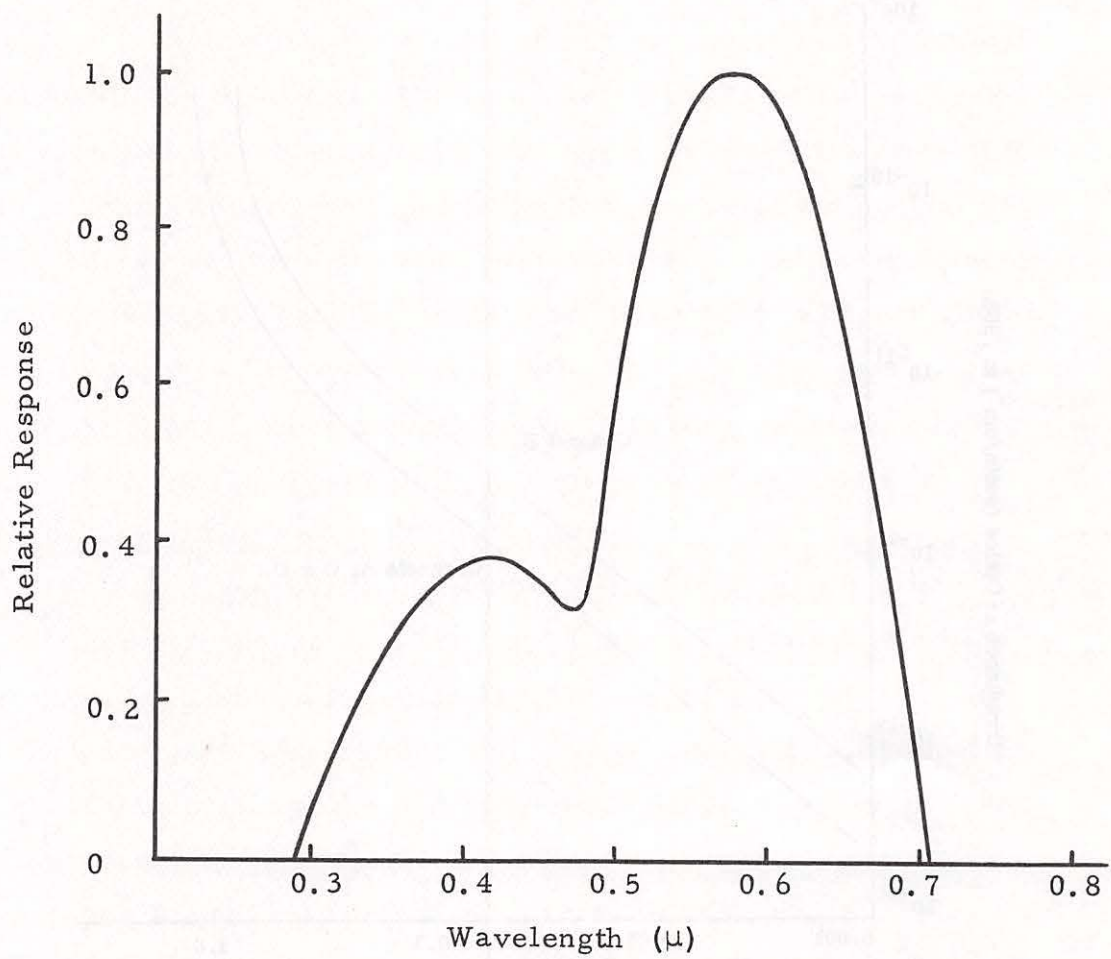


Figure B2. Relative Response of the Pioneer 10 Asteroid/Meteoroid Detector

1. Select an increment, $\Delta \lambda$, of the spectrum at λ with ΔH_{λ} irradiance.
2. From the relative response curve (Figure B2) determine the response, R_{λ} , at λ relative to that at 568 milli-micrometers.
3. Multiply ΔH_{λ} by R_{λ} to obtain ΔH_{568} , the equivalent 568 m μ irradiance.
4. Repeat steps 1 through 3 for each increment of λ across the sensor acceptance waveband.
5. Sum ΔH_{568} values to obtain the total H_{568} equivalent irradiance.
6. From the 568 m μ response curve (Figure B1) determine the expected signal level.

In calculating the background and signal irradiance levels, a solar spectrum was assumed both for the radiation reflected from the particles and the star background irradiance. The choice of this spectrum was obvious for the particles' irradiance since they merely reflected the incident sunlight and it was felt to be a good average value for the star background.

It should be pointed out that the above calibrations were performed at room temperature and since the response of the preamplifiers is temperature dependent (for instrument outputs greater than 0.1 volts), the above measurements were scaled to obtain the instrument response at cold temperatures (-140°C). This was done by relating the incident irradiance to the preamplifier current, at low signal levels. Since the temperature relationship between preamp input current and output voltage was known (from laboratory calibrations) it was then possible to obtain the input irradiance corresponding to the AMD output voltage.

In-Flight Sensitivity Measurements

Opportunities for verifying the laboratory calibrations presented themselves when a bright star or the planet Jupiter was observed by the AMD. The procedure was to calculate irradiance due to the calibration source (star or planet) by using two independent methods and comparing the two values.

The expected signal from the calibration star can be calculated by using the methods described above. Specifically, the spectrum of the source is convolved with the relative response of the instrument to obtain the expected equivalent irradiance at 568 m μ . The source irradiance can also be determined from measurements performed in-flight. Background readings obtained just before and/or after the source appeared in the viewfields can be used to infer the background of the source contained field. Subtracting this value from the background measurement with the source in the field-of-view will yield a value for the irradiance of the source. This latter value will depend solely on the laboratory sensitivity measurements. The results of this procedure are illustrated below for two cases: the star Rigil Kentaurus and Jupiter.

It was assumed that Rigil Kentaurus could be treated as a Planckian emitter with a blackbody temperature of 4700^oK. A visual magnitude of -.27 (Allen, 1963) was used to determine the irradiance as a function of wavelength. Using the relative response curve of Figure B2 it was calculated that the equivalent 568 m μ irradiance in the AMD bandpass should be 1.07×10^{-12} watts/cm².

The in-flight data used to obtain the measured irradiance due to Rigil Kentaurus was taken on a day when the star passed through the approximate centers of the viewfields and

when the background variation was minimal. The irradiance values obtained from readings of the four Pioneer 10 AMD channels are:

Channel A - 1.0×10^{-12} watts/cm² @ 568 mμ

Channel B - 1.5×10^{-12} "

Channel C - 1.2×10^{-12} "

Channel D - 8.7×10^{-13} "

The average for the four channels is 1.1×10^{-12} watts/cm² which is nearly the same as the value obtained previously.

The irradiance expected from Jupiter can be calculated using the formula developed in Appendix A, namely;

$$I = \frac{I_o a^2 f(\gamma) r}{S^2 4 R^2} \quad (B-1)$$

The calculations will be performed for 28 June 1972 when the Pioneer 10 spacecraft was approximately 3.5 AU from Jupiter. The quantities to be used in the above equation are:

I_o - solar irradiance = 0.064 watts/cm²

(in AMD bandpass at 1 AU)

a - radius of Jupiter = 7×10^4 km

$f(\gamma)$ - phase law = $f(135^\circ) = 2.0$

S - Jupiter - sun distance = 5 AU

R - Jupiter - spacecraft distance = 5.26×10^8 km

r - bond albedo of Jupiter = .7

The expected irradiance from Jupiter at the instrument can easily be calculated as:

$$I = 1.6 \times 10^{-11} \text{ w/cm}^2.$$

Using the in-flight data for that day we obtain the following irradiance values (converted to a solar type spectrum in the AMD bandpass) for Jupiter:

Channel A - 1.7×10^{-11} watts/cm²
 Channel B - 2.3×10^{-11} "
 Channel C - 2.7×10^{-11} "
 Channel D - 0.9×10^{-11} "

The average for the four channels is about 1.9×10^{-11} watts/cm² or approximately the same as the expected value.

In-flight observations of Jupiter from Pioneer 11 were compared with those just described to determine the calibration correction factors appropriate to the specific AMD detectors flown on Pioneer 11. Data from two days was used: 28 June 1973 and 10 August 1973. The signals minus the backgrounds were compared with those obtained on Pioneer 10 and, after correcting for slight differences in the Sun-Jupiter distance, the ratios (PN 11:PN 10) for the three functioning channels were found to be:

	28 June 1973	10 August 1973	Average
Channel A	4.15	3.14	3.65
Channel C	3.14	2.67	2.91
Channel D	.64	.72	.68

These numbers represent the differences in absolute sensitivity between the detectors on Pioneer 10 and those on Pioneer 11. For example, in the case of Channel A, the same irradiance would result in about 3.7 times the signal on Pioneer 11 as on Pioneer 10. The average factors given in the third column were incorporated into the computer program used to analyze the Pioneer 11 data. It should be noted that the relatively large differences in absolute detector sensitivity between Pioneers 10 and 11 have only a small effect on the overall ability of the system to detect events. This is because the sensitivity differences result in nearly compensating changes in the threshold values.

AMD Threshold Level on Pioneer 10

As stated in Section III, the threshold level is a function of the background signal due to the varying star field and the noise associated with that background. Specifically, the threshold is set according to the following formulae:

Threshold (normal) = $1.1 \times \text{dc background} + 1.5 \times \text{average peak}$
and

Threshold (high) = $1.2 \times \text{dc background} + 1.5 \times \text{average peak}$

This threshold behavior was verified during pre-flight tests conducted at both ambient and low (-120°C) temperatures by varying the input signal until the system "triggered" and then comparing the peak of this signal with the theoretical threshold.

In order to illustrate this varying background and threshold, the Pioneer 10 AMD data obtained on a typical day in the narrow bandwidth, normal threshold, mode of operation were presented in Figures 26 and 27 for each of the four channels. It was quite apparent from these figures that the absolute outputs of the four telescopes were quite different. These differences are due to a combination of internal (photocathode sensitivity, gain, etc.) and external (different light input to the telescopes) parameters.

As a result of these inter-channel differences the signal required to exceed threshold in each channel also varied. A reasonably accurate value for this minimum detectable signal in each channel can be obtained by subtracting the average peak signal from the threshold corresponding to that average peak. The results of this simple subtraction are presented in Figure B3 for one channel. Since a three-fold coincidence is required (i. e., three channels simultaneously above threshold for $3.2 \mu\text{s}$) the system sensitivity will nominally be determined by the third most sensitive channel. Thus, from Figure B3 we can obtain a mean instrument sensitivity of 7.2×10^{-13} watts/cm² of wavelength $568 \text{ m}\mu$ for this day of mission. The influences of Jupiter and the direct solar illumination of the light shield are not included in this average sensitivity. It should be pointed out, however, that the galactic equator was viewed twice by the

instrument during each spacecraft rotation on that day so that this is not representative of average sky background conditions.

The above sensitivity can be converted to a solar spectral sensitivity. The mean triggering level on that day would have been at a solar bolometric irradiance of 2.7×10^{-12} watts/cm². A particle which scattered 2.7×10^{-12} watts/cm² of sunlight without color modification into the AMD optics is the minimum size which would have been detected under the given mode of operation and the average background condition. The medium bandwidth mode would result in mean sensitivity of 1.3×10^{-12} watts/cm² of 568 mμ light and 4.8×10^{-12} watts/cm² of sunlight. In the wide bandwidth mode the mean sensitivity was 6.7×10^{-12} watts/cm² of sunlight.

Post Launch Laboratory Measurements

During the flight of the Pioneer 10 spacecraft several measurements were performed in the laboratory to duplicate or verify the behavior of the AMD on Pioneer 10. These measurements were conducted using a prototype instrument and a flying laser spot to simulate the particle trajectory (Figure B4).

The apparent simultaneous entry of a particle into two or more channels was reproduced using the particle simulator. The problem was first thought to be one of optical cross talk. However, since careful baffling of the optical sensors did not eliminate the problem it was isolated as being electronic in nature.

The possibility of recording an event seen only by two sensors (i. e., without the required coincidence) was also explored. This was done by successively shielding two telescopes as the simulated particle passed through the field of view. This test confirmed that the coincidence circuitry was functioning properly since no events were recorded in this mode of operation.

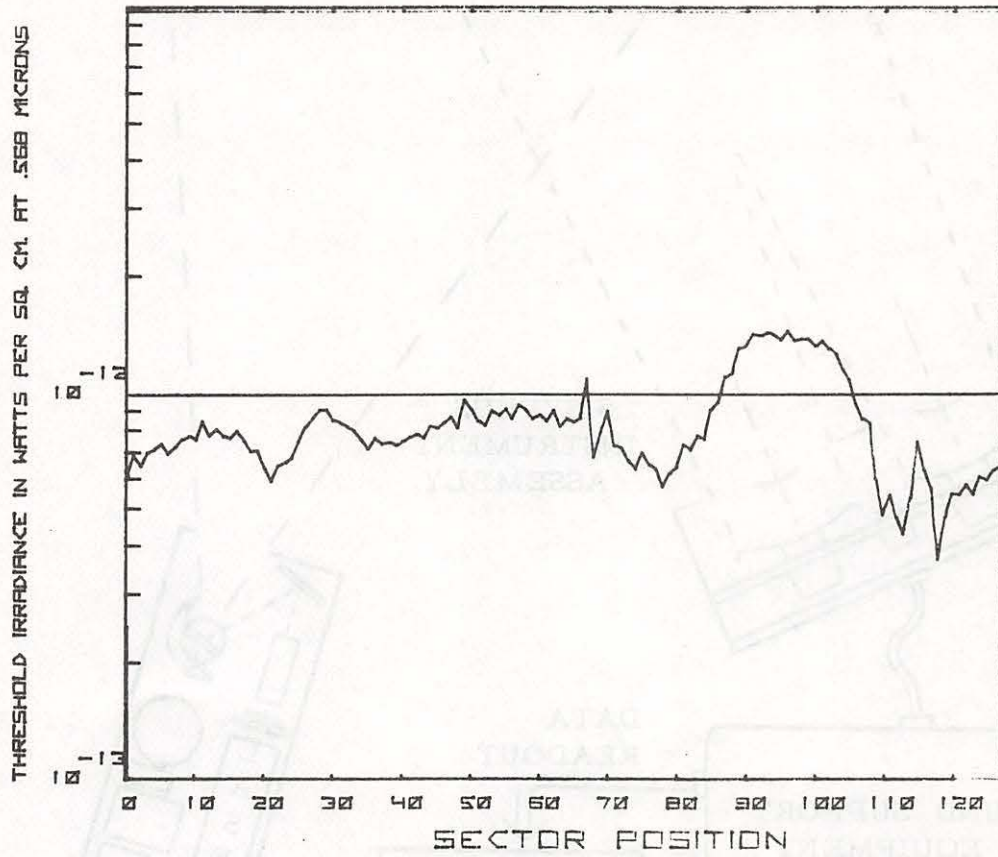


Figure B3. Minimum Detectable Signal

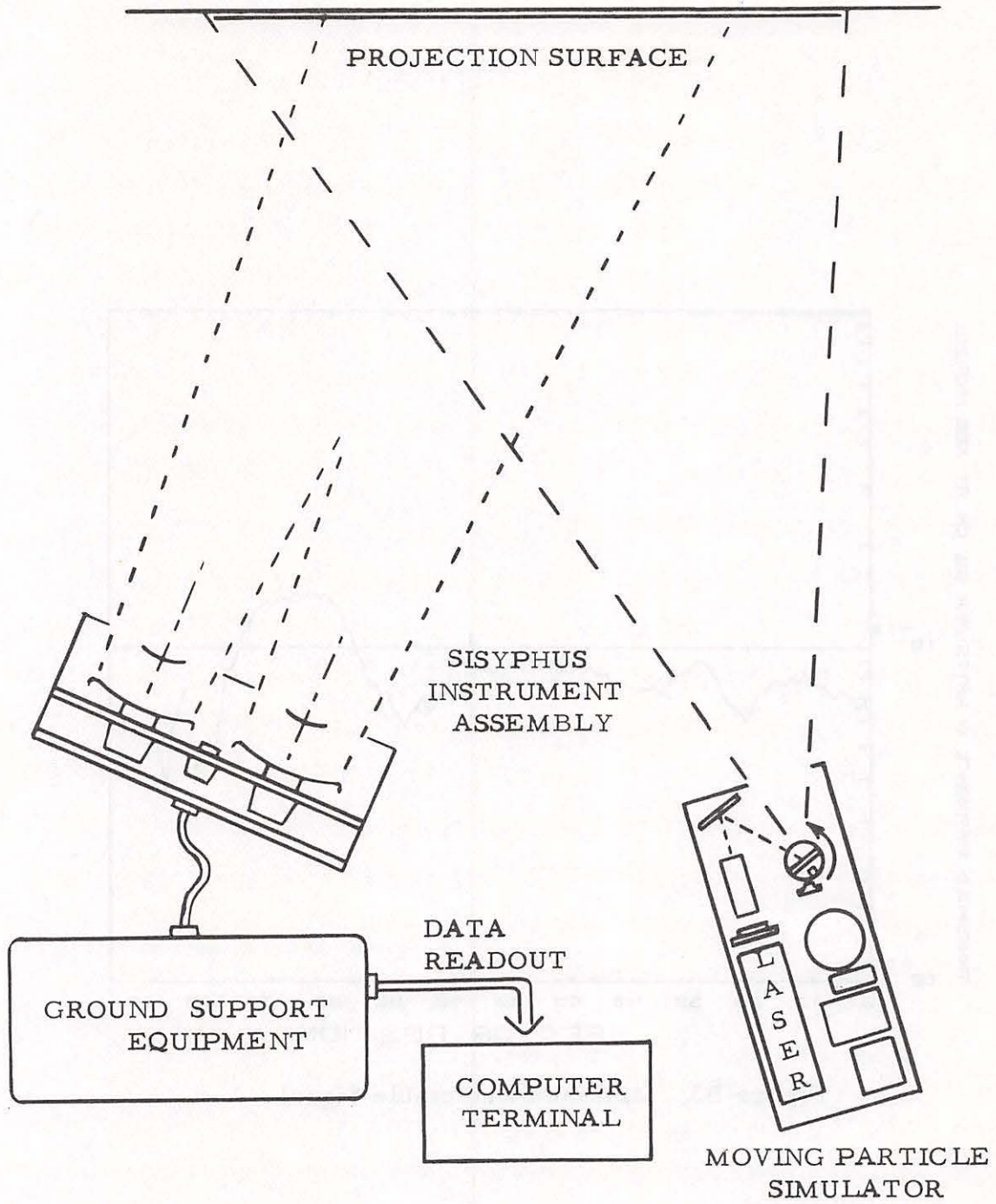


Figure B4. Equipment Used for Simulating and Detecting Particles in the Laboratory

The large difference in signal levels between channels which recorded the same event was also investigated. The signal levels for a star or planet which moved through the fields-of-view slowly (i. e., a transit time of ~ 250 ms) were within a factor of three or better, as shown above, while signal levels for a particle detection differed by as much a factor of 10. It therefore was thought that the signal level might be a function of the transit time. However, the peak signal recorded when the laser spot moved through the field-of-view in $100 \mu\text{s}$ (typical of a real event) was the same as the level recorded when the spot was held stationary in the viewfield. Thus, the signal level was shown to be independent of observation time.

Finally, a varying particle brightness was simulated by changing the intensity of the laser spot as it passed through the fields-of-view. This was done by placing obstructions in the beam path which decreased its intensity at various points in the trajectory. The recorded times of entry and exit were then compared to the times recorded when the signal was constant. Both the entry and exit times were altered by this varying signal and resembled some of the actual flight data. However, the maximum transit time recorded was a good representation of the correct transit time.

The results of this last experiment indicate that varying signal levels do present a problem. However, the ability to reproduce the characteristics of the measured flight data by this simple procedure further supports the contention that the interplanetary particles observed by the AMD do present a varying intensity as they pass through the fields-of-view.

APPENDIX C

DATA MEASURED BY THE AMD

The actual data used in determining the particle size and spatial distribution are presented in the two tables which follow. Tables C1 and C3 give the event identification data (event number and day of year) followed by the sector and bandwidth indication and the four sets of entry and exit times for the AMD on Pioneers 10 and 11 respectively. One revolution of the spacecraft was divided into 128 sectors of 2.8° each to indicate the area of the sky in which the instrument was observing. The 0 sector was in the northern celestial hemisphere with sectors 32 and 96 in the ecliptic.

The conversion of the measurements from bits (listed in the tables) to times is as follows:

Narrow Bandwidth (3):	1.6 μ sec/bit
Medium Bandwidth (4):	1.6 μ sec/bit
Wide Bandwidth (5):	0.4 μ sec/bit

Tables C2 and C4 again give the event identification data followed by the sector number and the background and peak signal levels for each channel for the AMD on Pioneers 10 and 11 respectively. The conversion from bits to volts for the backgrounds and signals is:

$$1 \text{ bit} = 0.00975 \text{ volts.}$$

TABLE C1. ENTRY AND EXIT TIMES FOR EVENTS
MEASURED BY THE AMD ON PIONEER 10

Event No.	Day	Sector	Band-width	ENTRANCE TIMES (Bits)				EXIT TIMES (Bits)			
				A	B	C	D	A	B	C	D
1	74	94	3	0	0	20	1	16	20	20	17
2	75	101	3	1	0	4	1	266	275	198	561
3	75	107	3	1	0	2	1	28	45	28	80
4	76	76	3	0	57	200	66	190	29	200	75
5	76	104	3	1	0	19	1	18	10	19	7
6	76	87	3	0	0	1	1	232	192	19	327
7	83	89	3	0	0	1	0	1191	975	808	1353
8	86	104	5	0	23	299	591	55	29612	22729	27960
9	89	85	3	485	0	431	720	7224	11074	435	11074
10	90	99	5	2	1	1	0	6	9	46	107
11	92	117	5	64	0	93	537	315	6849	87	726
12	93	89	5	12	0	15	13	1472	1830	1544	1543
13	93	114	5	0	0	1	0	118	2	42	182
14	94	91	5	0	745	0	0	235	745	33	745
15	95	90	5	0	51	2	0	1079	546	310	895
16	97	85	5	1	0	2	0	1412	1815	2093	3229
17	97	116	5	1	0	2	0	80	681	1032	2723
18	98	72	5	1	0	493	1	1227	1771	501	1408
19	99	115	5	9213	0	817	1111	9212	4105	824	6502
20	100	88	5	552	8	0	846	644	5188	4588	380
21	100	90	5	0	179	2427	33311	27624	239	25910	33311
22	100	89	5	1	0	2	0	1241	561	128	483
23	103	71	5	1095	26	87	0	82	56	113	5365
24	103	112	5	0	0	1	0	507	595	425	550
25	103	76	5	0	0	2	0	618	74	182	1046
26	105	2	5	0	71	140	381	160	164	243	381
27	105	67	5	1	0	7	0	695	200	8	290
28	105	112	5	28	98	0	14	113	405	747	232
29	107	5	5	0	35	57	58	68	66	83	75
30	107	103	5	266	0	889	541	397	842	891	830
31	107	81	5	13	0	2	16	104	628	12	39
32	108	5	5	1	0	2	0	657	509	688	1806
33	109	58	5	0	137	77	417	148	417	215	422
34	109	71	5	341	0	0	45	1891	3963	2	2963
35	109	99	5	1	1	2	0	55	9	37	426
36	110	127	5	323	279	0	41	44602	45531	47506	94474
37	110	47	5	0	153	3835	178	545	465	3835	667
38	110	119	5	221	0	1198	1855	7574	11260	1281	1867
39	110	102	5	86	0	144	101	143	140	144	95
40	110	119	5	961	925	2396	0	987	25318	2543	46481
41	111	11	5	1	0	2	0	1593	116	66	372
42	112	100	5	1	0	2	0	19	8	7	29
43	112	106	5	178	3	0	465	198	25979	20911	19175
44	112	82	5	1	0	8	8	725	1667	17	542
45	114	8	5	223	0	180	475	9476	10456	191	481
46	114	10	5	68	2647	495	0	567	2717	797	659
47	114	2	5	0	0	1	4	88	28	52	140
48	114	10	5	514	0	935	696	23083	21824	941	795
49	114	104	5	1	0	8	0	451	26	50	1161
50	115	71	5	0	0	5	0	520	369	288	536

TABLE C1. (CONTINUED)

Event			Band- width	ENTRANCE TIMES (Bits)				EXIT TIMES (Bits)			
No.	Day	Sector		A	B	C	D	A	B	C	D
51	115	32	5	2	49	17	0	253	142	240	421
52	115	45	5	0	0	26	17	36864	40845	19272	31718
53	115	108	5	42	0	174	52	133	138	174	174
54	116	56	5	53	103	4757	0	148	206	4757	146
55	116	18	5	1810	4947	3554	0	6407	6791	3575	7907
56	116	120	5	174	76	0	142	734	1785	1329	1090
57	119	93	5	638	0	1385	1939	659	5474	1400	1987
58	120	40	5	118	142	1744	0	146	466	1764	581
59	127	8	5	21	54	2	0	98	57	886	461
60	128	34	5	0	0	2	0	1346	803	42	986
61	128	82	5	1	0	3	0	194	166	45	289
62	129	83	5	0	0	2	0	315	196	328	485
63	129	80	5	1	0	2	0	26	45	176	203
64	129	103	5	10	0	22	6	182	250	193	211
65	137	122	5	776	58	68	0	776	102	90	166
66	137	87	5	362	0	297	188	394	1724	311	206
67	138	65	5	0	95	1	0	39	95	32	95
68	138	75	5	0	93	2	0	507	1183	626	2296
69	139	100	5	349	0	2	51	356	112	4	700
70	139	105	5	165	3801	942	0	324	3879	964	8043
71	146	86	3	0	8	66	13	322	153	235	114
72	148	105	3	174	360	42	0	177	368	3400	2039
73	151	125	3	3	2	8	0	7	8	8	7
74	151	62	3	0	1833	265	42	1022	1833	1034	67
75	151	56	3	0	1	46	1	41	21	46	17
76	151	109	3	0	8	1	0	4	8	7	8
77	152	24	3	148	186	8	0	6186	187	7182	7701
78	153	81	3	8	5	487	0	11	18	487	487
79	154	64	3	2	1	0	0	2884	1145	1512	2393
80	159	104	3	0	0	0	0	619	12	243	470
81	159	5	5	4	0	0	0	66	44	134	134
82	160	26	3	0	10	677	2	677	15	677	204
83	160	51	3	0	2	4	0	917	180	276	521
84	163	56	3	548	0	0	0	548	136	548	134
85	163	17	3	0	12	3	1	56	14	27	23
86	163	110	3	0	42	11	0	38	42	17	42
87	166	26	3	6	0	114	8	48	114	114	55
88	167	59	5	73	73	0	106	9011	5382	9580	9994
89	171	42	4	0	0	17	0	17	7	17	10
90	171	124	4	1	0	1	0	187	46	30	116
91	172	4	4	0	0	1	0	1520	825	27	520
92	174	110	4	62	108	7252	0	63	608	7294	4527
93	174	19	4	0	0	1	0	844	576	418	938
94	175	76	4	1	0	1	0	2081	1264	986	1404
95	176	17	4	1	0	1	0	1817	1036	810	790
96	178	9	3	0	1	3	1	620	382	340	460
97	178	57	3	1	0	18	2	6	8	18	18
98	179	80	3	0	52	455	191	318	387	455	362
99	179	0	3	5	5	94	0	17	13	94	90
100	180	125	3	0	0	17	0	11	7	17	17

TABLE C1. (CONTINUED)

Event No.	Day	Sector	Band-width	ENTRANCE TIMES (Bits)				EXIT TIMES (Bits)			
				A	B	C	D	A	B	C	D
101	180	66	3	183	156	1032	0	228	172	1053	457
102	187	123	3	0	0	2	0	2271	2068	2791	3340
103	187	73	3	0	168	52	18	81	211	111	126
104	187	26	3	1	0	158	1	7	6	158	143
105	187	127	3	0	0	26	0	6	12	26	26
106	188	52	3	0	0	2	1	1213	889	1464	1333
107	189	51	5	0	0	2	492	491	13	13	492
108	191	104	5	1	0	2	0	2	132	107	846
109	197	1	3	1	0	49	1	13	36	49	12
110	198	13	3	18	0	2	10	38	4	280	103
111	201	7	3	1	0	27	19	803	872	754	954
112	202	60	3	133	0	386	21	239	386	386	151
113	204	19	3	0	0	2	0	311	298	328	522
114	204	22	3	1	0	21	1	5	16	21	2
115	206	6	3	0	10	54	19	49	38	54	35
116	206	52	3	0	6	33	0	62	32	172	180
117	209	72	3	25	24	168	0	29	33	168	152
118	209	6	3	1	0	131	1	22	5	131	57
119	210	118	3	3	0	2	243	9	8	243	248
120	214	126	3	1	0	37	1	9	12	37	23
121	215	88	3	1	0	99	1	26	95	99	41
122	216	2	3	1	0	19	1	8	5	19	19
123	216	122	3	0	0	0	0	32	1111	42	419
124	217	13	3	6	9	106	0	18	13	106	95
125	217	89	3	24	0	6	15	603	8101	1741	1674
126	224	126	5	0	0	2	0	122	43	115	0
127	225	5	5	0	19	108	20	32	38	108	42
128	225	4	3	0	300	1202	22	23	307	1202	1202
129	225	58	3	31	0	3	5	31	10	20	13
130	225	126	3	10	10	22	0	15	22	22	18
131	226	127	3	1	0	40	2	5	5	40	10
132	226	103	3	0	0	15	1	8	15	15	14
133	227	12	3	117	49	10	0	117	57	103	117
134	229	31	3	1	0	3	1	1265	1427	1712	3448
135	231	38	3	0	13	5556	465	5555	16	5556	756
136	231	10	3	1	0	27	1	14	12	27	25
137	234	33	3	0	7	24	0	21	11	24	11
138	234	44	3	0	0	37	0	9	5	37	37
139	235	30	3	0	167	672	151	671	170	672	184
140	241	47	3	1	0	15	1	5	13	15	10
141	243	5	3	0	6	21	15	272	428	386	338
142	243	36	3	0	27	2	2	10	28	27	6
143	246	126	3	1	0	21	1	19	8	21	18
144	247	39	3	24	24	118	0	32	28	118	97
145	249	24	3	0	127	74	72	92	127	122	95
146	250	38	3	0	0	159	1	18	159	159	23
147	251	124	3	1168	0	2	75	1168	1168	665	93
148	252	3	3	0	2	14	2	12	6	14	14
149	253	18	3	0	1	2	0	26	16	30	78
150	253	39	3	1	0	9	1	9	8	9	5

TABLE C1. (CONTINUED)

Event No.	Day	Sector	Band-width	ENTRANCE TIMES (Bits)				EXIT TIMES (Bits)			
				A	B	C	D	A	B	C	D
151	254	54	3	0	22	7282	202	6785	24	7282	7282
152	259	2	3	0	0	2	0	0	625	389	673
153	260	11	3	1	0	78	12	254	1130	162	28
154	260	17	3	0	0	16	0	4	4	16	16
155	261	45	3	1	0	15	0	7	7	15	10
156	262	1	3	196	0	5	4	196	196	22	12
157	262	11	3	0	0	12	0	12	7	12	10
158	262	115	3	64	0	43	15	69	4665	148	3909
159	263	62	3	58	35	37	0	58	48	58	42
160	263	58	3	0	0	15	0	4	4	15	15
161	264	36	3	0	8	13	0	13	12	13	12
162	265	30	3	0	0	1	1	5	7	8	6
163	267	3	3	0	0	12	1	12	12	12	10
164	268	46	3	79	0	648	51	97	189	648	489
165	269	2	3	6	235	0	1408	1408	236	596	1408
166	271	10	3	1	0	22	1	22	0	22	10
167	272	77	3	0	0	21	0	12	6	21	21
168	273	30	3	1	2	12	0	10	11	12	12
169	274	95	3	698	0	2	4	698	97	681	78
170	275	80	3	30	0	129	128	2596	2817	2200	2653
171	277	32	3	0	0	17	0	7	4	17	17
172	278	77	3	1	0	10	0	6	4	10	10
173	278	80	3	3	2	17	0	8	16	17	11
174	280	36	3	1	0	14	1	14	8	14	13
175	280	127	3	20	0	35	15	143	220	159	280
176	280	109	3	1	0	12	1	11	12	12	5
177	283	14	3	20	0	29	29	229	330	235	223
178	285	75	3	0	0	2	0	1166	1077	1246	1458
179	285	57	3	0	1	47	0	1063	0	536	1764
180	285	76	3	1	0	253	5	12	13	253	52
181	289	63	3	47	0	67	32	331	413	490	520
182	290	125	3	0	0	2	0	925	50	610	1133
183	291	49	3	0	0	17	4	11	13	17	9
184	295	10	3	1	0	12	1	10	6	12	12
185	295	84	3	22	0	2	1	22	19	15	9
186	296	88	3	0	25	245	17	45	87	292	39
187	299	31	3	0	6	49	0	48	10	49	12
188	301	10	3	0	0	24	1	8	20	24	15
189	303	15	3	0	0	8	1	5	5	8	8
190	304	106	3	1	0	16	1	5	6	16	10
191	304	12	3	1	0	9	0	9	5	9	8
192	307	109	3	15	0	2	2	5	6	14	14
193	311	82	3	1	0	24	1	10	6	24	24
194	311	99	3	0	0	7	1	7	6	7	7
195	315	36	3	36	0	3	126	41	14	126	126
196	316	96	3	0	0	12	1	12	12	12	10
197	317	8	3	209	0	2	5	209	29	209	15
198	318	37	3	0	0	12	0	8	5	12	12
199	321	7	3	1	0	24	1	5	14	24	22
200	322	48	3	1	0	18	1	18	8	18	7

TABLE C1. (CONTINUED)

Event No.	Day	Sector	Band-width	ENTRANCE TIMES (Bits)				EXIT TIMES (Bits)			
				A	B	C	D	A	B	C	D
201	323	123	3	2	1	27	0	6	6	27	27
202	332	58	3	1	0	17	1	16	7	17	5
203	332	114	3	61	0	3	3	61	46	50	8
204	333	76	3	1	0	150	1	124	10	150	8
205	335	94	3	0	1	11	1	11	5	11	7
206	336	41	3	1	0	14	1	9	9	14	10
207	338	97	3	1	0	19	0	4	11	19	7
208	339	85	3	0	0	9	0	9	4	9	9
209	339	59	3	1	0	88	1	70	51	88	27
210	342	21	3	1	0	16	0	6	5	16	12
211	344	51	3	0	0	10	0	10	6	10	10
212	345	6	3	1	0	12	1	7	12	12	11
213	345	69	3	0	0	25	0	4	8	25	12
214	346	19	3	1	0	10	1	9	10	10	10
215	346	41	3	0	0	14	0	13	6	14	9
216	348	44	3	0	0	9	2	347	389	369	314
217	351	26	3	0	0	2	0	311	196	341	446
218	353	111	3	2	0	2	66	272	160	97	320
219	355	35	3	1	0	2	1	20	645	505	302
220	362	45	3	1	0	21	1	16	10	21	21
221	363	45	3	1	0	1	21	8	20	19	21
222	365	50	3	33	5	2	0	33	7	14	17
223	365	32	3	12	37	1	0	16	41	16	32
224	366	32	3	1	0	10	1	7	10	10	8
225	367	54	3	1	0	17	0	8	14	17	10
226	368	10	3	0	0	11	0	5	4	11	6
227	368	71	3	0	1	64	0	6	11	12	12
228	372	35	3	0	0	8	0	8	5	8	8
229	373	16	3	1	0	11	1	11	10	11	6
230	373	36	3	0	21	1	1	16	21	8	9
231	388	7	3	0	0	0	1	12	16	18	17
232	389	50	3	0	21	1	0	21	21	11	7

TABLE C2. BACKGROUNDS AND PEAK SIGNALS FOR
EVENTS MEASURED BY THE AMD ON PIONEER 10

Event No.	Day	Sector	Band- width	BACKGROUND (Bits)				PEAK SIGNALS (Bits)			
				A	B	C	D	A	B	C	D
1	74	94	3	34	16	48	29	49	26	54	44
2	75	101	3	31	14	46	28	68	66	119	123
3	75	107	3	29	13	45	28	43	20	76	78
4	76	76	3	41	18	56	39	56	23	61	48
5	76	104	3	28	13	44	27	49	21	51	34
6	76	87	3	36	19	50	31	115	68	72	90
7	83	89	3	31	18	47	31	136	69	119	241
8	86	104	5	25	15	41	28	103	100	120	82
9	89	85	3	32	19	46	33	65	55	80	59
10	90	99	5	24	14	36	25	50	22	80	92
11	92	117	5	22	14	39	28	52	31	62	50
12	93	89	5	29	18	41	29	74	60	89	62
13	93	114	5	22	14	37	27	69	25	87	107
14	94	91	5	27	17	39	28	106	21	88	132
15	95	90	5	28	17	39	28	146	33	88	128
16	97	85	5	36	19	43	32	160	97	166	171
17	97	115	5	20	14	37	28	79	116	142	180
18	98	72	5	30	18	48	35	142	95	75	85
19	99	116	5	20	15	43	33	36	41	80	82
20	100	88	5	29	18	42	34	67	50	81	57
21	100	90	5	33	21	49	32	78	56	85	40
22	100	89	5	29	18	40	36	152	90	87	121
23	103	71	5	29	19	51	36	64	37	80	68
24	103	112	5	20	13	34	25	144	74	178	152
25	103	76	5	26	17	44	32	88	38	128	164
26	105	2	5	26	24	59	39	96	70	114	53
27	105	67	5	38	24	59	44	166	94	87	124
28	105	112	5	20	13	35	25	68	56	160	121
29	107	5	5	26	26	60	40	72	68	104	67
30	107	103	5	22	14	33	24	83	28	60	44
31	107	81	5	28	19	43	31	102	136	93	63
32	108	5	5	28	24	60	40	188	106	174	255
33	109	58	5	34	20	54	40	64	46	94	71
34	109	71	5	28	19	50	36	87	80	118	92
35	109	99	5	21	13	33	24	77	22	91	148
36	110	127	5	22	22	60	46	151	142	178	170
37	110	47	5	109	68	138	128	185	99	168	174
38	110	119	5	21	16	44	32	64	46	84	69
39	110	102	5	20	13	32	24	45	32	54	55
40	110	119	5	21	16	46	37	95	83	148	156
41	111	11	5	30	29	63	38	183	72	123	160
42	112	100	5	20	13	32	24	90	56	82	83
43	112	106	5	20	14	34	26	98	90	117	85
44	112	82	5	28	20	42	30	209	208	85	116
45	114	8	5	27	22	59	38	89	80	114	83
46	114	10	5	26	22	57	35	91	37	126	96
47	114	2	5	23	20	56	36	110	33	103	75
48	114	10	5	24	22	56	35	81	49	106	76
49	114	104	5	19	12	31	23	94	51	75	183
50	115	71	5	24	16	44	31	171	44	83	151

TABLE C2. (CONTINUED)

Event No.	Day	Sector	Band-width	BACKGROUND (Bits)				PEAK SIGNALS (Bits)			
				A	B	C	D	A	B	C	D
51	115	32	5	107	68	127	86	180	89	171	174
52	115	45	5	45	38	102	70	158	158	182	168
53	115	108	5	20	14	34	24	82	57	46	59
54	116	56	5	29	20	52	40	68	41	79	84
55	116	18	5	42	38	74	54	113	72	134	168
56	116	120	5	20	16	45	32	50	40	88	66
57	119	93	5	21	14	32	23	53	32	63	45
58	120	40	5	21	13	33	25	64	32	75	64
59	127	8	5	21	18	48	28	61	32	205	184
60	128	34	5	26	20	50	38	255	99	114	136
61	128	82	5	23	16	35	24	144	83	86	120
62	129	83	5	22	15	32	22	134	43	124	104
63	129	80	5	25	18	37	25	71	40	118	115
64	129	103	5	16	11	29	21	49	34	69	68
65	137	122	5	16	12	34	24	29	22	61	46
66	137	87	5	24	17	40	28	57	34	73	61
67	138	65	5	30	21	52	38	116	27	116	74
68	138	75	5	24	17	44	31	123	50	132	206
69	139	100	5	19	13	30	22	108	69	116	114
70	139	105	5	18	12	28	20	60	25	64	50
71	146	86	3	24	18	37	24	108	83	77	56
72	148	105	3	15	10	25	17	33	22	66	31
73	151	125	3	14	12	35	24	20	34	49	33
74	151	62	3	32	23	55	38	71	25	88	86
75	151	56	3	26	20	48	38	74	77	60	69
76	151	109	3	14	10	23	17	24	11	42	27
77	152	24	3	23	20	50	35	65	72	111	109
78	153	81	3	22	16	38	25	28	61	54	108
79	154	64	3	34	25	54	42	255	174	192	255
80	159	104	3	16	10	23	16	182	29	48	106
81	159	5	5	15	14	38	26	31	49	78	32
82	160	26	3	26	21	49	34	198	45	64	82
83	160	51	3	25	20	48	37	224	167	136	182
84	163	56	3	26	20	48	38	135	102	61	78
85	163	17	3	19	17	49	31	98	36	81	58
86	163	110	3	14	9	22	16	23	10	44	65
87	166	26	3	19	17	42	26	60	108	56	75
88	167	59	5	27	22	50	39	88	81	108	85
89	171	42	4	23	18	43	32	80	30	56	60
90	171	124	4	13	10	28	20	148	31	77	108
91	172	4	4	16	14	39	27	255	155	97	160
92	174	110	4	19	14	60	28	90	117	94	172
93	174	19	4	22	18	49	32	174	94	182	220
94	175	76	4	26	20	44	30	255	171	208	255
95	176	17	4	24	20	52	33	255	180	164	176
96	178	9	3	17	18	48	31	183	92	118	168
97	178	57	3	25	20	46	36	34	27	60	54
98	179	80	3	21	19	40	24	36	29	55	35
99	179	0	3	13	12	32	23	25	16	48	56
100	180	125	3	13	10	29	20	23	15	43	33

TABLE C2. (CONTINUED)

Event No.	Day	Sector	Band-width	BACKGROUND (Bits)				PEAK SIGNALS (Bits)			
				A	B	C	D	A	B	C	D
101	180	66	3	29	22	50	38	68	61	80	78
102	187	123	3	15	12	32	26	255	187	255	255
103	187	73	3	26	21	50	40	78	45	92	72
104	187	26	3	22	18	43	28	37	25	59	80
105	187	127	3	13	12	32	22	20	15	47	36
106	188	52	3	24	20	48	37	214	161	236	224
107	189	51	5	23	19	45	34	159	64	103	65
108	191	104	5	121	36	94	107	154	76	156	202
109	197	1	3	14	14	37	25	24	33	50	38
110	198	13	3	20	18	49	30	27	26	173	47
111	201	7	3	16	17	46	30	69	57	91	76
112	202	60	3	25	20	44	34	37	33	58	47
113	204	19	3	18	16	41	25	55	53	160	178
114	204	22	3	19	16	40	24	24	28	54	36
115	206	6	3	36	30	64	35	49	36	76	44
116	206	52	3	22	19	44	36	73	24	94	140
117	209	72	3	30	22	46	31	38	28	60	84
118	209	6	3	15	16	42	28	34	20	58	73
119	210	118	3	20	10	42	28	27	19	136	43
120	214	126	3	14	12	32	23	21	19	46	51
121	215	89	3	135	41	91	86	187	61	100	114
122	216	2	3	14	14	38	25	23	18	51	41
123	216	122	3	17	13	32	24	175	255	177	137
124	217	13	3	20	18	48	30	33	23	61	78
125	217	89	3	136	46	95	97	172	179	181	162
126	224	125	5	14	13	34	24	83	26	98	137
127	225	5	5	16	17	44	28	73	55	69	69
128	225	4	3	16	16	43	29	25	22	56	168
129	225	58	3	24	18	43	33	27	28	73	48
130	225	126	3	14	13	33	24	22	22	50	40
131	226	127	3	14	14	35	24	24	22	50	37
132	226	103	3	124	32	88	98	164	45	96	137
133	227	12	3	21	18	48	29	24	22	82	58
134	229	31	3	24	19	40	32	226	184	255	255
135	231	38	3	19	15	34	24	38	23	49	38
136	231	10	3	20	18	47	29	40	26	60	56
137	234	33	3	20	16	33	23	48	19	47	32
138	234	44	3	19	15	38	28	29	18	52	58
139	235	30	3	22	16	35	24	152	25	48	33
140	241	47	3	20	15	40	31	24	24	55	43
141	243	5	3	19	17	44	28	30	28	72	40
142	243	36	3	19	15	32	22	30	18	60	30
143	246	126	3	17	14	36	25	37	21	51	52
144	247	39	3	18	14	33	23	26	18	46	76
145	249	24	3	20	15	33	21	72	18	81	37
146	250	38	3	18	15	32	23	43	69	47	36
147	251	124	3	18	14	36	25	20	142	164	46
148	252	3	3	20	17	44	28	42	21	59	40
149	253	18	3	22	16	38	23	44	21	75	84
150	253	39	3	18	14	33	24	26	18	47	33

TABLE C2. (CONTINUED)

Event No.	Day	Sector	Band-width	BACKGROUND (Bits)				PEAK SIGNALS (Bits)			
				A	B	C	D	A	B	C	D
151	254	54	3	24	16	44	43	53	28	64	70
152	259	2	3	21	17	43	27	172	105	164	178
153	260	11	3	23	19	46	27	45	173	70	36
154	260	17	3	22	16	39	24	29	20	52	33
155	261	45	3	22	14	38	30	28	20	54	45
156	262	1	3	20	16	41	26	24	85	66	41
157	262	11	3	24	18	47	28	49	25	60	45
158	262	115	3	21	13	43	28	33	28	79	62
159	263	62	3	26	17	42	37	28	28	68	74
160	263	58	3	24	15	41	40	36	19	54	61
161	264	36	3	19	14	31	22	39	16	45	30
162	265	30	3	20	15	30	20	31	21	44	27
163	267	3	3	22	16	43	26	34	24	58	41
164	268	46	3	24	16	42	34	33	22	56	47
165	269	2	3	24	16	45	26	44	21	76	29
166	271	10	3	24	18	47	27	48	24	60	37
167	272	77	3	26	18	39	29	50	28	54	52
168	273	30	3	21	15	30	20	36	23	43	38
169	274	95	3	74	26	77	40	76	54	255	64
170	275	80	3	27	19	40	30	51	44	78	56
171	277	32	3	20	15	30	20	26	19	43	38
172	278	77	3	24	17	37	29	32	23	52	39
173	278	80	3	30	20	42	30	36	26	55	47
174	280	36	3	21	15	31	22	35	20	46	32
175	280	127	3	23	16	40	26	36	28	66	45
176	280	109	3	25	15	46	25	46	19	57	33
177	283	14	3	26	18	43	25	46	50	81	39
178	285	75	3	31	21	45	35	224	128	212	179
179	285	57	3	28	16	43	44	175	37	82	188
180	285	76	3	26	17	38	31	34	22	54	44
181	289	63	3	26	16	40	36	37	24	69	53
182	290	125	3	26	15	39	28	163	24	102	184
183	291	49	3	28	15	42	39	48	21	56	52
184	295	10	3	30	19	46	28	49	24	59	46
185	295	84	3	26	18	33	29	28	44	57	36
186	296	88	3	47	22	51	31	108	136	170	136
187	299	31	3	27	17	31	28	72	20	45	46
188	301	10	3	30	18	42	28	45	36	54	51
189	303	15	3	34	21	46	33	45	25	59	43
190	304	106	3	24	14	30	26	38	18	44	38
191	304	12	3	31	19	43	29	48	23	58	42
192	307	109	3	26	15	33	28	38	17	48	51
193	311	82	3	29	18	36	32	48	22	51	59
194	311	99	3	28	17	30	27	38	22	45	38
195	315	36	3	30	16	32	33	37	40	103	37
196	316	96	3	29	18	31	28	48	23	45	39
197	317	8	3	30	17	38	29	35	23	137	39
198	318	37	3	30	15	32	33	45	20	46	46
199	321	7	3	31	17	36	31	40	30	50	58
200	322	48	3	28	14	34	35	54	22	49	49

TABLE C2. (CONTINUED)

Event No.	Day	Sector	Band-width	BACKGROUND (Bits)				PEAK SIGNALS (Bits)			
				A	B	C	D	A	B	C	D
201	323	123	3	29	16	36	33	34	20	49	76
202	332	53	3	26	16	38	38	58	20	53	49
203	332	114	3	30	16	36	36	32	45	84	68
204	333	76	3	33	22	45	36	108	28	57	48
205	335	94	3	33	20	34	30	46	22	49	39
206	336	41	3	26	14	27	28	32	20	42	36
207	338	97	3	34	20	36	32	39	28	50	46
208	339	85	3	32	20	38	32	54	24	52	53
209	339	59	3	27	16	39	37	86	36	55	72
210	342	21	3	29	16	28	30	46	19	43	47
211	344	51	3	26	14	33	32	46	17	48	49
212	345	6	3	31	17	35	36	47	22	51	50
213	345	69	3	28	19	43	31	48	28	56	46
214	346	19	3	29	16	29	31	43	21	43	45
215	346	41	3	25	13	25	27	48	18	38	36
216	348	44	3	24	13	26	26	170	98	127	89
217	351	26	3	29	16	26	29	154	34	103	160
218	353	111	3	34	17	38	41	166	28	89	132
219	355	35	3	23	13	22	24	42	31	156	97
220	362	45	3	22	12	24	23	45	19	40	39
221	363	45	3	22	12	24	23	28	28	57	26
222	365	50	3	22	13	29	24	24	15	56	40
223	365	32	3	21	13	20	22	28	14	48	48
224	366	32	3	22	13	20	22	32	20	35	31
225	367	54	3	22	13	33	26	36	26	48	38
226	368	10	3	29	16	34	35	39	24	48	50
227	368	71	3	29	20	50	28	38	29	65	38
228	372	35	3	20	12	20	21	27	18	0	29
229	373	16	3	25	14	28	29	45	27	41	40
230	373	36	3	20	12	20	20	44	13	41	32
231	388	7	3	33	16	42	45	62	32	75	68
232	389	50	3	16	11	17	16	39	12	32	25

TABLE C3. ENTRY AND EXIT TIMES FOR EVENTS
MEASURED BY THE AMD ON PIONEER II

Event No.	Day	Sector	Band-width	ENTRANCE TIMES (Bits)				EXIT TIMES (Bits)			
				A	B	C	D	A	B	C	D
1	110	15	3	1	0	14	1	1393	819	16	576
2	112	75	3	2	0	1	5	28	120	72	158
3	113	6	3	1	0	1	0	298	181	191	515
4	114	41	3	1	0	1	0	92	407	218	965
5	114	53	3	98	0	5588	39	111	1864	5588	1184
6	115	3	3	1	0	552	58	552	188	552	114
7	116	54	3	1	0	2	1	39520	34406	100	29883
8	120	5	3	0	6	1	0	23826	5108	21476	9431
9	121	92	3	21	0	32	30	29	77	35	102
10	122	51	3	1	0	1	0	84	27	7	81
11	122	40	3	1	0	6	8	165	305	18	125
12	123	3	3	0	297	3	1	179	297	153	294
13	124	9	3	6500	27	9	43	4822	2323	6499	1731
14	125	125	3	0	5	1	5	1049	693	4226	4812
15	125	102	3	1	0	1	0	235	116	292	581
16	125	42	3	67	74	235	0	68	1627	240	2406
17	126	44	3	0	95	17	0	200	104	21	342
18	129	84	3	1	0	1	1	276	218	245	538
19	129	112	3	3	0	0	2	2466	6039	2743	5831
20	131	44	3	8	0	9	8	133	27	22	110
21	131	37	3	11	0	11	10	1964	27	2636	3358
22	138	22	3	3	3	0	146	373	30	193	1383
23	150	10	3	35	0	26	49	572	26	431	1093
24	151	7	3	305	0	78	16	347	27	102	184
25	157	104	3	2	8	0	23	189	35	191	312
26	158	45	3	3	0	5686	2	81	27	5686	85
27	159	111	3	6	0	6	6	18	27	208	212
28	159	41	3	21	0	22	22	122	27	106	190
29	164	23	3	10	0	10	9	427	98	342	586
30	164	96	3	9	0	9	9	712	28	741	1258
31	171	67	3	6	0	6	5	142	27	29	254
32	173	9	3	4	2	5414	0	70	28	5414	324
33	182	57	3	14	0	8	12	80	28	232	170
34	182	34	3	33	0	16	12	49	27	717	815
35	188	4	3	5	0	5	4	298	16	461	418
36	190	46	3	5	4	0	1	33	7	262	307
37	192	0	4	28	0	10296	28	259	28	10296	1272
38	193	63	4	22	0	4664	22	114	28	4664	85
39	194	41	4	9	0	6734	9	329	11	6734	74
40	208	104	5	90	136	91	88	6045	138	3568	7352
41	218	106	5	264	0	42	77	3079	128	3628	5362
42	220	126	5	1	0	3	0	63	124	2205	4165
43	224	13	5	6	17	54	2	16384	0	6528	128
44	235	54	5	524	0	205	34	2098	117	1759	2471
45	236	125	5	62	0	17	105	9311	115	7023	7307
46	240	111	5	37	0	38	36	466	129	118	369
47	253	40	5	103	834	104	102	2878	831	2882	2614
48	268	119	5	61	140	43	65	1642	129	1552	1777
49	287	7	5	123	0	124	121	1411	133	695	2003
50	346	104	5	1	7	40219	0	191	133	40219	287
51	26	83	5	26	0	34819	25	892	136	34821	216

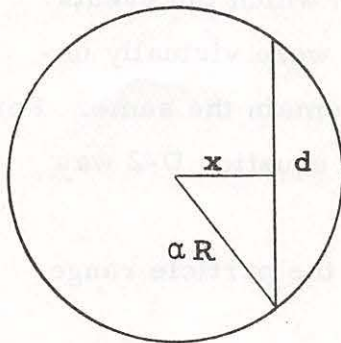
TABLE C4. BACKGROUNDS AND PEAK SIGNALS FOR
EVENTS MEASURED BY THE AMD ON PIONEER II

Event No.	Day	Sector	Band- width	BACKGROUND (Bits)				PEAK SIGNALS (Bits)			
				A	B	C	D	A	B	C	D
1	110	15	3	60	39	74	44	255	53	96	95
2	112	75	3	60	24	62	23	80	67	120	42
3	113	6	3	58	56	72	44	144	129	255	183
4	114	41	3	84	52	116	26	112	111	181	118
5	114	53	3	58	31	108	24	70	47	111	36
6	115	3	3	59	30	77	43	147	101	81	56
7	116	54	3	60	34	108	37	255	255	255	255
8	120	5	3	61	52	85	50	170	255	255	255
9	121	92	3	58	20	52	18	68	35	61	28
10	122	51	3	56	24	90	23	122	40	107	60
11	122	40	3	57	30	88	20	115	137	112	34
12	123	3	3	59	51	58	40	113	51	111	62
13	124	9	3	64	50	66	45	70	102	124	72
14	125	125	3	57	54	58	23	120	77	125	55
15	125	102	3	56	18	54	19	145	46	128	92
16	125	42	3	56	25	86	21	68	36	101	34
17	126	44	3	58	24	85	22	137	33	104	92
18	129	84	3	61	18	56	19	206	59	198	126
19	129	112	3	56	16	58	22	127	120	149	98
20	131	44	3	68	0	95	33	160	7	124	88
21	131	37	3	67	0	76	34	159	7	255	255
22	138	22	3	101	0	95	68	160	7	167	150
23	150	10	3	86	0	81	27	129	5	115	60
24	151	7	3	84	0	92	42	110	4	120	58
25	157	104	3	224	0	80	30	0	4	112	65
26	158	45	3	80	0	80	27	162	8	83	71
27	159	111	3	200	0	80	30	104	4	255	86
28	159	41	3	86	0	77	25	165	8	176	136
29	164	23	3	80	0	71	22	255	13	255	186
30	164	96	3	84	0	80	30	223	8	234	211
31	171	67	3	88	0	76	25	187	8	114	103
32	173	9	3	80	0	70	23	156	7	74	149
33	182	57	3	79	0	82	30	167	8	200	120
34	182	34	3	82	0	72	23	136	6	210	47
35	188	4	3	82	0	82	30	188	8	255	170
36	190	46	3	81	0	78	27	172	8	205	167
37	192	0	4	78	0	75	28	212	7	86	177
38	193	63	4	0	0	79	27	167	7	91	77
39	194	41	4	76	0	69	22	231	8	80	118
40	208	104	5	81	0	72	30	255	13	255	255
41	218	106	5	75	0	70	25	142	7	135	70
42	220	126	5	73	0	72	27	141	6	214	181
43	224	13	5	87	0	80	31	105	5	139	124
44	235	54	5	72	0	76	26	128	7	135	75
45	236	125	5	72	0	72	27	144	7	135	73
46	240	111	5	70	0	67	24	174	7	120	84
47	253	40	5	66	0	57	19	255	68	255	200
48	268	119	5	12	0	72	28	178	7	196	146
49	287	7	5	87	0	82	32	200	6	206	186
50	346	104	5	78	0	66	26	172	7	84	136
51	26	83	5	78	0	78	30	255	9	93	132

APPENDIX D

EQUATIONS RELATING PARTICLE RANGE, SIZE AND TRANSIT TIME

Since the particle range could not be obtained directly by solving the equations of particle motion derived for the AMD system it was necessary to use an alternate method. Although the following solution is not unique, other methods give approximately the same results. It was assumed that a particle would pass through the field-of-view at any point with equal probability. Therefore, an average path length was computed for the particle's transit through a field-of-view as shown below.



d - chord length of circle whose average value is to be determined.

αR - radius of circle at a distance R from apex of cone with half-angle α .

x - perpendicular distance from center of circle to chord.

The chord length can be expressed as:

$$d = 2\sqrt{(\alpha R)^2 - x^2} \quad (D-1)$$

The average value of the chord length can be written as:

$$\bar{d} = \frac{1}{\alpha R} \int_0^{\alpha R} 2\sqrt{(\alpha R)^2 - x^2} dx$$

$$\begin{aligned}
\bar{d} &= \frac{2}{\alpha R} \cdot \frac{1}{2} \left[x \sqrt{(\alpha R)^2 - x^2} + (\alpha R)^2 \sin^{-1} \frac{x}{\alpha R} \right]_0^{\alpha R} \\
&= \frac{1}{\alpha R} \alpha^2 R^2 \frac{\pi}{2} \\
&= \frac{\pi \alpha R}{2} \tag{D-2}
\end{aligned}$$

The average path length for a particle is therefore $\frac{\pi \alpha R}{2}$, and the average transit time will be given by:

$$\bar{\tau} = \frac{\pi \alpha R}{2v} \tag{D-3}$$

where v is the particle encounter velocity relative to the AMD assuming a circular orbit for the particle.

It should be pointed out that, in general, the path length through the field-of-view would be the chord of an ellipse determined by the direction of the particle's motion relative to the optical axis. The effect of this refinement was considered and it was determined that because of the manner in which the events were grouped the resulting size distributions were virtually unaffected and the conclusions of the analysis remain the same. For simplicity the mean path length as defined by equation D-2 was used in the analysis.

The particle radius a is related to the particle range via the equation:

$$I_{\min} = \frac{I_o \text{ r f } (\gamma)}{4 S^2} \left(\frac{a}{R} \right)^2 \tag{D-4}$$

which can be written as:

$$\frac{R}{a} = \left[\frac{I_o \text{ r f } (\gamma)}{4 S^2 I_{\min}} \right]^{1/2} \tag{D-5}$$

where I_0 is the solar irradiance at 1 AU, r is the bond albedo, $f(\gamma)$ is the phase law, S is the heliocentric distance of the spacecraft in AU and I_{\min} is the minimum detectable signal. The quantity in brackets can be evaluated for each particle detected and then using Equation (D-3) the particle size is obtained. Evaluating Equation (D-5) for the following values typical at 1 AU:

$$\begin{aligned} I_0 &= .14 \text{ watts/cm}^2 \\ r &= .3 \\ f(135^\circ) &= 2.0 \\ I_{\min} &= 2.3 \times 10^{-12} \text{ watts/cm}^2 \end{aligned}$$

$$\text{yields: } \frac{R}{a} = 9.6 \times 10^4. \quad (\text{D-6})$$

The above equation is an alternate way of defining the instrument sensitivity, e.g., a particle of radius 1 mm would be observed out to a range of 96 meters.

Equation (D-6) also defines the sensitive volume within which a particle of a given size can be observed. For example, if a particle can be seen out to a range R the volume within which it can be seen is given by:

$$V = \pi/3 \alpha^2 R^3 - V_0 \quad (\text{D-7})$$

where V_0 is a small unavailable volume due to the required three-fold coincidence. Thus, by calculating the sensitive volume for all particle sizes observed and combining it with the measured transit times and the instrument observation time, the cumulative particle concentration was computed from the equation:

$$N = \frac{\Delta \tau}{\tau \Delta V} \quad (\text{D-8})$$

where T is the effective observation time and $\Delta \tau$ is the total transit time of particles in the volume element ΔV . N is the number per

unit volume of all particles which can be detected in the volume element. The ratio $\frac{\Delta \tau}{\tau}$ in equation D-8 can be interpreted as the average number of particles in the volume element ΔV .

APPENDIX E

TABULATIONS OF PARTICLE CONCENTRATIONS

The particle concentrations were determined by grouping the data into thirds of decades of particle size and computing the concentration due to all particles in the group using Equation (D-8). The concentrations were then centered at the logarithmic means within each one-third decade of size. The Pioneer 10 results are presented in Table E1 for the pre-asteroid belt region (1-2 AU) and in Table E2 for the asteroid belt region (2-3.5 AU). The Pioneer 11 results are presented in Table E3.

TABLE E1

PARTICLE CONCENTRATION FROM 1-2 AU
DETERMINED FROM PIONEER 10

\bar{a} (m)	Δa (m)	$\Sigma d \tau$ (μ sec)	$\Sigma T d V$ (sec-m ³)	N (m ⁻³)
1.00E-1	6.81E-2 to 1.47E-1	37770	2.49E16	1.52E-18
4.64E-2	3.16E-2 to 6.81E-2	34930	2.47E15	1.41E-17
2.15E-2	1.47E-2 to 3.16E-2	88150	2.47E14	3.57E-16
1.00E-2	6.81E-3 to 1.47E-2	34450	2.50E13	1.38E-15
4.64E-3	3.16E-3 to 6.81E-3	20750	2.49E12	8.33E-15
2.15E-3	1.47E-3 to 3.16E-3	15610	2.51E11	6.21E-14
1.00E-3	6.81E-4 to 1.47E-3	6929	2.59E10	2.67E-13
4.64E-4	3.16E-4 to 6.81E-4	3568	2.70E9	1.32E-12
	> 3.16E-4	1620	3.38E8	4.79E-12

TABLE E2
 PARTICLE CONCENTRATIONS FROM 2-3.5 AU
 DETERMINED FROM PIONEER 10

\bar{a} (m)	Δa (m)	$\Sigma d\tau$ (μsec)	$\Sigma T dV$ ($\text{sec}\cdot\text{m}^3$)	N (m^{-3})
1.00E-1	6.81E-2	12960	9.75E15	1.33E-18
	to 1.47E-1			
4.64E-2	3.16E-2	18790	9.69E14	1.94E-17
	to 6.81E-2			
2.15E-2	1.47E-2	20000	9.69E13	2.06E-16
	to 3.16E-2			
1.00E-2	6.81E-3	14780	9.81E12	1.51E-15
	to 1.47E-2			
4.64E-3	3.16E-3	6442	9.83E11	6.56E-15
	to 6.81E-3			
2.15E-3	1.47E-3	6010	9.98E10	6.02E-14
	to 3.16E-3			
1.00E-3	6.81E-4	1645	1.04E10	1.58E-13
	to 1.47E-3			
4.64E-4	3.16E-4	1051	1.12E9	9.37E-13
	to 6.81E-4			
	> 3.16E-4	2143	1.52E8	1.41E-11

TABLE E3

PARTICLE CONCENTRATIONS FROM 1-3.5 AU
DETERMINED FROM PIONEER 11

\bar{a} (m)	Δa (m)	$\Sigma d\tilde{\tau}$ (μ sec)	$\Sigma T dV$ ($\text{sec}\cdot\text{m}^3$)	N (m^{-3})
1.00E-1	6.81E-2	63230	2.98E16	2.12E-18
to	1.47E-1			
4.64E-2	3.16E-2	44673	2.96E15	1.51E-17
to	6.81E-2			
2.15E-2	1.47E-2	11963	2.96E14	4.04E-17
to	3.16E-2			
1.00E-2	6.81E-3	37357	2.99E13	1.25E-15
to	1.47E-2			
4.64E-3	3.16E-3	16058	2.99E12	5.37E-15
to	6.81E-3			
2.15E-3	1.47E-3	6353	3.00E11	2.12E-14
to	3.16E-3			
1.00E-3	6.81E-4	5843	3.11E10	1.88E-13
to	1.47E-3			
4.64E-4	3.16E-4	493	3.25E9	1.52E-13
to	6.81E-4			
2.15E-4	1.47E-4	200	3.60E8	5.56E-13
to	3.16E-4			
1.00E-4	6.81E-5	133	4.48E7	2.96E-12
to	1.47E-4			

APPENDIX F

COMPUTER SIMULATION OF ANALYSIS PROCEDURE

The procedure used to analyze the AMD data was tested by using a computer to first generate the type of data measured by the instrument and second to analyze this data via the methods described in Chapter V and in Appendix D.

A particle flux distribution of the form

$$\phi = K a^{-\beta} \quad (F-1)$$

was first selected. For each size a , the average calculated fluence (i. e., number of particles per unit area per second) was randomized by a Poisson distribution. The trajectory relative to the instrument (i. e., range from instrument) was then selected for each particle using a uniform random number generator. The velocity was generated from a Gaussian distribution with a mean of 14 and a σ of 4 kilometers per second. This is the range of vehicle encounter velocities that would be expected from an asteroid distribution. The transit time through a single field-of-view was then calculated. This process generated data of the type received from the instrument which was then analyzed using the procedure described previously.

Particle fluxes with size exponents of -1.5, -2 and -3 were tested in this fashion. In each case, with a limited number of events, this procedure resulted in a particle distribution which was nearly identical to the original input as shown in Figure F-1. Segmented distributions with several different slopes were also

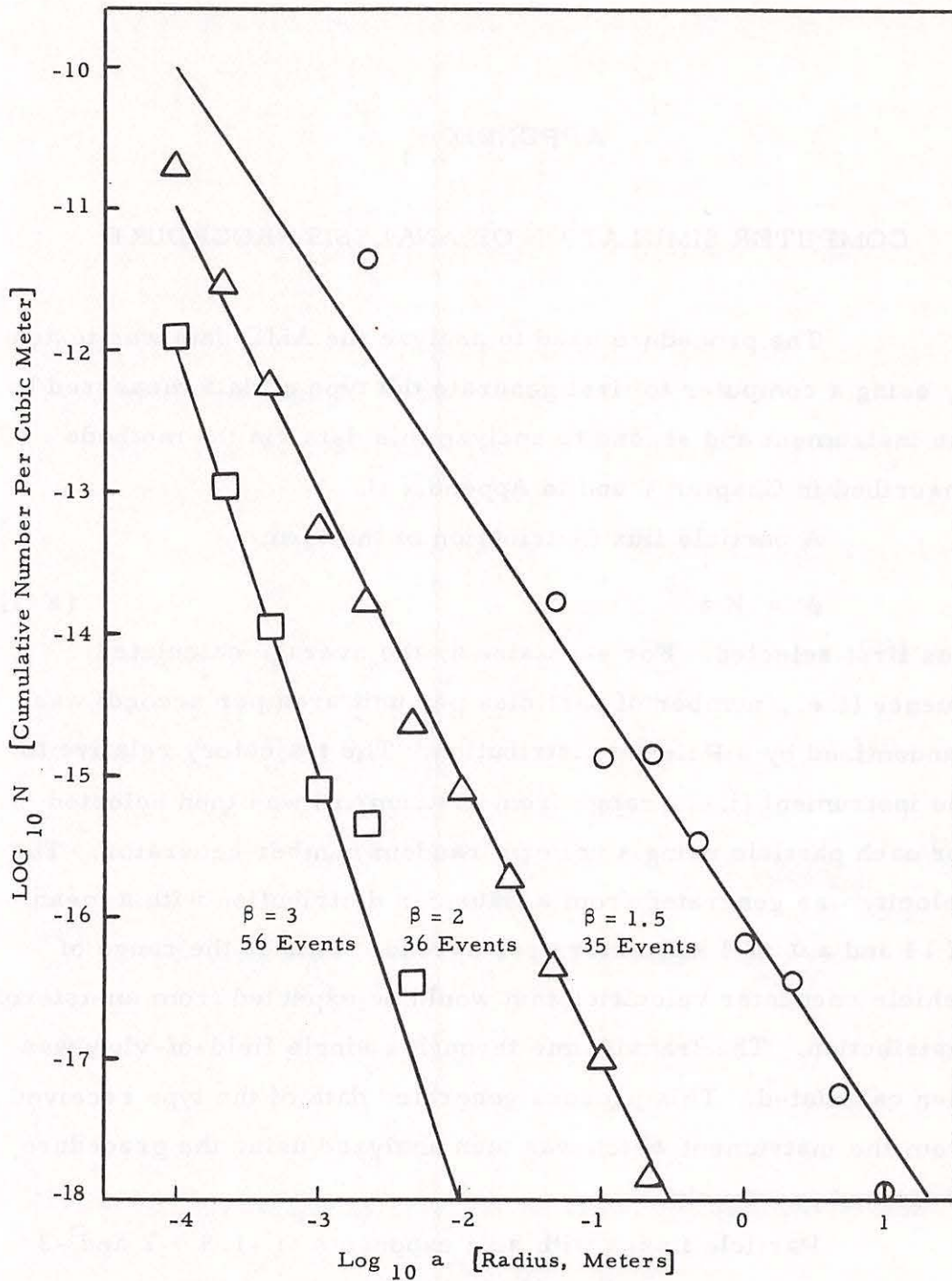


Figure F1. Results of Computer Simulation of Data Analysis Technique. Symbols Indicate Variation About the Input Distribution.

tested with similar results.

It should be pointed out that this simulation procedure also provided a method of estimating the errors associated with the actual analysis procedure. For example, the σ of 4 kilometers per second is in effect an uncertainty in the correct velocity which will be manifested in an uncertainty in the calculated concentration. As can be seen from Figure F-1, such an uncertainty in the assumed velocity resulted in about a factor of three (maximum) uncertainty in the resulting concentration.

APPENDIX G

DERIVATION OF GEGENSCHWEIN BRIGHTNESS EQUATION

The gegenschein brightness can be calculated quite easily if the spatial concentration is known. The analysis used is one suggested by D. J. Kessler (1968). Suppose that the spatial density of particles of radius a depends on the distance from the sun in the following manner:

$$n_a(S) = \begin{cases} 0 & S < S_1, \quad S > S_2 \\ n_a & S_1 \leq S \leq S_2 \end{cases} \quad (G-1)$$

where $n_a(S)$ is the assumed spatial density in the ecliptic plane of particles of radius a and at a distance S from the sun. This distribution is illustrated in Figure G1 below. The sun is assumed to be at the origin, the earth at S_0 , and S_1 and S_2 are the limits of the region in which it is assumed that particles are confined.

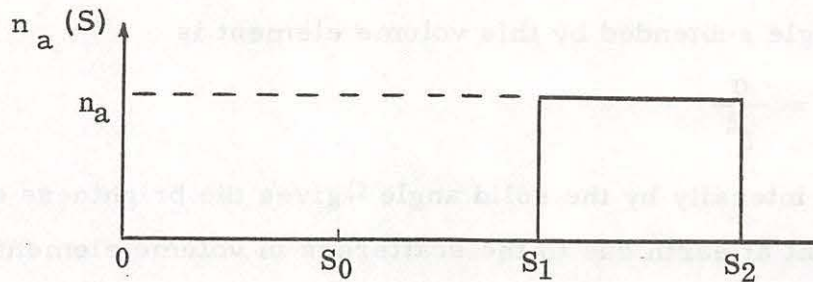


Figure G1. Spatial Density for Gegenschein Brightness Calculation

The brightness of reflected sunlight due to these particles is now easily calculated. The brightness due to volume element $\sigma d \Delta$ is first calculated, where σ is the cross-section and $d \Delta$ is the thickness of the volume element as illustrated in the figure below.

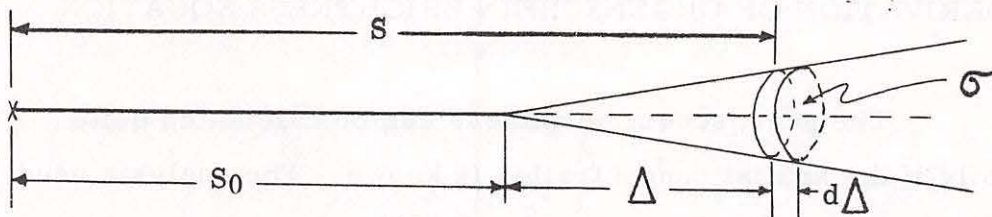


Figure G2. Volume Element for Gegenschein Brightness Calculation

If I_o is the solar intensity at 1 AU, $I_o (S/S)^2$ is the intensity at distance S from the sun. Then,

$$I_o \left(\frac{S_o}{S} \right)^2 n_a(S) \pi a^2 \sigma d \Delta$$

represents the total amount of light intercepted by particles of radius a in volume element $\sigma d \Delta$. If $j(\pi)$ is defined as the fraction of incident light scattered per unit scattering area and per unit solid angle through a scattering angle of π radians, then the irradiance at earth due to volume element $\sigma d \Delta$ is given by

$$I_o \left(\frac{S_o}{S} \right)^2 n_a(S) \pi a^2 \sigma d \Delta \frac{j(\pi)}{\Delta^2}$$

The solid angle subtended by this volume element is

$$\Omega = \frac{\sigma}{\Delta^2}$$

Dividing the intensity by the solid angle Ω gives the brightness of reflected light at earth due to the scatterers in volume element $\sigma d \Delta$. This brightness is represented by:

$$I_o \left(\frac{S_o}{S} \right)^2 n_a(S) \pi a^2 j(\pi) d\Delta.$$

Note that $d\Delta = dS$ and by integrating over all values of S greater than S_o , one obtains the irradiance per unit solid angle at earth due to all scatterers in the anti-solar direction (van de Hulst, 1947), i. e.,

$$H(\pi) = \int_{S_o}^{\infty} I_o \left(\frac{S_o}{S} \right)^2 \pi a^2 j(\pi) n_a(S) dS. \quad (G-2)$$

The brightness due to scatterers in the region bounded by S_1 and S_2 will be:

$$\begin{aligned} H(\pi) &= \int_{S_1}^{S_2} I_o \left(\frac{S_o}{S} \right)^2 \pi a^2 j(\pi) n_a(S) dS \\ &= I_o S_o^2 \pi j(\pi) a^2 n_a \left(\frac{1}{S_1} - \frac{1}{S_2} \right). \end{aligned} \quad (G-3)$$

By evaluating Equation (G-3) for all size ranges and for all helio-centric distance segments the total gegenschein brightness can be calculated.

The brightness can be stated in units of 10^{-13} times the average brightness of the sun. Since the sun subtends a solid angle of 0.22 square degrees or $0.22/(57.3)^2$ steradians, the mean brightness of the sun is given by:

$$H(\text{sun}) = \frac{I_o}{\Omega_{\text{sun}}} = I_o 1.49 \times 10^4. \quad (G-4)$$

Defining $\bar{H}(\pi)$ as the particle backscatter brightness in units of 10^{-13} times the mean solar brightness, Equation (G-3) becomes:

$$\bar{H}(\pi) = \frac{H(\pi)}{H(\text{sun})} = 6.7 \times 10^8 S_o p a^2 n_a \left(\frac{S_o}{S_1} - \frac{S_o}{S_2} \right)$$

where the geometric albedo p is defined by $p = \pi j(\pi)$.

(G-5)

APPENDIX H

CALCULATION AND TABULATION OF GEGENSCHHEIN BRIGHTNESS

The equation for the gegenschein brightness

$$\bar{H}(\pi) = 6.7 \times 10^8 S_o p a^2 n_a \left[\frac{S_o}{S_1} - \frac{S_o}{S_2} \right] \quad (\text{H-1})$$

can be written as:

$$\bar{H}(\pi) = 2.01 \times 10^6 a^2 n_a \left[\frac{1}{S_1} - \frac{1}{S_2} \right] \quad (\text{H-2})$$

using $S_o = 1.5 \times 10^{11}$ meters and assuming a geometric albedo of $p = 0.2$. Equation (H-2) is the contribution to the gegenschein brightness in units of 10^{-13} times the mean solar brightness due to a concentration n_a of particles of radius a located between the heliocentric distances of S_1 and S_2 expressed in AU.

The following steps were used to calculate a value for the gegenschein brightness:

1. Divide the pre-asteroid belt region (1-2 AU) into five equal heliocentric segments.
2. Divide the asteroid belt region (2-3.5 AU) into six equal heliocentric segments.
3. Divide the cumulative particle concentration for a heliocentric distance segment into three decades of particle size.
4. Calculate $\overline{a^2}$ for each size decade.
5. Determine n_a for each average size.
6. Calculate $\overline{a^2} n_a$ and subsequently $\bar{H}(\pi)$ for each size decade.
7. Sum the values of $\bar{H}(\pi)$ obtained in 6 to obtain the contribution to the gegenschein brightness for that helio-

centric distance segment.

8. Repeat 3 through 7 for each heliocentric distance segment.
9. Sum the contribution to $\bar{H}(\pi)$ for each segment to obtain a value for the gegenschein brightness.

The value of $\overline{a^2}$ can be calculated from the definition

$$\overline{a^2} = \frac{\int a^2 V(a) dN(a)}{\int V(a) dN(a)} \quad (\text{H-3})$$

where N is the cumulative particle concentration, and $V(a) dN(a)$ is the number of particles of size a to $a + da$ in the volume $V(a)$.

$N(a)$ and $V(a)$ can be expressed as:

$$N(a) = K a^{-\beta}$$

$$dN(a) = -\beta K a^{-\beta-1} da \quad (\text{H-4})$$

and

$$\begin{aligned} V &= \frac{\pi}{3} \alpha^2 (R^3 - R_{\min}^3) \\ &= \frac{\pi}{3} \alpha^2 C^3 (a^3 - a_{\min}^3) \end{aligned} \quad (\text{H-5})$$

where R and R_{\min} are ranges from the instrument which define the volume element and C is a constant relating the range and particle size. Equation (H-3) now becomes:

$$\begin{aligned} \bar{a}^2 &= \frac{\int a^2 a^{-\beta-1} (a^3 - a_{\min}^3) da}{\int a^{-\beta-1} (a^3 - a_{\min}^3) da} \\ &= \frac{\int a^{4-\beta} da - a_{\min}^3 \int a^{1-\beta} da}{\int a^{2-\beta} da - a_{\min}^3 \int a^{-\beta-1} da} \end{aligned} \quad (\text{H-6})$$

For the size interval a_{\max} to a_{\min} the above equation integrates to:

$$\bar{a}^2 = \frac{(5-\beta)^{-1} (a_{\max}^{5-\beta} - a_{\min}^{5-\beta}) - (2-\beta)^{-1} a_{\min}^3 (a_{\max}^{2-\beta} - a_{\min}^{2-\beta})}{(3-\beta)^{-1} (a_{\max}^{3-\beta} - a_{\min}^{3-\beta}) - \beta^{-1} a_{\min}^3 (a_{\max}^{-\beta} - a_{\min}^{-\beta})} \quad (\text{H-7})$$

where β is the slope of the cumulative spatial concentration applicable to the size regime defined by a_{\min} and a_{\max} .

Calculations of \bar{a}^2 for each of the three decades of size together with the values of n_a from Figure 34 for the corresponding \bar{a} yielded the contributions to the gegenschein brightness for each solar distance segment. The results are presented in Table H-1.

Summing the last column in Table H-1 gives a value for the gegenschein brightness of

$$\bar{H}(\pi) = 8.87 \times 10^{-13} \text{ solar brightness units.}$$

In order to readily compare this value to other measurements it must be converted to the equivalent number of tenth magnitude stars per square degree. Thus, we have

$$\bar{H}(\pi) = \frac{8.87 \times 10^{-13} I_o}{I(10) \times \Omega(\text{sun})} \quad (\text{H-8})$$

where

$$I_o - \text{solar bolometric irradiance} = 0.14 \text{ watts/cm}^2$$

(Allen, 1963)

TABLE H-1

GEGENSCHEIN BRIGHTNESS AS A FUNCTION OF HELIOCENTRIC
DISTANCE

S_1	S_2	$N(a) a^2$	$\Delta \bar{H} (\pi)$
1.0	1.2	6.22×10^{-19}	2.09×10^{-13}
1.2	1.4	9.97×10^{-19}	2.39×10^{-13}
1.4	1.6	3.51×10^{-19}	6.32×10^{-14}
1.6	1.8	4.17×10^{-19}	5.84×10^{-14}
1.8	2.0	6.63×10^{-19}	7.43×10^{-14}
2.0	2.25	6.34×10^{-19}	7.10×10^{-14}
2.25	2.50	5.50×10^{-19}	4.92×10^{-14}
2.50	2.75	5.70×10^{-19}	4.17×10^{-14}
2.75	3.00	6.87×10^{-19}	4.19×10^{-14}
3.00	3.25	5.08×10^{-19}	2.62×10^{-14}
3.25	3.5	3.03×10^{-19}	1.34×10^{-14}
			$\Sigma \Delta \bar{H} (\pi) = 8.87 \times 10^{-13}$

$I(10)$ - bolometric irradiance of tenth magnitude star
= 2.27×10^{-16} watts/cm² (Allen, 1964)

Ω - solid angle subtended by the sun = 0.22 square
degrees

Substituting these values in Equation (H-8) gives:

$\bar{H}(\pi) = 2487$ tenth magnitude stars per square degree.

APPENDIX I

LIST OF SYMBOLS

- a - particle radius
- $f(\gamma)$ - phase function relating radiation incident on a particle to that reflected at an angle γ
- g - absolute magnitude of an object
- H - gegenschein brightness per unit solid angle
- I - intensity of reflected sunlight incident on optical sensors
- I_o - solar irradiance at 1 astronomical unit
- I_{min} - minimum irradiance detectable by the sensor
- m - particle mass
- N - cumulative particle concentration/unit volume
- p - geometric albedo
- r - bond albedo
- R - distance from particle to optical sensor
- S - distance from the sun
- S_o - distance from the earth to the sun
- T - observation time of sensor
- v - velocity of particle
- V - sensitive volume for particle detection
- α - telescope field-of-view half angle
- β - exponent relating particle size to concentration, i. e.,
$$N \sim a^{-\beta}$$

- γ - angle between direction of incident radiation and direction of reflected radiation
- ρ - particle density
- $\bar{\tau}$ - average transit time of a particle passage through the sensor field-of-view
- Φ - cumulative flux in particles/unit area/sec

APPENDIX J

PUBLICATIONS OF AMD RESULTS

May, 1973

Paper C.3.7
COSPAR Meeting XVI
Konstanz, Germany

The Radial Dependence of the Zodiacal Light. ZOOK, H. A. (NASA Johnson Space Center, Houston, Texas, USA), SOBERMAN, R. K. (General Electric Space Sciences Laboratory and Drexel University, Philadelphia, Pennsylvania, USA).

ABSTRACT

The Asteroid/Meteoroid Detector (Sisyphus) has, in addition to its primary role of detecting and analyzing individual meteoroids, been measuring the brightness of the night sky from its platform on board the Pioneer 10 spacecraft. This spacecraft has traversed the asteroid belt and will fly by Jupiter in December 1973. It was quickly found that the brightness of the night sky in the antisolar hemisphere, decreased rapidly with increasing distance from the sun. This decrease is due solely to the decrease in the brightness of the zodiacal light. The heliocentric dependence of the zodiacal light is deduced from several months of data and is presented. Some raw data is shown to illustrate the sensitivity of the instrument to features in the night sky and the technique used for subtracting out the integrated brightness due to starlight is presented. Preliminary results showing the decrease of the zodiacal light with solar distance are not inconsistent with an inverse square dependence.

I. INTRODUCTION

On March 2, 1972, the Pioneer 10 spacecraft was launched on an interplanetary trajectory to fly by Jupiter on December 4, 1973. During the interplanetary cruise portion of its journey, it traversed the asteroid belt during the latter half of 1972 and early portion of 1973. Among the experiments carried by Pioneer 10 is the Asteroid/Meteoroid Detector or Sisyphus. The Sisyphus instrument collects two types of data. The first deals with the individual particles passing through the fields of view in the vicinity of the spacecraft. The data from this portion of the experiment is treated in a separate paper (Neste and Soberman, 1973). The instrument is also designed to perform photometric mapping of the sky background. The objective of this latter portion of the experiment is to measure the radial dependence of the zodiacal light as the spacecraft traverses the region from 1 to 5 AU.

The Sisyphus sensors consist of four 20 cm F 1.0 Ritchey-Cretien telescopes mounted with their optical axes approximately parallel. A photograph of the sensors is shown in Figure 1. In this figure, one can also see the light shield that surrounds the four telescopes. The primary purpose of this light shield was to protect the telescopes from sunlight reflected or scattered from the spacecraft. The telescopes each have a 7.5° full field of view and are mounted to view the sky at an angle of 45° to the spin axis of the spacecraft. Located in the telescope focal plane (focussed for infinity) is a 2.705 cm diameter field stop. The photomultiplier tube, an RCA 7151Q with an S20 photocathode,

is located approximately 2 cm behind the field stop. This placement defocusses regions in the focal plane to minimize the effect of variations in photocathode sensitivity. To avoid light loss between the focal plane and photomultiplier, a gold coated reflecting cylinder surrounds the intervening space. The lightweight primary and secondary mirrors of the telescope are also coated with electrodeposited gold.

As the spacecraft rotates at a rate of approximately 4.8 revolutions per minute, the four telescopes view an annular region of the celestial sphere. A spoke wheel generator divides the rotation cycle into 128 sectors. In a semi-random fashion, photometric data from each of the four telescopes as a function of rotation sector is telemetered from the spacecraft. From this data, photometric maps of the viewed annulus can be prepared. The spacecraft spin axis, through the center of the high gain antenna, remains approximately earth pointing throughout the mission. Thus, the viewed annulus moves across the celestial sphere during the course of the interplanetary cruise. While this yields the possibility of mapping a zone approximately 90° wide and 210° long (approximately 45° above and below the ecliptic plane), there is the disadvantage that only a limited number of points on the celestial sphere can be viewed at different heliocentric distances.

II. PRIMARY DATA

In Figure 2, we show the photometric data for one day. The instrument response, as a function of rotation sector number, is shown for all four telescopes. These data were obtained on July 3, 1972. The spread of experimental points obtained from multiple readings in the same sectors can be seen in the figure. Photometric contributions include light from the sky background within the field of view, light from those portions of the sky which directly illuminate the field stop, and scattered sunlight leaking through and around the light shield. On this date, the spacecraft spin axis was pointed approximately 23° from the sun and thus the sun could illuminate the light shield directly during a portion of the rotation cycle. On July 3, 1972, the spacecraft was located approximately 1.9 AU from the sun.

To analyze the photometric data it is first necessary to separate the three components listed above. This was first done by a detailed mapping of the out-of-field illumination of each of the four telescopes. Portions of the rotation cycle where the light shield is illuminated directly by the sun are discarded. Fortunately, during most of the interplanetary cruise, the instrument remains entirely within the shadow of the high gain antenna.

The extra-terrestrial sky brightness is composed of starlight (including diffuse faint stellar sources), diffuse galactic light, cosmic light, and the zodiacal light. Only the zodiacal light should vary within the solar system. In Figure 3, we show a flow chart which depicts how the sky background photometric data is separated into zodiacal light and the solar system invariant remainder.

III. SISYPHUS STELLAR BRIGHTNESS ANALYSIS

This section describes how the expected response of the Sisyphus instrument to the published star backgrounds is calculated. The two sources used for the star backgrounds are the Smithsonian Astrophysical Observatory (SAO) Star Catalogue (1967) for stars brighter than 8th magnitude and the Roach and Megill (1961) analysis for stars of higher magnitude.

Because Sisyphus responds to a broad band of wavelengths centered in the visible, it is not correct to assume that it will respond similarly to all stars of the same visual or photographic magnitude. This is because stars have different radiation curves (due primarily to intrinsically different temperatures or to reddening by interstellar dust). Figure 4 illustrates the Sisyphus optical response to direct light (i. e., light that enters the aperture plane via the primary and secondary mirror system) and a stellar radiation curve reddened by interstellar dust. Below we present an outline of the sequence of events to obtain the relative Sisyphus response to a star.

- A. SAO catalogue lists M_{PV} (photovisual magnitude) M_{PH} (photographic magnitude), and spectral type, if they are all known, for each star.
- B. Knowing the spectral type of a star implies that we know its effective stellar temperature, T_e (we assume a blackbody approximation which does not fit some stars very well).
- C. Using T_e , we calculate the intrinsic radiation distribution curve $I_I(\lambda, T_e)$ using the blackbody approximation.
- D. From $I_I(\lambda, T_e)$, we can deduce the intrinsic color index $C_I = (M_{PH} - M_{PV})_I$. An unreddened A_0 star is assumed to have zero for an intrinsic color index.
- E. The apparent color index $C_{APP} = (M_{PH} - M_{PV})$ is obtained from the information in the SAO catalogue.
- F. Hence, the color index $C_R = C_{APP} - C_I$ which is due to interstellar reddening is obtained.
- G. C_R together with $I_I(\lambda, T_e)$ gives the observed (or apparent) spectral distribution of the stars as $I_{APP}(\lambda) = R(\lambda) I_I(\lambda, T_e)$ where $R(\lambda) = 10^{-K/\lambda}$ and where $C_R = 2.5 \left(\frac{1}{\lambda_{PV}} - \frac{1}{\lambda_{PH}} \right)$. $R(\lambda)$ is the reddening factor.
- H. Intersect the Sisyphus response curve $S(\lambda)$ (determined experimentally) with 48 different types of apparent spectral distributions defined by 6 different amounts of reddening and 8 different effective temperatures. This creates a table of

Table 1. The Sisyphus Response Curve Intersected With the Radiation Distribution Curve For 48 Different Combinations of Spectral Types and Interstellar Reddening Coefficients, C_R .

Temp. ($^{\circ}$ K) (Spec. Type) C_R	2700 (M8)	5120 (K0)	6000 (G0)	8700 (A5)	11,000 (A0)	15,600 (B5)	25,000 (B0)	50,000 (05)
0.0	.324	.210	.206	.207	.213	.224	.236	.247
0.5	.419	.237	.224	.209	.207	.206	.208	.211
1.0	.562	.285	.263	.234	.224	.217	.213	.210
1.5	.777	.361	.327	.280	.264	.249	.239	.233
2.0	1.101	.475	.423	.352	.327	.305	.289	.278
2.5	1.596	.646	.569	.462	.424	.390	.366	.349

values for the Sisyphus response to different stellar spectral types and different interstellar dust reddenings (See Table 1).

- I. For any SAO star, the computer analysis program interpolates the reddening of the star and its effective temperature between values in the table and extracts an interpolated intersection response. This intersection response is then multiplied by the photovisual intensity of the star to obtain the Sisyphus response to the star.

If the photographic or the photovisual magnitude or the spectral type of the star is not given in the SAO star catalogue then it is assumed that the star has not been reddened by interstellar dust and only a blackbody curve is used. If only M_{PV} or M_{PH} is known for the star and nothing else, the star is assumed to be of type K 0, as this is the most common type of star in the catalogue.

The Roach and Megill (1961) analysis is used in the present calculations in the following way: We used only the star contributions from stars dimmer than 8th magnitude (they analyzed stars between 6th and 18th magnitude) and used their extrapolation curve to estimate the numbers of stars with apparent photographic magnitudes greater than 18th magnitude. We also used their suggested color index $C_R = 0.16 + 0.05 M_{PH}$. This color index has a significant but not drastic effect on the results. For example, at $M_{PH} = 20$ (corresponding to $M_V = 18.84$) the Sisyphus intersection value from Table 1 is approximately 0.24 (the Roach and Megill stars were all assumed to be type G 0 and reddened by dust). This is a reasonable modification to the unreddened value of 0.206.

As we shall note later, there appear to be some significant discrepancies between our calculated stellar background from the Roach and Megill data and that which is actually measured by our instrument. The authors of that paper were well aware of possible disagreements of their data with other types of analyses and, in particular, noted differences between their results and the photometric results of Elsasser and Haug (1960).

IV. INDIRECT LIGHT

The photomultiplier used in each telescope not only receives light via the primary optical system but also responds to all light entering the aperture in front of the photomultiplier tube. Light entering by the first route will be called "direct" light and that by the second path "indirect" light.

Although the collecting efficiency per unit solid angle for direct light is from 40 to over 100 times greater than that for indirect light, the collecting solid angle of 44.2 deg² for direct light is less by a similar factor. Also, the intensity of the light received indirectly by the photomultiplier tubes has not been reduced by partial absorption of the shorter wavelengths as they reflect off of the primary and secondary gold-coated mirrors.

To somewhat counterbalance this latter effect, the indirect light usually does reflect one or more times off of the gold collimator sleeve located between the aperture and the photomultiplier tube.

The indirect star background is calculated in nearly the same way as the direct star background. The difference is due to the response curve for the photomultiplier alone which is significantly different from that for the photomultiplier with two gold reflections. In short, a new table, similar to Table 1, is constructed in which the photomultiplier response curve (without gold reflection) is intersected with various stellar distributions. Each light ray is then reduced by an average gold absorptivity (wavelength independent) for each reflection it makes with the gold collimator.

The amount of indirect starlight received is then calculated to 3 significant figures after an exact accounting has been taken of the shielding afforded by the instrument light shield, the respective secondary mirrors, and the struts supporting the secondary mirrors. The result is that, for a uniform sky, about 65% of the light would come into telescopes #1 and #4 by the indirect route (35% via direct). For telescopes #2 and #3 the percentage of light arriving indirectly from a uniform sky is about 75%.

Figure 5a shows the calculated contributions to direct light for the SAO stars alone (lower curve) and for the sum of the Roach and Megill and the SAO stars (upper curve) for May 29, 1972. In Figure 5b, the calculated total response of telescope #1 is plotted in the upper curve. The lower curve plots that portion of the starlight that we calculate to enter indirectly. The difference between the two curves is exactly equal to the SAO and Roach and Megill contributions (the upper curve in Figure 5a).

V. THE SEPARATION OF THE BACKGROUND LIGHT COMPONENTS

In Figure 6 is shown the experimental data obtained by telescope #1 and the star background as calculated for this telescope for May 28, 1972. On that day, the spacecraft was about 1.57 AU from the sun. The ordinate is in instrument output units and the abscissa is in degrees of rotation (or clock angle) of our experiment about the spacecraft spin axis. The zero degree point is when the instrument passes north through the ecliptic plane. Apparent in the figure are Arcturus ($M_{PV} \approx 0$) at 55° , Jupiter at 175° and a peak where the pointing axis of the instrument crosses the south galactic plane near the constellation Centaurus at about 280° clock angle. We note that the peak is much smaller experimentally than it was calculated to be from the star catalogues. This indicates that either the SAO catalogue or the Roach and Megill analysis has produced too great a brightness for this portion of the sky. From Figure 5, we see that the Roach and Megill analysis contributes considerably more to this portion of the sky than does the SAO catalogue. Also, Elsasser and Haug disagree most strongly with Roach and Megill in this portion of the sky. In short, it becomes clear that the stellar background maps need to be corrected.

An error in the calculated sky background at one point leads to errors at other points. For example, if a variance exists as seen by a telescope in its direct field-of-

view, the indirect field-of-view will also give incorrect values when that part of the sky comes into the indirect field (normally about 30 degrees of clock angle before and after it enters the direct field-of-view). The error so propagated will be clock angle dependent. Note that if a single star is in error, this has little effect on the indirect light. Even Jupiter does not show up in the indirect field, although it could cause the output count to change by, perhaps, one unit. Errors show up in the indirect light when large regions are not correctly catalogued (as appears to be the case when the south galactic plane is crossed). Note also in Figure 6 that Jupiter is not as high experimentally as it is theoretically. This is a designed instrumental effect. The ordinate is linear with respect to incoming light to about 40 units (depending upon the preamplifier temperature) and then becomes nonlinear at higher light levels to compress the high amplitude data.

Figure 7 illustrates the results of subtracting the calculated star backgrounds from the total Sisyphus response as a function of distance from the sun. In Figures 7a and 7c, a clock angle of 0° was chosen for telescopes 1 and 3. In Figures 7b and 7d, a clock angle of 50° was chosen for the same telescopes. The constants were chosen as described in Figure 3 (i. e., to make all of the light equal starlight as nearly as possible at large distances from the sun). Once a constant is chosen for a telescope, it is maintained for all clock angles at all distances from the sun. The different curves shown are preliminary attempts to fit the data.

In general, it can be seen that the zodiacal light goes to zero within our instrument resolution between 3 and 4 AU from the sun. However, in order to deduce the spatial density of particles, as a function of distance from the sun, it is necessary to calculate very precisely the behavior of these zodiacal light curves. As a minimum, the second derivatives of these curves must be well determined. The latitude dependence must also be determined.

Because of the uncertainties in the stellar backgrounds derived from SAO and Roach and Megill, we are not at present able to reliably derive the radial or latitudinal distributions of the particles responsible for the zodiacal light. However, after these catalogues are adjusted to fit the sky as seen by Sisyphus we should be able to determine the zodiacal light brightness radially out from 1 AU to an accuracy of approximately 5% of its value at 1 AU.

With the present data, we are able to calculate a weighted average for the zodiacal light brightness at any heliocentric distance traversed by the spacecraft. This is crudely calibrated by comparison with Arcturus as it was measured in the direct field-of-view of the instrument. In telescope #1, Arcturus raises the light level by $7\frac{1}{2}$ units and in telescope #3 by $9\frac{1}{2}$ units. Extrapolating Figure 7 back to 1 AU, we find that telescope #1 indicates about 8 units of zodiacal light, while telescope #3 yields 17 units. Taking into account the different indirect fields-of-view and assuming Arcturus to be of magnitude 0 (no color correction), gives a weighted average for the zodiacal brightness of approximately $90 S_{10}$ units at 1 AU.

VI. CONCLUSIONS

From the foregoing, it should be clear that, beyond the extensive effort already expended, a large amount of work remains to be performed on the Pioneer 10 sky background analysis. The data and the techniques we are applying to the analysis of the data gives us confidence that we will be able to deduce in reasonably precise form, the radial distribution of the zodiacal light and consequently the spatial concentration of the zodiacal dust. We believe that the uncertainties in the existing star brightness catalogues remain as our largest problem, but the data now being obtained beyond 4 astronomical units will enable us to provide the proper corrections. Variation in solar elongation angle for a given spacecraft reference angle must be examined in greater detail to determine how much this influences our determinations on both the average zodiacal brightness and the elongation angle dependence at a given radial distance. Preliminary estimates indicate that this is a comparatively small correction to the average brightness.

Our results to date indicate that the zodiacal light drops below the sensitivity of our instrument between 3 and 4 astronomical units. Early estimates place the Sisyphus sky background uncertainty limit at about $10 S_{10}$ units. As we showed above, the zodiacal brightness as measured by this instrument at 1 AU was approximately $90 S_{10}$ units. Thus, our preliminary results are not inconsistent with a gross inverse square fall off with heliocentric distance. Further efforts with the Pioneer 10 and now the Pioneer 11 Sisyphus data should result in a precise definition of this radial dependence.

REFERENCES

1. Haramundanis, K. L., "SAO Star Catalogue" (Smithsonian Institution Astrophysical Observatory June 1967).
2. Roach, F. E. and Megill, L. R., "Integrated Starlight Over the Sky", *Ap. J.* 133, 228 (1961).
3. Neste, S. L. and Soberman, R. K., "Results of the Asteroid/Meteoroid Particle Experiment on Pioneer 10 (1.0 - 3.2 AU)", presented at the XVI COSPAR Meeting (Konstanz, Germany, May 1973).
4. Elsasser, H. and Haug, U., *Zs. f. Ap.*, 50, 121 (1960).

ACKNOWLEDGEMENT

The authors gratefully acknowledge the cooperation and assistance of the personnel of the Pioneer Project Office, National Aeronautics and Space Administration/Ames Research Center without which this effort would not have been possible.

This work was supported in its entirety by the National Aeronautics and Space Administration, partially under contract number NAS 2-6559.

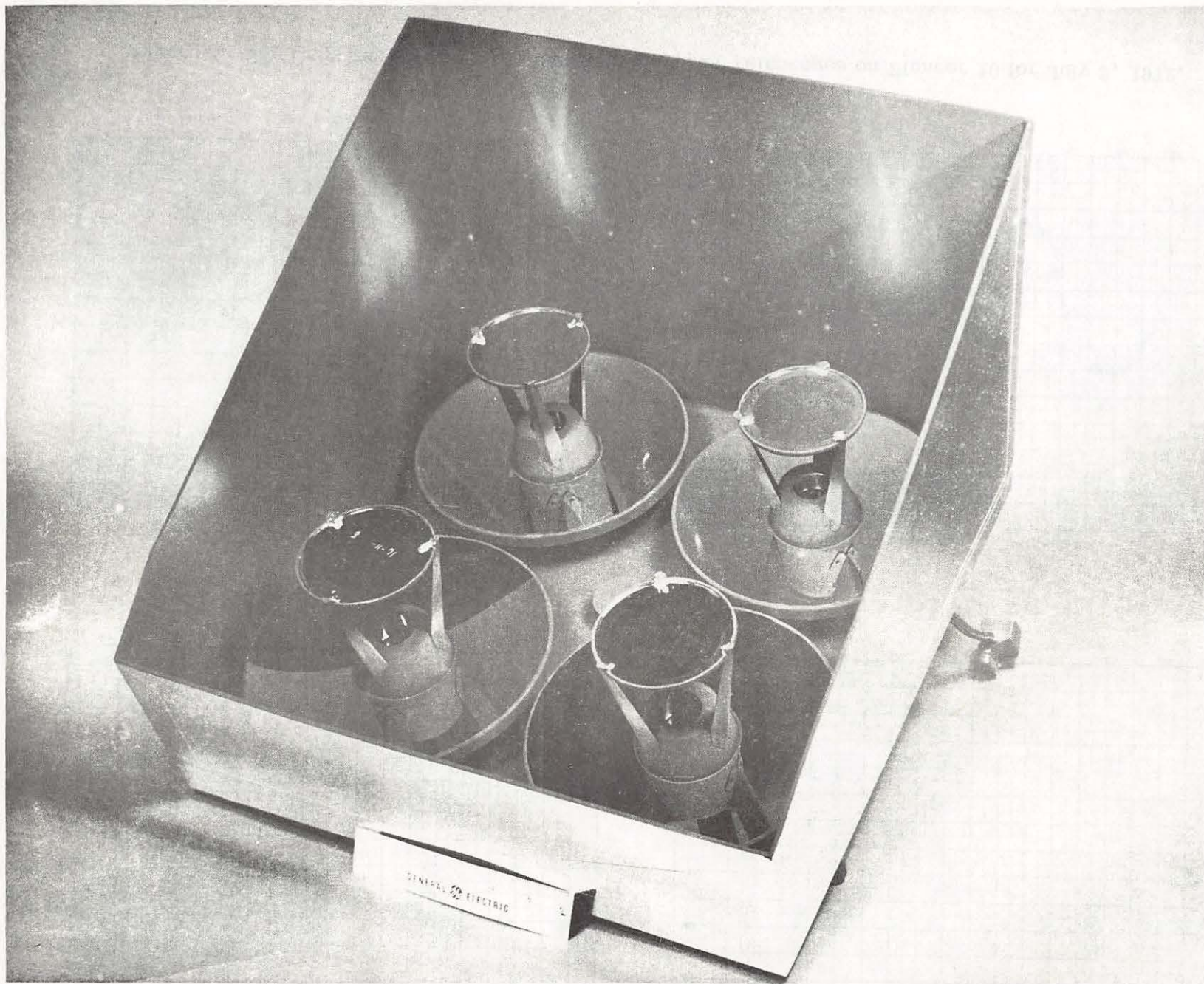


Figure 1. Photograph of the Sisyphus Telescope Assembly Showing Light Shield and Indirect Light Path to Photomultipliers.

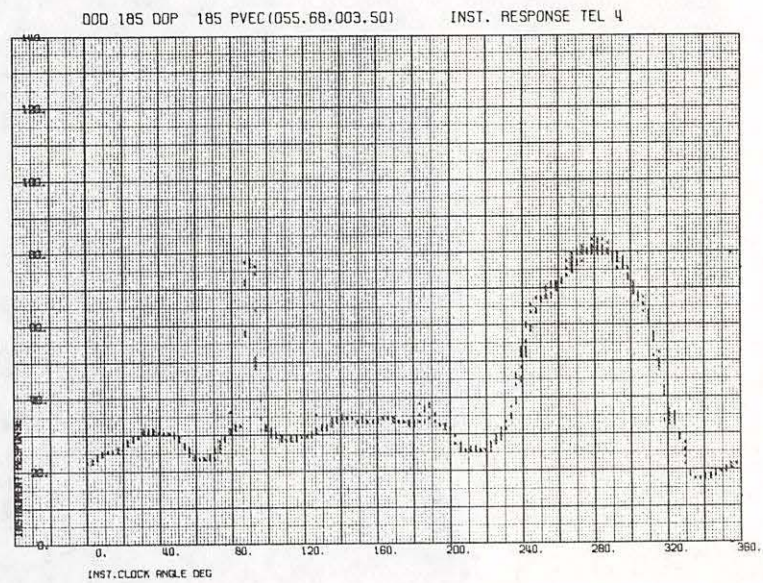
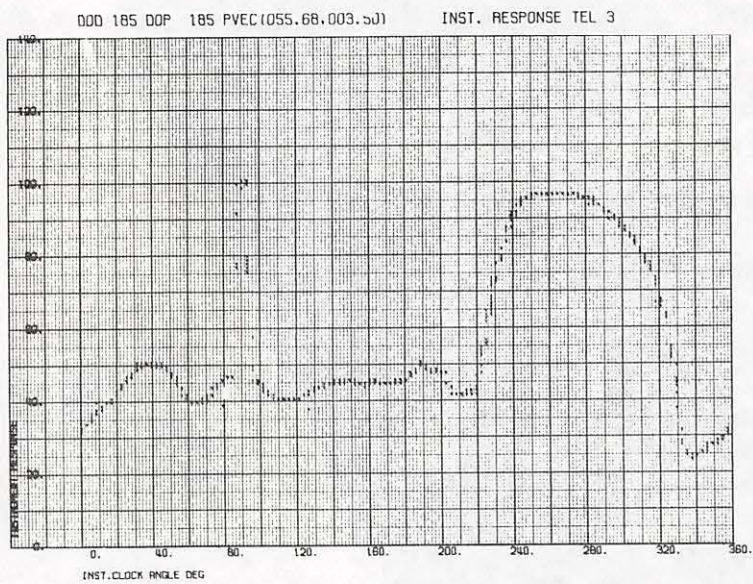
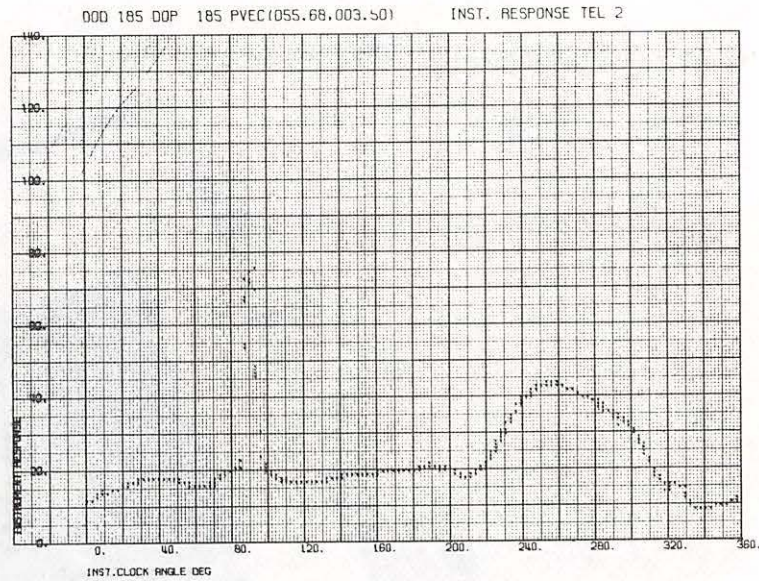
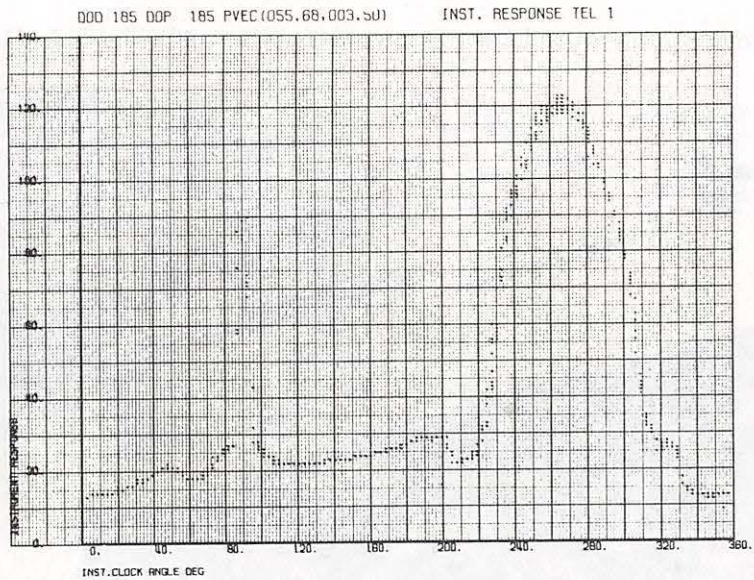
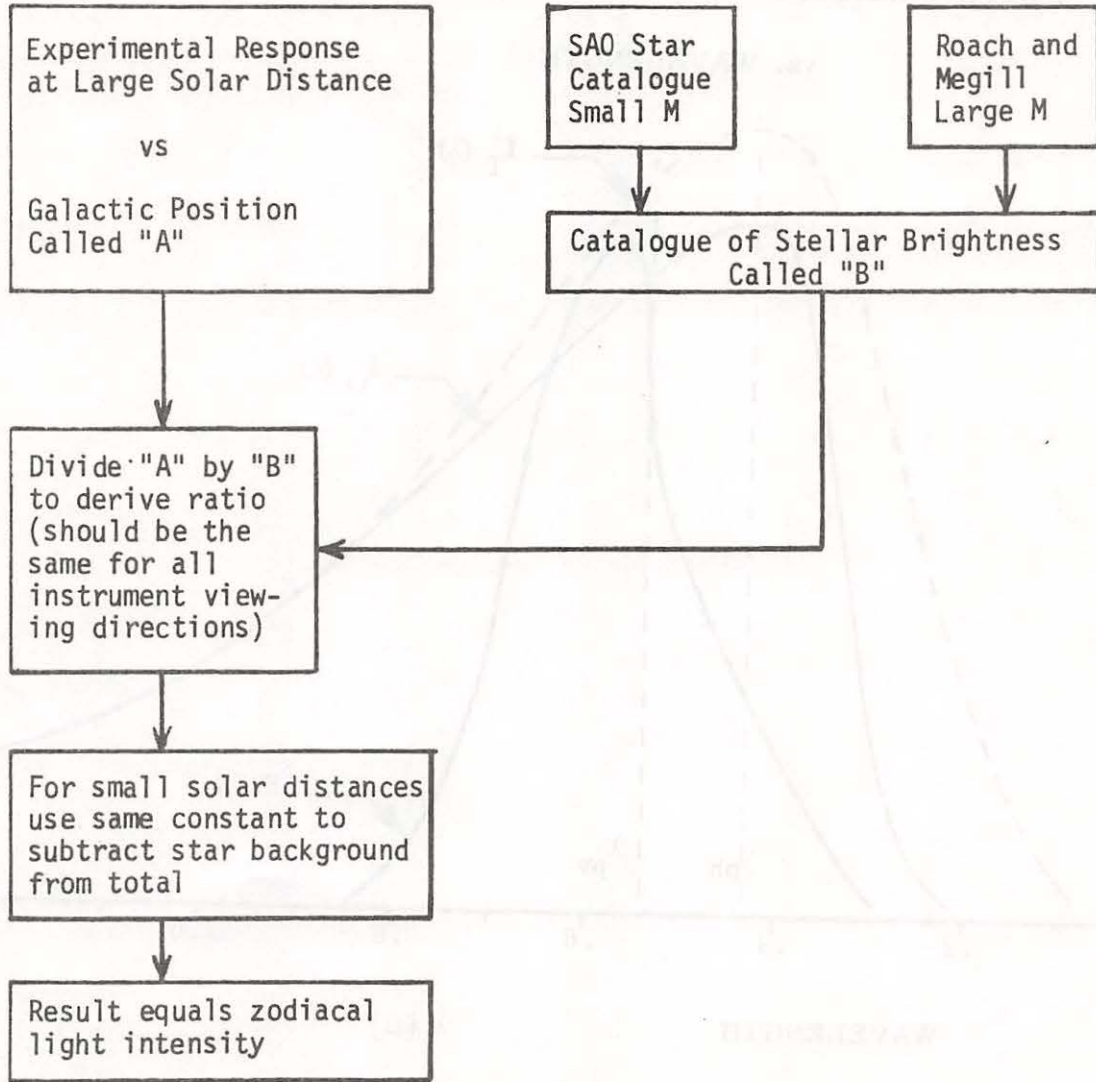


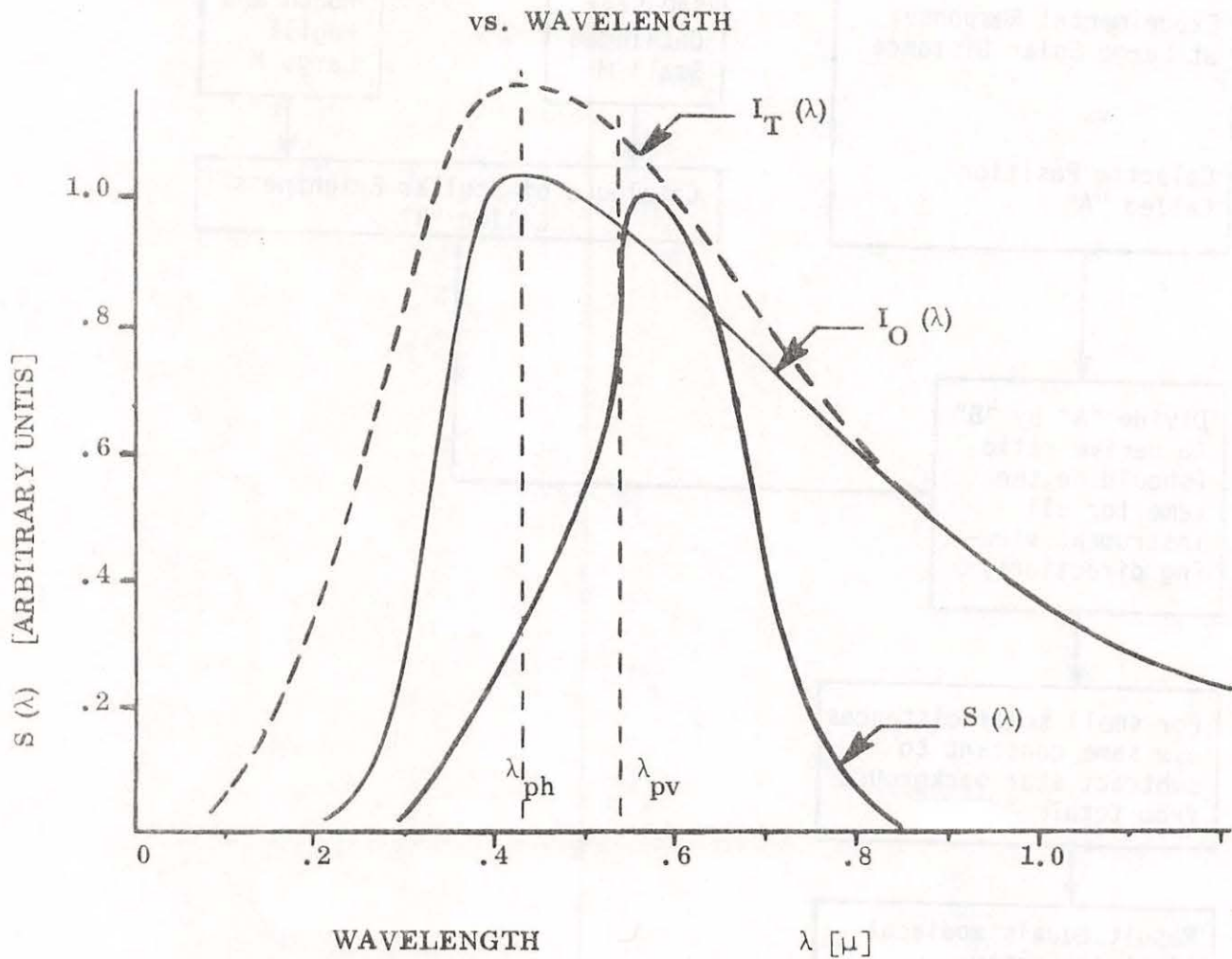
Figure 2. Sky Brightness Data From the Four Sisyphus Telescopes on Pioneer 10 for July 3, 1972.

Figure 3. Data Reduction Flow Chart



Problem: Uncertainties in the existing star catalogues need to be resolved and corrected.

SISYPHUS RESPONSE AND STELLAR BRIGHTNESS



$I_T(\lambda)$ = True (or intrinsic) energy distribution for a star at temperature T

$I_O(\lambda)$ = Observed (or apparent) energy distribution

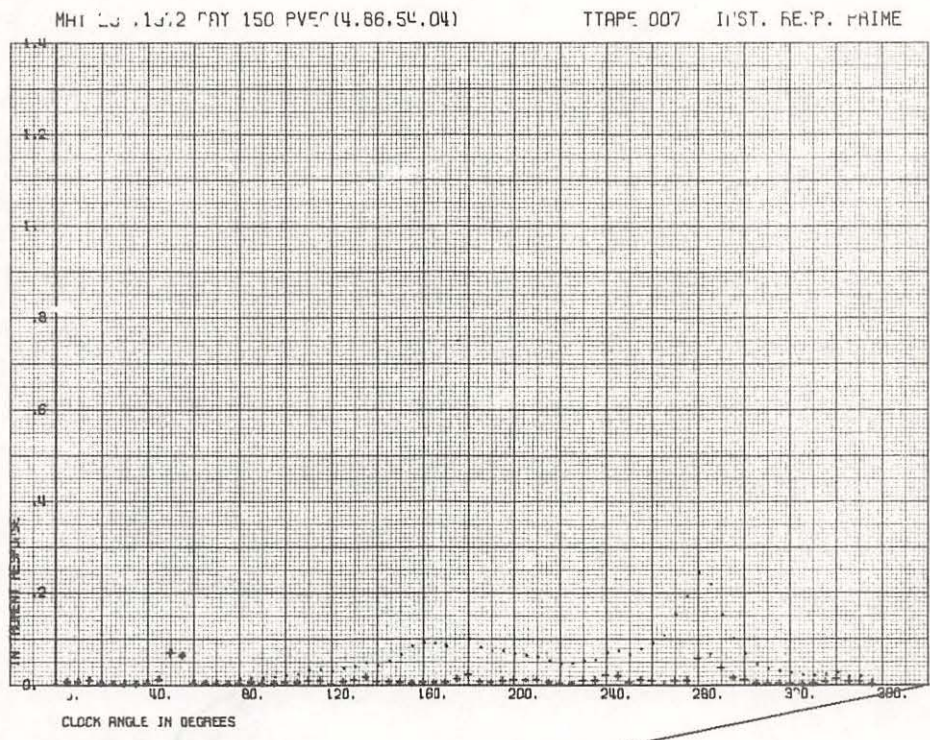
$S(\lambda)$ = Instrument response curve

λ_{pv} $\hat{=}$ 5400 Å = effective wavelength at which photovisual magnitude is measured

λ_{ph} $\hat{=}$ 4300 Å = effective wavelength at which photographic (or blue) magnitude is measured

Figure 4

(A)



(B)

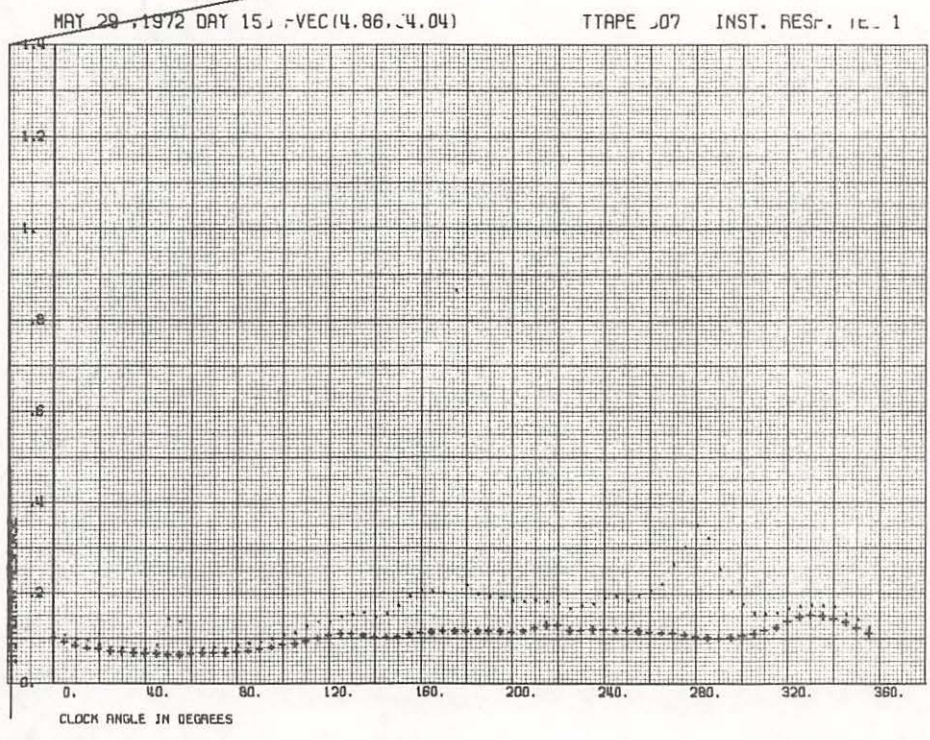


Figure 5. (a) Calculated contributions to direct light from SAO star catalogue alone (lower points) and for the sum of the Roach and Megill and SAO catalogues (upper points) for May 29, 1972. (b) Calculated response of telescope #1 for May 29, 1972 from indirect light (lower points) and the sum of direct and indirect light (upper points).

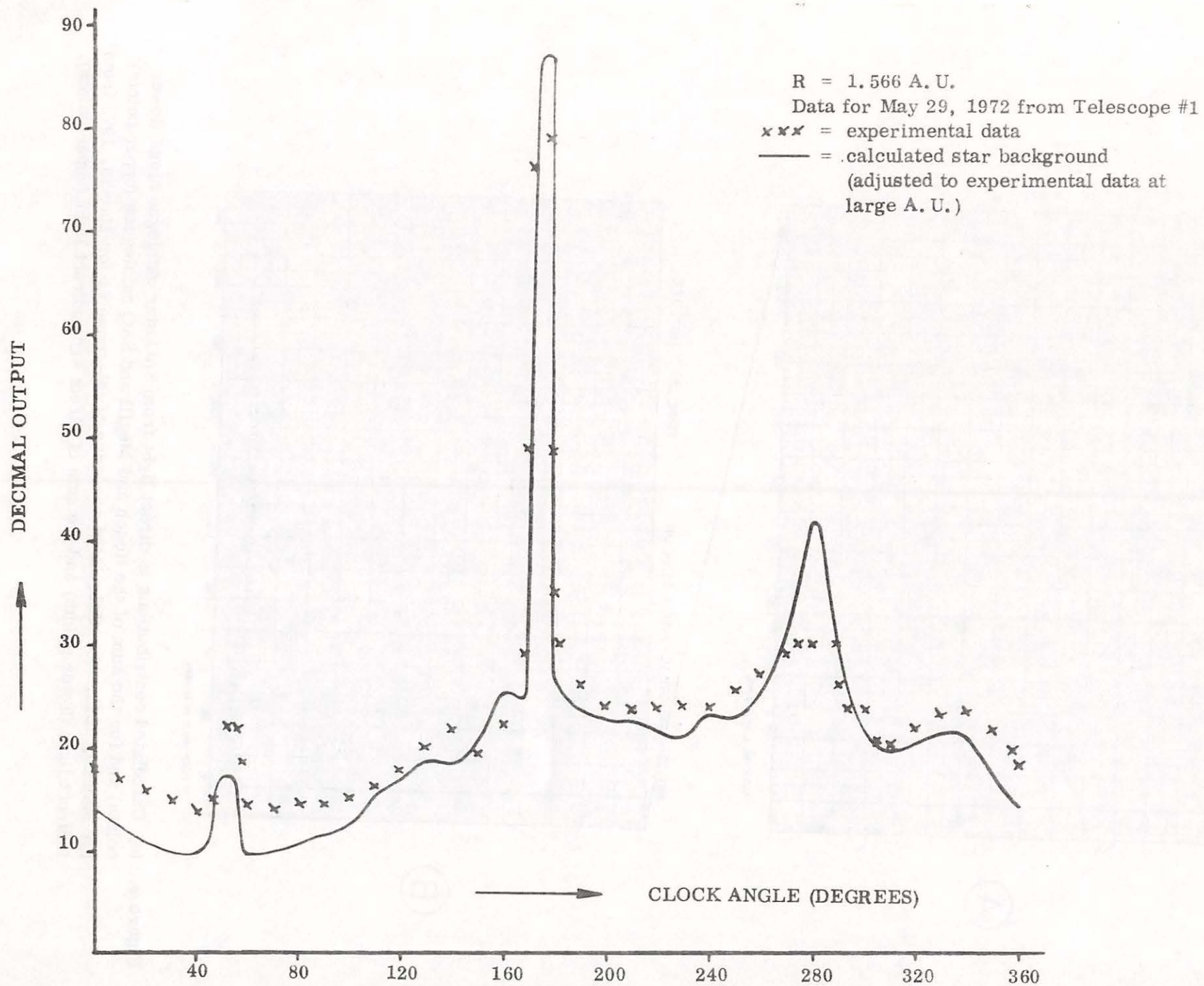


Figure 6

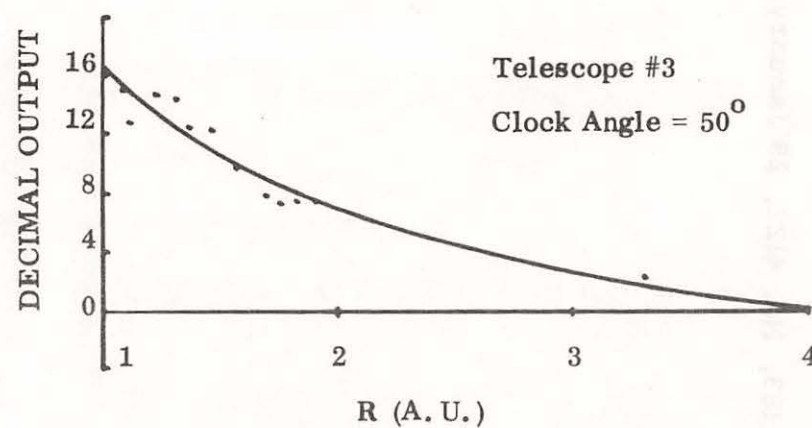
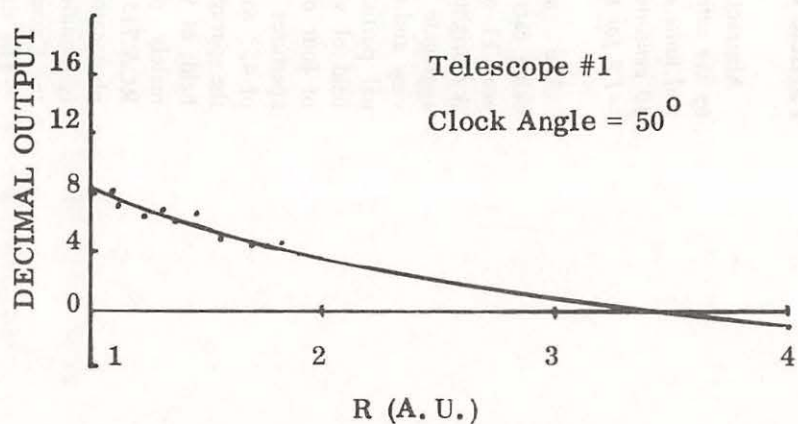
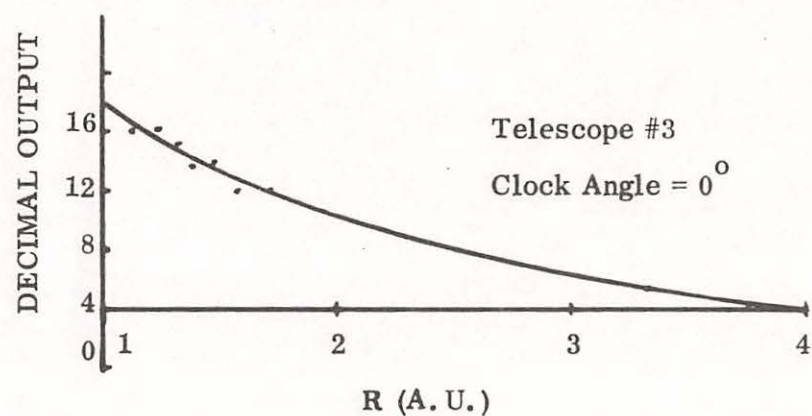
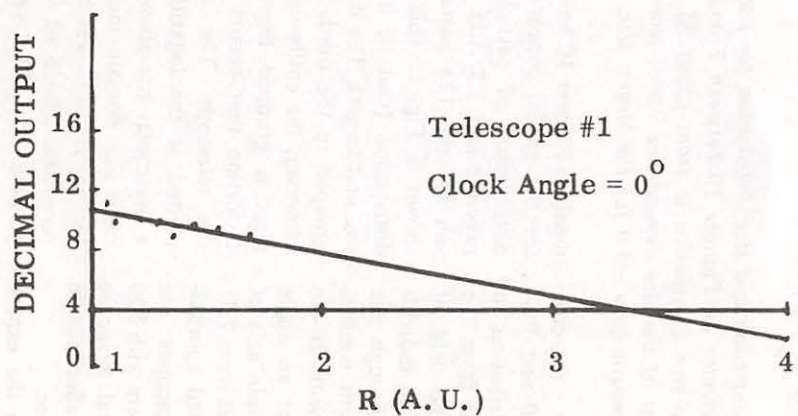


Figure 7. Weighted average for Zodiacal Brightness versus Heliocentric Distance with preliminary attempts at curve fitting.

Particle Concentration in the Asteroid Belt from Pioneer 10

Abstract. The spatial concentration and size distribution for particles measured by the asteroid/meteoroid detector on Pioneer 10 between 2 and 3.5 astronomical units are presented. The size distribution is from about 35 micrometers to 10 centimeters. The exponent of the size dependence varies from approximately -1.7 for the smallest to approximately -3.0 for the largest size measured.

The asteroid/meteoroid detector being carried on Pioneer 10 and Pioneer 11 measures the contribution to sky brightness in white light from the aggregate of particles in the field of view and the light from bright individual particles which pass through the field of view. The instrument consists of four optical telescopes with 20-cm apertures which look out at an angle of 45° with respect to the spin axis of the spacecraft. The telescopes have 7.5° fields of view and are aligned approximately parallel. The telescopes use RCA 7151 Q photomultipliers with S20 photocathodes. The spectral response is modified by two gold reflections in the Cassegrain-type telescope.

The data obtained from the experi-

ment on Pioneer 10 have been analyzed for the spatial concentration and size distributions of particles observed between 2 and 3.5 A.U. An average result for the 123 particles observed is shown in Fig. 1. This is a cumulative distribution (that is, it is for a given size and larger). The data are generally grouped in the thirds of size decades. However, the entire decade of smallest sizes is grouped together due to the distortion that occurs within 10 m of the telescope. The data points are plotted at the logarithmic mean with a horizontal bar showing the approximate size domain included. Following Dohnanyi (1) we have assumed a geometric albedo of 0.2 to derive the particle size. The vertical bars were

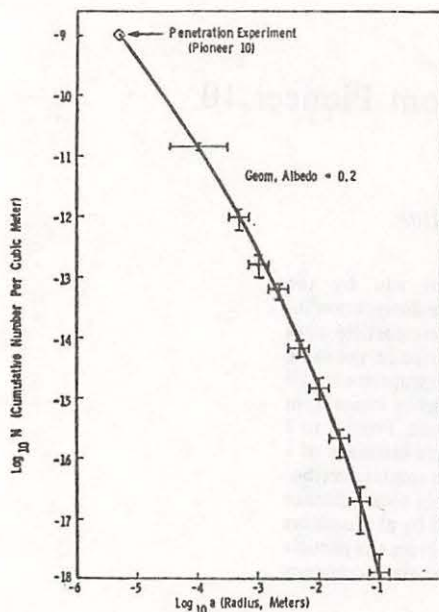


Fig. 1. Particle size distribution in the asteroid belt (2 to 3.5 A.U.).

derived by making the assumption that the uncertainty was proportional to the square root of the number of particles observed multiplied by the average transit time through the field of view. The particles were assumed to be traveling in direct circular orbits with no inclination. For a distribution function of the form $N \sim a^{-\beta}$, the value of β varies from about 1.7 for the smallest to about 3 for the largest size measured. We have also plotted in Fig. 1 the point obtained by the meteoroid detector (penetration experiment) on Pioneer 10 (2).

To illustrate the change in size distribution we combined the data into decades of size for solar distance increments of 1/4 A.U. This is shown in the histograms of Fig. 2. Since the changes in size distribution that were noted in the data as the region from 2 to 3.5 A.U. was transited are not appreciable on the logarithmic scale used in Fig. 1, they are shown in the histograms of Fig. 2. The particle size domains are shown with each histogram. We have shown the number of events in each bar to give an idea of the statistical uncertainty; this shows why it was necessary to combine data into larger size groupings. Note that the ordinates on these histograms are linear and are expressed in mass per unit volume, which is more meaningful for such a large range of sizes. We assumed a density of 3 g/cm³ for the conversion. From Fig. 2 it can be seen

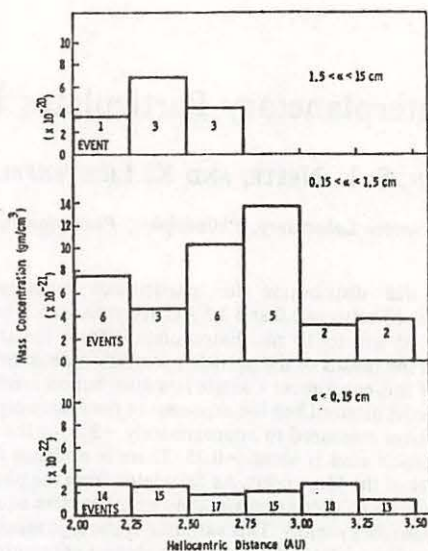


Fig. 2. Mass concentration for three ranges of particle radius.

that the largest sizes were observed in the region from 2 to 3.0 A.U., with an apparent peak at the heliocentric distance where the visible asteroids are most heavily concentrated. The inter-

mediate sizes appear to show the greatest concentration at a somewhat larger solar distance. The change in concentration of the smallest sizes is only a factor of 2 and one can easily conclude a distribution which does not vary with solar distance. The latter is in agreement with the results of the penetration measurement on Pioneer 10 (2).

R. K. SOBERMAN

S. L. NESTE

K. LICHTENFELD

General Electric Space Science
Laboratory, Philadelphia, Pennsylvania

References and Notes

1. J. S. Dohnanyi, in *Physical Studies of Minor Planets*, T. Geherls, Ed. (NASA SP-267, National Aeronautics and Space Administration, Washington, D.C., 1971), pp. 263-295.
2. W. H. Kinard, R. L. O'Neal, J. M. Alvarez, D. H. Humes, "Pioneer 10 meteoroid penetration data," paper presented at the 16th Plenary Meeting of the Committee on Space Research (COSPAR), Konstanz, Germany, 1973.
3. Supported by NASA contract NAS 2-6559. We would like to express our deep appreciation to the personnel of the Pioneer Project Office, NASA Ames Research Center, for their outstanding work with the Pioneer 10 spacecraft and their unstinting cooperation with the investigators to maximize the scientific yield from this historic mission.

21 December 1973

Optical Measurement of Interplanetary Particulates From Pioneer 10

R. K. SOBERMAN, S. L. NESTE, AND K. LICHTENFELD

General Electric Space Sciences Laboratory, Philadelphia, Pennsylvania 19101

The spatial concentration and size distribution for particulates measured in situ by the asteroid/meteoroid detector on Pioneer 10 between 1.0 and 3.5 AU are presented. The size distribution includes particles of radii from about 35 μm to 10 cm. Extrapolation from the smallest particle sizes measured shows good agreement with the results of the particle penetration detector carried on the same spacecraft. Within the uncertainties of this experiment a single size distribution seems appropriate for all but the smallest particles measured. In the asteroid belt the exponent of the radius dependency varies from approximately -1.7 for the smallest sizes measured to approximately -3.2 for the largest. From 1 to 2 AU the exponent for the smallest particle sizes is about -0.75 . There is evidence for the existence of a planetary sweeping effect in the vicinity of the Mars orbit. As calculated from the particle spatial distribution, the zodiacal light brightness is found to vary approximately as the inverse square of solar distance out to about 2.25 AU and then decrease more rapidly. This variation is the type measured by photometers on the same spacecraft. The absolute value of the zodiacal light brightness as calculated from the particle spatial concentration is found to be too high by a factor of 10. A possible explanation for this discrepancy is offered.

There are three experiments being carried by Pioneer 10 and 11 whose objective is to determine the nature of the particulate environment traversed by the spacecraft. The asteroid/meteoroid detector (AMD), or Sisyphus, is one of these. This instrument serves the dual purpose of measuring the contribution to sky brightness in white light from the aggregate of particles in the field of view and measuring individual particles as they pass through the field of view if they reflect or scatter sufficient sunlight to be detected above the sky brightness background. This paper deals with the concentration and size distribution of individual particles measured by the AMD on Pioneer 10 during the interplanetary cruise portion of the mission.

The detector consists of four 20-cm aperture optical telescopes mounted at an angle of 45° with respect to the vehicle spin axis (135° to the earth line), as is shown in Figure 1. The telescopes have 7.5° fields of view and are aligned approximately parallel. The telescopes utilize RCA 7151 Q photomultipliers with S20 photocathodes as the sensors. Their spectral response is modified by two gold reflections in the Cassegrain type telescopes. The instrument was designed to yield trajectory information for those particles with a good signal to noise ratio. The use of multiple telescopes also allows for noise rejection, since coincident readings are required for a particle transiting the fields of view.

Each telescope sets its own threshold as a function of the total background and noise being measured. Consequently, the threshold varies during the rotation cycle of the spacecraft and during the reorientation of the spacecraft spin axis. Maps of the sky background and noise in the individual telescopes are accumulated during the prolonged times between particle events. These readings are used to determine the threshold level and also to analyze the aggregate sky brightness.

Noise sources inherent in the background, such as bright stars and regions where the light level increases rapidly during a scan, are rejected in analysis by their recurrence at the same point in the rotation cycle of the spacecraft. Electronic noise, which has not been noticed in any of the ground or flight tests, could be rejected by its coincident appearance in all four telescope channels that are on the same power supply. The

operating levels of the telescopes are background-limited. Consequently, dark current and other noise sources inherent in the photomultipliers and amplifiers are negligible. The noise sensitivity tests included operating a flight instrument in the laboratory continuously for 1 week with cyclically varying light levels similar to those encountered in flight. No spurious events were noted in this test. Theoretical calculations predicted a false event rate of about 1 per month. Photometric calibration was performed in the laboratory, using standard sources and filters. These calibrations were confirmed during flight by using Jupiter and Rigel Kentaurus [Neste, 1974].

A low signal to noise ratio in most of the events noted and other anomalies that may be associated with a peculiar particle phase function (see the section on zodiacal light) have made the orbit analysis a far more difficult process than was originally envisioned. However, one can still readily derive brightness and transit time data from individual particles. It should be recognized that the total transit time is, in general, larger than the differential time of crossing between the individual telescope fields of view, and consequently the signal to noise ratio (which is integration time dependent) is higher. The transit times between fields of view do allow us to distinguish between spacecraft-generated and environmental particles. Such spacecraft-generated particles have been noted only at times of pulsed spacecraft precessions and for a single event when a protective cover was ejected from another instrument.

ANALYSIS

The transit times of particles can, on the average, be related to a range from the telescopes and consequently to particle size if certain assumptions are made. One must first assume an encounter velocity. On the theory that most of the particles were asteroidal, a circular orbit encounter velocity with the spacecraft has been assumed in this analysis. The cumulative spatial concentration of the particles can be expressed as

$$N = \frac{d\tau}{T dV} \quad (1)$$

where T is the observation time, $d\tau$ is the total dwell time of particles in the volume element dV , and N is the number per

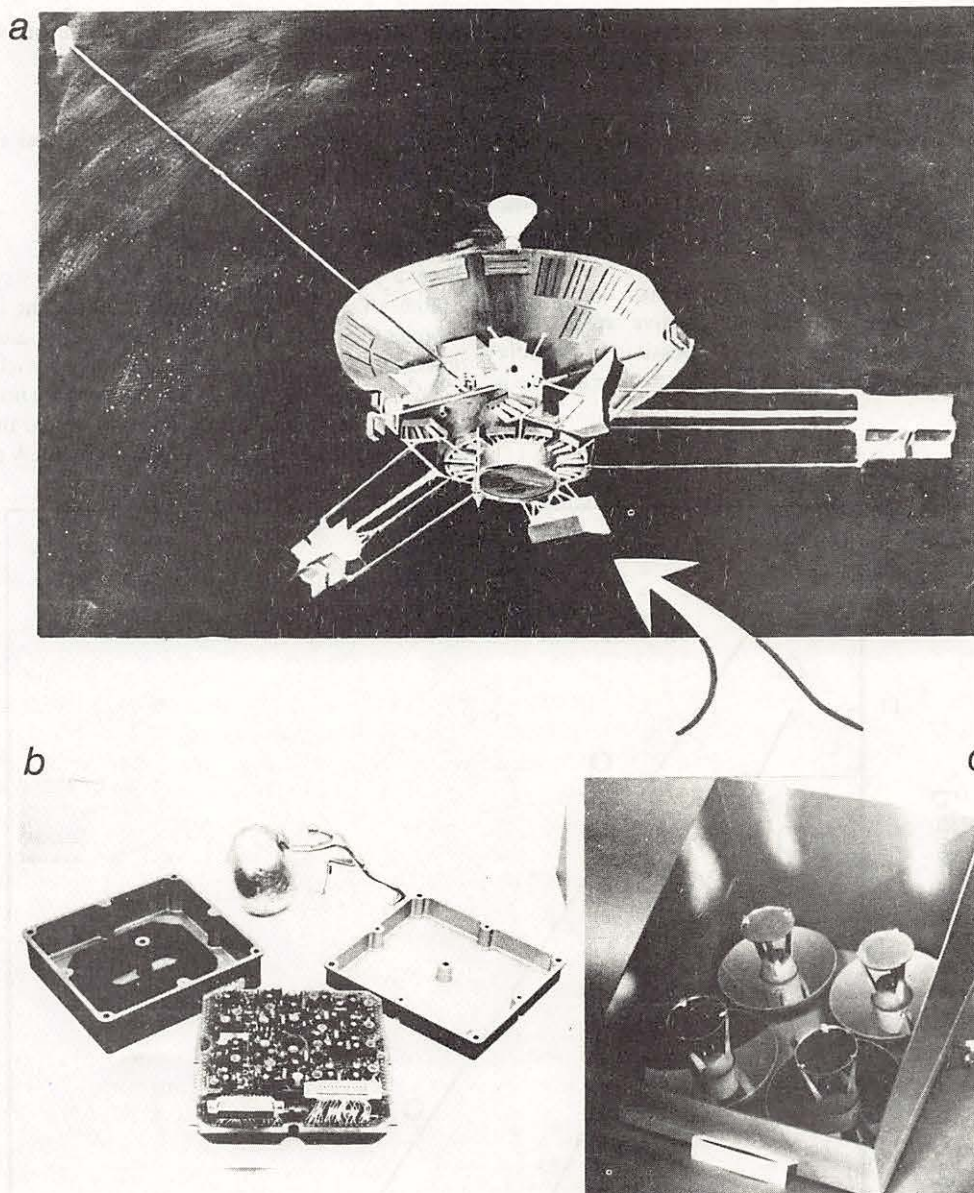


Fig. 1. (a) Artist's rendition of the Pioneer 10 spacecraft. (b) AMD electronics subsystem. (c) AMD optical subsystem (location on spacecraft indicated by arrow).

unit volume of all particles that can be detected in the volume element.

The cumulative flux can be expressed as

$$\Phi = \frac{dE}{T dA} \quad (2)$$

where dE is the observed number of events in the area element dA .

We can write

$$\Phi = Nv \quad (3)$$

where v is the particle encounter velocity.

For a cone with a small half angle,

$$dV = \pi\alpha^2 R^2 dR \quad (4')$$

and

$$dA = 2\alpha R dR \quad (4'')$$

where R is the distance to the apex and α is the half angle. Combining (1)-(4), we obtain

$$d\tau/dE = \bar{\tau} = \pi\alpha R/2v \quad (5)$$

For a photometric instrument the range can be related to the particle size by

$$\mathcal{R} = \left[\frac{I_0 r f(\gamma)}{I_{\min}} \right]^{1/2} \frac{S_0}{S} a \quad (6)$$

where \mathcal{R} is the distance to the telescope, I_0 is the solar irradiance at 1 AU, I_{\min} is the minimum irradiance that can be detected, r is the bond albedo, $f(\gamma)$ is the scattering function, S_0 and S are the heliocentric distances of earth and the particle, respectively, and a is the particle radius. From the foregoing it can be seen how transit time, range, and particle size are directly proportional to each other for an average particle.

To derive spatial concentrations and size distributions, we divided our events into thirds of decades from the minimum

range (beyond the shadow of the spacecraft antenna) to the largest transit time corresponding to the largest range or particle size observed. Smaller subdivisions were not deemed practical in view of the limited number of events observed (we measured 232 events in transiting from 1.0 to 3.5 AU, and most of these were in the smallest size or range regime). As we shall show, for some of the analysis it was necessary to use larger size domains. The one-third decade corresponds to 1 order of magnitude in mass.

It should be borne in mind that a photometric instrument, unlike a fixed area detector, increases its effective cross section as the square of the particle size. Thus it is possible to measure over a large range of particle sizes. Specifically, if we assume a flux of the form

$$\Phi \sim a^{-\beta} \quad (7)$$

and the effective cross section area can be written as

$$A \sim a^2 \quad (8)$$

the number of events that will be observed as a function of particle radius will be of the form

$$E \sim a^{2-\beta} \quad (9)$$

Thus a photometric instrument such as Sisyphus effectively stretches the size distribution by adding the factor of 2 in the exponent. Specifically, if β is near 2 in value, then one can measure over orders of magnitude of particle size.

To assure ourselves that our results were not being biased by the foregoing analysis procedure, we tested the method by using a computer simulation of the problem. A particle flux with

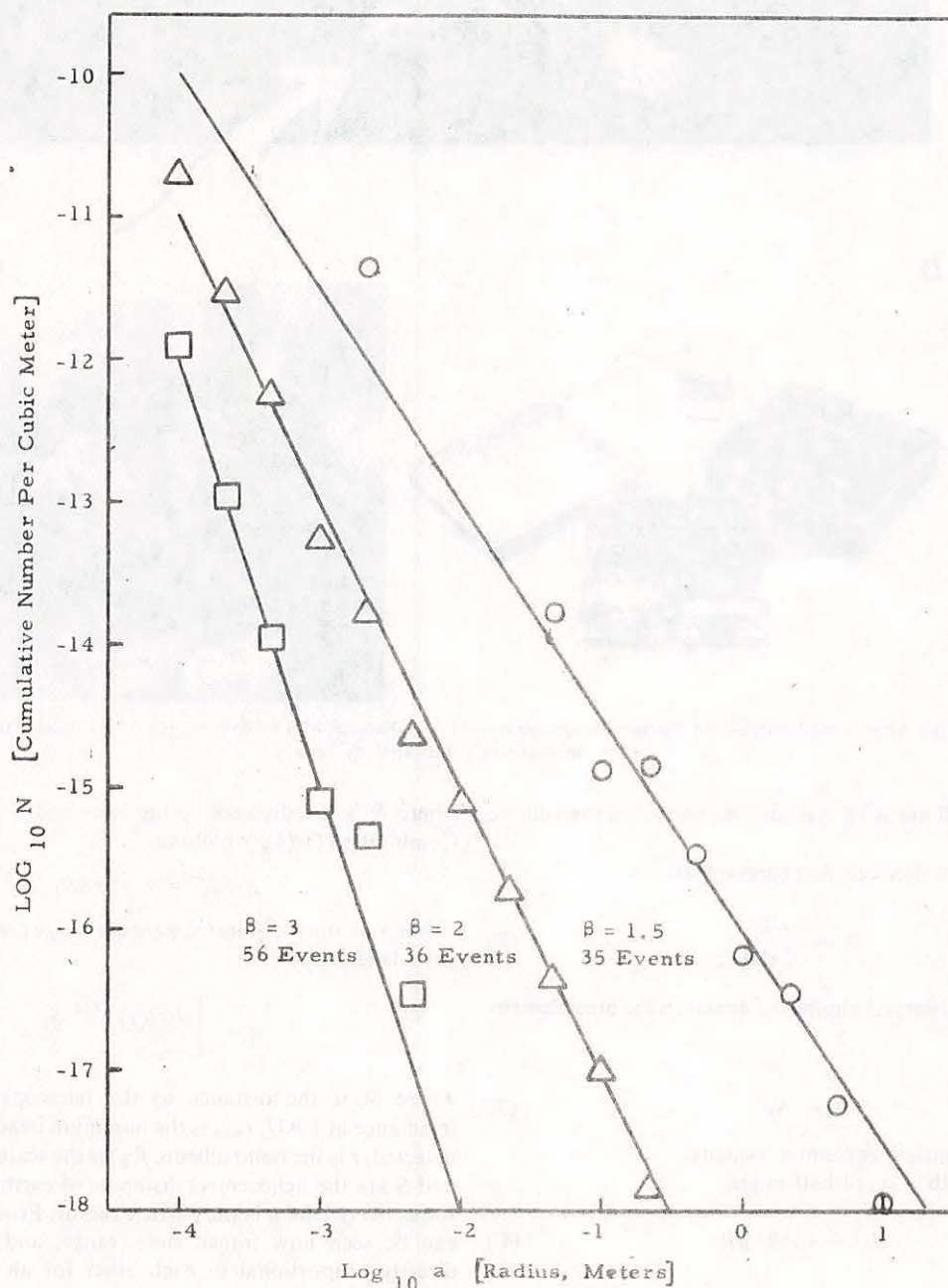


Fig. 2. Results of computer simulations of the data analysis technique. Symbols indicate variation about the input distribution.

a size distribution of the form

$$\Phi = Ka^{-\beta} \tag{10}$$

was first selected. For each size the average calculated fluence was randomized by a Poisson distribution. The trajectory relative to the instrument for each particle was then selected by using a uniform probability random number generator. To date, only trajectories perpendicular to the optic axis have been used. The velocity was generated from a Gaussian distribution with a mean of 14 and a σ of 4 km/s. This is the range of vehicle encounter velocities that would be expected from an

asteroid distribution. The transit time through a single cone of view was then calculated. This process generated data of the type received from the instrument, which were then analyzed by using the procedure described above.

Particle fluxes with size exponents of -1.5 , -2 , and -3 were tested in this fashion. In each case with a limited number of events this procedure resulted in a particle distribution that was nearly identical with the original input (Figure 2). We also tested segmented distributions with several different slopes and obtained similar results. Thus our method of analysis does not appear to introduce any systematic bias into the results.

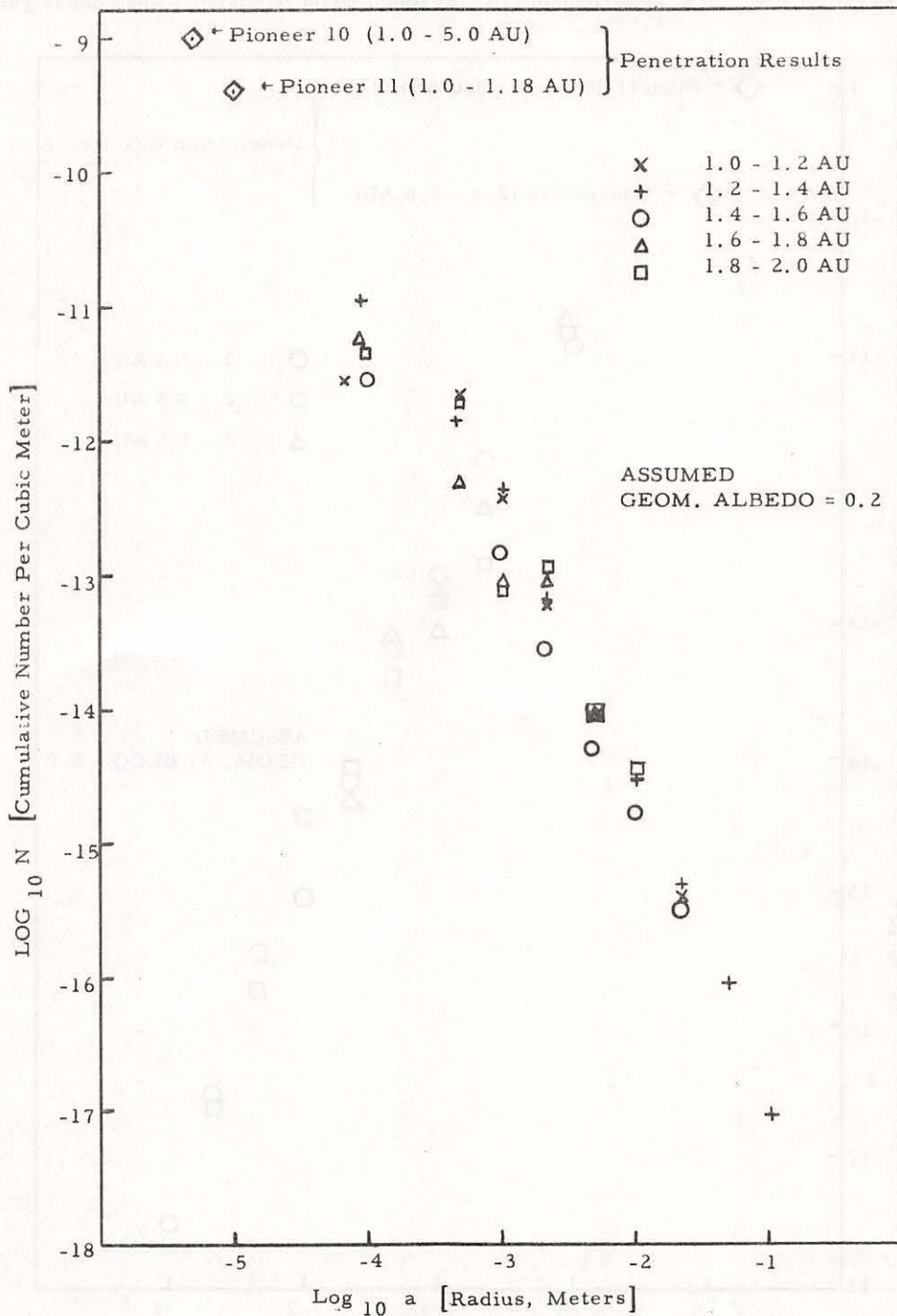


Fig. 3. Particle size distributions for five segments of the 1- to 2-AU region. The points labeled penetration results were derived from results of *Humes et al.* [1973].

SIZE AND SPATIAL DISTRIBUTIONS

The data obtained during the flight of the Pioneer 10 spacecraft were separated into two heliocentric regions for analysis. The data obtained prior to spacecraft entrance into the asteroid belt (1.0–2.0 AU) compose one set, and the data obtained during the transit of the asteroid belt were placed in the second group. The preasteroid belt data were separated into five equal heliocentric segments, and the data obtained in the asteroid belt were treated in three such segments. The results are shown in Figures 3 and 4, respectively.

These distributions are cumulative in that they are for the particle size shown and larger sizes. The smallest size domains

were combined, since transit times are distorted within approximately 10 m of the telescopes, where the image blur becomes comparable to or greater than the aperture. Also, close to the telescopes the cone approximation that we used breaks down.

Following *Dohnanyi* [1971] we have assumed a geometric albedo of 0.2 for the particles. We have also plotted in these figures the points obtained by the penetration detectors on Pioneer 10 and 11 [*Humes et al.*, 1973].

It can be seen that the variations in size distribution are not significant on a logarithmic plot to this scale. Consequently, we combined the results into a single plot (Figure 5). As we did

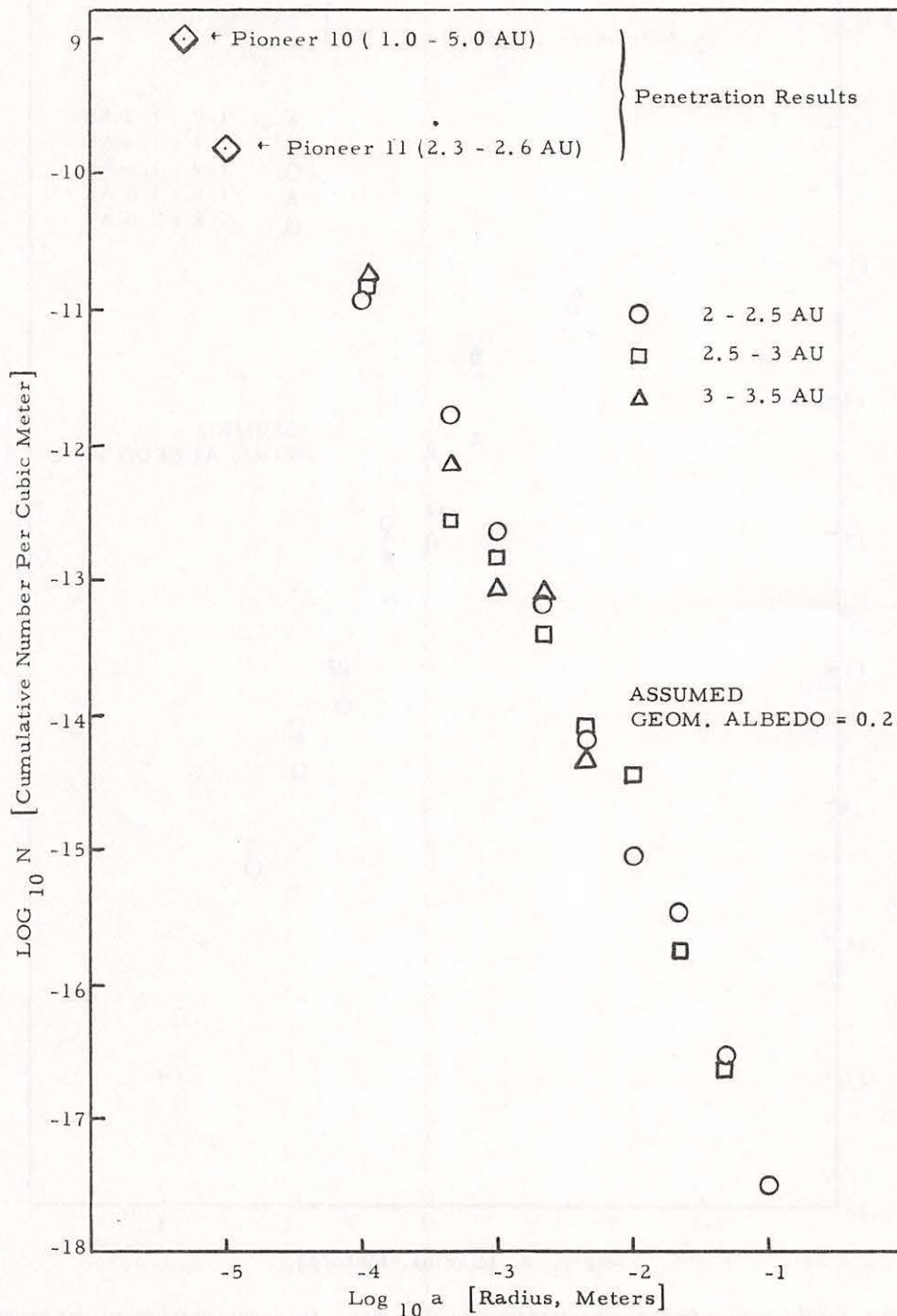


Fig. 4. Particle size distributions for three regions of the asteroid belt. The points labeled penetration results were derived from the results of *Humes et al.* [1973].

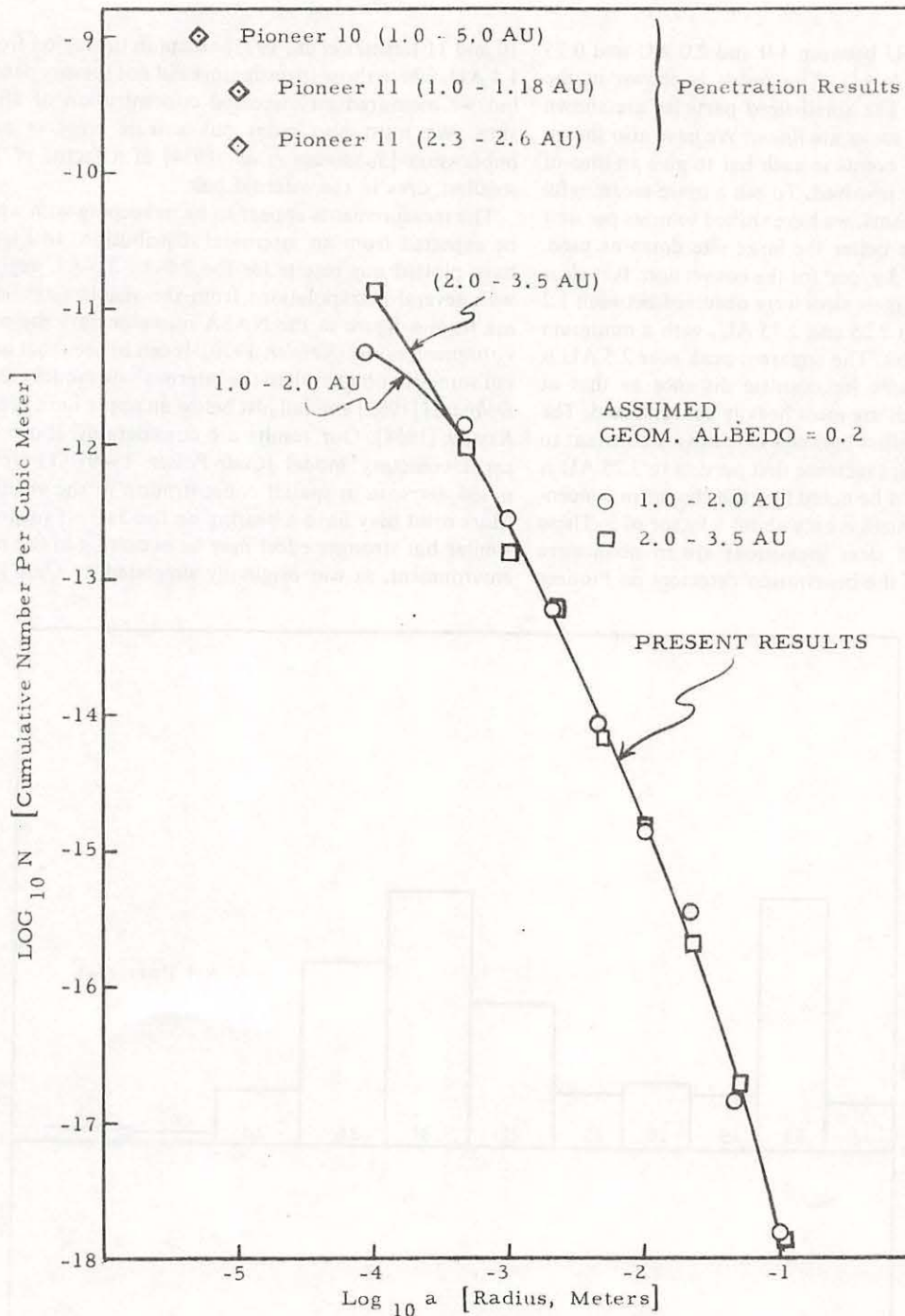


Fig. 5. Particle size distributions from 1 to 3.5 AU. The points labeled penetration results were derived from the results of *Humes et al.* [1973].

in Figures 3 and 4, we have also plotted the Pioneer 10 and 11 penetration points [*Humes et al.*, 1973]. The AMD points are shown at the logarithmic mean within the one-third decade. The uncertainty in albedo would cause the curve to be shifted horizontally by the square root of the ratio of the true albedo to our assumed value. *Dohnanyi* [1971] gives plus or minus a factor of 3 in value, but this can be open to question (see below). The penetration detector on Pioneer 10 was taken to be sensitive to particles of radius 5 μm and larger, whereas the one on Pioneer 11 was assumed to be sensitive to 10 μm and larger.

Figure 5 shows that on this scale the size distribution is nearly constant from instrument turnon (1 week after launch)

to 3.5 AU. The only significant difference occurs at the smallest sizes measured. The results of the AMD indicate a greater flattening of the distribution from 1.0 to 2.0 AU than is found in the asteroid belt. It is noteworthy that the penetration detector on Pioneer 11, which initially recorded a relatively large number of penetrations out to 1.18 AU, indicated only one penetration between 1.18 AU and 2.3 AU [*Humes et al.*, 1973]. No data point for this region was assigned by the investigators, but it should be in keeping with the trend from our 1.0- to 2.0-AU results.

Changes in size distribution and spatial concentration, although they were negligible on a logarithmic scale, were noted in the data. To illustrate these changes, we combined the data

into increments of 0.2 AU between 1.0 and 2.0 AU and 0.25 AU between 2.0 and 3.5 AU. The result is shown in the histograms of Figure 6. The small-sized particles are shown separately. Note that the scales are linear. We have also shown the number of measured events in each bar to give an idea of the statistical uncertainty involved. To put a more meaningful ordinate on these histograms, we have shifted to mass per unit volume to accommodate better the large size domains used. We assumed a density of 3 g/cm^3 for the conversion. It is clear from Figure 6 that the largest sizes were observed between 1.2 and 1.4 AU and between 2.25 and 2.75 AU, with a minimum in the region of Mars orbit. The apparent peak near 2.5 AU is at approximately the same heliocentric distance as that at which the visible asteroids are most heavily concentrated. The concentration of the smallest particles is relatively constant to 2.0 AU, where an apparent increase that persists to 3.25 AU is noted. However, it should be noted that the change in concentration of these smallest sizes is only about a factor of 3. These results (for the smallest sizes measured) are in qualitative agreement with those of the penetration detectors on Pioneer

10 and 11 [Humes *et al.*, 1973] except in the region from 1.2 to 1.4 AU, where those investigators did not see any penetrations but we measured an increased concentration of all particle sizes. We must also point out a scale error in an earlier publication [Soberman *et al.*, 1974] of a factor of 2 for the smallest sizes in the asteroid belt.

The measurements appear to be in keeping with what might be expected from an asteroidal distribution. In Figure 7 we have plotted our results for the 2.0- to 3.5-AU region along with several extrapolations from the visible asteroids. These are from a figure in the NASA interplanetary meteoroid environment model [Kessler, 1970]. It can be seen that our results fall somewhat higher than the intermediate model proposed by Dohnanyi [1969] and fall just below an upper limit proposed by Kessler [1968]. Our results are considerably above the near-earth cometary model [Cour-Palais, 1969]. The previously noted decrease in spatial concentration in the vicinity of the Mars orbit may have a bearing on this fact. It suggests that a similar but stronger effect may be occurring in the near-earth environment, as was originally suggested by Öpik [1951] for

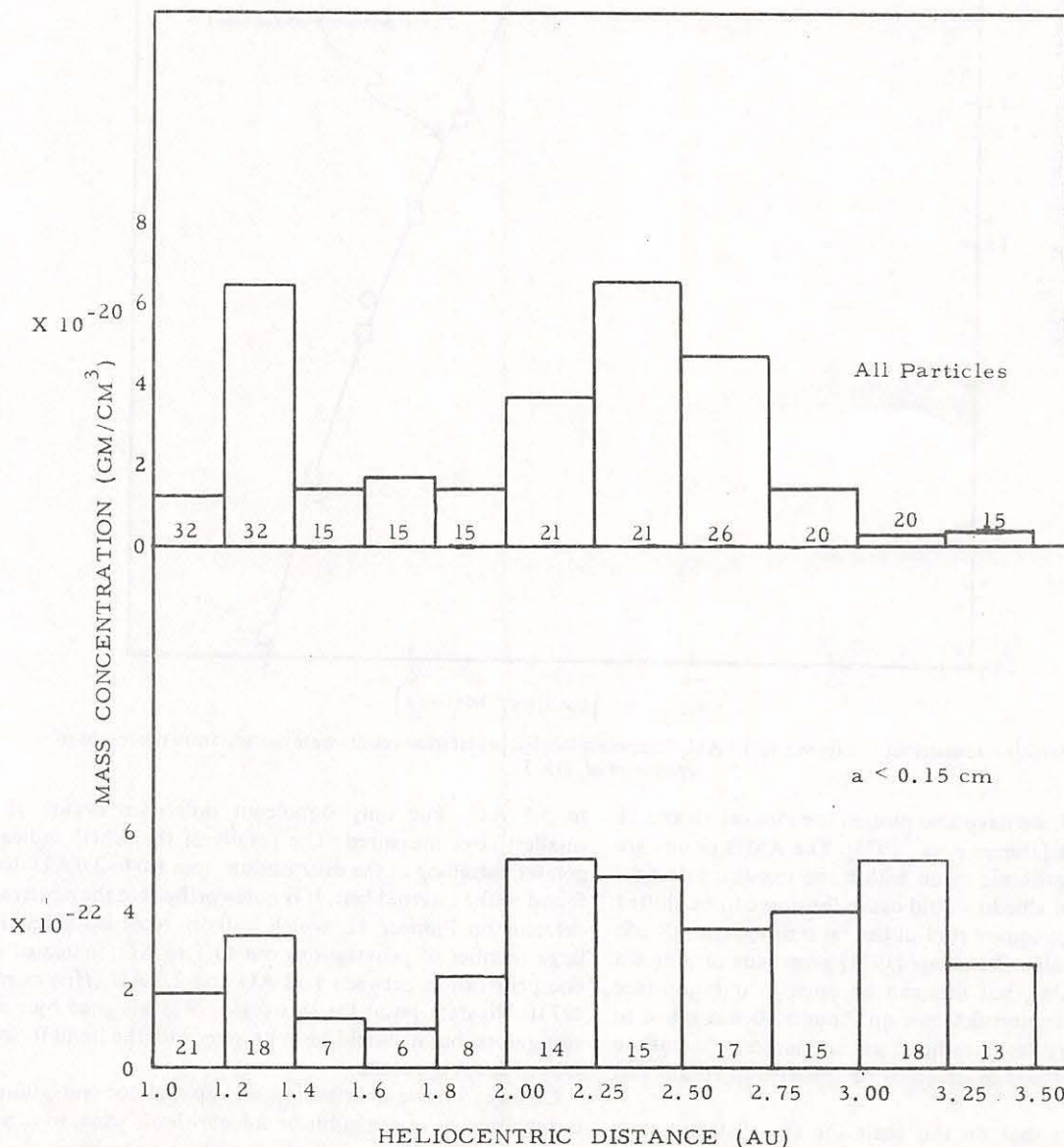


Fig. 6. Mass concentration due to all particles (upper) and the smallest particles (lower). The number of particles measured is shown in each bar.

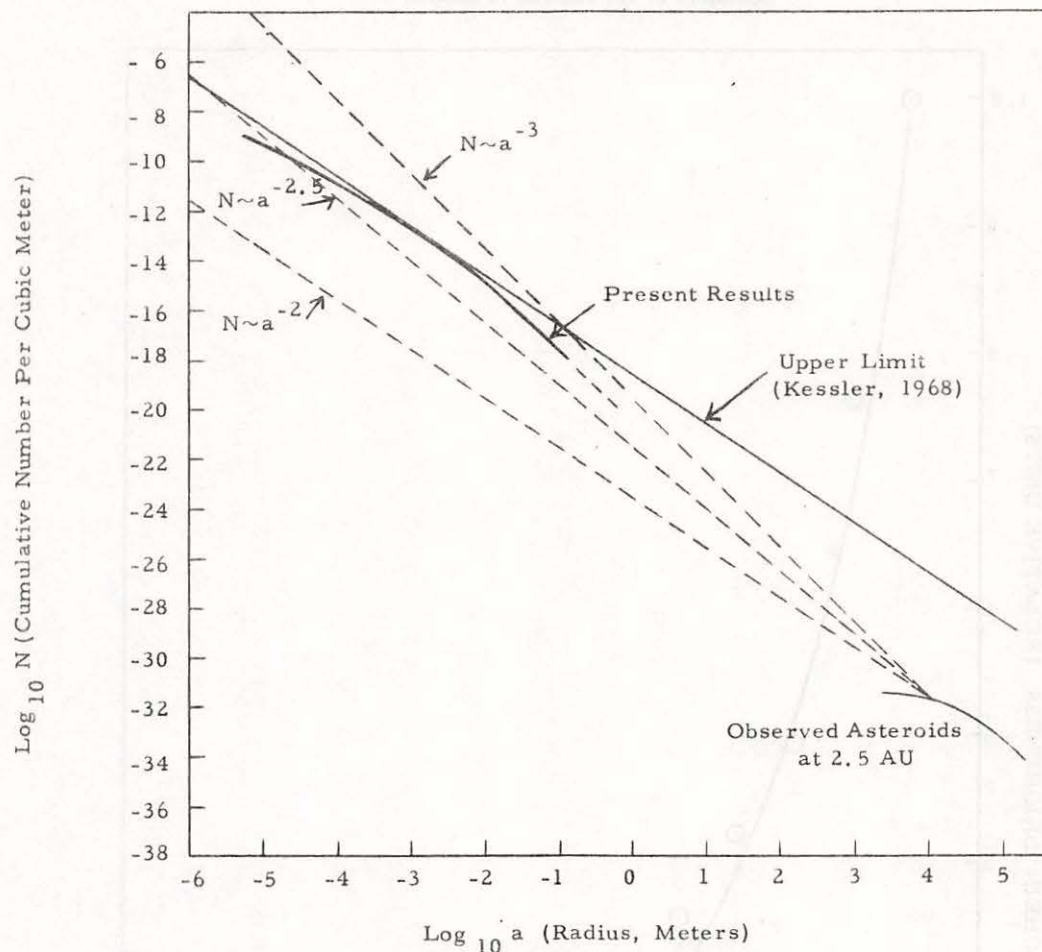


Fig. 7. Various asteroidal size distribution models compared with the present results. Models are after a figure from Kessler [1970].

somewhat larger particles. Although we did not see any dramatic change in the early data, it should be borne in mind that the instrument was not turned on until 1 week after launch, and with our statistics no dramatic change would be expected. There is a suggestion of an increasing concentration with initially increasing solar distance in the histograms of Figure 6.

ZODIACAL LIGHT

The contribution of our measured particles to the sky brightness can readily be calculated. For the gegenschein, calculations can be made from the relationship [van de Hulst, 1947]

$$H(\pi) = I_0 S_0^2 \int_{S_1}^{S_2} \int_{a_{\min}}^{\infty} \frac{pa^2}{S^2} dN(a, S) dS \quad (11)$$

where $H(\pi)$ is the backscatter brightness per unit solid angle and as used before, I_0 is the solar irradiance at 1 AU, S_0 and S are the heliocentric distances to the earth and the particles, respectively, a is the particle radius, p is the geometric albedo, and dN is the differential size concentration.

The $H(\pi)$ was calculated for each solar distance segment on the basis of the spatial density corresponding to each average particle size. Summing these individual contributions gave an integrated value for the gegenschein brightness between 1.0 and 3.5 AU, which is approximately a factor of 10 too high according to earth-based observations [Roosen, 1970], the IPP

(imaging photopolarimeter) experiment on Pioneer 10 [Hanner and Weinberg, 1973], and also our own measurements in the average sky background mode [Zook and Soberman, 1974].

In Figure 8 we have plotted the relative variation of the zodiacal light with heliocentric distance by successively subtracting out the contributions due to each solar distance segment. As can be seen from the figure, the zodiacal light decreases approximately as the inverse square of the solar distance out to about 2.25 AU, where it begins to fall off more rapidly. This observed variation is in good agreement with results obtained from the IPP experiment [Hanner and Weinberg, 1973; Hanner et al., 1974] as well as our own sky background measurements [Zook and Soberman, 1974].

The relative variation of zodiacal brightness deserves a brief discussion. It cannot be explained by the kind of particle spatial concentration variation shown by the Pioneer penetration detectors. Further, a recent paper by Southworth and Sekanina [1973] showed that the concentration of radio meteors increased with increasing heliocentric distance, at least to 3 AU, which would also not be in keeping with the observed variation of zodiacal brightness. An examination of (11) shows that the maximum contribution should come from the particle size for which the exponent of the cumulative size distribution is -2 . The variation of the zodiacal brightness shown in Figure 8 is predominantly due to the spatial concentration variations measured in the size domain for which the exponent is near -2 . This variation could not be anticipated from the results shown in Figure 6, which are dominated by

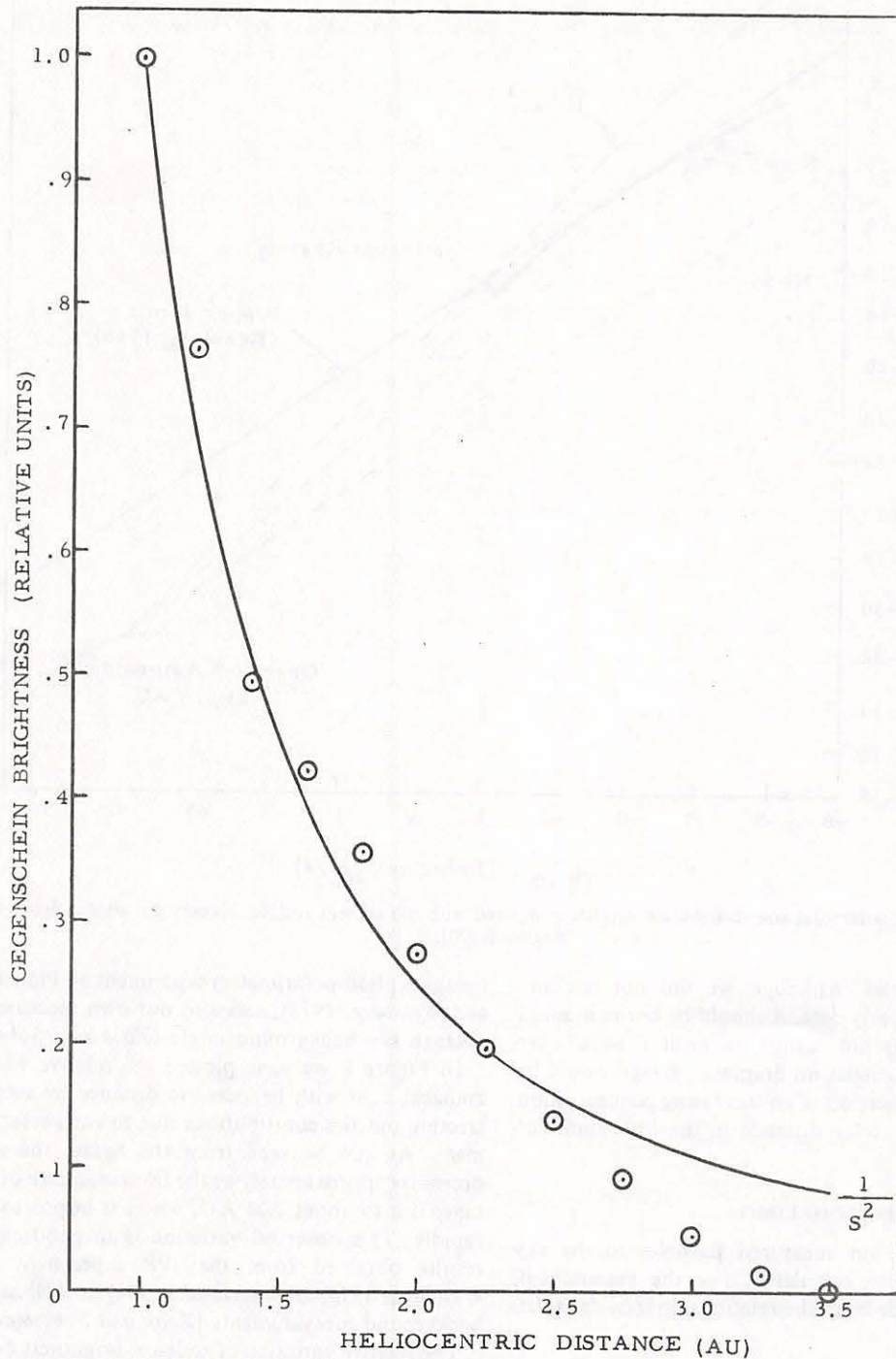


Fig. 8. Relative variation of gegenschein brightness, heliocentric distance being derived from the present results.

the largest (upper histogram) and smallest (lower histogram) sizes measured. These results show how it is possible to obtain an inverse square decrease in the gegenschein brightness with heliocentric distance, although an earth-based observer would not be able to detect the shadow of the earth in the gegenschein [Roosen, 1970].

Thus the individual particle results of the AMD give a zodiacal light, or gegenschein brightness, variation that is consistent with the photometer measurements, although the absolute value obtained is too high.

The simple explanations unfortunately fail to solve this discrepancy. To say that we were more sensitive than our calibrations indicate would be inconsistent with the operation

of the instrument. Further, from the nature of the measurements it can be shown that the derivation is independent of the assumed albedo.

That the problem goes deeper than the present measurements was already pointed out by Whipple [1971]. He showed that the near-earth particle model, even when it is allowed to fall off inversely with the heliocentric distance, would give too large a value for the zodiacal light for any reasonable albedo assumption. A general decrease in the spatial concentration with heliocentric distance at least to 2.5 AU is inconsistent not only with the present results but also with those of the Pioneer penetration detector and the radio meteor measurements cited above. We have calculated that if

the near-earth particle model even remained constant out to 3 AU, not only would it fail to show the proper form for the zodiacal light decrease, but the average albedo of the particles would have to be less than 0.02 to agree in absolute brightness.

To resolve the discrepancy, particularly in relation to the present results, a hypothesis is offered. It was suggested by the difference between the AMD acting as an individual particle sensor and any sky brightness photometer. While the AMD measures only the peak signal due to a single particle, normally at a distance much less than a kilometer away, the photometer is measuring the averaged intensity of many particles at very large distances from the instrument. If the phase function of the particle consisted largely of narrow, intense specular reflection peaks observed as the particle rotates rapidly, then the average irradiance due to the particle could be many times less than the peak intensity. This type of phase function would also explain other anomalies observed by the AMD including disparate readings from the different telescopes on many particles and signals that drop below threshold and subsequently recover.

Although such a phase function for interplanetary particles cannot be established with existing data, films of several manned space missions clearly show that the vast majority of the solar illuminated particles visible therein display this type of phase function. It should be borne in mind that, apart from our transit time discrimination, the present results cannot be attributed to spacecraft particles, since this would require that either the concentration or the size of such particles would have to increase with solar distance to compensate for the diminishing solar illumination. However, if the phase function exhibited by contaminant particles is also characteristic of interplanetary particles, it will provide an explanation for the apparent discrepancy between the zodiacal light photometric brightness and the results of discrete particle counters. Each instrument may be responding to the particle concentration in its own fashion. Although the effective albedo could be quite small for the photometer, specular reflections could give a very high albedo for discrete light pulses.

CONCLUSIONS

The results presented herein suffer from a number of uncertainties that are believed to have resulted primarily from highly variable light levels measured from rapidly rotating partly specularly reflecting particles. The measured transit times are believed to have been influenced by these light level variations. In our analysis we have used the longest transit time observed in the four telescopes. The uncertainty in transit time has necessitated assuming a circular orbit encounter velocity for the particles and using mean values for transit parameters of the observation cone. We have also assumed the minimum size for a diffusely reflecting particle. This assumption appears reasonable in view of our belief that we are dealing with specular rather than diffuse reflection. These assumptions plus the statistically small number of events may have influenced some of the observed variations in spatial concentration and size distribution. It appears obvious, however, that the variations in size and concentration of particulates encountered are less than an order of magnitude.

The largest uncertainty lies in the nature and the reflecting properties of the particles. If the present hypothesis is correct, then the mean albedo of the particles may be quite small (~0.01). The albedo used in deriving the results of Figures 3, 4,

and 5 should therefore be interpreted as an instantaneous peak value applicable to specular reflection as the particle rotates. This specular reflection from the particle fine structure could be responsible for the polarization observed in the zodiacal light [Weinberg, 1970].

Finally, note that the dynamics of a solar illuminated particle would be modified by rotation [Jacchia, 1963]. If the particles are charged, it is possible that the rotations are magnetically aligned, and this alignment could drastically alter the lifetimes of these particles in the solar system.

Acknowledgments. The authors gratefully acknowledge the cooperation and assistance of the personnel of the Pioneer Project Office, NASA, Ames Research Center, without which this effort would not have been possible. They are also deeply indebted to the many people of the General Electric Space Division who contributed to this project, in particular, G. Zomber, K. Krause, and E. Howard, who contributed to the design and building of the instrument. This work was supported in its entirety by NASA under contracts NAS 2-5609 and NAS 2-6559.

REFERENCES

- Cour-Palais, B. G., Meteoroid environment model-1969 (near earth to lunar surface), *NASA Spec. Publ. 8013*, March 1969.
- Dohnanyi, J. S., Collisional model of asteroids and their debris, *J. Geophys. Res.*, **74**, 2531-2554, 1969.
- Dohnanyi, J. S., Fragmentation and distribution of asteroids, *Physical Studies of Minor Planets, NASA Spec. Publ. 267*, 263-295, 1971.
- Hanner, M. S., and J. L. Weinberg, Gegenschein observations from Pioneer 10, *Sky Telesc.*, **45**, 217-218, 1973.
- Hanner, M. S., J. L. Weinberg, L. M. DeShields II, B. A. Green, and G. N. Toller, Zodiacal light and the asteroid belt: The view from Pioneer 10, *J. Geophys. Res.*, **79**, this issue, 1974.
- Humes, D. H., J. M. Alvarez, R. L. O'Neal, and W. M. Kinard, Cosmic dust encountered by Pioneer 10 and 11, paper presented at Fall Annual Meeting, AGU, San Francisco, Calif., Dec. 1973.
- Kessler, D. J., Upper limit on the spatial density of asteroidal debris, *Amer. Inst. Aeronaut. Astron. J.*, **6**, 2450, 1968.
- Kessler, D. J., Meteoroid environment model-1970 (interplanetary and planetary), *NASA Spec. Publ. 8038*, 1970.
- Jacchia, L. G., Meteors, meteorites, and comets: Interrelations, in *The Moon Meteorites and Comets*, edited by B. M. Middlehurst and G. P. Kuiper, pp. 774-798, University of Chicago Press, Chicago, Ill., 1963.
- Neste, S. L., An experimental model of the asteroid/meteoroid environment from 1.0 to 3.5 AU—Its characteristics and implications, Ph.D. dissertation, Drexel Univ., Philadelphia, Pa., in press, 1974.
- Öpik, E. J., Collision probabilities with the planets and the distribution of interplanetary matter, *Proc. Roy. Irish Acad.*, **54**, 165-199, 1951.
- Roosen, R. G., The gegenschein and interplanetary dust outside the earth's orbit, *Icarus*, **13**, 184-201, 1970.
- Soberman, R. K., S. L. Neste, and K. Lichtenfeld, Particle concentration in the asteroid belt from Pioneer 10, *Science*, **183**, 320-321, 1974.
- Southworth, R. B., Space density of radio meteors, *Proceedings of the Symposium on Zodiacal Light and Interplanetary Medium, NASA Spec. Publ. 150*, 179-188, 1967.
- Southworth, R. B., and Z. Sekanina, Physical and dynamical studies of meteors, *NASA Contract. Rep. 2316*, Oct. 1973.
- van de Hulst, H. C., Zodiacal light in the solar corona, *Astrophys. J.*, **105**, 471-488, 1947.
- Weinberg, J. L., Current problems in the zodiacal light, *Space Res.*, **10**, 233-243, 1970.
- Whipple, F. L., On the amount of dust in the asteroid belt, *Physical Studies of Minor Planets, NASA Spec. Publ. 267*, 363-371, 1971.
- Zook, H. A., and R. K. Soberman, The radial dependence of the zodiacal light, *Space Res.*, **14**, 763-767, 1974.

(Received May 14, 1974;
accepted July 15, 1974.)

Lecture Notes in Physics

Edited by J. Ehlers, München, K. Hepp, Zürich,
H. A. Weidenmüller, Heidelberg, and J. Zittartz, Köln
Managing Editor: W. Beiglböck, Heidelberg

48

Interplanetary Dust and Zodiacal Light

Proceedings of the IAU-Colloquium No. 31,
Heidelberg, June 10-13, 1975

Edited by H. Elsässer and H. Fechtig



Springer-Verlag
Berlin · Heidelberg · New York 1976

DUST IN THE OUTER SOLAR SYSTEM - REVIEW OF EARLY
RESULTS FROM PIONEERS 10 AND 11R. K. Soberman¹, J. M. Alvarez², and J. L. Weinberg³

Abstract. The Pioneer 10/11 spacecraft, launched in 1972 and 1973, carried three experiments to measure cosmic dust. A comparison of these first direct measurements of dust in the outer solar system indicates that the sizes, optical properties, and spatial distribution are more complex than previously supposed.

Three interplanetary dust detectors were carried on Pioneers 10 and 11: the Imaging Photopolarimeter (IPP) in the Sky Mapping Mode, the penetration detectors of the Meteoroid Detection Experiment (MDE), and the Asteroid Meteoroid Detector (AMD). Table 1 summarizes for each instrument the measured parameters, the particle size range, and various assumptions used to derive the properties and spatial distribution of the particles. The question marks added to the size range of the zodiacal light detectors are discussed later. In the analysis of the MDE and AMD data, it was necessary to assume relative encounter velocities. From the penetration data it was concluded that the particles have circular or near-circular orbital velocities. For the AMD this was a starting assumption.

The penetration detectors indicate a constant spatial concentration with heliocentric distance, with no apparent indication of asteroid belt passage (Humes, et al., 1975). Early results from both the IPP (Hanner, et al., 1974) and the AMD zodiacal light mode (Zook and Soberman, 1974) have shown that the zodiacal light brightness decreases monotonically with increasing heliocentric distance. The IPP results indicate that the zodiacal light initially decreases faster than the inverse square of the heliocentric distance, R , then more rapidly in the asteroid

¹General Electric Space Sciences Laboratory, Philadelphia, Pennsylvania, USA

²Langley Research Center, National Aeronautics and Space Administration,
Hampton, Virginia, USA

³Space Astronomy Laboratory, State University of New York at Albany, Albany,
New York, USA

TABLE I
COMPARISON OF PIONEER 10/11 DUST EXPERIMENTS

Experiment	Measurement	Particle Diameter Range	Assumptions	Derived Results
MDE Penetration Detectors	Penetration Rate of Stainless Steel 25 μm 50 μm	$\sim 10 \mu\text{m}$ $\sim 20 \mu\text{m}$	Distribution of Orbital Parameters for Relative Velocity	Spatial concentration
IPP Zodiacal Light Mode	Polarization & Brightness in 2 Colors	Micron and/or Sub-micron ?	Mie Theory - Constant Size Distribution	Spatial distribution Size Shape Refractive index
AMD Zodiacal Light Mode	Brightness	Micron and/or Sub-micron-?	Mie Theory - Constant Size Distribution	Spatial distribution
AMD Individual Particle Mode	Peak Intensity Transit Time	50 μm and Larger	Circular Orbit Encounter Vel. - Average Transit Thru View Cone - Diffuse Geometrical Reflection From Spherical Particles	Size distribution Spatial concentration Zodiacal light brightness

belt, with no measurable contribution beyond 3.3 AU (Hanner et al., 1976). Based on the assumption that the scattering properties do not change significantly with heliocentric distance, these results suggest that the spatial distribution can be represented by a power law, $R^{-\gamma}$ ($\gamma \approx 1$) or by a two-component model ($\gamma \approx 1.5$) with increased dust in the asteroid belt.

The discrete particle results from the Pioneer 10 AMD (Soberman, et al., 1974) show an increase in the number of particles out to the asteroid belt. There appear to be minima in the vicinity of both the Earth's and Mars' orbits which are more pronounced for the larger particles. Beyond 3.5 AU the event rate drops below instrumental limits, the fall-off occurring first for the larger particles. The size distribution differs significantly from the 1 AU model for the larger sizes and is of the type expected for an asteroidal population (Dohnanyi, 1969). Particle sizes

were obtained by assuming a value of 0.2 for the albedo in order to extrapolate to the penetration detector results.

Figure 1 shows the relative change in zodiacal light brightness with

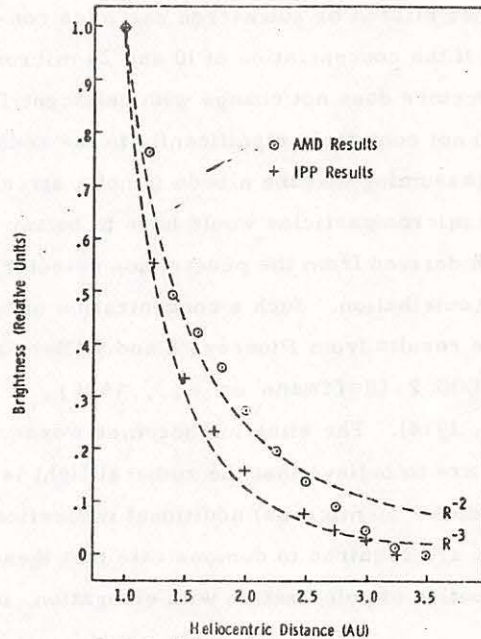


Figure 1. Variation of Zodiacal Light Brightness With Heliocentric Distance

heliocentric distance as measured by the IPP and as derived from the AMD discrete particle mode. Although the relative brightnesses are in satisfactory agreement, the absolute brightness derived from the AMD results is more than an order of magnitude too large by comparison with the photometric results from the same instrument and from the IPP. For example, the AMD gives a gegenschein brightness at 1 AU of approximately $2500 S_{10} (V)^*$. This difference is believed to arise from the fact that the AMD measures peak rather than average values for particle brightness when operating in the discrete particle mode, and that the particles contain many re-

reflecting surfaces that give off bright glints of light as the particles rotate (such as observed from sunlit particles in the vicinity of Earth-orbiting vehicles). Because of this glint effect, the planned orbital measurements could not be made with the AMD, and it was necessary to assume particle velocities relative to the instrument to derive sizes and heliocentric variations.

The results from the three dust experiments on Pioneers 10 and 11 seem to be completely discordant. The zodiacal light results indicate that the concentration of dust decreases initially at least as fast as the inverse heliocentric distance and then more rapidly while passing through the asteroid belt. The penetration detectors indicate a uniform spatial concentration with the exception of the gap regions (Humes, et al., 1975). The discrete particle results of the AMD indicate a varying concentration going outward, peaking in the asteroid belt and then dropping off to a negligible value at approximately 3.5 AU. The simplest explanation for this

*Equivalent number of tenth magnitude (V) stars of solar spectral type, per square degree.

divergence would be that the three sensors were measuring in three different size domains as was indicated in Table 1. This simple explanation cannot be ruled out, although it is not likely that the two extreme sizes are similar in concentration but different from the concentration of the intermediate sizes.

A further question is whether micron or submicron particles contribute appreciably to the zodiacal light. If the concentration of 10 and 20 micron particles measured by the penetration detectors does not change with heliocentric distance, then these particles probably do not contribute significantly to the zodiacal light. Comparing the cross-sections (assuming that the albedo is not a strong function of size), the concentration of one micron particles would have to be two orders of magnitude higher than the concentration derived from the penetration detector results to yield even an equal brightness contribution. Such a concentration of one micron particles is not consistent with the results from Pioneers 8 and 9 (Berg and Grün, 1973), MTS (Alvarez, 1976), HEOS 2 (Hoffmann et al., 1975), and the Lunar Cratering Results (Neukum, 1974). The situation becomes worse if one relies on submicron particles. If we are to believe that the zodiacal light is produced primarily by large particles (radius > 50 microns) additional theoretical calculations and laboratory measurements are required to demonstrate that these particles can produce the observed distribution of polarization with elongation, including polarization reversal.

The zodiacal light and individual particle brightness results from Pioneer 10 suggest the presence of a dust component in the asteroid belt and a negligible concentration beyond. The penetration results show a nearly uniform concentration with no measurable contribution from the asteroid belt and no measurable decrease in concentration beyond. These results suggest different sources for the particles responsible for the penetrations and those which give rise to the individual and aggregate brightness measurements. To explain these differences, additional studies of the sources and sinks for the interplanetary dust beyond 1 AU appear warranted.

Acknowledgements

The Pioneer 10 and 11 Meteoroid Detection Experiment was directly supported by the National Aeronautics and Space Administration at the Langley Research Center; the Imaging Photopolarimetry Zodiacal Light Experiment was supported by NASA through contract NAS 2-7963 with the State University of New York at Albany; the Asteroid-Meteoroid Astronomy Experiment was supported by NASA through contract NAS 2-6559 with the General Electric Space Sciences Laboratory.

References

- Alvarez, J.M. (1976), "The Cosmic Dust Environment at Earth, Jupiter and Interplanetary Space: Results from Langley Experiments on MTS, Pioneer 10 and Pioneer 11", these proceedings.
- Berg, O.E., and Grün, E. "Evidence of Hyperbolic Cosmic Dust Particles" Space Research XII, Eds. M. J. Rycroft and S. K. Runcorn (Akademie-Verlag, Berlin, 1973).
- Dohnanyi, J.S. "Collisional Model of Asteroids and Their Debris" Jour. Geophys. Res. 74, 2531-2554 (1969).
- Hanner, M.S., Spáarrow, J.G., Weinberg, J.L., Beeson, D.E. (1976), "Pioneer 10 Observations of Zodiacal Light Brightness Near the Ecliptic; Changes with Heliocentric Distances", these proceedings.
- Hanner, M. S. and Weinberg, J. L. "Changes in Zodiacal Light With Heliocentric Distance: Preliminary Results from Pioneer 10" Space Research XIV, Eds. M. J. Rycroft and R. D. Reasenberg, 769-772 (Akademie-Verlag, Berlin, 1974).
- Hoffmann, H. J., Fechtig, H., Grün, E., and Kissel, J. "First Results of the Micrometeoroid Experiment S215 on the HEOS 2 Satellite" Planet. Space Sci. 23, 215-224 (1975).
- Humes, D. H., Alvarez, J. M., Kinard, W. H. and O'Neal, R. L. "Pioneer 11 Meteoroid Detection Experiment: Preliminary Results," Science 188, 473-474 (1975).
- Neukum, G. "Micrometeoroid Erosion of Lunar Rocks" Space Research XIV, Eds. M. J. Rycroft and R. D. Reasenberg, 739-740 (Akademie-Verlag, Berlin, 1974).
- Soberman, R. K., Neste, S. L. and Lichtenfeld, K. "Optical Measurement of Interplanetary Particulates from Pioneer 10" Jour. Geophys. Res. 79, 3685-3694 (1974).
- Zook, H. A., and Soberman, R. K. "The Radial Dependence of the Zodiacal Light" Space Research XIV, Eds. M. J. Rycroft and R. D. Reasenberg, 763-767 (Akademie-Verlag, Berlin, 1974).

Paper III.C.3.3.
COSPAR XIX
Philadelphia
June, 1976

RESULTS OF THE ASTEROID-METEOROID
PARTICLE EXPERIMENT ON PIONEER 11

R. K. SOBERMAN, S. L. NESTE, and K. LICHTENFELD

General Electric Space Sciences Laboratory
Philadelphia, Pennsylvania, USA

ABSTRACT

The Asteroid-Meteoroid Detector (AMD), an electro-optical instrument that detects and measures particles in space by sensing the sunlight reflected from them, is part of the payload of both the Pioneer 10 and 11 spacecraft. The Pioneer 11 instrument is essentially identical to that on Pioneer 10 (described previously), with some minor modifications. Reduction of the Pioneer 11 data was complicated by the failure of one of the four sensor channels at about 1.1 AU from the sun. Detailed analysis yielded 51 events between 1.0 and 3.5 AU, which were used to determine the particle concentration distribution in that region of space. Weighted curve-fitting of the results shows agreement with the concentrations derived from Pioneer 10 to within about a factor of two. As with the Pioneer 10 results, the exponent of the size dependency varies from about -1.7 for 100 μm radius particles to about -3.2 for 10 cm bodies. The instrument, its operation, and the method of data analysis will be reviewed.

I. Introduction

The Pioneer 11 spacecraft was launched on 5 April 1973 and encountered Jupiter on 2 December 1974, essentially duplicating the pre-encounter mission of its twin, Pioneer 10, which was launched approximately a year earlier. The primary mission of these two spacecraft included investigation of the interplanetary medium, the asteroid belt, and the environment of Jupiter. (See Figure 1). As in the case of Pioneer 10, Pioneer 11 carried an Asteroid-Meteoroid Detector (AMD), the purpose of which was to measure the particulate environment beyond Earth's orbit.

The AMD is an electro-optical instrument that detects and measures particles in space by sensing the sunlight reflected from them. It consists of four parallel Cassegrain-type telescopes with associated sensors and electronics. Figure 2 shows the AMD subsystems as well as the entire spacecraft. The telescopes have 20 cm apertures and 7.5° fields-of-view, and use RCA 7151Q photomultipliers with S20 photocathodes as the sensors. They are surrounded by a light shield to reduce the effects of sunlight reflected or scattered from other parts of the spacecraft. The electronics subsystem includes four channels of amplifying and thresholding circuits, coincidence logic, counters, and storage registers. The optical subsystem is located behind the three-meter diameter high-gain antenna, and is pointed at an angle of 45° relative to the spacecraft spin axis. As the spacecraft rotates (at ~ 5 rpm), the telescopes sweep out an annulus on the celestial sphere. The instrument is basically identical to that flown on Pioneer 10 and has been described in detail (Neste, 1974).

Sun-lit particles are detected as they cross the overlapping fields-of-view of the telescopes. The instrument records the entrance and exit times in each field-of-view, as well as the appropriate irradiances. As a noise rejection technique the AMD requires a three-fold coincidence (i.e., three of the four channels must detect a pulse) in order to constitute a valid particle detection ("event"). A geometric model of the three superimposed fields-of-view is shown in Figure 3.

The data analysis was made more difficult than was the case with Pioneer 10 because one of the channels malfunctioned early in the mission (at 1.1 AU from the sun), resulting in its triggering on noise continually. Thus only two of the other channels had to trigger for an event to be recorded. The malfunction is attributed to a thermally-induced crack in the envelope of the photomultiplier resulting in degradation of the photocathode.

II. Data Analysis

The first step in the data analysis was to screen the recorded events to eliminate those due to noise or other extraneous sources (e.g., stars, spacecraft debris, thruster gas reflections). The following criteria were used:

1. The transit time in two or more channels had to be at least 75 μ sec. This criterion eliminated most of the noise-generated events (almost all of which were of short duration) and took account of the poor reliability of particle detection closer than 10 m to the detectors.
2. Either four-fold coincidence was required, or the peak intensity in the malfunctioning channel had to exceed a predetermined value (7 data bits). Although the sensitivity of that channel degraded considerably, it did not go to zero (as evidenced by its response to Jupiter, which was 8 data bits) and could still be used as a gross indicator of real particles.

The next step in the analysis was to determine the instrument sensitivity as a function of time, pointing direction, and channel. This sensitivity is expressed in terms of a "range-to-radius" (R/a) ratio. For example, a ratio of 10^5 would mean that a 1-cm-radius particle could be detected at a maximum distance of 1 km. The light intensity I reflected from a diffuse sphere is given by

$$I = \frac{I_0 r (\pi a^2) f(\gamma)}{(4\pi R^2) S^2} = \frac{I_0 r}{4S^2} f(\gamma) \left(\frac{a}{R}\right)^2 \quad (1)$$

where I_0 is the solar irradiance at 1 AU from the sun, r is the Bond albedo of the sphere, S is the heliocentric distance in AU, and $f(\gamma)$ is the phase function for scattering from a sphere (van de Hulst, 1957). When the intensity I is set equal to the triggering threshold value, based upon the measured sky background intensity, Equation (1) gives the corresponding R/a ratio. A computer program has been written which calculates the appropriate R/a ratio based on the background data measured by the AMD. As with Pioneer 10, we have assumed a geometric albedo of 0.2 (Bond albedo of 0.3). This value was chosen to extrapolate to the penetration detector results from Pioneers 10 and 11 (Kinard, et al., 1974; Humes, et al., 1975).

It was originally thought that an accurate determination of a particle's range and velocity could be made using the AMD data. However, when the appropriate trajectory equations were solved, conflicting results were obtained. This was due to what we believe to be the peculiar reflecting properties of the particles (Soberman, et al., 1974). An estimate of the range R was obtained from the average transit time $\bar{\tau}$, expressed as

$$\bar{\tau} = \frac{\pi \alpha R}{2v} \quad (2)$$

where α is the half-angle of the field-of-view cone (65 mr) and v is the particle's encounter velocity. Equation (2) assumes the particle moves perpendicularly to the field-of-view axis, and is based on a calculation of average path length across a circle. This assumption

was shown, by computer simulation, to introduce a minimal error in the results (Neste, 1974). Because of the possibility of premature timer shut-off due to noise, as well as the particles' apparent reflecting properties, the transit time used in the range calculation was the longest one recorded in any of the four channels. The encounter velocity used was that corresponding to a circular heliocentric orbit (assuming the particles to be of asteroidal origin) at the position of the spacecraft.

From the calculated values of R/a and R , an estimate of the minimum radius a of each detected particle was obtained. The particles were divided into size categories, each category representing a third of a decade in radius.

The instrument sensitivity (R/a ratio) can be related to a "sensitive volume" within which particles of a given size or larger may be detected. This volume V is approximated by a truncated cone:

$$V = \frac{\pi}{3} \alpha^2 R^3 - V_0 \quad (3)$$

where V_0 is a small volume which is unavailable because it is too close to the detectors.

The primary result to be obtained from the AMD was the concentration of particles as a function of size and heliocentric distance. The concentration (number per unit volume) is given by

$$N = \frac{\Delta\tau}{T\Delta V} \quad (4)$$

where $\Delta\tau$ is the total transit (dwell) time of all detected particles within a particular size regime, T is the effective time of observation, and ΔV is the average sensitive volume corresponding to the size regime. The quantity $\Delta\tau/T$ is the average number of particles in the volume ΔV . Note that the concentration calculated from Equation (4) is cumulative, i.e., it is for particles of a given size and larger.

III. Results and Conclusions

After performing the screening procedure outlined above, it was determined that 51 real events were observed between 1.0 and 3.5 AU. This number was considerably less than that used to derive the Pioneer 10 results (Soberman, et al., 1974), primarily because of the elimination of close-range events, which had been included in the Pioneer 10 analysis. In view of the small number of events it was not considered statistically significant to divide the Pioneer 11 data into regimes of heliocentric distance. All the events were grouped according to estimated minimum size, and the corresponding

cumulative concentrations were calculated as described previously. The results are shown in Figure 4. The number of events in each group is shown in parentheses next to the corresponding data point, and the curve shown gives more weight to the points with a comparatively large number of events. Figure 5 shows the concentration distribution calculated here together with that obtained from Pioneer 10. It is seen that the two results agree to within a factor of two. As with the Pioneer 10 results, the exponent β of the size dependency ($N \sim a^\beta$) varies from about -1.7 for 100 μm particles to about -3.2 for 10 cm bodies. In the case of the smallest particles, the agreement in β applies specifically to the 2.0-3.5 AU results of Pioneer 10.

One should keep in mind the basic assumptions inherent in the results of Figures 4 and 5. These are:

- 1) Particles are treated mathematically as diffuse spheres.
- 2) Geometric albedo = 0.2.
- 3) Encounter velocity corresponds to circular heliocentric orbit.
- 4) Particle transit corresponds to average perpendicular path through viewing cone.

The first assumption is particularly questionable since the results from Pioneer 10 (Soberman, et al., 1974) indicate that the particles have phase functions with many high (specular) peaks. Individual rotating particles with such phase functions would be characterized by high peak intensities as they transit the field of view, while an aggregate of particles, as would be representative of the zodiacal light, would exhibit a low average intensity. The diffuse sphere approximation was used for the lack of a better mathematical model.

The Pioneer 11 AMD experiment appears to confirm the particle concentration distribution obtained earlier from Pioneer 10. Because of the assumptions that were necessary, the absolute positioning of the derived concentration curve remains uncertain. However, the form of the distribution obtained appears to be accurate, and should prove to be of particular value to those formulating new models of the zodiacal light since these were the first experiments to measure scattered light from individual particles in space.

ACKNOWLEDGEMENT

The authors gratefully acknowledge the cooperation and assistance of the personnel of the Pioneer Project Office, NASA Ames Research Center. This work was supported by NASA contracts NAS 2-5609 and NAS 2-6559.

REFERENCES

Humes, D. H., J. M. Alvarez, W. H. Kinard, and R. L. O'Neal, "Pioneer 11 Meteoroid Detection Experiment: Preliminary Results," *Science* 188, 473-474 (1975).

Kinard, W. H., R. L. O'Neal, J. M. Alvarez, and D. H. Humes, "Interplanetary and Near-Jupiter Meteoroid Environments: Preliminary Results from the Meteoroid Detection Experiment," *Science* 183, 321-322 (1974).

Neste, S. L., "An Experimental Model of the Asteroid-Meteoroid Environment From 1.0 to 3.5 AU - Its Characteristics and Implications," General Electric Technical Information Series Report 74SD241, November, 1974.

Soberman, R. K., S. L. Neste, and K. Lichtenfeld, "Optical Measurement of Interplanetary Particulates From Pioneer 10," *J. Geophys. Res.* 79, 3685-3694 (1974).

van de Hulst, H. C., *Light Scattering By Small Particles*, John Wiley and Sons, New York, 1957.

PIONEER 10 AND 11 TRAJECTORY PROFILES

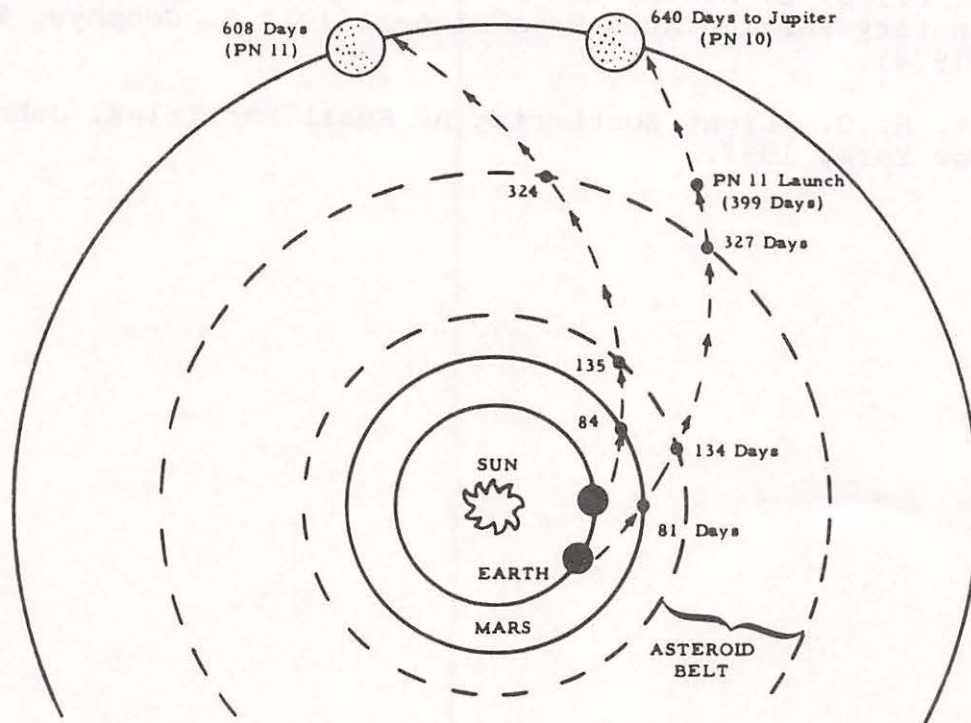
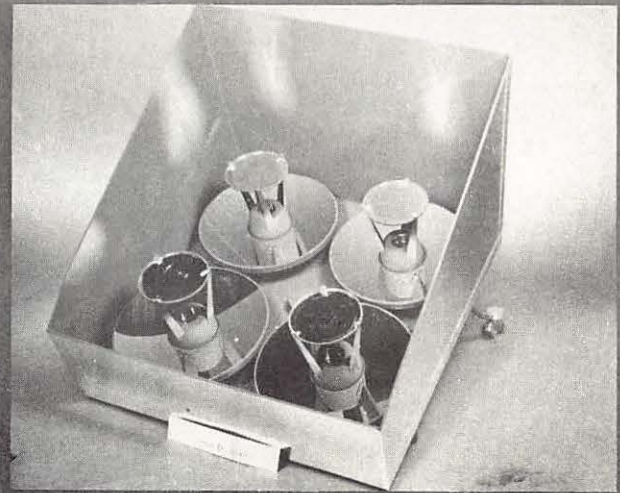
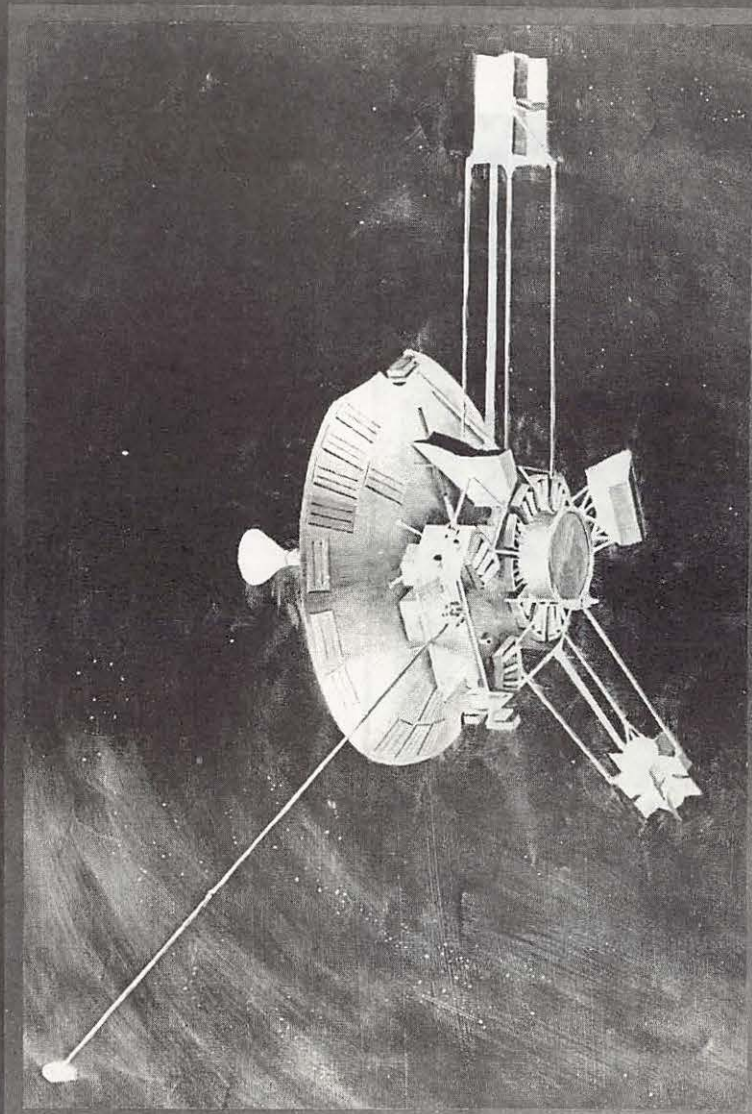
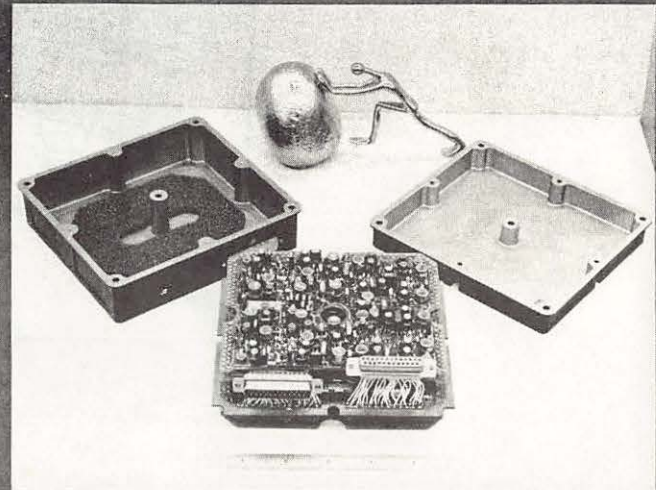


Figure 1. Pioneer 10 and 11 Trajectory Profiles

PIONEER - A M D



OPTICS



ELECTRONICS

Figure 2. Pioneer Spacecraft and Asteroid-Meteoroid Detector Subsystems

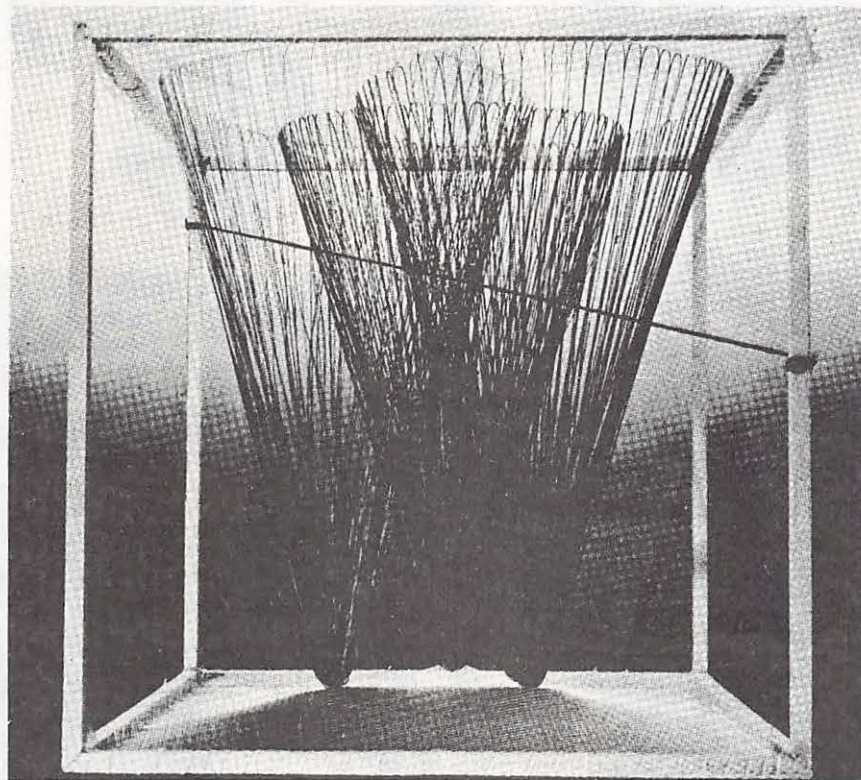


Figure 3. Geometric Model of AMD Fields-of-View

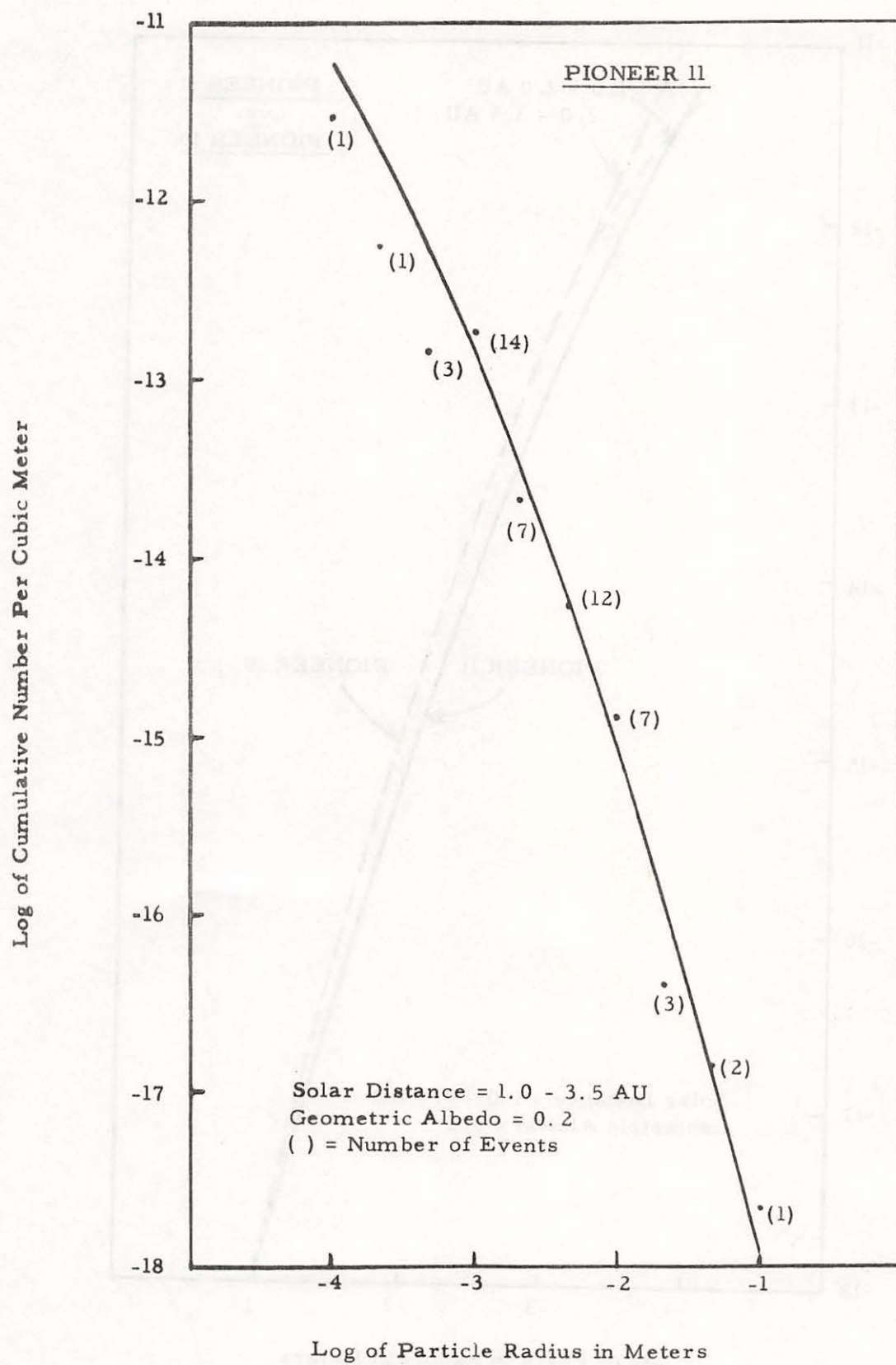


Figure 4. Particle Concentration Distribution from Pioneer 11

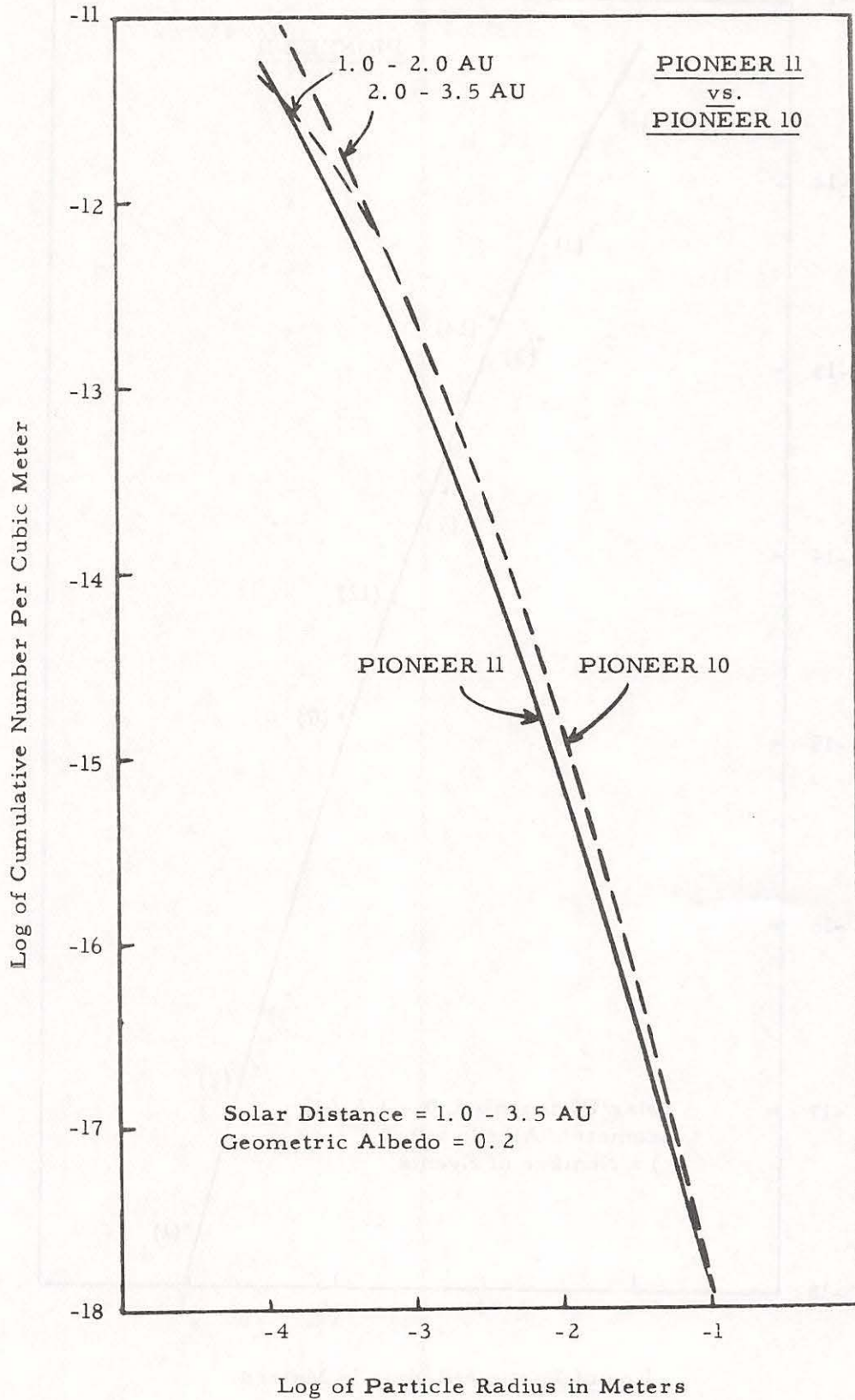


Figure 5. Particle Concentration Distributions from Pioneers 10 and 11